UNIVERSITAT DE BARCELONA

Optimized PET module for both pixelated and monolithic scintillator crystals

David Sánchez Gonzalo

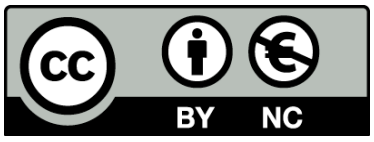

Optimized PET module for both pixelated and monolithic scintillator crystals

David Sánchez Gonzalo

UNIVERSITAT DE BARCELONA

Optimized PET module for both pixelated and monolithic scintillator crystals

Programa de doctorat en Física

Autor/a: David Sánchez Gonzalo

Director/a: David Gascón Fora, Sergio Gómez Fernández

Tutor/a: Blas Garrido Fernández

UNIVERSITAT DE BARCELONA

Optimized PET module for both pixelated and monolithic scintillator crystals

This thesis was submitted to the Faculty of Physics, Universitat de Barcelona (UB), as a fulfillment of the requirements to obtain the PhD degree. The work presented was carried out in the years 2016-2020 in the Department of Quantum Physics and Astronomy at UB with the help of my advisors Sergio Gómez and David Gascón.

Short abstract: The new developments on TOF-PET medical imaging technique are achieving impressive timing performance and thus resulting in an improvement on the final image of the patient. This thesis is focused on the evaluation of the HRFlexToT ASIC which has excellent timing performance on SiPM readout for both pixelated and monolithic scintillator crystal configuration for a TOF-PET module. The results of Coincidence Time Resolution (CTR) shows that the ASIC belongs to the state-of-the-art technology comparing with their direct competitors on TOF-PET applications. This thesis also proposes a simulation framework that encompasses the whole gamma detector, including the crystal, the SiPM sensor and the electronics. It allows to optimize the performance of the module and thus would enable the study of the ultimate timing.

Keywords: Time of flight, positron emission tomography, monolithic scintillator crystal, application-specific integrated circuit, silicon photomultiplier

Contents

List of Figures

List of Tables

Acknowledgements

There are many many people I would like to thank for all their help and support along these years. I will probably forget many of you and I am sorry for that, please forgive me.

I begin with my supervisors David Gascón and Sergio Gomez, both guided, supported and encouraged me during my PhD and helped in the reviewing process. They are the key for this thesis to be a reality. I wish to express my gratitude to Joan Mauricio and Adrià Casajús, who stayed with me many hours helping me understand and debug the control firmware and software used in HRFlexToT ASIC. I would also like to thank Andreu Sanuy and Eduard Picatoste for their fundamental work on PCB design and manufacturing, which was used to test the HRFlexToT ASIC. I would like to thank to the rest of people from the Technological Unit of the Institute of Cosmos Sciences (ICCUB).

I would like to thank David Castrillo from Hamamatsu France sucursal in Spain for all the bureaucratic help during the Industrial PhD as well as for the material provided in all these years. I would like to thank Shunsuke Adachi-san and Shigeyuki Nakamura-san among many other people from Hamamatsu Photonics K. K. in Japan, who helped and supported me with technical issues from the industrial point-of-view.

I would like to thank all the people from the imXgam group during my short-term scientific mission (STSM) at the Centre de Physique des Particules in Marseille, and Emilie Roncalli from UC Davis. Their help was crucial for running the simulations presented in this thesis. I would like to thank Stefan Gundacker and the whole group during my short-term scientific mission (STSM) at the Conseil Européen pour la Recherche Nucléaire (CERN) Crystal Clear lab in the framework of the COST (European Cooperation in Science and Technology) Action TD1401 - Fast advanced Scintillator Timing (FAST). I would like to thank the Instituto de Instrumentación para Imagen Molecular (I3M) research group from Valencia that embrace me during my stay for monolithic crystal characterization and where they exchanged a huge knowledge from PET scanners. I will always be in debt with all of you, and I am at your disposal for anything you may need.

Finally, I wish to thank my parents and my sister for their unconditional support, my whole family and friends that gave me support on the hardest moments. Specially Carol, who helped me on the writing schedule, checking and refining the format of this dissertation and with many good moments in these difficult times, thank you.

Abstract

Technology innovation in Positron Emission Tomography (PET) has experienced tremendous improvements in the last decades since the first commercialized devices back in the 1960s. Recently, the PET scanner has been successfully combined with X-ray Computed Tomography (CT) or Magnetic Resonance (MR), thus making PET-CT and PET-MR a key medical diagnosis tool to combat cancer diseases and several brain disorders such as Alzheimer. Although PET is the most sensitive molecular imaging modality, allowing dynamic and quantitative studies of the metabolic processes inside the body, a number of medical challenges are calling for a further improvement of the sensitivity. Henceforth, the new developments will enable the possibility to perform *in vivo* tracking of the cell dynamics, which will allow to study the activity at the tinniest level in the patient body.

The sensitivity improvement is related to a better Signal-to-Noise Ratio (SNR) in the image quality that would allow detecting smaller tumors, thus accelerating the patient treatment strategy and increasing the recovery chances. Moreover, the sensitivity enhancement also allows to either extend the duration with the same injection dose or decrease the dose quantity. On one hand, a higher scanning time would be particularly useful for those "slow" tracers such as brain imaging using ^{11}C or ^{89}Zr used in immunotherapy research studies. On the other hand, the possibility to reduce the patient dose while keeping the image quality allows to integrate PET protocols into other areas such as inflammation studies, cardiac or infectious diseases. Furthermore, a low enough dose would open PET imaging for pediatric patients, neonatal or prenatal depending on the reduction of the dose.

Three main ways can be considered to improve the sensitivity of PET scanners: improving the detector efficiency, increasing the geometrical acceptance of the gamma photons and improving the Time-Of-Flight (TOF) performance of the system. The first two elements are related to the PET system capability of collecting the gamma photons generated during the radiotracer emission inside the patient. A high detection efficiency is needed to convert each gamma photon arriving to the detector into a signal and ultimately into an image of the organ under study. Additionally, many photons are missed by the PET scanner as the axial length in commercial devices are limited to 20-30 cm. Extending the axial length to 2 m (total body PET) increases the gamma collection a factor 40, thus increasing the sensitivity by the same factor in a full body scan. Lastly, precise TOF information of the two gamma photons emitted in coincidence towards two independent detectors can be combined with the other two approaches in order to further improve PET sensitivity.

This dissertation is focused on the TOF capabilities from a gamma detector module for PET application using monolithic crystal configuration readout by an ASIC developed by our group. The main contributions that addresses this thesis are: (1) full electrical and optical characterization of the ASIC readout named HRFlexToT; (2) energy and time resolution performance using pulsed laser source and segmented crystals; (3) energy and time resolution performance using monolithic crystal and a novel method of time-walk correction using pulsed laser source; (4) development of a new simulation framework that enables the optimization of the whole TOF-PET system.

The first part of the thesis provides a full understanding of the gamma radiation medical imaging focused on PET technology and the basic elements that compose a detector module comprising the scintillator crystal, the sensor and the readout electronics. The major difference in the crystal usage came from its geometry, where one can choose between segmented or monolithic approach. This part measures the intrinsic performance of the module by using segmented crystals in terms of energy and time resolution. An energy resolution of 10% at 511 keV is achieved along with a Coincidence Time Resolution (CTR) of 117 ps in FWHM using an LSO:Ce 0.4% Ca of 2 mm $\times$ 2 mm $\times$ 5 mm size. Additionally, state-of-the-art Single Photon Time Resolution (SPTR) is reported for an ASIC suitable for TOF-PET applications, reaching 142 ps in FWHM using the SiPM model NUV-HD with 4 mm $\times$ 4 mm active area from FBK.

The second part of this dissertation presents the monolithic approach results for energy, spatial and time resolution. The monolithic crystal is a cost-effective configuration in terms of a PET system performance as the cost of the manufacturing process is cheaper while the spatial resolution and DOI information could be improve with respect to segmentation approach. Although the time resolution worsens as the light sharing among many sensor channels reduces the individual photon collection, the DOI information as well as the excellent spatial resolution could lead to new opportunities for TOF-PET systems using monolithic crystal. A CTR of 333 ps is obtained using an LFS of 25 mm $\times$ 25 mm $\times$ 20 mm size covered in teflon. The same length (20 mm) using segmented crystal can reach a CTR below 200 ps FWHM but without any DOI information and a limited spatial resolution (limited to the sensor size). By using this crystal size, a DOI of 4 mm and spatial resolution of 2.2 mm can be obtained.

The last part of the thesis describes a new simulation framework that combines the physics part from GATE/Geant4 and utilizes an electrical simulation to compute the sensor and readout response of the system. Thus, enabling a global optimization of the TOF-PET system that considers the scintillator, the sensor (sensor size, pixel pitch, dead area, capacitance) and the readout electronics (input impedance, noise, bandwidth, summation). Simulations of a segmented approach, in this case form the sensor site, are carried out using this framework. The main objective is to reduce the intrinsic capacitance of the SiPM by segmenting a big one into smaller pieces, which impacts on the rise time of the signal and therefore the time jitter of the sensor. Afterwards, a specific summation circuit is used to sum the N number of channels and obtain a single electrical signal improving the time resolution compared to a big SiPM channel. A CTR improvement of 15% results by implementing the segmentation technique.

The result derived from this dissertation shows a clear state-of-the-art technology readout in terms of timing performance as well as the capabilities of the monolithic crystal to compete against the segmented approach. Nevertheless, a TOF-PET system that requires a CTR below 200 ps will not be integrate monolithic crystals as it requires further research and improvements in terms of time-skew calibration methods. Additionally, the simulation tool here explained could be used in many areas including the one here studied, TOF-PET systems. However, noise contribution terms must be added to the chain in order to have a better and more accurate simulation environment.

You have to make the right choice. As long as you don't choose, everything remains possible.

- Nemo

1

Introduction

In this first chapter, an overview on the medical imaging techniques, in particular Positron Emission Tomography (PET), is given. A brief comparison between functional and anatomical imaging will be shown to emphasize the importance of combining both approaches to achieve the best disease diagnosis and subsequent treatment. However, Time-of-Flight (TOF) PET has been gaining relevance inside the hospitals during the last decade thanks to the technological improvements of a new type of photodetector, the well-known Silicon Photomultiplier (SiPM). These new sensor, in combination with the development of a novel fast Front End (FE) electronics and the promising scintillator crystals, are leading the path to the holy grail on the Nuclear Medicine Imaging (NMI), a detector time resolution of 10 ps capable of generate 3D images in real time with an astonishing spatial resolution of around 1 mm. Indeed, this possibility could open a new era on clinical protocols, allowing to decrease the time exposure, reduce the dose or increase the sensitivity depending on what the doctor is looking at. In brief, this section provides the global description of the whole ToF-PET detector technology and the current state-of-the-art along with the operation principle and the image reconstruction quality. Thus, building the basic blocks to understand the current situation on ToF-PET medical imaging and the future trends.

Contents

1.1 Medical Imaging

Medical imaging is a bast concept that contains anything related to methods, technology and process of generating an image of the interior of a body. All medical imaging techniques are non-invasive and allows the doctor to diagnose and treat many diseases by using these technology capable of looking inside the patient.

Inside medical imaging there are two types of information a doctor would need. Those are the anatomical structure, or the physiological and activity function of the organ under study. The anatomical imaging could be obtained using techniques such as Computed Tomography (CT) [1] or Magnetic Resonance Imaging (MRI) [2], while the physiological part corresponds to the NMI field including Single Photon Emission Computed Tomography (SPECT) [3] and PET [4]. The combination of both types of images provides the position and tumor extent on many cancer diagnosis and treatment [5, 6, 7, 8].

Medical imaging comprises a very rich ecosystem that puts in contact many different disciplines in a common goal, which is of everybody interest, public health. In such a working environment, doctors talks to physicians, engineers and bio-engineers to exchange information, thus evolving the existing technology into a better one capable of detect diseases in an early stage or trace new studies to better understand the biological processes insider our bodies.

1.2 Positron Emission Tomography (PET)

A PET study begins with the injection or inhalation of a radiopharmaceutical (tracer). The scan begins after a delay ranging from seconds to minutes to allow for transport to and uptake by the organ of interest. This tracer is labeled with positron emitting radioisotopes as molecular probes to image and measure the desired biochemical processes. The radioactive isotope disintegrates via a β^+-decay, resulting in the emission of a positron which is being annihilated with an electron in the organ and it is converted into two almost gamma photons ($e^+ + e^- \rightarrow 2\gamma$). The emission of these two annihilation photons of 511 keV happens “back-to-back”, i.e. the angle between their propagation directions is $\sim 180°$. This coincident detection defines a line, the Line Of Response (LOR), along which the annihilation took place. From many LORs, a map of the concentration of the radionuclides can be generated using a tomographic reconstruction algorithm. Thus, resulting in the 3D image of the activity localization of this tracer inside the organ. The mean distance the positron will be spread is called the positron range and depends strongly on the initial kinetic energy and thus on the type of used radioactive isotope (see section 1.2.1).

A diagram of a PET scanner is shown in figure 1.1. The pair of gamma photons are collected by a cylindrical ring of radiation detectors placed around the patient. If two events are recorded with a delay time smaller than the selected "time window", a coincidence event

is recorded. This coincidence event forms a LOR between these two detectors. Finally, the cumulative of LORs permits, as said before, the 3D image reconstruction.

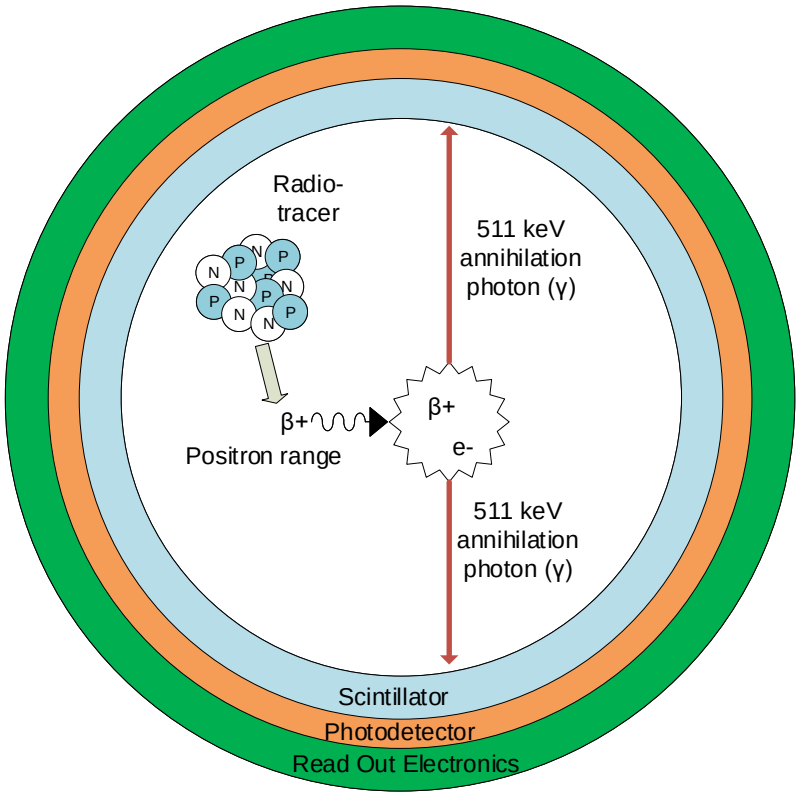

Figure 1.1.: PET system representation. The red line of both gamma photons forms the LOR. A real PET detector is formed by several modules of individual scintillator crystals and photodetectors.

The basic concepts of PET will be explained in the following subsections, i.e. spatial resolution, sensitivity, and image deterioration. Additionally, the explanation of Time-of-Flight PET as a key specification for the current and future PET scanners will be introduced.

1.2.1 Spatial Resolution

The limitations on the ultimate spatial resolution on a PET system will be driven by the laws of physics. This value is given by the positron range, which is defined as the mean distance traveled by the positron between the emission point and the moment when it loses the kinetic energy with the surrounding media during the "thermalization" process. This positron range depends on the emission energy of the positron and therefore depends on the radioisotope used in the tracer. Figure 1.2 illustrates the distribution of the positron range for the most common isotopes used on PET imaging.

One can notice that the distributions are sharp peaked with pronounced tails, thus resulting in a non-Gaussian distribution with FWTM of 1.03 mm, 1.86 mm, 2.53 mm and 4.14 mm for the isotopes of ^{18}F, ^{11}C, ^{13}N and ^{15}O respectively.

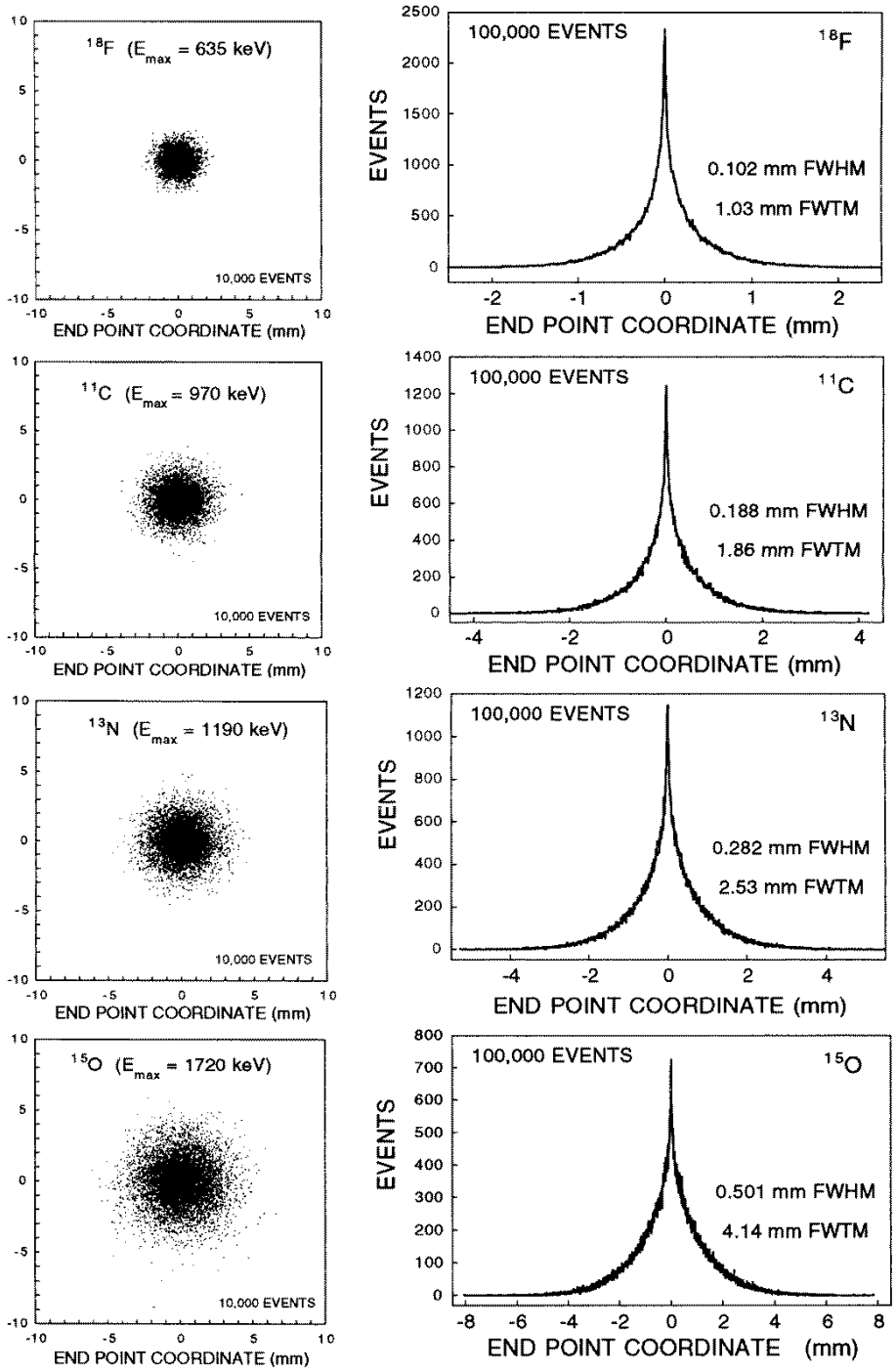

Figure 1.2.: Left: x-y distribution for the positron range in water for ^{18}F, ^{11}C, ^{13}N and ^{15}O isotopes. Right: histogram representation of the x projection from the leftside distribution for each radioactive source. Figure extracted from [9]

Another factor that contributes to the spatial resolution worsening is the fact that the angle between the two gamma photons is not exactly collinear. After thermalization, the momentum of the positron and the electron is non-zero (Fermi motion). Consequently, a deviation from the $\sim 180°$ is observed. The Gaussian distribution of this angulation is calculated to be about 0.5° FWHM at the center of the scanner [10]. The effect on the FWHM spatial resolution due to the non-collinearity ($R_{non-col}$) depends on the detector ring diameter (D) [11] following this expression:

$$R_{non-col} = 0.5 \cdot D \cdot tan(0.25°) = 0.0022 \cdot D \tag{1.1}$$

A large full-body PET system with 80 cm of diameter as an associated $R_{non-col}$ of 1.8 mm at the center of the tomograph. For small animal or brain PET systems with 20 cm of bore diameter, $R_{non-col}$ goes down to 0.4 mm. Besides the positron range is a limiting factor for spatial resolution, PET present another issue that must be addressed in order to improve the spatial resolution, this is the parallax error. One possible solution to solve it is to determine the Depth Of Interaction (DOI) of the gamma photon inside the scintillator crystal. A better explanation of this effect and how to deal with it is explained in section 1.2.3.

1.2.2 Sensitivity

The sensitivity in a PET scanner is defined as the number of true events detected with respect to the total amount of gamma photons emitted by the isotope attached to the tracer. Sensitivity is considered one of the most important system parameters, since it determines the image quality per unit scan time. The gamma photon attenuation coefficient for the scintillation detector is the main parameter which determines detector sensitivity. This means that a thick scintillator crystal with high stopping power (high Z) is preferred as it will increase the detection probability for the incoming gamma photons. Moreover, a high angle of coverage of the PET scanner is needed in order to be as close as possible to the solid angle of 4π from the emission source. The true coincidence event rate (r_{true}), where only non-Compton events are taken into consideration, and thus the sensitivity can be obtained from this expression [10]:

$$r_{true} = r_0 \cdot \varepsilon^2 \cdot \Omega^2 \cdot exp\left(-\frac{T}{\mu}\right) \tag{1.2}$$

r_0 represents the number of positrons/s emitted by the radioactive source. The detector efficiency ε is squared as both gamma photons must be detected in coincidence. The same argument applies to the solid angle coverage which is represented as Ω. In the exponential part, T stands for the patient thickness and μ is the attenuation length.

The current whole-body PET systems are limited by this sensitivity factor. The extremely poor sensitivity (<1%) of this kind of systems is directly related to a degradation on the Signal to Noise Ratio (SNR), thus worsening the image quality at the end of the day. One

solution to this problem consist on extending the number of detector rings in order to cover the entire body of the patient [12]. By using this approach, a massive increment on the solid angle coverage of the detector (Ω) can be achieved. Going from a 20 cm whole-body PET to a 200 cm total-body PET system will lead to multiplication of the sensitivity by approximately a factor 40, which represents an increment on the SNR of $\sqrt{40} \sim 6.3$ [13]. Thus allowing to perform dynamic imaging as seen from the Explorer total-body TOF-PET scanner, which has an axial field of view of 194 cm and a transaxial field of view of 68.6 cm [14].

1.2.3 Image deterioration

Additional degradation factors to the spatial resolution shown in section 1.2.1 are present on a PET scanner such as random and Compton event detection and parallax error. This section will address these effects that limit both, spatial resolution and the SNR of the system which can be partially corrected.

1.2.3.1 Random and Compton event detection

Random coincidences are caused by two unrelated events, where in both cases only one of the two gammas is measured. If these events occur within the time window of the PET detector, the two gamma hits are erroneously assumed to have a common origin resulting in an erroneous LOR. On top of that, the gamma photons can interact with the patient body by means of: photoelectric effect or Compton scattering. In the first case, the total energy of the photon is deposited in the body, which means that it is absorbed, and no detection is recorded. The absorption of gamma photons within the examined body leads to a reduction of the coincidence event rate by 1.1, and in addition to a larger amount of random coincidences. On the other side, the 511 keV photon can suffer a deviation and a loss of energy during a Compton scattering and therefore the coincidence event is recorded with a wrong LOR. At energy of 511 keV, the attenuation length in a human soft tissue is approximately 10.5 cm [15]. A more extensive explanation on radiation-matter interaction will be explained in section 2.2. Figure 1.3 illustrates the different cases of coincidence events taking place in a PET ring detector.

The number of random coincidences ($r_{rand.}$) is proportional to the time window (τ) and to the single events on channel A (s_A) and B (s_B) where the coincidences are detected:

$$r_{rand.} = 2\tau \cdot s_A \cdot s_B \tag{1.3}$$

This means that reducing the time window of the ring detector will reduce the number of random events. Nonetheless, this window must be large enough to detect the true coincidences off centered. An annihilation originated at 30 cm from the center of the FOV (center of the PET scanner) may have a time difference of 2 ns in the coincidence detection [16].

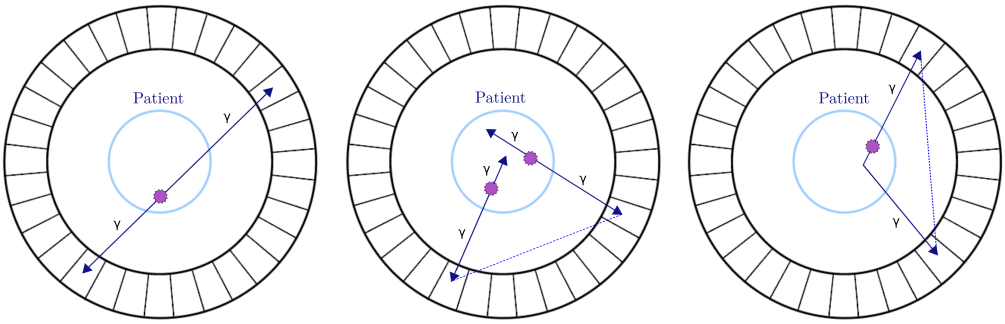

Figure 1.3.: Left: True coincidence with a correct LOR recorded. Middle: Random coincidence from two independent proton anihilations that took place within a delay time smaller than the coincidence time window of the detector. Right: One of the photons undergo Compton scattering and the coincidence detection generates a erroneous LOR.

Additionally, the electronic circuitry dedicated to the time pick-up could have a non-zero time skew which adds to this 2 ns. Typically, the time window is set to 4 times the FWHM of the coincidence time resolution (CTR) of the PET system. Thus, having a small CTR will lead to a lower noise and higher SNR PET system.

Regarding Compton scattering, as mentioned in the first paragraph of this section, the energy lost on the angular deflection of the gamma photon could be used to reject those events with an energy below a predefined threshold value. This requires radiation detectors with a good energy resolution. In a PET scanner, almost 50% of the detected events have suffered Compton scattering, thus leading to a reduction of the sensitivity, as these events will be filtered out from the total. Different approaches are being developed to deal with Compton scattering. TOF information in combination with an additional layer of plastic scintillator could be used to take advantage of Compton effect [17]. Another solution consists on lateral sides readout from a scintillator crystal slab, thus allowing to recover the DOI information and distinguish between photoelectric and Compton event [18].

Under those circumstances, random and Compton events leads to false LORs within the FOV and therefore, they will introduce noise on the final reconstructed image. NEC parameter is commonly used to compare different PET scanners performance [19]:

$$NEC = \frac{r_{true}^2}{r_{true} + r_{rand.} + r_{scat.}} \tag{1.4}$$

where $r_{scat.}$ is the scatter coincidence rate and the other two parameters r_{true} and $r_{rand.}$ accounts for the true and random coincidence events introduced in equation 1.2 and 1.3 respectively. The SNR can be expressed as:

$$SNR \propto \sqrt{NEC} \tag{1.5}$$

The SNR is related to the sensitivity of true coincidence events as expressed in equation 1.2, and the Noise Equivalent Count rate (NEC). The NEC parameter is a measure of valid true coincident events relative to unwanted scattered and accidental coincidence events

recorded by the scanner, and has been widely used as a measure of effective count sensitivity in PET scanners [20]. In other words, NEC can be seen to be the reduced r_{true} that without random and scatter components ($r_{rand.} = r_{scat.} = 0$), produces the same image SNR at the center of the ring as the true coincidence rate obtained by subtracting random and scatter components from the total coincidence count rate.

1.2.3.2 Parallax error

The spatial resolution degrades when the annihilation event occurs far from the center of the FOV. In this condition, the Volume Of Response (VOR), which is the extension of the LOR to the 3D volume probability of proton interaction, increases due to the parallax error. In ring geometry PET systems, for a source at the center of the FOV all emitted photons will enter the detectors perpendicularly to the detector face. However, when the source location has a radial offset from the center, the detectors become angled with respect to the LOR and the annihilation photons may penetrate through the first detector they encounter and be detected in an adjacent detector as shown in figure 1.4. As a consequence, the resolution in the radial direction degrades toward the peripheral FOV [21].

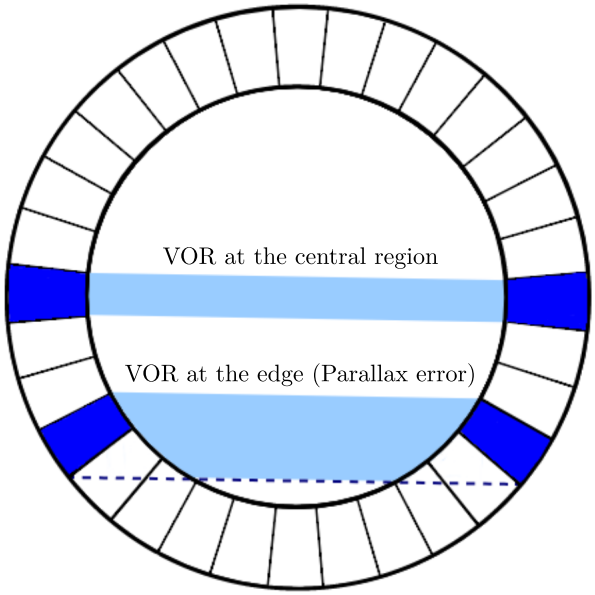

Figure 1.4.: Representation of the so-called parallax error [22], i.e. the broadening of the VOR towards the edge of the PET scanner.

Parallax error can be suppressed by detecting the 3D position interaction inside the scintillator crystal. This means enabling DOI information of the 511 keV gamma photon detection. Different solutions have been studied and implemented in order to extract a precision measurement of the DOI encoded on the light distribution of the scintillator crystal. Double side readout is one approach [23], where a single crystal is coupled to two photodetectors in both sides. This methods allows to quantify the difference in light collection between both ends, thus obtaining the DOI with a few millimeters in precision [24]. Another

method consist on stacking multiple layers of crystal plus photosensors in the axial direction in order to have a DOI in the order of the crystal length, thus achieving an impressive spatial resolution close to 1 mm [25] at expenses of increasing the price of the device by approximately a factor N depending on the number of layers. Further DOI information techniques such as phoswich [26] and monolithic crystal light sharing [27] are presented in section 2.2 of this work.

1.2.4 Time-Of-Flight PET

In conventional PET imaging a positron annihilation is recognized along the entire line of response, not at the actual location of the event. In Time-Of-Flight (TOF) PET the difference in the arrival times of the two photons is measured with high precision, this helps to localize the emission point along the LOR within a small region of the gamma emission. The uncertainty on the TOF measurement is proportional to the spatial accuracy resolution as shown in equation 1.6.

$$\Delta x = \frac{c\Delta t}{2} \tag{1.6}$$

where δt is the time resolution of the device, c corresponds to the speed of light and Δx value is the position resolution. Taking a TOF PET system with time resolution of 500 ps will lead to a spatial uncertainty of 7.5 cm in the LOR. Thus considering an 80 cm diameter scanner allows to reject almost 90% of the "false" annihilation positions along the LOR. Figure 1.5 illustrates the TOF implementation in a PET ring. In addition, if the time resolution of the detector is in the order of 10 ps, this corresponds to a precision of 1.5 mm along the LOR and hence coming close to the maximum positron range of commonly used radioisotopes. In this scenario, a direct 3D reconstruction of the β^+-decay would be possible without the need of any image reconstruction [28, 29].

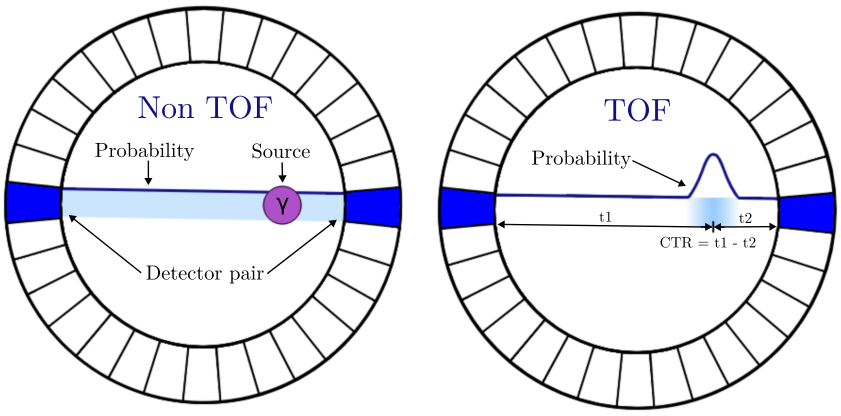

Figure 1.5.: Probability distributions of the annihilation point along LOR for a non-TOF and TOF PET systems.

The overall effect is lower noise and higher contrast recovery, thus resulting in a higher signal-to-noise ratio (SNR). The gain in SNR by using a TOF system can be expressed as a function of the patient body diameter (D) and the time resolution of the device [30]:

$$Gain_{SNR} = \frac{SNR_{TOF}}{SNR_{non-TOF}} = \sqrt{\frac{2D}{c\Delta t}} \tag{1.7}$$

Taking a body diameter of 40 cm and table 1.1 shows the $Gain_{SNR}$ as the time resolution of the system improves towards the 10 ps. At the same time, the sensitivity is represented by taking the gain squared. Notice that the gain on the brain scanner reduces as the FOV decreases, which means that the overall impact of TOF information is not as relevant as for a larger PET ring. At the same time, for a body scanner, heavier patients (higher Body Mass Index, BMI) would benefit the most on TOF information as the gain in SNR and sensitivty increases with D. A SNR and sensitivity improvement of factor 5 and 25 respectively can be achieved with a time resolution of 100 ps in a body PET scanner. This impressive increment on sensitivity allows to either, reduce the quantity on radiotracer injected into the patient, or reduce the exposure time while keeping the image quality of a non-TOF system [31].

Table 1.1.: Gain of a TOF-PET system with respect to a non-TOF device by improving the time resolution. Two cases with D = 40 cm (body scan) and D = 15 cm (brain scan) are computed.

Δt $[ps]$	$Gain_{SNR}$ (body)	$Gain_{SNR}$ (brain)	$Gain_{sens.}$ (body)	$Gain_{sens.}$ (brain)
500	2.3	1.4	5.3	2
200	3.7	2.2	13.3	5
100	5.2	3.2	26.7	10
10	16.3	10	266.7	100

It has also been observed that TOF PET reconstruction is less sensitive to erroneous or inconsistent attenuation correction, normalization and scatter correction. An example of real TOF-PET imaging can be found in [32]. In this case, the study was done using a Gemini TF scanner (Philips Medical Systems) with a time resolution of ∼600 ps. Figure 1.6 depicts the improved structural details by using TOF information even if this is not as low as 100 ps. Notice that in both cases (top and bottom), the patients have a high BMI as the TOF information benefits from higher D values.

The state-of-the-art TOF-PET scanner from Siemens Biograph Vision scanner reaches the 200 ps in coincidence time resolution [33]. From table 1.1 one can anticipate that the sensitivity impact is almost a factor 3 higher in a 200 ps system (Siemens Biograph Vision scanner) compared to 600 ps PET scanner (Siemens Biograph mCT Flow). This sensitivity burst permits to identify a smaller lesion by taking advantage of cutting-edge TOF-PET technology as can be seen in figure 1.7. Thus, opening the door to a new and previously mentioned time resolution target in PET imaging, everyone trying to reach the 10 ps time resolution wall [28].

In brief, precise TOF information increases the SNR and therefore the sensitivity of the system. Moreover, artifacts are dramatically reduced after image reconstruction, thus

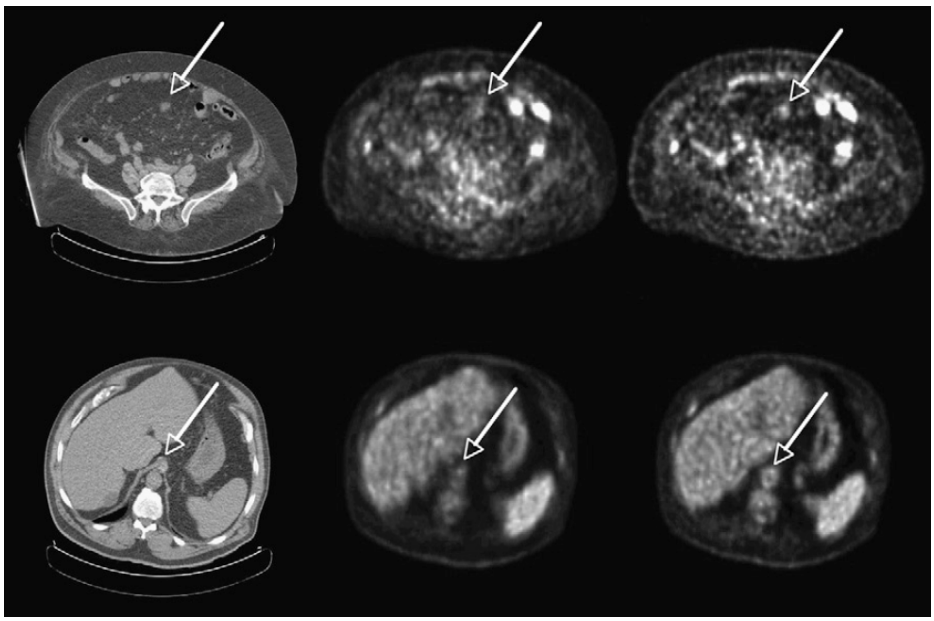

Figure 1.6.: Representative transverse sections of 2 different patients: low dose CT (left), non-TOF MLEM (middle), and TOF MLEM (right). (Top) Patient 1 with colon cancer (119 kg, BMI 46.5) shows a lesion in abdomen seen in CT much more clearly in TOF image than in non-TOF image. (Bottom) Patient 2 with abdominal cancer (115 kg, BMI 38) shows structure in the aorta seen in CT much more clearly in TOF image than in non-TOF image. Image taken from [32]

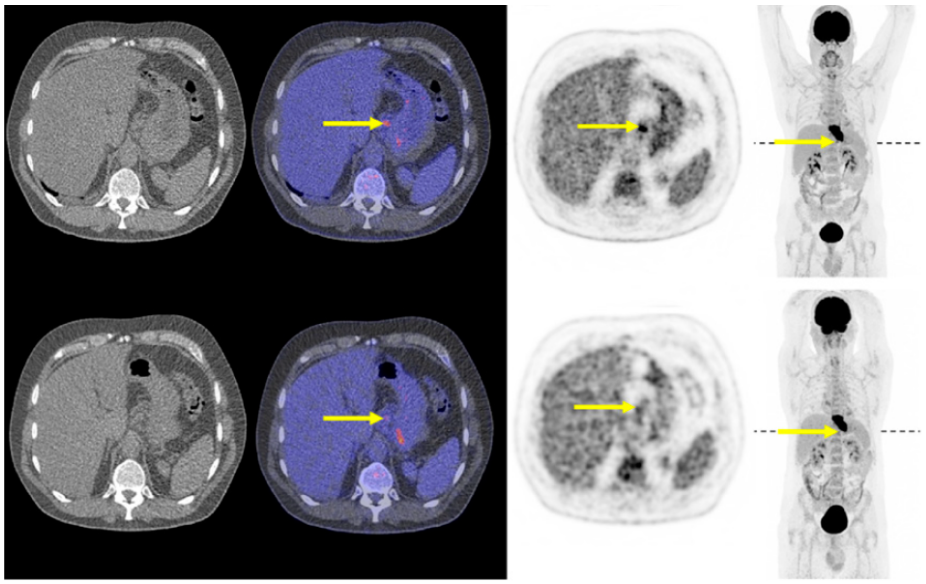

Figure 1.7.: Transaxial CT, PET/CT, PET, and maximum-intensity-projection PET images (from left to right) acquired on Biograph Vision (top) and Biograph mCT (bottom) for 59-y-old man (weight, 106 kg) with metastasized esophageal cancer. Position of transaxial slice is indicated on maximum-intensity projection (dashed line). Arrows indicate small lesion found on Biograph Vision images that did not appear as such on Biograph mCT images. Image taken from [34]

contributing to an overall better image quality. To put it differently, TOF provides a dramatic improvement in robustness of the image quality, since it is much less sensitive to any possible human or instrumentation error or even mismatch between PET and CT/MRI scan [35, 36].

1.3 Multimodal imaging

Multimodal or multiplexed imaging refers to simultaneous production of a combined image using both anatomical and functional information [37]. The most common combinations are PET/SPECT-CT [38] and now PET-MRI [39, 40] is becoming a reality too, on which the dynamic or physiological process (PET/SPECT) can be imaged along with a precise localization (MRI or CT) of this activity.

The multimodal imaging was taken into serious consideration in the 1990s decade. At this time, two approaches were coexisting. In one side, the asynchronous image acquisition where the patient goes through two different machines, one for the anatomical image acquisition (CT) and then to a functional information imaging detector (PET/SPECT). Afterwards, both images are merged by using computational image techniques. On the other side, the synchronous approach where both machines are integrated in one single device and the image is taken at the same time and merged automatically.

Several problems appear on the asynchronous acquisition system, mainly due to the uncertainty on the patient position along both scans. The misalignment between both imaging procedures hinders the software correction during the image merging. One approach to solve this problem consist on sticking a set of tracking marks to the body and then correct either the patient position on the second scan, or the image reconstruction algorithm by using the tracking marks coordinates [41].

Thanks to the pioneer work of Hasegawa, et. al. [42] on combining SPECT with CT opened the synchronous approach. Thus, integrating both modalities in the same devices was demonstrated to be the best solution to achieve a combined image. In this case, the problem seen with the asynchronous method disappears and each frame of the recorded image is taken simultaneously on both imaging systems and therefore the image reconstruction is automatically produced without any major correction.

The following subsections will account for a short illustration on how PET can be combined with CT or MRI and the benefits on using this hybrid technology.

1.3.1 PET-CT

At the same time, the PET-CT concept was also studied (early 1990s) by Townsend, Nutt and co-workers. The first prototype was developed by Siemens (Biograph) and tested in 1998 at the University of Pittsburgh [7]. From this point, the use of this type of equipment

has grown exponentially as the cost and specification improved over the last years. Together with Siemens, GE Healthcare introduced their own scanner (Discovery LS) [43] and close to these two, Philips Medical Systems was the last big company developing a PET-CT system (Gemini) [44]. Additionally, Toshiba Medical Corporation and Hitachi Medical companies are offering PET-CT scanners, making a total of 5 enterprises worldwide capable of providing with this specific multimodal system.

In PET imaging, loss of detection of true coincidence photons due to their absorption and loss of their energy in the body results in what is commonly known as attenuation [45]. Nevertheless, the anatomical information from a CT scan can be employed to extract an attenuation map that the PET image reconstruction will take advantage later on.

The main use of PET-CT is focused on oncology, neurology and cardiology. A multimodal image using a PET-CT scanner can be seen in figure 1.8.

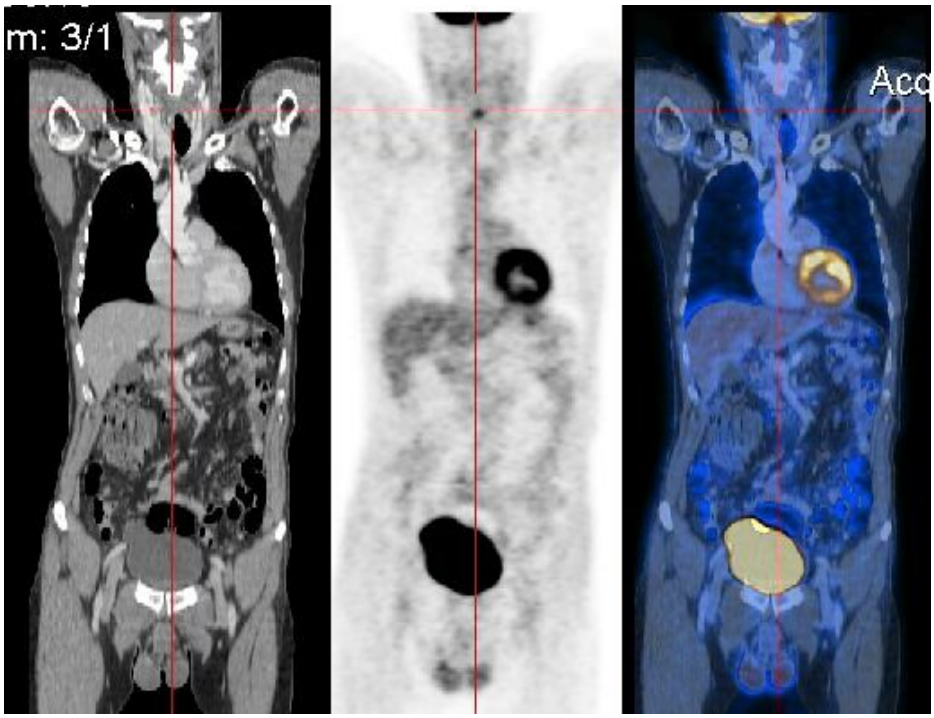

Figure 1.8.: Left) Anatomical structure from a CT image. Middle) Physiological information from a PET image. Right) Superposition of both images generating a single one containing the localization and size of the activity under study.

The CT scan on the left image allows to identify each organ, while the PET scanner on the middle accounts for the activity of the organ under study. In addition, the combination of both results on the right-side image, where the localization and the functionality can be quantified in a single composition.

1.3.2 PET-MRI

The last member to appear on the scene was the PET-MRI system because of the technological difficulties to integrate the PET device close to a MR with several Tesla of magnetic field [46, 47]. The photodetector used at this time was mainly the Photomultiplier Tube (PMT), which are not suitable to resist the strong magnetic fields close to the MR scanner and therefore, they were typically placed separated and enclosure outside the magnetic field. This problem, along with the electronics from the PET module, which could cause artifacts on the MR image, were the main drawbacks on using PET in combination with MR technology. At the same time, the MRI system can interfere with the PET device causing distortions on the signal generation. An alternative to PMT in order to solve the malfunction of the PET photodetector consist on using a solid-state detectors, in this case an Avalanche Photodiode (APD). APDs are insensitive to magnetic field, making them a good candidate to be integrated within the MRI [48, 49]. However, the APD has a lower gain and temperature variations in comparison with PMT, which could result in a worst Signal to Noise and requires a temperature controlled environment during the scanning process. The most recent developments on the solid-state detectors are dominated by the so called Silicon Photomultiplier (SiPM), which presents a high gain, comparable to the PMT, and it is insensitive to magnetic fields as the APD.

The MRI image has an excellent tissue contrast and opens the frontier to dynamic studies with pharmacological MRI, functional MRI, Dynamic Contrast-Enhanced MRI, and MR spectroscopy [50]. However, MRI image does not provide the attenuation information as the CT does and therefore a more sophisticated methods to extract the attenuation map are needed. It is challenging to separate air and bone, and measure the density variations in the lung with MRI.

The PET-MRI interest is focused on neurological diseases, where this higher contrast and dynamic studies can play a key role. Moreover, the radiation dose is lower compared to CT as no ionizing source is used in MRI. Figure 1.9 shows an image comparing both PET-MRI and PET-CT on a brain image.

A higher contrast on the edges and small tissues anatomy of the brain are clearly visible with MR imaging and the skull (bone) is less visible compared to CT image as has being explained above.

1.4 Dissertation outline

This PhD thesis is organized as follows:

Chapter 2 describes the basic elements involved in a gamma detector module for PET application. Firstly, the scintillator crystal used for gamma photon collection and how the new developments could impact on the timing performance is shown. Secondly, the solid

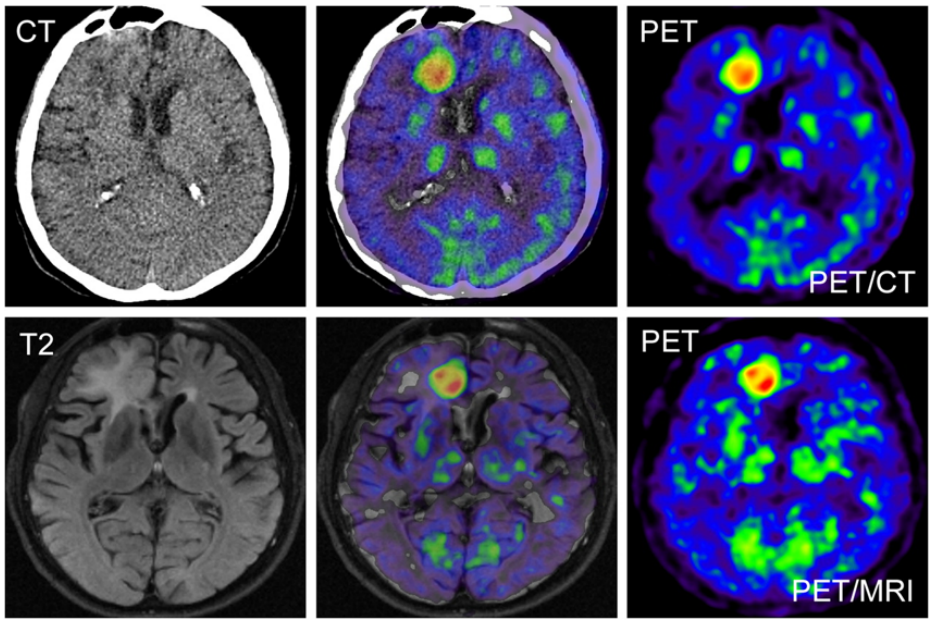

Figure 1.9.: PET/CT and PET/MRI images of 56-y-old patient with glioblastoma multiforme on right side in frontal area close to interhemispheric fissure. Figure extracted from [51].

stated detector, in this case the SiPM, working principle along with the characterization made in our lab and the drawbacks of this technology are outlined. Lastly, it describes the FlexToT ASIC used in the readout of the SiPM sensor signal and compares with the direct competitors for TOF-PET applications.

The segmented scintillator crystal approach and its CTR performance is presented in Chapter 3. Additionally, energy resolution measurements along with state-of-the-art SPTR results are also shown.

In Chapter 4 monolithic crystals are evaluated for TOF application. Encouraging results on CTR are here illustrated using medium size crystals and a novel time-skew calibration using a pulsed laser setup. The spatial resolution and DOI capabilities of this system are presented.

A new simulation framework for the full detector chain that includes the crystal, sensor and electronics is described in Chapter 5. The timing information from the gamma emission is degraded in every one of those three stages, which makes this simulation tool a handful kit to globally optimize the TOF-PET system. The sensor segmentation approach is also presented, and the preliminary results are given, where an improvement with respect to no segmentation is found.

Lastly, the conclusion of the thesis and the trending of the TOF technology are summarized in the concluding chapter of this work. In addition, the valorization of the industrial PhD work is also reported with some considering remarks in order to improve the already excellent program.

1.5 Bibliography

[1] T. M. Buzug, Computed Tomography, Springer Berlin Heidelberg, Berlin, Heidelberg, 2011, pp. 311–342. doi:10.1007/978-3-540-74658-4_16.
URL https://doi.org/10.1007/978-3-540-74658-4{_}16

[2] G. H. Glover, Overview of functional magnetic resonance imaging, Neurosurgery Clinics of North America 22 (2) (2011) 133–139. doi:10.1016/j.nec.2010.11.001.

[3] S. Knight, D. B. Min, V. T. Le, Implementation of a cardiac {PET} stress program: comparison of outcomes to the preceding {SPECT} era., JCI Insight (2018).
URL doi:10.1172/jci.insight.120949

[4] J. J. Vaquero, P. Kinahan, Positron Emission Tomography: Current Challenges and Opportunities for Technological Advances in Clinical and Preclinical Imaging Systems, Annual Review of Biomedical Engineering 17 (2015) 385–414. doi:10.1146/annurev-bioeng-071114-040723.

[5] H. Jadvar, P. M. Colletti, Competitive advantage of PET/MRI, European Journal of Radiology 83 (1) (2014) 84–94. doi:10.1016/j.ejrad.2013.05.028.
URL http://dx.doi.org/10.1016/j.ejrad.2013.05.028

[6] C. Catana, A. Drzezga, W. D. Heiss, B. R. Rosen, PET/MRI for neurologic applications, Journal of Nuclear Medicine 53 (12) (2012) 1916–1925. doi:10.2967/jnumed.112.105346.

[7] T. Beyer, D. W. Townsend, T. Brun, P. E. Kinahan, M. Charron, R. Roddy, J. Jerin, J. Young, L. Byars, R. Nutt, A combined PET/CT scanner for clinical oncology, Journal of Nuclear Medicine 41 (8) (2000) 1369–1379.

[8] E. L. Rosen, W. B. Eubank, D. A. Mankoff, FDG PET, PET/CT, and breast cancer imaging, Radiographics 27 (SPEC. ISS.) (2007) 215–230. doi:10.1148/rg.27si075517.

[9] C. S. Levin, E. J. Hoffman, Calculation of positron range and its effect on the fundamental limit of positron emission tomography system spatial resolution, Physics in Medicine and Biology 44 (3) (1999) 781–799. doi:10.1088/0031-9155/44/3/019.

[10] Simon R. Cherry, J. A. Sorenson, M. E. Phelps, Physics in Nuclear Medicine, Saunders, 2012.

[11] S. Derenzo, PRECISION MEASUREMENT OF ANNIHILATION POINT SPREAD DISTRIBUTIONS FOR MEDICALLY IMPORTANT POSITRON EMITTERS (July) (2010) 35–43.

[12] S. R. Cherry, T. Jones, J. S. Karp, J. Qi, W. W. Moses, R. D. Badawi, Total-Body PET: Maximizing Sensitivity to Create New Opportunities for Clinical Research and Patient Care., J Nucl Med. (2018) 3–12.
URL https://doi.org/doi:10.2967/jnumed.116.184028

[13] M. Conti, Focus on time-of-flight PET: The benefits of improved time resolution, European Journal of Nuclear Medicine and Molecular Imaging 38 (6) (2011) 1147–1157. doi:10.1007/s00259-010-1711-y.

[14] R. D. Badawi, H. Shi, P. Hu, S. Chen, T. Xu, P. M. Price, Y. Ding, B. A. Spencer, L. Nardo, W. Liu, J. Bao, T. Jones, H. Li, S. R. Cherry, First human imaging studies with the explorer total-body PET scanner, Journal of Nuclear Medicine 60 (3) (2019) 299–303. doi:10.2967/jnumed.119.226498.

[15] C. Burger, G. Goerres, S. Schoenes, A. Buck, A. Lonn, G. Von Schulthess, PET attenuation coefficients from CT images: Experimental evaluation of the transformation of CT into PET 511-keV attenuation coefficients, European Journal of Nuclear Medicine 29 (7) (2002) 922–927. doi:10.1007/s00259-002-0796-3.

[16] S. R. Meikle, R. D. Badawi, Quantitative Techniques in PET, Positron Emission Tomography (2006) 93–126doi:10.1007/1-84628-007-9_5.

[17] M. Kuramoto, T. Nakamori, S. Kimura, S. Gunji, M. Takakura, J. Kataoka, Development of TOF-PET using Compton scattering by plastic scintillators, Nuclear Instruments and Methods in Physics Research, Section A: Accelerators, Spectrometers, Detectors and Associated Equipment 845 (2017) 668–672. doi:10.1016/j.nima.2016.06.100.
URL http://dx.doi.org/10.1016/j.nima.2016.06.100

[18] J. Barrio, N. Cucarella, A. Gonzalez, M. Freire, V. Ilisie, J. Benlloch, Characterization of a high aspect ratio detector with lateral sides readout for Compton PET, IEEE Transactions on Radiation and Plasma Medical Sciences (2020) 1–1doi:10.1109/TRPMS.2020.3006862.

[19] M. Conti, State of the art and challenges of time-of-flight PET, Physica Medica 25 (1) (2009) 1–11. doi:10.1016/j.ejmp.2008.10.001.
URL http://dx.doi.org/10.1016/j.ejmp.2008.10.001

[20] S. C. Strother, M. E. Casey, E. J. Hoffman, Measuring PET Scanner Sensitivity: Relating Countrates to Image Signal-to-Noise Ratios using Noise Equivalent Counts, IEEE Transactions on Nuclear Science 37 (2) (1990) 783–788. doi:10.1109/23.106715.

[21] I. Mohammadi, I. F. Castro, P. M. Correia, A. L. Silva, J. F. Veloso, Minimization of parallax error in positron emission tomography using depth of interaction capable detectors: Methods and apparatus, Biomedical Physics and Engineering Express 5 (6) (2019). doi:10.1088/2057-1976/ab4a1b.

[22] Parallax error.
URL https://radiologykey.com/pet-physics-and-instrumentation/

[23] S. Seifert, D. R. Schaart, Improving the time resolution of TOF-PET detectors by double-sided readout, IEEE Transactions on Nuclear Science 62 (1) (2015) 3–11. doi:10.1109/TNS.2014.2368932.

[24] M. C. Maas, D. R. Schaart, D. J. Van Der Laan, P. Bruyndonckx, C. Lematre, F. J. Beekman, C. W. Van Eijk, Monolithic scintillator PET detectors with intrinsic depth-of-interaction correction, Physics in Medicine and Biology 54 (7) (2009) 1893–1908. doi:10.1088/0031-9155/54/7/003.

[25] M. Watanabe, A. Saito, T. Isobe, K. Ote, R. Yamada, T. Moriya, T. Omura, Performance evaluation of a high-resolution brain PET scanner using four-layer MPPC DOI detectors, Physics in Medicine and Biology 62 (17) (2017) 7148–7166. doi:10.1088/1361-6560/aa82e8.

[26] J. H. Jung, Y. Choi, Y. H. Chung, O. Devroede, M. Krieguer, P. Bruyndonckx, S. Tavernier, Optimization of LSO/LuYAP phoswich detector for small animal PET, Nuclear Instruments and Methods in Physics Research, Section A: Accelerators, Spectrometers, Detectors and Associated Equipment 571 (3) (2007) 669–675. doi:10.1016/j.nima.2006.10.293.

[27] D. R. Schaart, H. T. Van Dam, S. Seifert, R. Vinke, P. Dendooven, H. Löhner, F. J. Beekman, A novel, SiPM-array-based, monolithic scintillator detector for PET, Physics in Medicine and Biology 54 (11) (2009) 3501–3512. doi:10.1088/0031-9155/54/11/015.

[28] P. Lecoq, Pushing the Limits in Time-of-Flight PET Imaging, IEEE Transactions on Radiation and Plasma Medical Sciences 1 (6) (2017) 473–485. doi:10.1109/TRPMS.2017.2756674.
URL http://ieeexplore.ieee.org/document/8049484/

[29] S. Gundacker, E. Auffray, K. Pauwels, P. Lecoq, Measurement of intrinsic rise times for various L(Y)SO and LuAG scintillators with a general study of prompt photons to achieve 10 ps in TOF-PET, Physics in Medicine and Biology 61 (7) (2016) 2802–2837. doi:10.1088/0031-9155/61/7/2802.

[30] T. F. Budinger, Time-of-Flight Positron Emission Tomography: Status Relative to Conventional PET 24 (1) (1983) 13–15.

[31] T. Sekine, G. Delso, K. G. Zeimpekis, F. D. G. Barbosa, E. E. Voert, M. Huellner, P. Veit-Haibach, Reduction of 18F-FDG dose in clinical PET/MR imaging by using silicon photomultiplier detectors, Radiology 286 (1) (2018) 249–259. doi:10.1148/radiol.2017162305.

[32] J. S. Karp, S. Surti, M. E. Daube-Witherspoon, G. Muehllehner, Benefit of time-of-flight in PET: Experimental and clinical results, Journal of Nuclear Medicine 49 (3) (2008) 462–470. doi:10.2967/jnumed.107.044834.

[33] J. Van Sluis, J. De Jong, J. Schaar, W. Noordzij, P. Van Snick, R. Dierckx, R. Borra, A. Willemsen, R. Boellaard, Performance characteristics of the digital biograph vision PET/CT system, Journal of Nuclear Medicine 60 (7) (2019) 1031–1036. doi:10.2967/jnumed.118.215418.

[34] J. van Sluis, R. Boellaard, A. Somasundaram, P. H. van Snick, R. J. Borra, R. A. Dierckx, G. N. Stormezand, A. W. Glaudemans, W. Noordzij, Image quality and semi-quantitative measurements on the biograph vision PET/CT system: Initial experiences

and comparison with the biograph MCT, Journal of Nuclear Medicine 61 (1) (2020) 129–135. doi:10.2967/jnumed.119.227801.

[35] C. Lois, B. W. Jakoby, M. J. Long, K. F. Hubner, D. W. Barker, M. E. Casey, M. Conti, V. Y. Panin, D. J. Kadrmas, D. W. Townsend, An assessment of the impact of incorporating time-of-flight information into clinical PET/CT imaging, Journal of Nuclear Medicine 51 (2) (2010) 237–245. doi:10.2967/jnumed.109.068098.

[36] R. Minamimoto, C. Levin, M. Jamali, D. Holley, A. Barkhodari, G. Zaharchuk, A. Iagaru, Improvements in PET Image Quality in Time of Flight (TOF) Simultaneous PET/MRI, Molecular Imaging and Biology 18 (5) (2016) 776–781. doi:10.1007/s11307-016-0939-8.
URL http://dx.doi.org/10.1007/s11307-016-0939-8

[37] L. Martí-Bonmatí, R. Sopena, P. Bartumeus, P. Sopena, Multimodality imaging techniques, Contrast Media and Molecular Imaging 5 (4) (2010) 180–189. doi:10.1002/cmmi.393.

[38] G. K. von Schulthess, H. C. Steinert, T. F. Hany, Integrated PET/CT: Current Applications and Future Directions, Radiology 238 (2) (2006) 405–422. doi:10.1148/radiol.2382041977.
URL https://doi.org/10.1148/radiol.2382041977

[39] G. Delso, S. Fürst, B. Jakoby, R. Ladebeck, C. Ganter, S. G. Nekolla, M. Schwaiger, S. I. Ziegler, Performance measurements of the siemens mMR integrated whole-body PET/MR scanner, Journal of Nuclear Medicine 52 (12) (2011) 1914–1922. doi:10.2967/jnumed.111.092726.

[40] A. Drzezga, M. Souvatzoglou, M. Eiber, A. J. Beer, S. Fürst, A. Martinez-Möller, S. G. Nekolla, S. Ziegler, C. Ganter, E. J. Rummeny, M. Schwaiger, First clinical experience with integrated whole-body PET/MR: Comparison to PET/CT in patients with oncologic diagnoses, Journal of Nuclear Medicine 53 (6) (2012) 845–855. doi:10.2967/jnumed.111.098608.

[41] D. W. Townsend, Multimodality imaging of structure and function, Physics in Medicine and Biology 53 (4) (2008). doi:10.1088/0031-9155/53/4/R01.

[42] B. H. Hasegawa, E. L. Gingold, S. M. Reilly, S.-C. Liew, C. E. Cann, Description of a simultaneous emission-transmission CT system, in: R. H. Schneider (Ed.), Medical Imaging IV: Image Formation, Vol. 1231, International Society for Optics and Photonics, SPIE, 1990, pp. 50–60. doi:10.1117/12.18783.
URL https://doi.org/10.1117/12.18783

[43] O. Mawlawi, D. A. Podoloff, S. Kohlmyer, J. J. Williams, C. W. Stearns, R. F. Culp, H. Macapinlac, Performance characteristics of a newly developed PET/CT scanner using NEMA standards in 2D and 3D modes, Journal of Nuclear Medicine 45 (10) (2004) 1734–1742.

[44] S. Surti, A. Kuhn, M. E. Werner, A. E. Perkins, J. Kolthammer, J. S. Karp, Performance of Philips Gemini TF PET/CT scanner with special consideration for its time-of-flight imaging capabilities, Journal of Nuclear Medicine 48 (3) (2007) 471–480.

[45] S. Basu, T. C. Kwee, S. Surti, E. A. Akin, D. Yoo, A. Alavi, Fundamentals of PET and PET/CT imaging, Annals of the New York Academy of Sciences 1228 (1) (2011) 1–18. doi:10.1111/j.1749-6632.2011.06077.x.

[46] J. E. Mackewn, D. Strul, W. A. Hallett, P. Halsted, R. A. Page, S. F. Keevil, S. C. R. Williams, S. R. Cherry, P. K. Marsden, Design and development of an MR-compatible PET scanner for imaging small animals, IEEE Transactions on Nuclear Science 52 (5 I) (2005) 1376–1380. doi:10.1109/TNS.2005.858260.

[47] R. R. Raylman, S. Majewski, S. K. Lemieux, S. S. Velan, B. Kross, V. Popov, M. F. Smith, A. G. Weisenberger, C. Zorn, G. D. Marano, Simultaneous MRI and PET imaging of a rat brain, Physics in Medicine and Biology 51 (24) (2006) 6371–6379. doi:10.1088/0031-9155/51/24/006.

[48] B. J. Pichler, B. K. Swann, J. Rochelle, R. E. Nutt, S. R. Cherry, S. B. Siegel, Lutetium oxyorthosilicate block detector readout by avalanche photodiode arrays for high resolution animal PET, Physics in Medicine and Biology 49 (18) (2004) 4305–4319. doi:10.1088/0031-9155/49/18/008.

[49] C. Catana, Y. Wu, M. S. Judenhofer, J. Qi, B. J. Pichler, S. R. Cherry, Simultaneous acquisition of multislice PET and MR images: Initial results with a MR-compatible PET scanner, Journal of Nuclear Medicine 47 (12) (2006) 1968–1976.

[50] S. R. Cherry, Multimodality Imaging: Beyond PET/CT and SPECT/CT, Seminars in Nuclear Medicine 39 (5) (2009) 348–353. doi:10.1053/j.semnuclmed.2009.03.001. URL http://dx.doi.org/10.1053/j.semnuclmed.2009.03.001

[51] A. Boss, S. Bisdas, A. Kolb, M. Hofmann, U. Ernemann, C. D. Claussen, C. Pfannenberg, B. J. Pichler, M. Reimold, L. Stegger, Hybrid PET/MRI of intracranial masses: Initial experiences and comparison to PET/CT, Journal of Nuclear Medicine 51 (8) (2010) 1198–1205. doi:10.2967/jnumed.110.074773.

2

Gamma detector module for PET

The vast majority of the modern PET systems that are being build today are based on scintillator crystal coupled to a SiPM and readout by a specific front-end electronics. Depending if Time of Flight (ToF) information is necessary or not, the front-end may be implemented in an Application-Specific Integrated Circuit (ASIC) or designed using discrete components respectively. As the miniaturization and 3D integration seems to be a market trend, the ASIC solution is a hot topic for many of big companies on PET imaging systems, such as General Electric or Siemens.

This second chapter explains the working principle of the three elements involved in the radiation detector block used along this thesis. First, the front-end electronics ASIC (FlexToT), followed by the sensor technology (SiPM) and finally the scintillator crystal. There has being a large and fast improvement during the last decade that has entrenched the TOF-PET technology as the most sensitive method to detect dynamic activities inside the human body.

Contents

2.1 Introduction

The basic state-of-the-art module used on a PET system is composed by the three key elements described below. First, a fast scintillator crystal to convert the gamma photon into visible light. Lutetium based crystals are the most common nowadays, i.e. lutetium (-yttrium) oxy-orthosilicate (L(Y)SO) family, which has high light output (∼25000 photons/MeV [1]), really fast rise time (∼60 ps) and relatively short decay pulse time (∼50 ns), which leads to an excellent CTR for a pet system as the best cost-effective scintillator. Second, the fast light extraction must be addressed with also a fast response photosensor in order to convert the light into electrical signal [2]. Traditionally, the PhotoMultiplier Tube (PMT) [3] was used for this matter, but the semiconductor technology lead by the SiPM is substituting the aforementioned PMT. This new photosensor is more compact, robust, insensitive to the electromagnetic radiation and has lower bias voltage requirements compared to PMTs. The working principle of the SiPM will be explained in the following sections. Finally, the electrical signal generated from the SiPM must be managed by the front-end electronics, if ToF information has to be preserved, an ASIC is needed. The ASIC takes the analog current signal of the SiPM and extracts the important features such as the energy (number of photons arriving) and the timestamp of the gamma interaction.

The present section concentrates on an ASIC for ToF-PET imaging system named HRFlexToT [4], which is the evolution of the FlexToT, a previous ASIC developed by the group. A full description and characterization have been carried out in order to evaluate the capabilities of the chip. Moreover, a theoretical approach mixed with experimental data will be shown regarding the SiPM and crystal as well. These three elements are the basic blocks for a single detector module, the full ring of a PET imaging system (figure 1.1) is composed by tens to thousands of those individual modules.

2.2 Scintillator crystal for PET

The scintillator crystal is a key element in a PET detector, it allows to detect high energy gamma particles that otherwise would go through the photodetector without being captured. The energy of the gamma photon is deposited in the crystal in one or several places, depending on the interaction process. In these processes, the gamma ray is either absorbed completely or its trajectory is changed abruptly into other directions. As a result, this deposited energy is converted into scintillation photons in the visible and ultraviolet range of wavelengths. Parameters such as timing or energy resolution of the whole detector are strongly dominated by the scintillator material and its geometrical shape. In this section, an overview on the main scintillator crystals characteristics and the different inorganic materials used on PET applications is given.

2.2.1 Working principle

There are two possible mechanisms involved in the energy deposition for a 511 keV gamma photon. Those are photoelectric absorption and Compton scattering. In PET imaging, the probability of the pair production event compared to Compton scattering and photoelectric absorption remains very low until the gamma energy approaches several MeV. Therefore, pair production will be neglected from now on. An extended explanation on radiation-mater interaction and scintillator processes can be found in [5, 6]

On one hand, if a gamma photon interacts with the crystal by means of the photoelectric effect, the entire energy of the photon is transferred to an electron bound to an atom. Consequently, this electron is ejected and excites higher energy states of the crystal lattice, which decay by emitting lower energy (2-6 eV) scintillation photons. Then, those photons can be detected by the photodetector, which typically has a spectral response between the near ultraviolet (UV) to the near infrared (IR), depending on the sensor model and technology. On the other hand, during a Compton scatter event, only part of the energy is converted into scintillation light. Afterwards, the same photon can either produce additional Compton and photoelectric effect or escape the crystal. Thus, resulting in various active centers and introducing a position blurring and affecting the gamma interaction point determination. The photoelectric cross section (σ_{PE}) increases with the density of the material (ρ) and the atomic number (Z_{eff}) as can be seen in the following equation:

$$\sigma_{PE} = cnt \cdot \frac{Z_{eff}^{x}}{E_{gamma}^{3.5}} \tag{2.1}$$

where the "x" power from the atomic number varies 3 and 4 depending on the energy of the gamma ray, and E_{gamma} is the energy of the incident gamma photon. On the contrary, the Compton cross section is proportional to the electron density, which is directly related to ρ [1]. Under those circumstances, a higher probability of gamma interaction with the crystal will be fulfilled for those scintillator crystals with both, high density for a higher absorption probability, and high atomic number in order to increase the photoelectric effect (all energy deposited and no blurring). These two parameters are directly related to the detector efficiency, which measures the capability of the system to stop a gamma particle, e.g. 511 keV gamma photons in this case.

The detection efficiency of a gamma detector may be characterized by the fraction of incident gamma rays that are partially or fully absorbed by it (photoelectric of Compton effect). Considering "L" as the total thickness of the scintillator crystal, exposed to a mono-energetic beam of 511 keV, the initial gamma ray intensity (I_0) is attenuated according to:

$$I = I_0 \cdot exp(-L\lambda) \tag{2.2}$$

where I denotes the intensity (number) of the gamma rays without interacting with the scintillator crystal, and λ corresponds to the attenuation length. The smaller the λ, the higher the stopping power and therefore, a higher number of gamma photons will be collected. Figure 2.1 compares different linear attenuation coefficients ($1/\lambda$) for five high Z_eff crystals used in radiation detectors.

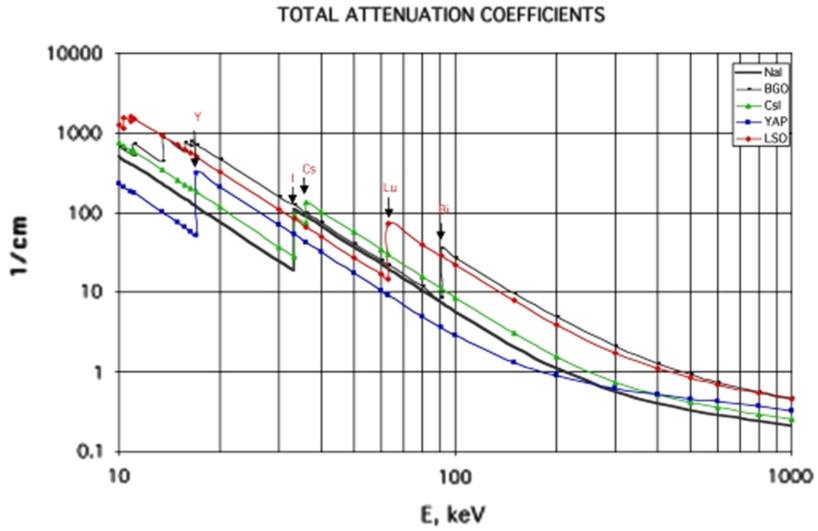

Figure 2.1.: Attenuation coefficient as a function of the gamma energy in different scintillators crystal used in PET. Image taken from [7]

From the upper plot, one can see that for X-rays photons (energy below 63 keV), the best candidates to be built in a X-ray imaging detector are YAP and CsI, which have higher attenuation coefficients with respect to the other materials. On the contrary, considering gamma photons with energies above 90 keV, BGO and Luthetium based scintillator [8] crystals will be clearly favored for PET scanners (511 keV). To put it in another way, to achieve similar efficiency, NaI detectors must be more than twice as thick compared with BGO and LSO detectors. A comparison table with many more materials can be seen in section 2.2.2.

The number of the aforementioned scintillator photons emitted after the gamma ray interaction with the crystal are parameterized as the light yield (LY). A typical LSO crystal can produce up to 30.000 photons/MeV [9] in a short emission pulse of about 50 ns duration. To collect as many scintillation photons as possible, the crystal is enclosed in a reflective light tight case, e.g. teflon or Enhanced Specular Reflector (ESR), at all surfaces except at the entrance window of the photodetector, where an optical coupler is used in order to maximize the number of extracted photons. Not all the emitted fluorescence photons reach the light collection system of the photodetector. A full 3D simulation process from gamma absorption to optical photon collection can be seen in figure 2.2.

There are absorptive losses in the crystal due to the partial overlap of the emission and absorption bands of the crystal. Another key point on the scintillator characteristics is the time resolution which depends strongly on the response time of the scintillator, its light yield and light-detection efficiency as equation 2.3 shows in first approximation [11].

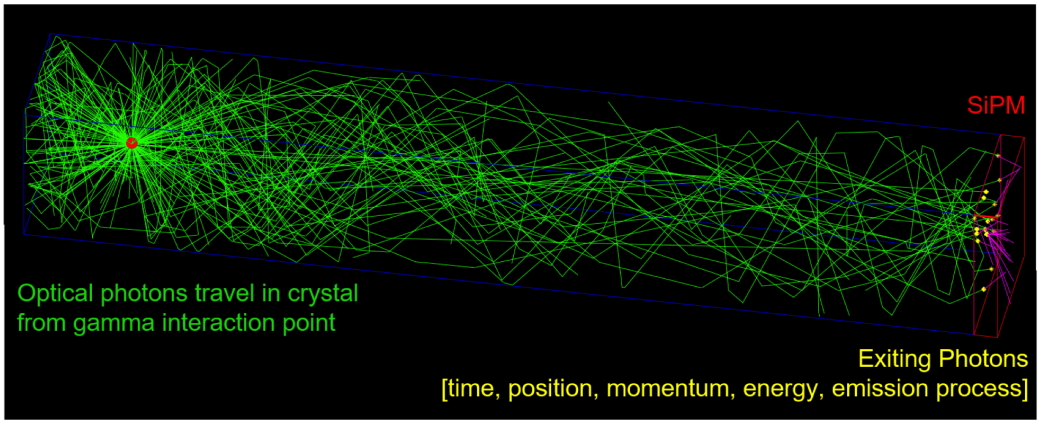

Figure 2.2.: Optical simulation of a gamma photon absorption inside a scintillator crystal (blue) and the scintillation photon extraction to a SiPM photodetector (red). Image taken from [10]

$$CTR \propto \sqrt{\frac{\tau_r \tau_d}{LY}} \tag{2.3}$$

where τ_r and τ_d corresponds to the rising time and decay time on the emission pulse shape. Improving the timing performance of the crystal represents an increment on the LY as well as shortening the scintillation pulse on the rise and decay time. Additionally, high count rate applications requires a short decay time to permit good coincidence timing resolution so as to minimize random coincident events and pileup effects [12].

2.2.2 Inorganic scintillator on PET scanners

Inorganic scintillator crystals are the ones selected for all current PET systems as they have a good relation between stopping power, light yield and timing performance compared to organic crystals (liquid or plastic). Inorganic scintillators commonly contain impurities such as Cerium (Ce^{3+}) in LSO or NaI co-doped with Talium (Tl). Those impurities act as activators centers in which the scintillation process takes place. A certain number of steps are following from the gamma energy deposition until the scintillation photons are generated. These steps can be divided in:

- Photo-electron creation: as mentioned on section 2.2.1, the unbound electron generated in the photoelectric process generates a large number of electron-hole pairs until the energy is falling below the ionization threshold, i.e. twice the bandgap energy of the crystal.
- Trapping: the electron-hole pairs may be trapped in the activation areas created by ions present on the crystal lattice, e.g. the Ce^{3+} ions on the LSO crystal.
- Recombination and emission: The electron-hole pair recombination process starts, and the emission of photons are produced with an energy equivalent to the energy gap

between the exited and ground states. This gap depends on the dopant and it is chosen in order to match the sensitivity response of the photodetector (visible scintillator photons preferred).

As mentioned before, scintillator materials suitable for PET have a small attenuation length (higher probability of gamma interaction), high photofraction, in order to have photoelectric effect dominant over Compton scattering. Additionally, a high light yield increases the energy resolution which allows a higher rejection of tissue-scattered events and Compton events in the crystal. Finally, a fast rise and decay time improving the CTR of the system. The properties of several relevant inorganic scintillators for PET imaging are summarized in table 2.1. Note that there is no scintillator crystal that fulfill the best values for each one of the parameters. On the positive side, there are a few materials that are close to be the best candidate, all the Luthetium crystal family (LSO, LYSO and LFS). It combines high detection efficiency (attenuation length of 12.3 mm), a high photofraction (Z_{eff}), high light yield ($\sim$ 30 photons/keV), short decay time ($<$ 40 ns) and a fast time ($<$ 100 ps). They are all not hygroscopic and have good mechanical properties. An improvement on the performance on the luthetium materials is possible by co-doping it with Ca^{2+} [9]. Under these circumstances, a relatively high LY of almost 40 ph/keV, faster rise time of less than 10 ps and short decay times below 35 ns can be achieved. These are excellent conditions for ToF-PET application. Nevertheless, one disadvantages observed in this material is the purported non-proportionality of light output to the deposited energy, and possible different decay times in samples obtained from larger and different ingots. For example, the energy resolution shows an $E^{-1/2}$ type dependence with photon energy [13, 14]. Another disadvantage of LSO is the presence of a naturally long-lived isotope of lutetium (176Lu) within the crystal. It has been estimated that 2.6% of the lutetium in LSO is ^{176}Lu, which has a half-life of approximately 4×10^{10} years undergoing β^--decay. From the abundance, half-life, density and atomic mass one can easily calculate that this isotope accounts for a background singles count rate of 280 counts per second in 1 cm^3 LSO. Since PET scanners are operated in coincidence mode, most of these events are automatically filtered out. However, it could have a strong impact on small animal PET detectors where the count rate is lower compared to human PET scanners.

Another crystal that presents excellent performance on energy resolution LY and decay time is $LaBr_3$, although the stopping power and hence the efficiency of the detector is lower compared to LSO. Whatsmore, it is hygroscopic and requires hermetic sealing which increases the manufacturing and mechanics assembly of the system. In spite of the rich assortment of inorganic scintillators now available, there is a continual search for new inorganic scintillator materials.

As a part of the Crystal Clear Collaboration at CERN, many groups are working on new scintillator development with a better combination of price/performance. New metamaterials with extraordinary properties allowing to increase LY and extraction efficiency from the scintillator crystal are being studied [19].

Table 2.1.: Overview on intrinsic properties for the most common scintillator crystals used on PET imaging systems. Data collected from [7, 15, 16, 17, 18]

	NaI:Tl	BGO	GSO:Ce	LYSO:Ce	LSO:Ce:0.2%Ca	LFS	LuAP:Ce	$LaBr_3 : Ce$
peak of emission (nm)	410	480	440	420	**420**	425	365	360
refractive index	1.85	2.15	1.85	1.81	1.82	**1.81**	1.94	1.9
density (g/cm^3)	3.67	7.13	6.71	7.19	7.4	7.35	**8.34**	5.3
LY (ph/keV)	41	9	8	30	39	28	12	**60**
τ_r (ps)	600	> 1000	> 1000	68	**9**	90	600	-
τ_d (ns)	230	300	60	39	31	33	**17**	35
Z_eff	70	53	**78**	64	66	64	65	46
λ @ 511 keV (cm)	2.59	1.12	1.5	1.12	1.14	1.15	**1.1**	2.23
Energy res. @ 662 keV (%)	6	10	8	9	8	8	15	**3**
Hygroscopic	Yes	No	No	No	No	No	No	Yes
Magnetic susceptibility	No	No	Yes	No	No	No	No	No

NOTE: Bold values stands for the best value among all the crystal materials here presented

2.2.3 Timing information and state of the art

The 10 ps challenge "healthy" competition on ToF-PET imaging faces major technological barriers [11]. In one side, the scintillation light emitted by the crystal is limited by the time constrains (rise and decay time) and the number of photons (LY). On the other side. And on the other side, the single photon time resolution of the state-of-the-art photodetector and the readout electronics. Taking a closer look into the state-of-the-art scintillator crystals as LSO:Ce co-doped with Ca^{2+}, there are between 1-2 photons/ps emitted in the first 10 ps after the gamma absorption. Thus, the number of available photons inside the crystal are to few. Furthermore, those photons travel in a random path until they reach the photodetector, thus smearing the timing of the first emitted photon. Hence, light emission and transport constitute nowadays the main bottlenecks to achieve ultrafast timing with moderate energies and standard scintillators. One simple solution to improve timing performance consist on shortening the crystal length, where the travel path and also de DOI is being stretched and therefore reducing the photon time arrival dispersion [20]. However, the efficiency of the detector is reduced dramatically as the width of scintillator crystal available to interact with the gamma photon decreases. On the contrary, the combination of high photon density emitters, e.g. plastic scintillator BC442, in combination with typical scintillator crystals could be a solution to overcome the low photon density [19], thus reducing the CTR towards the 10 ps. Looking in the direction of increasing the light extraction from the crystal, a novel approach combining Photonic Crystals (PhCs) and the actual scintillator crystals has being proposed in [11]. By means of photonic nano-structuring of the different surfaces of the scintillator, the light transport can be optimized, which has a direct impact on the timing and LY performance of the detector. With this solution, enhancements in the scintillation light extraction by over 40%, and in the energy resolution, ranging from 9% to nearly 40% for LSO (compared to the standard grease-coupling), have been experimentally demonstrated in [21].

Production and collection of prompt photons is also a possibility in addition to the scintillation pulse, even in relatively small numbers (a few hundreds) would significantly improve the time resolution. Among the possible sources of prompt photons, the Cherenkov effect must be considered by either, pure Cherenkov radiators (PbF_2) or taking advantage on the few Cherenkov photons emitted in conventional scintillator crystals (about 10 Cherenkov photons per 511 keV) [22, 23]. Most of these photons are on the mid-NIR UV region which makes it even difficult to detect with conventional photodetectors. New SiPM models are being developed which have impressing PDE values on the deep-UV region (up to 30%) [24]. Another possible way to produce prompt photons is to develop hetero-structures based on a combination of standard scintillators (such as LSO, LYSO, BGO) and nanocrystals [25]. In such systems quantum confinement offers very attractive properties, among which a very high quantum efficiency and ultrafast decay time.

Additionally, high quality semiconductors, e.g., GaAs or CdSe, based on nanostructures have an LY that can reach 70%–80% of absorbed energy as compared to at most 15% in standard scintillators such as LSO or $LaBr_3$. Moreover, the emission lifetime is usually shorter than 1ns (crucial on CTR). These impressive performances are attributed to electron

confinement, phonon confinement and optical resonances taking place in these nanomaterials. Embedded in meta-structures based on polymers or heavy scintillators (such as LSO, LYSO or heavy scintillating glasses) they could complement the standard scintillation signal with a very fast light component that could be exploited for reaching an ultimate timing resolution [25]. Combining some layers with standard scintillator crystals are being tested in order to take advantage on this ultrafast timing performance.

2.3 SiPM as the next generation of photodetector on PET

Silicon Photomultiplier is a trending semiconductor device that is replacing the most extensively used photodector, which is the Photomultiplier Tube (PMT) [26]. The SiPM combines low-light level detection capability up to single photon as the PMT does, it is insensitive to magnetic fields while the PMT is not, more compact and robust design plus high uniformity of response. Moreover, the SiPM operates at bias voltages around 30-60 V, while the PMT must be powered at 100-1000 V, which overall simplifies the integrated electronics and the device handling. All these characteristics make the SiPM suitable for many applications that were dominated by PMTs until now. Taking advantage on the insensitive to magnetic fields characteristic of the SiPM, a new generation PET detectors appeared. In these systems, the SiPM is integrated as the main photodetector instead of the PMT, thus improving the TOF capability of the system. The first PET-SiPM scanner ever build and commercialized using SiPMs was SIGNA PET/MR from GE Healthcare [27, 28]. An overview on the working principle as well as the drawbacks and state of the art related to SiPM technology is shown in this section.

2.3.1 SiPM working principle

The SiPM, also named MultiPixel Photon Counter (MPPC), is a semiconductor photodiode build of many Single Photon Avalanche Detectors (SPADs) or microcells joint together on silicon substrate with common load [2]. Typically, in SiPMs, the microcells are of identical size and arranged in a rectangular pattern. Depending on the device, the size of a microcell varies from 10 μm to 100 μm and the number of microcells per device ranges from several hundreds to several tens of thousands, depending on the active area. An equivalent circuit [29] of the SiPM can be seen in figure 2.3a. Detailed information is given in section 5.2.2.

All the fired microcells represented are connected in parallel. A microcell is a series combination of SPADs and a quenching resistor R_q, in parallel with a its associated parasitic capacitance at the high-impedance SPAD node represented as C_q. The electrical model considers that the fired SPAD is a parallel combination of a capacitor C_d (representing the junction capacitance) with a series combination of a switch S_A, voltage source V_{bd} (equal to the breakdown voltage), and a resistor R_d (representing the resistance of the entire SPAD during a discharge).

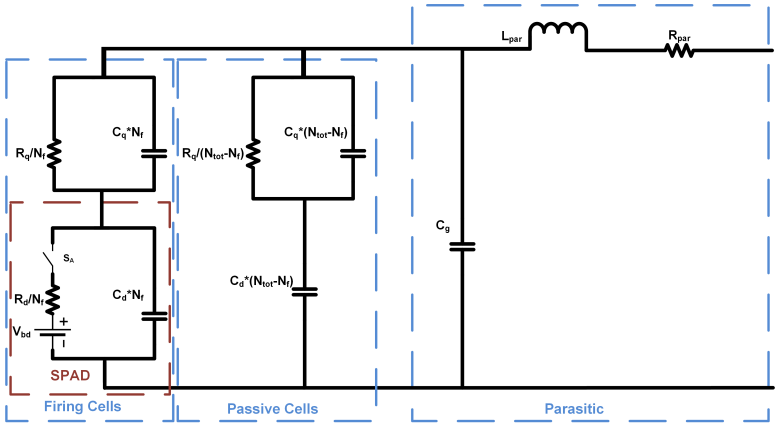

(a)

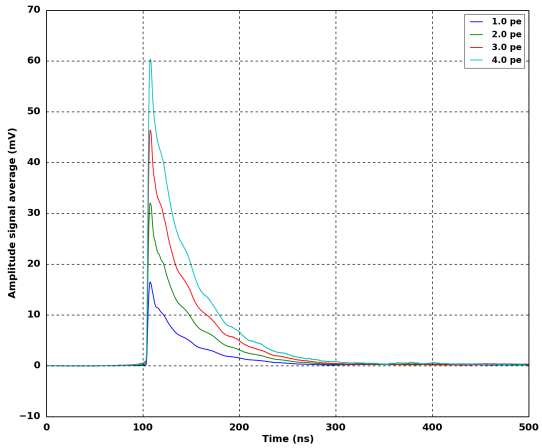

(b)

Figure 2.3.: (a) SiPM schematic representing firing and passive cells. (b) Averaged waveform of 1 to 4 cells fired (photons detected) from a S13360-3075 Hamamatsu MPPC, 3x3 mm^2 sensor with 75 μm microcell size, bias at 60 V.

SiPMs have active areas ranging from 1 mm^2 to 6 mm^2 and spectral sensitivities from UV to IR, peaking in the visible (400 nm - 500 nm). Every SPAD operates in Geiger mode, under bias voltage (V_{bias}) of 5-15% over the breakdown voltage (V_{vd}) ranging from 20 to 60 V. Each carrier generated by either photon arriving or by thermal generation gives rise to a Geiger-type avalanche discharge. At the instant the avalanche begins, S_A closes causing C_d to be discharging through R_d (R_d « R_q) with the time constant R_dC_d. This Geiger discharge is stopped when the voltage goes below the breakdown value due to the external polysilicon resistor (R_q) that decouples electrically each cell and S_A opens; the typical values of these resistors goes from 100 to 500 kΩ. Then, V_{bias} recharges C_d with a time constant $R_q(C_d+C_q)$ in the order tens to hundreds of nanoseconds. The single microcell gain is determined by the charge accumulated in the intrinsic capacity ($C_d + C_q$); typical value associated to this capacity are in the order of tens of femtofarads. The resultant voltage waveform generated of a N number of cells fired at the same time is shown in figure 2.3b.

From the physical point of view, the topology of a SPAD is similar to the APD structure [30]. A few micron epitaxy layer on low resistive p substrate creates the drift region with a low built-in electric field as can be seen in figure 2.4. The thin depletion region between the p^+

and n^+ layers with very high electric field, up to 10^6 V/cm is created, where the conditions for Geiger mode discharge take place ($V_bias > V_vd$). The electrical decoupling between the adjacent pixels is provided by polysilicon resistive strips and uniformity of the electric field within a pixel by the n^- guard rings around each SPAD. All SPADs are connected by common aluminum (Al) strips, in order to readout the SiPM signal.

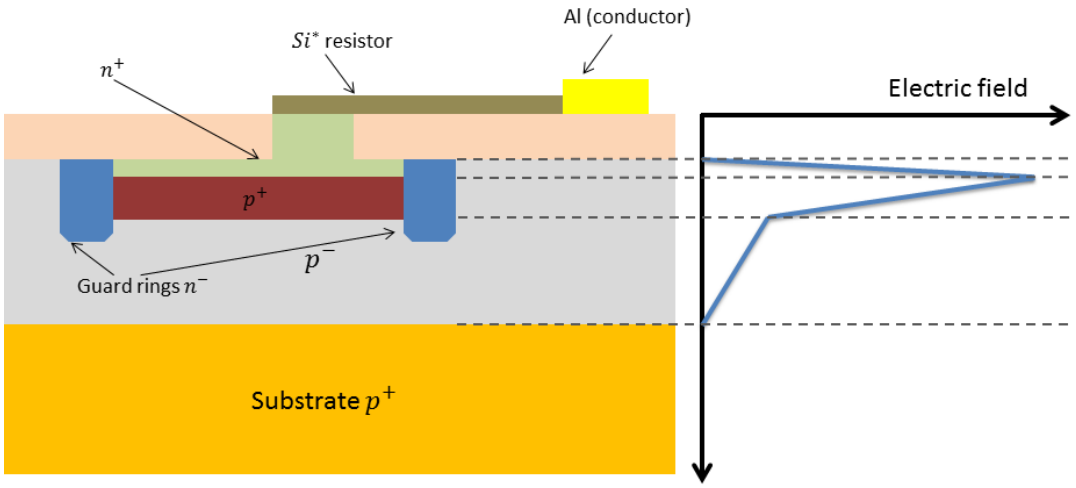

Figure 2.4.: Schematic representation of a single pixel structure and the corresponding electric field shape.

Photon Detection Efficiency (PDE) gives the probability of a SiPM to produce an output in response of an incident photon. In other words, it quantifies the ability of a photodetector to detect photons. The PDE value represents the ratio between the number of detected photons and the total number of photons impinging into the SiPM. It varies as a function of the V_{ov} and the wavelength λ of the incoming light, and the equation can be calculated as follows:

$$PDE(V_{ov}, \lambda) = QE(\lambda) \cdot P_{Tr}(V_{ov}, \lambda) \cdot FF(V_{ov}, \lambda) \tag{2.4}$$

QE stands for Quantum Efficiency, which includes all the probability factors involving the photon capture. Including the transmittance of the surface, and the absorption into the region of interest on the SiPM. This absorption depth will depend on the wavelength, for what the later structure can be optimized through the Beers-Lambert law and therefore optimize the SiPM for a given range of wavelengths [31]. The p-on-n junction enhances the blue-UV photon collection while n-on-p arrangement has an optimal drift towards green-red photons. This could affect the timing performance (SPTR) of the SiPM depending on the incident light [32]. Blue-UV detectors are chosen in PET applications since the photons generated on the most common scintillator crystals have a narrow emission spectrum around 400 nm (see table 2.1).

The effective Fill Factor (FF) depends on the layout design for the microcell interconnection. Consequently, this factor determines de active area of the microcell, thus decreasing in most of the cases the total PDE of the SiPM. This becomes critical specially for small microcell size, where the non-sensitive area reaches almost the 60% of the total microcell area, thus reducing the FF to 40%. On the other side, big microcells will have larger FF up to 80%, so that increasing the sensor PDE. This FF also accounts for the non-uniformities of the intrinsic electric field and the border effect [33].

Finally, the P_{Tr} is related to the probability of avalanche triggering or also named as Geiger discharge. This probability strongly depends on the type of carriers generated (electrons or holes) and on the electric field, which is proportional to the voltage applied. Electrons are the majority carriers when the SiPM is built on a p-on-n junction, and holes for a n-on-p junction type when blue light is absorbed above the junction. Hence, the carrier type generation will also depend on the depth of this junction and where the photons are absorbed. While blue photons are absorbed close to the surfaces, green and red photons penetrate deep on the SiPM.

2.3.2 SiPM characterization

In this section, the characterization of a 64 channel MPPC is presented, although the same methodology is followed for any kind of sensor shape or array. The characterization will allow to extract the dependence of the gain with the overvoltage, the breakdown voltage, and the intrinsic capacity of each of the channels. This test-bench will provide the capability of extracting the necessary intrinsic SiPM parameters to be used on the simulation environment on chapter 5. The setup consist on a picosecond pulsed laser (PiLas Picosecond Diode Laser at 405 nm, 30 ps pulse width [34]) impinging into the SiPM, a preamplifier chip named PACTA that takes the amplified electrical signal and send it to the oscilloscope, where the waveform is recorded with an Agilent MSO9404a oscilloscope with 20Gsa/s and 4 GHz.

For each SiPM channel, a number of 5000 waveforms at four different voltages were saved. Then, the analysis consists on: first, the pedestal (waveform before the signal arrives) per waveform is calculated and subtracted. Second the waveform is integrated to determine the collected charge as in figure 2.5a, where a charge histogram for a given overvoltage and channel is shown. The distribution presents a peak structure, where each centroid corresponds to the signal of a given number of detected photoelectrons. Lastly, all peaks were fitted using a Gaussian shape in order to determine its mean value. Figure 2.5b shows the relation between the charge and the number of photoelectrons, a linear fit can be easily adjusted and the gain at this voltage is given by the slope parameter of this linear regression.

This off-line analysis has been repeated for each of the 64 channels from an old S12642-0808 Hamamatsu SiPM version, and at four different voltages ($68.0\ V, 68.5\ V, 69.0\ V$ and $69.5\ V$). This SiPM was used as a full characterization example in a specific matrix configuration as we did not have a newer version. The following three main SiPM intrinsic parameters were extracted:

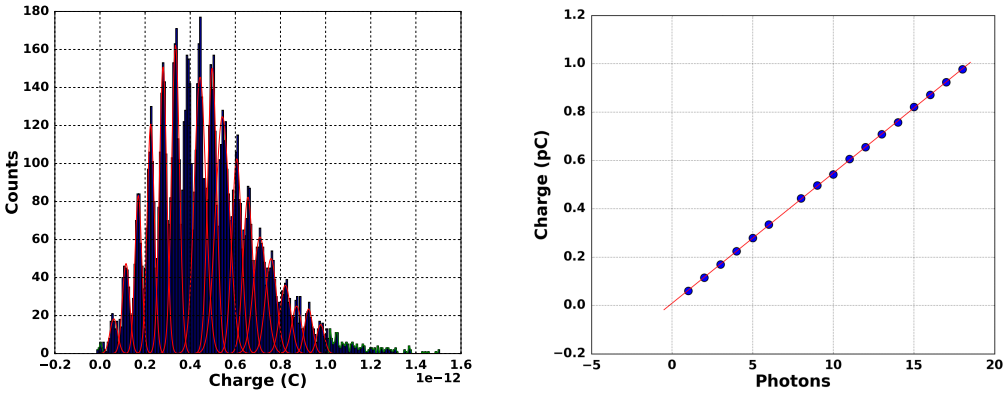

(a) (b)

Figure 2.5.: (a) Charge histogram for a single channel at 68.5 V of bias voltage. (b) Centroid position of every gaussian versus the corresponding photoelectron.

- Gain per volt applied to the SiPM. A linear dependence of the gain with the applied voltage is expressed as in equation 2.5. With q denoting the fundamental charge $q = 1.602 \cdot 10^{-19} C$.

$$G/V_{ov} = \frac{Q}{q} = \frac{V_{ov} \cdot (C_q + C_d)}{q} = \frac{(V_{bias} - V_{bd}) \cdot (C_q + C_d)}{qV_{ov}} \tag{2.5}$$

Therefore, the gain versus the applied voltage is fitted using a first order polynomial. Consequently, the slope of the fit represents the variation of the gain per volt of overvoltage. The figure 2.6 illustrates, in a 2D map, the distributions of this gain parameter. All values are within ±10 % of the observed mean ($6.0 \cdot 10^5/V$).

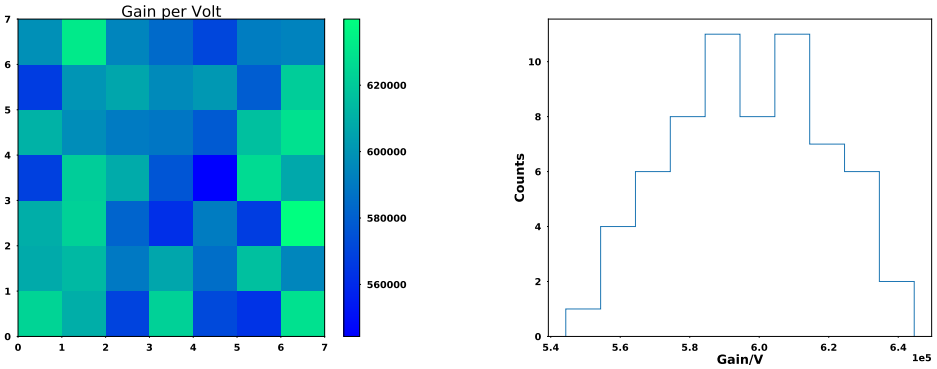

(a) (b)

Figure 2.6.: (a) Gain per volt for all 64 channels in a 2D map. (b) Gain/volt histogram distribution.

- Breakdown voltage. This is an important parameter since most applications, the SiPM array is grouped together and supplied by a common bias voltage. Thus, it is important to measure the breakdown voltage for each channel of the SiPM array to ensure that the breakdown voltages are close enough to have a good homogeneity. Difference in

break down voltage will imply that the gain at a given bias is different depending on the channel, therefore parameters like the PDE, charge or any other depending on the voltage applied will not be equal in all channels.

The fit performed to determine the gain per volt is extrapolated towards zero gain. The voltage at which this happens is defined as the breakdown. This method assumes that the gain is linearly proportional to the excess bias voltage in all the range. Breakdown voltages on this SiPM array are within $\pm 0.2\ V$, centered at $65.5\ V$. Figure 2.7 presents the breakdown voltage for each of the channels.

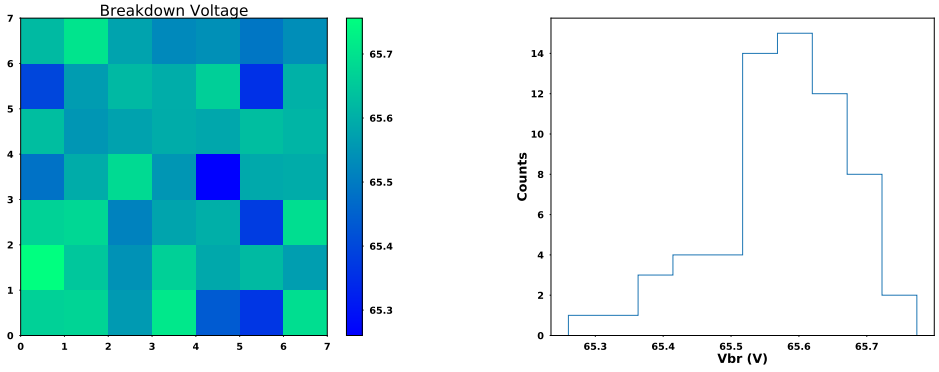

(a) **(b)**

Figure 2.7.: (a) Breakdown voltage for all 64 channels in a 2D map. (b) Breakdown voltage histogram distribution.

- Intrinsic capacity (Cd + Cq). This is a relevant parameter due to the fact that it has a direct relation with the rise time of the electric response of the SiPM [35]. Faster rising times imply a better time measurement. Given the fit of the gain versus voltage described before from equation 2.5:

$$C_d + C_q = \frac{qG}{V_{ov}} \tag{2.6}$$

Figure 2.8 shows a slight variation of the capacity on some of the channels, but the deviation is not very large, the 64 values remains within $\pm 10\%$ of the measured mean value ($167\ pF$).

2.3.3 SiPM drawbacks

As any other light sensor, SiPMs are not perfect at all. They have many disadvantages when comparing with other photodetectors like PMTs. Different sources of both correlated and uncorrelated noises are present on the SiPM, temperature drift variations on the break down voltage and no big areas can be covered by a single channel SiPM, thus increasing the total capacitance of the device. Moreover, due to the limited number of microcells

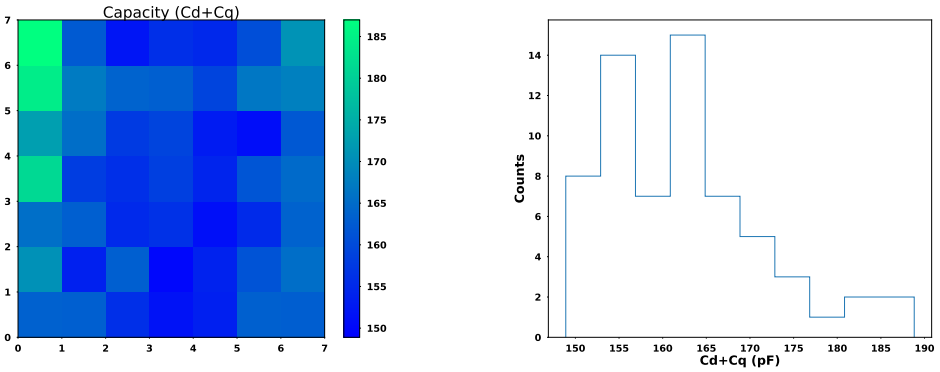

(a) (b)

Figure 2.8.: (a) Intrinsic capacity for all 64 channels in a 2D map. (b) Intrinsic capacity histogram distribution.

available in each SiPM, the dynamic range is limited and a nonlinear response appears as a consequence [36].

The noise on the SiPM at SPAD level can be divided in two different types [37, 38]:

1. *Uncorrelated noise*: the main source of noise on a SiPM came from "false" avalanche pulses, triggered by thermally generated carriers on the active junction. Each of those pulses are the result of a thermally generated electron that initiates an avalanche in the high field region, for this reason, the uncorrelated noise depends on the V_{ov} applied to the SiPM. This signal is generated even at dark conditions and are identical to the "real" signals from a light source, that noise is called Dark Count Rate (DCR). The number of dark pulses is typically given in units of kHz/mm^2. Furthermore, it depends on the microcell fill-factor and the depleted region width. Importantly, the DCR is reduced a 50% factor every time the temperature decreases 10 degrees [39]. Nevertheless, this reduction reaches a limit where the DCR is not reduced that much anymore, due to other phenomena like tunneling generation.

2. *Correlated noise*: this type of pulses are mainly due to (1) at the same microcell by afterpulsing or (2) caused by optical light coming from an adjacent cell, where in this case it is called optical crosstalk.

    a) Afterpulsing: on every avalanche process during the photoconversion, there is a probability that some carriers become trapped in defects in the silicon. After a certain delay, the trapped carriers are released, leading to a possible second avalanche (typically exponential distribution from the release times) after some nanoseconds from the original one. If the release time is smaller than the recharge time of the cell, the charge contained in this afterpulse will be smaller compared with a normal cell signal. Moreover, the afterpulse can be induce optically by the secondary photons generated during the avalanche process, that can be reabsorbed in the neutral region and the carriers will be diffused to the depleted region and trigger a second avalanche.

b) Crosstalk: as mentioned above, several secondary optical photons are emitted during the carriers avalanche process. Typically 2 to 3 $\cdot$ 10^{-5} NIR photons are emitted in isotropic directions for a single avalanche. Those photons can reach neighboring cells and trigger a second instantaneous avalanche, resulting in a signal output of amplitude and charge N times the single cell signal, with N the number of optical crosstalk photons absorbed. There are three main transport paths used by the optical photons to reach a neighboring cell (figure 2.9): (1) direct crosstalk, where an adjacent cell triggers and avalanche right after the primary one is detected, the NIR photons travels directly in straight line. (2) The NIR photons escape from the cell and is being reflected in the window cover and bounces back to a next by cell, or (3) reflected from the bottom of the substrate. 2 and 3 are also called delayed crosstalk. An extensive study on the crosstalk characterization can be found in[40, 41].

Both afterpulsing and crosstalk increase with the overvoltage. Because of that, there is a trade-off between the noise induced and the PDE. Different techniques are being implemented to avoid crosstalk. The most effective one consists in trenches implantation between the microcells in order to isolate optically the triggering cell and its neighbors. This solution implies a drastic reduction of crosstalk and it is now implemented in every new SiPM, but at a cost of reducing the total PDE as the FF also decreases.

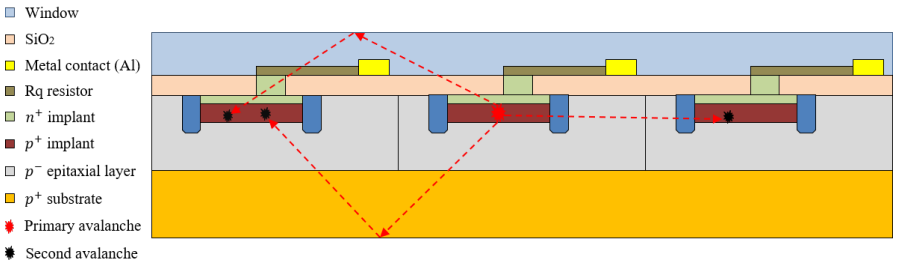

Figure 2.9.: SiPM structure and the three main NIR photon crosstalk propagation paths from cell-to-cell.

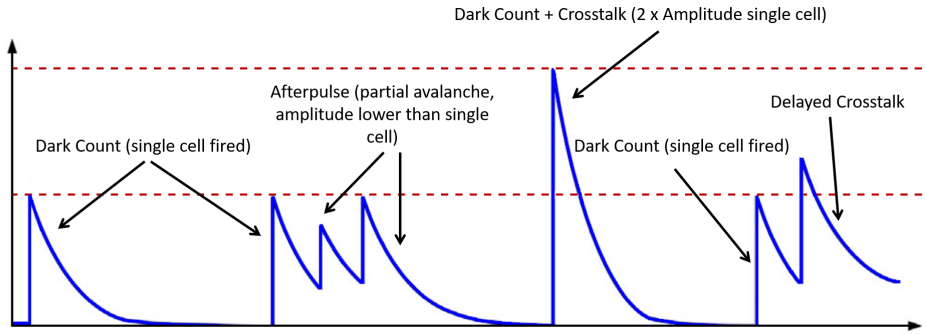

Figure 2.10.: Different noise signals from a SiPM output at dark conditions. Image reproduced from [2]

Another problem related to the SiPM is known as temperature drift. The breakdown voltage changes linearly as a function of the temperature variation. Depending on the manufacturing process, i.e. the structure of the microcell, this value can go from 21 mV/°C to 54 mV/°C. This effect must be addressed if big temperature variations are expected during the operation time. Otherwise, internal parameters like the gain (PDE), quenching resistance or the junction capacitance may change. Hence, distorting the signal shape and system capabilities. Any experiment that employs SiPM must remain at stable temperature in order to reduce as much as possible this effect.

Finally, the limited number of microcells in a SiPM will limit the amount of light that can be absorbed in a small time window. If the number of detected photons (N_{ph}) times the PDE is smaller compared to the number of available microcells ($N_{\mu cells}$), the output signal divided the input signal remains constant. On the contrary, if the number of photons arriving increases, this relation is not true anymore and a non-linearity effect appears. Equation 2.7 represents the analytic approximation to the number of microcells fired with respect to the input photons and the total number of microcells available in the device [37].

$$N_{fired\mu cells} = N_{\mu cells} \cdot \left(1 - exp\left[-\frac{N_{ph} \cdot PDE}{N_{\mu cells}}\right]\right) \tag{2.7}$$

This effect is translated into a saturation curve that depends on the SiPM parameters. Upper plots from figure 2.11 illustrates the number of microcells fired with respect to the amount of incident photons following equation 2.7. On the bottom part, the deviation from the ideal linearity is represented. Smaller microcells allow to have more firing cells available, increasing the linearity percentage for an extended number of incident photons. As a counterpart, the PDE for the 25 μm cell size is 25%, while the 50 μm reaches values around 45%.

As an experimental example, figure 2.12 shows the collected light from different gamma sources, i.e. ^{22}Na, ^{60}Co and ^{137}Cs, using a detector composed by a LYSO scintillator crystal of 3x3x20 mm^3 is readout by a SiPM of 3x3 mm^2 and 3600 microcells of 50 μm. On the left, the raw histogram of light collection shows that for energies above the 511 keV photopeak, the number of scintillation photons is too high, and the energy spectrum starts to suffer some sort of reconstruction compression. On the right, the spectrum after calibration and SiPM correction shows the expected linear behavior.

This indicates a limitation on the dynamic range by means of the number of microcells available at the very moment of a gamma detection event. An increment on the number of microcells of the device could solve the problem. However, this comes at the expenses of reducing the PDE of the SiPM as the fill factor of each microcell decreases as the size does. In brief, a trade-off between these two factors is present in every SiPM model and it should be checked and adjusted depending on the needs of the final detector. A spectrum calibration taking into account the dynamic range adjustment from the SiPM will be shown in chapter 3.

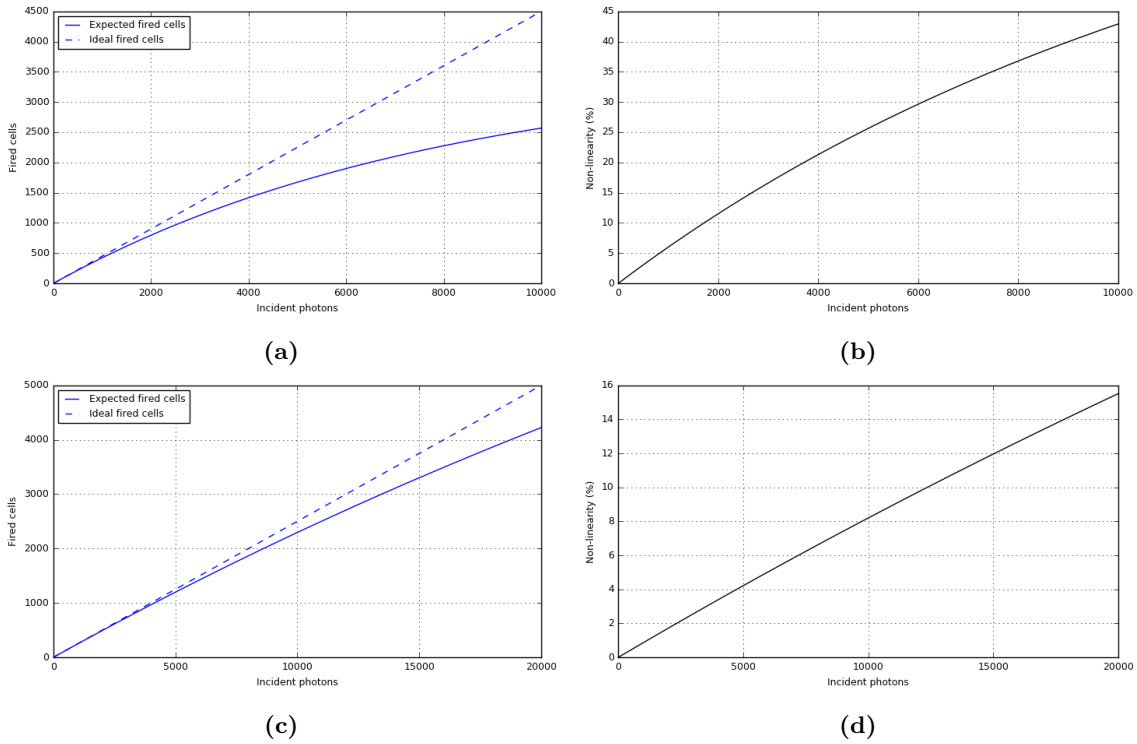

Figure 2.11.: Fired cells as a function of the number of incident photons for a SiPM of 3x3 mm^2 with specifications such as: (a) and (b) 50 μm cell size and 45% of PDE. (c) and (d) accounting for 25 μm cell size and PDE of 25%.

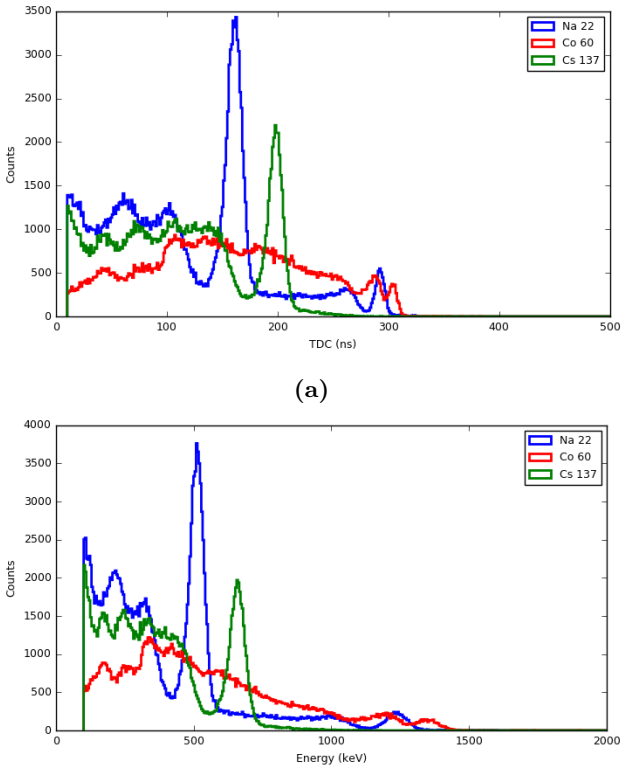

Figure 2.12.: Energy spectrum for ^{22}Na, ^{60}Co and ^{137}Cs radioactive sources. (a) Before SiPM compression correction and (b) once the calibration is performed.

2.3.4 State of the art on SiPM technology

Every time a new SiPM model appears in the market, all these intrinsic problems regarding noise, temperature variation and the limit on PDE are being improved. Nowadays, the state-of-the-art SiPM can reach a PDE above 60%, crosstalk and afterpulse below 10%, DCR in the order of 30 kHz/mm^2 at room temperature, and around 20 mV/°C of temperature drift. The problem is that all these values cannot be set with a single specific configuration of the SiPM. This high PDE of 60% can only be reached with high over-voltages, where the correlated and uncorrelated noise is no longer at the values above exposed. In other words, a trade-off is inevitable when talking about the operation point of a SiPM, one cannot maximize the positive parameters while minimizing the negative ones. The main SiPM manufacturers are Hamamatsu, KETEK, Broadcom with license from FBK technology and On Semiconductor who has acquired SensL Technology Ltd. The widest range of SiPMs for different applications are offered today by FBK and Hamamatsu and the SiPM model and characteristics depends on the application. PET applications with blue light detection requires a p-on-n fabrication while LIDAR focused on red towards IR photons needs a n-on-p device. This last application seems to be the way for many new disrupting technologies such as autonomous vehicle, and a lot of effort is being pulled in this direction. FBK has acoplished a PDE of 12% with 35 μm pixel pitch and KETEK is surpassing this value reaching almost 20% with 15 μm pixel pitch, promising results on red-IR photon detection using SiPMs. Table 2.2 illustrates the characteristics of the common SiPM models employed in PET applications from the main companies devoted to SiPM manufacturing.

Table 2.2.: SiPM models and its main characteristics from different manufacturers.

Company (model)	V_{ov} [V]	PDE [%]	Cap. [pf]	p.p. [μm]	V_{br} [V]	Gain	DCR [kcps]	x-talk [%]
Hamamatsu (S13360-3050CS)	3	40	320	50	53	1.7 $\times 10^6$	500	3
SensL (ONSEMI) (Jseries-30035)	2.5	38	1070	35	24.5	2.9 $\times 10^6$	450	8
FBK (AdvanSiD) (ASD-NUV3S-P)	6	43	497	40	26	3.6 $\times 10^6$	900	<5
KETEK (PM3325-WB-D0)	3.5	31	1000	25	24.5	0.9 $\times 10^6$	450	12

Time-of-Flight PET requires the best SiPM in order to achieve the 10 ps holy grail and still the intrinsic time resolution of this technology is not yet there. If these conditions could be reached at some point, a new paradigm will appear on imaging techniques as never before. The next section will explain another element on the gamma collection chain that is limiting this challenging objective, the scintillator crystal.

2.4 Fast Readout Electronics: FlexToT technology

Efficient electronics that are stable and perform at high count-rates are also required to extract the best timing performance from the photo-sensor devices [42]. In general, this electronics should have the following specifications: (1) Multi-channel SiPM readout; (2) anode voltage adjustment to correct gain differences between channels; (3) low input impedance for fast SiPM response; (4) configurable signal shaping to cope with different recovery time constants; (5) low input referred noise; (6) low power consumption. This custom Front-End (FE) electronics should provide a measurement of the arrival time of the photons, an energy measurement and a trigger signal as main features. All this information should be digitized using Analog or Time to Digital Converters (ADCs or TDCs) [43, 44]. FE electronics and ADCs/TDCs can be implemented in different ASICs (Application Specific Integrated Circuits) to minimize any noise from the digital circuitry to the analog FE readout or in a single ASIC for a more compact design.

The ASIC here employed is called HRFlexToT. It is designed to provide both time and energy information of the detected photons for each individual input channel. This ASIC is built with a totally redesigned energy measurement readout to provide a linear ToT with an extended dynamic range while at the same time reducing the power consumption and its timing response. This enhancement in time resolution is translated into better SPTR. As a summary, it features 16 channels, high dynamic range, high speed, a low input impedance stage, common cathode connection and directly coupled (DC) input with common-mode voltage control. The HRFlexToT block diagram is illustrated in Figure 2.13 and its main features are outlined next.

- **Individual channel output.** The information of the detected photons is given at each individual output using a CMOS driver with three different possibilities:
  1. **Time response.** The time measurement encodes the arrival time of the photons in the rising edge of a pulse with low jitter. It provides a non-linear Time-over-Threshold (ToT) output.
  2. **Energy block.** The energy measurement provides a pulse with a linear width with respect to the input current, the so called, Pulse Width Modulation (PWM). It provides a linear ToT output.
  3. **Time+Energy event.** Combines the pulse of the timing signal with the pulse of the energy measurement to form the so-called Time+Energy. It encodes the time of arrival and the pulse energy into two consecutive PWM pulses per channel. A representation of the combined pulse will be seen in chapter 4.
- **Fast Timing OR.** The arrival time measurement is also given as a Fast OR between all channels using a Low Voltage Differential Signaling (LVDS) driver.
- **Low level trigger.** A trigger pulse with a configurable threshold level set above Dark Count Rate (DCR) noise is provided as an OR between all input channels in CMOS mode.

- **Cluster high level trigger.** A trigger pulse is obtained as a discriminated sum of a fraction of the input signal from each channel.

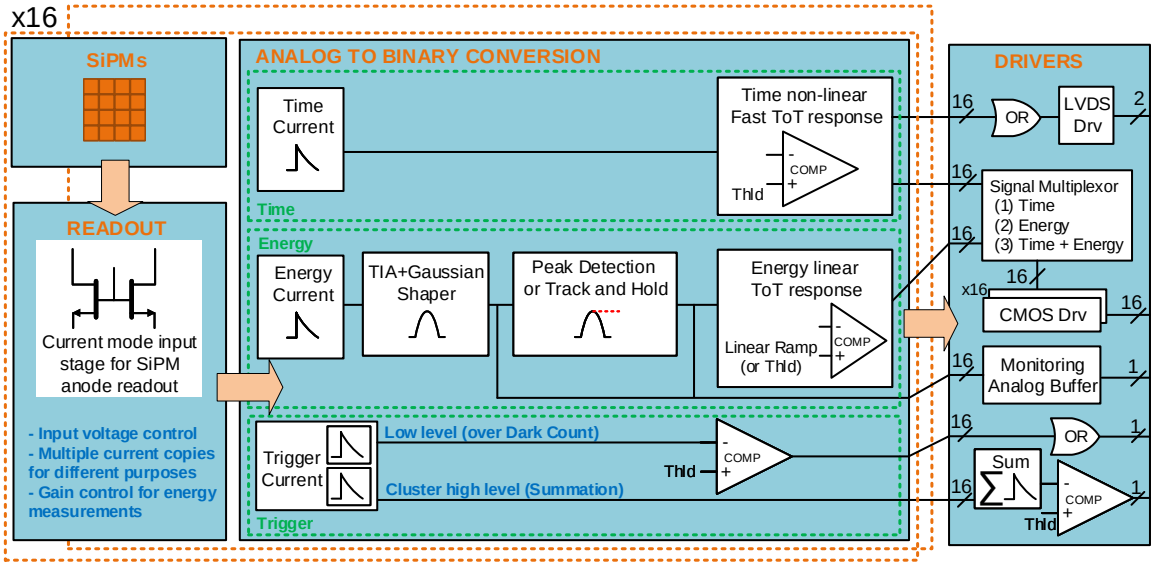

Figure 2.13.: Functional block diagram of the HRFlexToT ASIC.

2.4.1 Input Stage

Although the electronic design is out of the scope of this thesis, a brief summary of electronic architecture from the HRFlexToT is here presented in order to complete the knowledge of the reader. A patented low input impedance stage [45] based on a MOSFET current mirror with double feedback loop is employed for SiPM anode readout. Figure 2.14 details the Front-End circuit at transistor level. The Low Frequency feedback loop (LF_{FB}), based on a low input-impedance current amplifier with a regulated cascode [46, 47], controls the DC voltage of the input node and thus enabling the possibility to adjust the anode voltage of the SiPM. This feature can be used to equalize the SiPM response (over-voltage control) and thus compensate for voltage breakdown variations (≈1 V range). The High Frequency feedback path (HF_{FB}) employs a common-gate regulated cascode configuration [48] to keep the input impedance low at signal bandwidth and thus not affect the fast timing behavior of the SiPM.

The design has been implemented considering that the dominant pole should be set at the input node (SiPM parasitic capacitance is at least at the order of tenths of pF). Using this strategy, stability is not compromised when a sensor with large capacitance is added at the input. The current division scheme at the very front-end part of the circuit splits input current into differently scaled copies which are connected to independent current mirrors to provide the different features of the ASIC, as previously detailed. An outline of the main characteristics of the input stage are provided next.

- Low input impedance: $\approx 35\,\Omega$ along signal bandwidth.

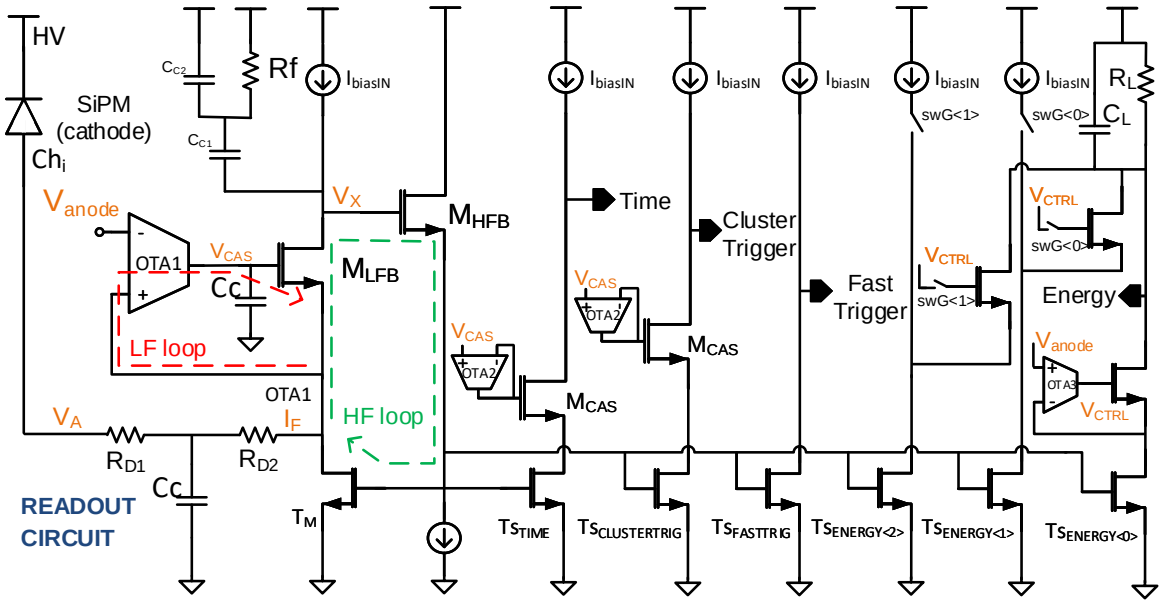

Figure 2.14.: Input stage Current Conveyor for SiPM readout.

- Anode connection for multi-channel SiPMs arrays with common cathode.
- Anode voltage control per channel to adjust the SiPM bias voltage with 1 V (9 bits) dynamic range. It may be used to adjust non-uniformities in gain or photon detection efficiency of each SiPM.
- High bandwidth: larger than 500 MHz.
- Low input referred noise for sensor capacitances between 10 pF - 10 nF: (1) series noise lower than 2 nV/$\sqrt{Hz}$; (2) parallel noise lower than 20 pA/$\sqrt{Hz}$.
- Power down mode for each individual channel.

2.4.2 Time and Trigger measurement

Time response is achieved by using a leading edge current comparator, based in [49], just after the input current conveyor, as depicted in Figure 2.15. It provides a non-linear Time over Threshold (ToT) response encoding the collected charge of the photoelectrons following a pulse width modulation. Moreover, it encodes the arrival time of the incoming photons in the rising edge of the generated pulse. The main advantage of this fast comparator is its simplicity that enables it to provide a fast response with low jitter. On the other hand, the main limitation of these kind of ToT comparators is that the relation between the input charge to be measured, i.e., the number of photoelectrons detected, and the width of the encoded pulse is non-linear. Therefore, an alternative readout system is needed for the energy measurement. Lastly, the time response is provided as a fast OR between all timing channels using a differential LVDS output and the individual time response can be read out as a single-ended output per channel.

The ASIC is designed to provide different levels of trigger depending on the application. The trigger is provided as a pulse where the rising edge indicates that an event has been detected. Firstly, a low-level trigger is generated using a fraction of the input signal and the same discriminator employed to generate the time response. This non-linear ToT response is provided as an OR between all channels in CMOS mode. The trigger level is set above Dark Count Rate (DCR) noise, i.e., a few photoelectrons, to filter out these non-desired events. Note that this trigger output is aimed for pixelated crystals where the OR between all channels provides the information of the first event detected.

A second level of trigger, referred as cluster high level trigger, is generated summing first a fraction of the input signal from each channel and then using it as input of the current comparator to generate the discriminated output. This trigger is very useful for monolithic crystals where the signal is spread among several channels and a single channel might not trigger and thus lose the event. Lastly, the time signal can be also used as trigger for those cases where high sensitivity is needed, and the events are close to the single photoelectron.

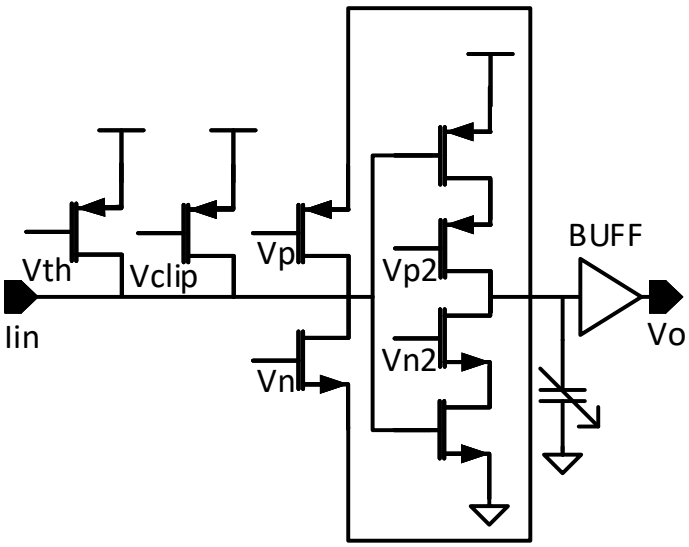

Figure 2.15.: Leading-Edge current comparator used for Time and Trigger measurements.

2.4.3 Energy measurement

The energy processing (Figure 2.13) is the main difference of the HRFlexToT with respect to its predecessor[50]. The previous energy measurement circuit was composed by an RC integrator and a constant DC current source. The linear response was achieved by initially charging a capacitor with the incoming signal, then discharging it using a constant DC current and thus providing a linear discharge, and lastly feeding this signal into a voltage discriminator. The problem of this method is that for low currents, the discharge of the capacitor stops behaving linearly since part of the DC current starts flowing through the feedback network of the RC integrator instead of discharging the capacitor. This effect for

low currents is translated into a reduction of the dynamic range (input peak current range is from around 2.5 mA to at least 18 mA) where the energy acquisition behaves linearly.

The new energy measurement block, which is conceptually similar to a Wilkinson ADC, does not suffer the linearity problem for low currents. This redesigned energy path provides a linear ToT output encoding the collected charge in a binary pulse width with an extended dynamic range (input peak current range is from a few tens of μA up to at least 35 mA). The main improvement in terms of dynamic range is achieved by increasing the minimum current that provides a linear energy response. For instance, this new version can detect pulses with a width between 0.5 ns (noise floor) and 500 ns with its default configuration, and thus allowing a resolution of 10 bits. The increase of the sensitivity at low currents is rather important to preserve the linear response specially in monolithic crystals where signal is spread among several channels in SiPM arrays.

The energy acquisition is achieved in three stages. The first stage is composed by a trans-impedance amplifier (TIA) and a semi-Gaussian shaper, as illustrated in Figure 2.16. The energy output from the input stage current conveyor is followed by a closed-loop trans-impedance amplifier where the SiPM current signal is converted into voltage for further processing and the output voltage is controlled to keep linearity. For this purpose, an OTA Miller with an Slew Rate (SR) enhancement circuit based in [51] is employed. The advantage of this SR boosting circuit is that it is only activated when the amplifier detects at the input the incoming event and thus saving power consumption.

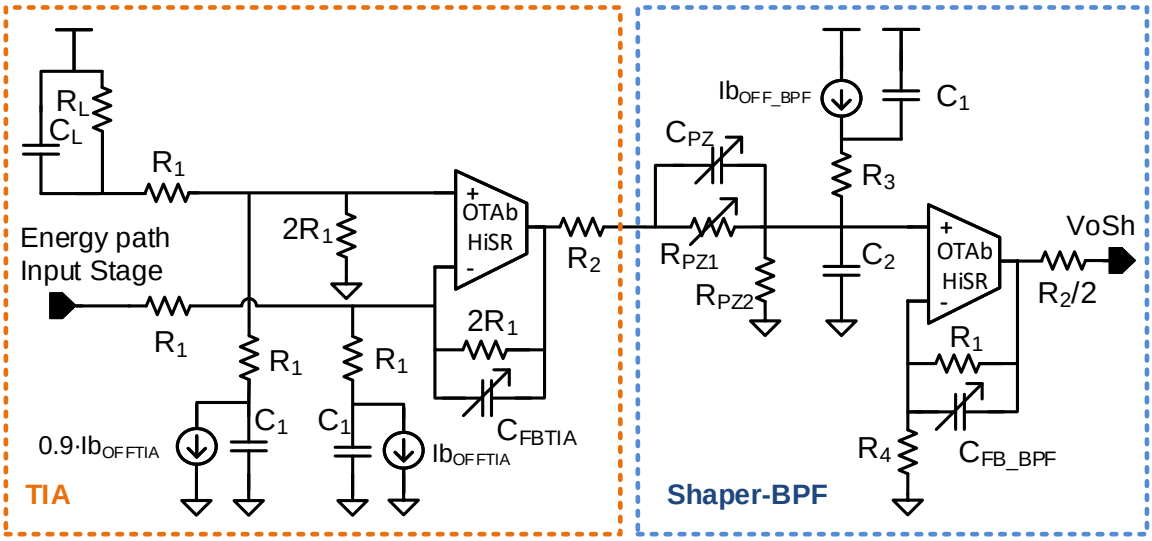

Figure 2.16.: Energy Measurement: Trans-impedance amplifier and Band Pass Filter (BPF) used as shaper circuit.

The TIA output is followed by the semi-Guassian shaper which can be configured to cope with different scintillator and SiPM recovery time constants. The shaper block or Band Pass Filter (BPF) is implemented using a CR-RC pulse shaping network which contains a passive pole zero cancellation (CR block) and an active integrator (RC block). The purpose of this block is to "shape" the signal by shortening the decay time of the pulse to minimize the pile-up of pulses and thus enable a high rate, this effect is achieved by the CR filter. Moreover, the RC filter increases the peaking time of the pulse and thus slew rate requirements in

subsequent processing stages are less demanding. More specifically, the CR-RC network is adjustable to achieve peaking times between 50 to 80 ns.

Secondly, the shaper output is connected to a Peak Detector and Hold (PDH) block, which is implemented based on [52, 53] and detailed in Figure 2.17. The PDH circuit operates in two phases. Firstly, write stage (WR) switches are closed and read (RD) ones are opened. During this stage, the hold capacitor (C_H) is being charged by the input signal (shaper output) until the peak is detected and then holds it, i.e., the circuit tracks the input signal until it reaches its maximum. Secondly, switches are inverted during the read stage (RD). The PDH is isolated from the input signal to avoid undesired pulses to affect the detected peak saved in the hold capacitor. In this stage, the amplifier operates as a follower sending the detected peak (V_{HOLD}) to the next stage in the energy processing chain. The rail-to-rail input/output amplifier with dynamic biasing to minimize power consumption used in [52] is here modified replacing the two stage amplifier by a classic symmetric OTA [54]. The advantage of this amplifier is that it only has a low frequency pole and it is easier to stabilize with lower power. Note that the C_c and R_c are used to compensate the Symmetric OTA in the read mode. Once the peak voltage is processed by the subsequent stage, the (C_H) is discharged and set to the baseline voltage (Vbl) by means of closing the RST switch and thereby enabling the PDH to process the next event.

The original Peak Detector designed by De Geronimo et al., has been modified to include two features. Firstly, a discharge current circuit is added to eliminate the charge of non-desired pulses. The discharge circuit is enabled in the write stage as long as a valid trigger signal is not generated; if an event is detected, the discharge mode is switched off immediately to avoid losing a valid event. Note that this circuit is necessary for the proper behavior of the PDH to avoid saturation due to the Dark Count Rate (DCR) of the SiPMs. Secondly, an optional circuit has been added to transform the PDH into a Track and Hold circuit (TH). The TH mode can be employed to capture different moments of the input signal apart from the peak.

Lastly, a rail-to-rail comparator generates a linear ToT energy pulse using the peak detected and a linear ramp signal as a threshold, as illustrated in Figure 2.18. Hence, this mechanism provides a linear ToT response since the ramp used as threshold is linear and the amplitude of the incoming signal (encoding the collected charge) follows a linear relation with respect to the number of photoelectrons detected. The ramp is activated once the incoming signal is sampled by the PDH. The ramp generator is based on a DC current source that charges an integrator and it is common to all channels. The slope of the ramp is configurable to work with different signal rates. The voltage rail-to-rail comparator is composed by a voltage rail-to-rail differential amplifier, a voltage differential amplifier [54], a comparator with internal hysteresis and class AB output stage [55], and a digital buffer. The amplifiers are used to amplify the difference between the input signal and the ramp and thus ease the comparison. Lastly, individual control of the threshold at the comparator instead of the ramp is available to provide a non-linear ToT response independent of the ramp.

The control of the energy acquisition is performed by an asynchronous Finite State Machine (FSM). This control block does not require any kind of clock to operate, and thus avoiding any simultaneous switching noise produced by digital circuitry. The FSM is illustrated in Figure 2.19 and the mechanism to generate the linear energy response is as follows.

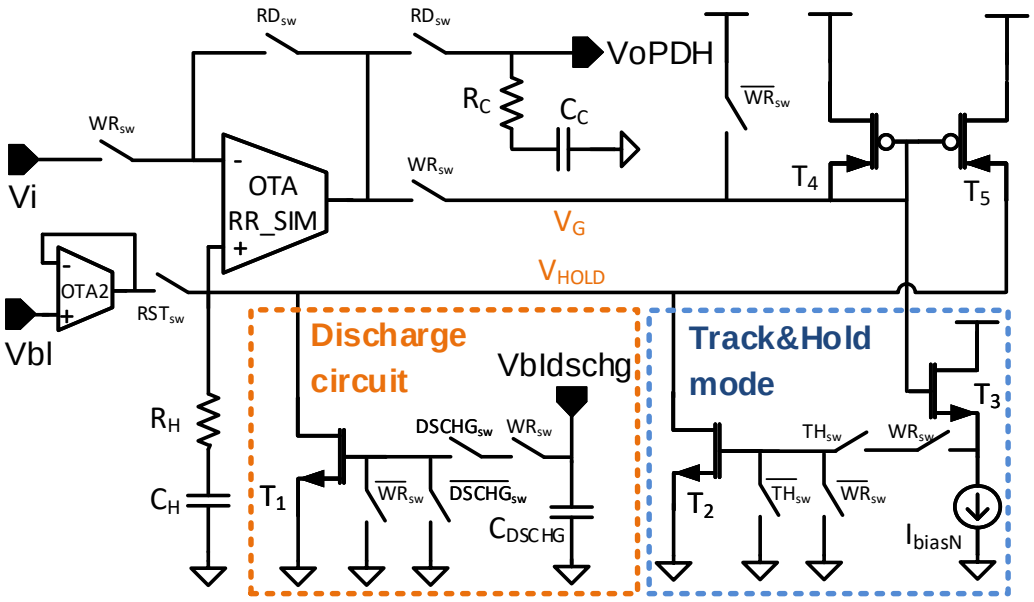

Figure 2.17.: Energy Measurement: Peak Detector and Track and Hold (PDH) circuit.

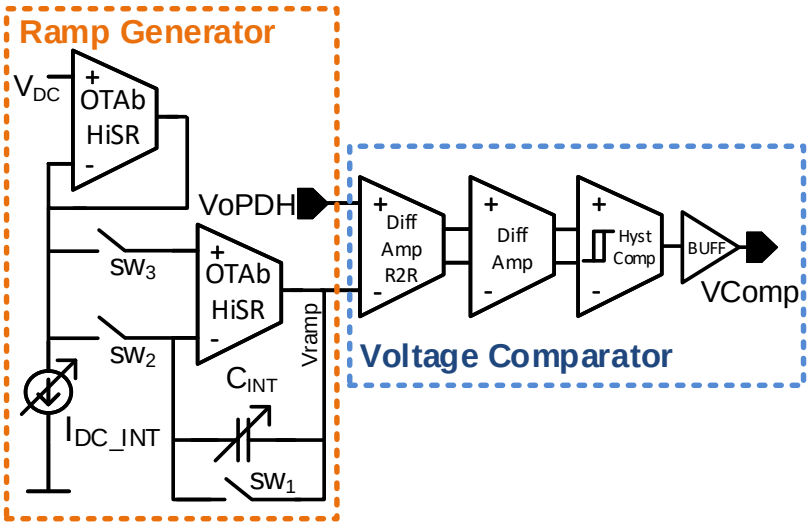

Figure 2.18.: Energy Measurement: Ramp Generator and voltage comparator.

1. System waits until an event is received (seen by any of the triggers) in the *Wait* state.

2. The FSM goes to the *Armed* state waiting for the trigger if time is seen before the trigger. If a trigger signal is not detected within a given period of time, the events are discarded, the FSM returns to the *Wait* state and the PDH is discharged.

3. The Band Pass Filter shapes the input pulse (*Shaper Start*) and the peak of the shaper output is sampled by the PDH, which is set to Write Mode (WR).

4. When the shaping ends (*Shaper Stop*), the system lies in a steady state during a certain delay (*Hold*) and the PDH is set to the Read Mode (RD).

5. The voltage ramp starts with a DC level below the quiescent voltage of the PDH (*Conversion Start*).

6. The rising edge of the energy pulse is generated once the ramp reaches the first voltage threshold (ThSoC) and then the system goes to the *Conversion* state.

7. A pedestal or minimum energy pulse is generated when the ramp crosses the quiescent level of the PDH. This pedestal can be captured in absence of signal and it is used for calibration purposes. The pedestal must be subtracted from the energy pulse during data analysis.

8. The falling edge of the energy pulse is generated once the ramp reaches the voltage captured by the PDH.

9. The conversion finishes (*Conversion Stop*) when the ramp reaches the second voltage threshold (ThEoC).

10. The system is reset after ending the conversion (*Reset*) and the system comes back to the *Wait* state to process the next event.

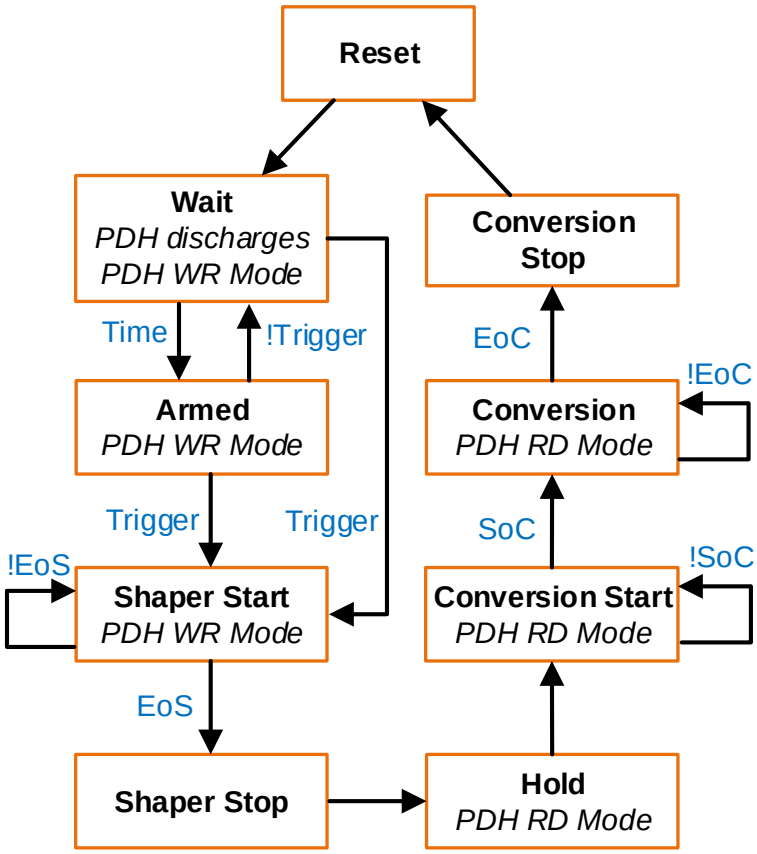

Figure 2.19.: Finite State Machine used for the energy acquisition. EoS represents the End of Shaping, SoC refers to the Start of Conversion and EoC accounts for the End of Conversion.

Figure 2.20 shows how the energy pulse is captured and how the Time+Energy is multiplexed in the same output as two consecutive pulses. Different triggers can be used for the energy measurement as previously explained in section 2.4.2: the low-level trigger, the timing

signal and the cluster high-level or summation trigger. Moreover, the ASIC provides the option to inject an external trigger for pedestal calibration (minimum pulse width detected in the absence of signal) to compensate variations among different channels. Lastly, it is important to highlight that the energy processing time can be adjusted, by changing the slope of the ramp, and thus the energy measurement can sustain a trigger rate of around 1M counts/s (1 Mcps).

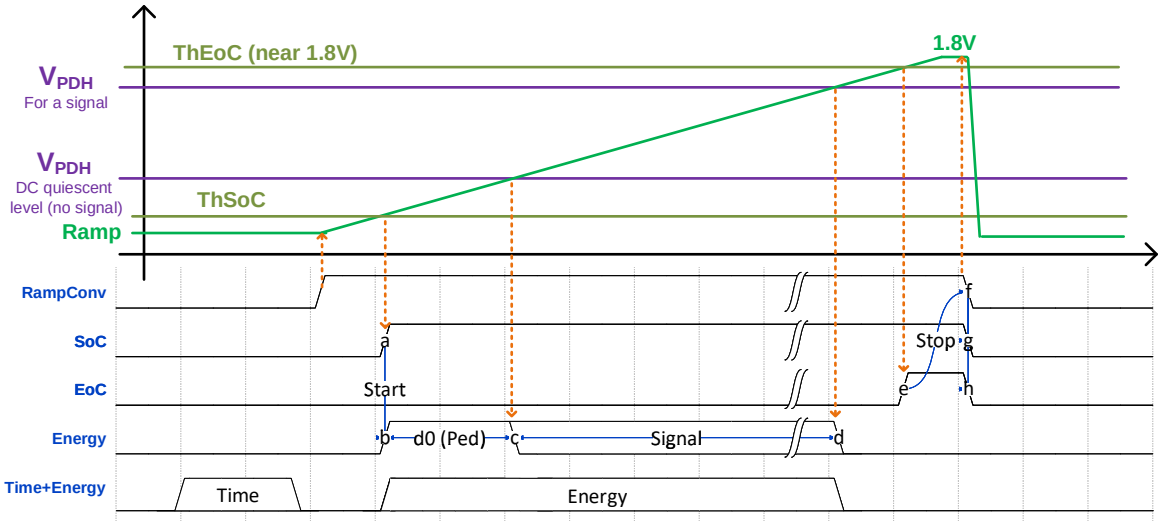

Figure 2.20.: Energy acquisition mechanism to provide the linear ToT response and example of the Time+Energy output. Time pulse is generated at the time comparator stage and multiplexed into this single output.

2.4.4 PET electronics state of the art

Currently, the clinical Siemens Digital Biograph Vision PET/CT system has the lowest CTR achieved, setting this value in ≈210 ps for a complete PET system [56]. In this particular case, the detector block was composed by an array of SiPMs of 16 mm × 16 mm coupled to an array of 5 × 5 LSO pixelated crystals of size 3.2 mm × 3.2 mm × 20 mm. The electronics employed in the Vision scanner are not public disclosed but serve as reference for CTR performance evaluations. The first total body PET scanner, called Explorer [57], has a 194 cm axial field of view and a transaxial field of view of 68.6 cm. The crystal here employed are LYSO of 2.76 mm × 2.76 mm × 18.1 mm size. Crystals are arranged in 7 × 6 arrays coupled to 4 SiPMs of 6 mm × 6 mm, achieving 430 ps of CTR. No ASIC is here employed, instead, discrete components are used.

Several ASICs have been developed over the years to provide precise time and energy measurements [58]. For instance, an 8 channel ASIC, referred as NINO [59] can be employed for time measurements and some discrete electronics for the energy acquisition [60]. These electronics yield a 64 ps sigma (148 ps FWHM) for single-photon time resolution (SPTR) with Hamamatsu SiPM S13360-3050CS and a CTR of 93 ps with 2 mm × 2 mm × 5 mm

LSO:Ce,Ca crystals and the same SiPM [61]. On the other hand, NINO suffers from high power consumption (27 mW/ch) and it does not provide a linear energy measurement.

An alternative ASIC that provides both time and energy measurement and includes internal TDCs with a time binning of 30 ps is the 32-channel ASIC Petiroc2A [62] developed by Weeroc [63]. This ASIC provides a SPTR of 190 ps FWHM, an energy resolution of 12.9% for 511 keV photon after correction and a CTR of 223 ps FWHM measured with internal TDCs and using an LSO:Ce,Ca crystal of 3 mm × 3 mm × 20 mm and Hamamatsu MPPC S13360-3050PE. Lastly, the analog core of the ASIC consumes 6 mW/ch and it is capable to process up to 40k counts/s.

TOFPET2 [64] is an ASIC developed by PETsys Electronics [65] that includes the SiPM readout and internal digitization with TDCs with a time binning of 30 ps. TOFPET2 is able to resolve 0 Energy resolution of the 511 keV photo-peak is 10.5 % FWHM with a LYSO crystal of 3 mm × 3 mm × 5 mm mounted on a KETEK-PM3325-WB SiPM. It achieves a CTR of 118 ps FWHM with 2 mm × 2 mm × 3 mm LSO:Ce,Ca crystals and both FBK SiPM NUV-HD (4 mm × 4 mm pixel, 40 μm cell) and Hamamatsu SiPM S13361-3050AE-04. Lastly, power consumption is about 8.2 mW/ch (depending on the configuration) and maximum channel hit rate is 600k counts/s.

The ASIC here employed is the FlexToT ASIC [50, 61, 66, 67]. The electronics developed in our group achieves an SPTR of 91 ps sigma (214 ps FWHM) and a CTR of 123 ps FWHM with 2 mm × 2 mm × 5 mm LSO:Ce,Ca crystals and Hamamatsu SiPM S13360-3050CS. Lastly, power consumption is about 11 mW/ch.

Lastly, the authors in [9, 68], employ a High Frequency (HF) readout electronics based on a RF amplifier (BGA616) with a high -3 dB bandwidth of ≈1.5 GHz and a large power consumption of about 360 mW [69]. This large bandwidth electronics serves as reference to experimentally evaluate the limits of SiPMs and scintillators, or at least, to vastly reduce the impact of the electronic noise. The HF readout achieves an SPTR of 144 ps FWHM coupled to a Hamamatsu S13360-3050PE SiPM and a CTR of 75 ps FWHM when using an LSO:Ce Ca 0.4% scintillator of 2 mm × 2 mm × 3 mm size. An SPTR of 92 ps FWHM is obtained employing an FBK SiPM NUV-HD (4 mm × 4 mm pixel, 40 μm cell) and a CTR of 63 ps FWHM is achieved utilizing the same crystal.

2.5 Bibliography

[1] C. W. Van Eijk, Inorganic scintillators in medical imaging detectors, Nuclear Instruments and Methods in Physics Research, Section A: Accelerators, Spectrometers, Detectors and Associated Equipment 509 (1-3) (2003) 17–25. doi:10.1016/S0168-9002(03)01542-0.

[2] F. Acerbi, S. Gundacker, Understanding and simulating SiPMs, Nuclear Instruments and Methods in Physics Research, Section A: Accelerators, Spectrometers, Detectors and Associated Equipment 926 (September 2018) (2019) 16–35. doi:10.1016/j.nima.2018.11.118.
URL https://doi.org/10.1016/j.nima.2018.11.118

[3] M. Watanabe, H. Okada, K. Shimizu, T. Omura, E. Yoshikawa, T. Kosugi, S. Mori, T. Yamashita, High resolution animal PET scanner using compact PS-PMT detectors, IEEE Nuclear Science Symposium & Medical Imaging Conference 2 (3) (1996) 1330–1334. doi:10.1109/nssmic.1996.591690.

[4] S. Gomez, D. Sanchez, D. Gascon, J. Cela, L. Freixas, R. Graciani, R. Manera, J. Marin, J. Mauricio, J. Navarrete, J. Oller, J. Perez, P. Rato Mendes, A. Sanmukh, O. Vela, A High Dynamic Range ASIC for Time of Flight PET with pixelated and monolithic crystals, in: 2019 IEEE Nuclear Science Symposium and Medical Imaging Conference, NSS/MIC 2019, 2019. doi:10.1109/NSS/MIC42101.2019.9059762.

[5] C. S. COOK, GAMMA-RAY SCINTILLATION SPECTROMETRY, American Scientist 45 (3) (1957) 245–262. doi:10.2307/27826909.
URL http://www.jstor.org/stable/27826909

[6] G. F. Knoll, Measurement, Radiation detection and, John Wiley & Sons, 2010.

[7] P. Lecoq, Development of new scintillators for medical applications, Nuclear Instruments and Methods in Physics Research, Section A: Accelerators, Spectrometers, Detectors and Associated Equipment 809 (2016) 130–139. doi:10.1016/j.nima.2015.08.041.
URL http://dx.doi.org/10.1016/j.nima.2015.08.041

[8] J. S. Schweitzer, Cerium-doped Lutetium Oxyorthosilicate: A Fast, Efficient New Scintillator 39 (4) (1992) 502–505.

[9] S. Gundacker, R. Martinez Turtos, N. Kratochwil, R. H. Pots, M. Paganoni, P. Lecoq, E. Auffray, Experimental time resolution limits of modern SiPMs and TOF-PET detectors exploring different scintillators and Cherenkov emission, Physics in Medicine and Biology 65 (2) (2020). doi:10.1088/1361-6560/ab63b4.

[10] E. Roncali, Optical Simulation.
URL https://cherrylab.bme.ucdavis.edu/research/optical-simulation/

[11] P. Lecoq, Pushing the Limits in Time-of-Flight PET Imaging, IEEE Transactions on Radiation and Plasma Medical Sciences 1 (6) (2017) 473–485. doi:10.1109/TRPMS.

2017.2756674.
URL http://ieeexplore.ieee.org/document/8049484/

[12] T. Szczesniak, M. Moszynski, L. Swiderski, A. Nassalski, P. Lavoute, M. Kapusta, Fast photomultipliers for TOF PET, IEEE Transactions on Nuclear Science 56 (1) (2009) 173–181. doi:10.1109/TNS.2008.2008992.

[13] M. E. Casey, L. Eriksson, M. Schmand, S. Member, M. S. Andreaco, M. Paulus, M. Dahlbom, R. Nutt, Investigation of LSO Crystals 44 (3) (1997) 1109–1113.

[14] A. Saoudi, C. Pepin, C. Pépin, D. Houde, R. Lecomte, Scintillation light emission studies of LSO scintillators, IEEE Transactions on Nuclear Science 46 (6 PART 2) (1999) 1925–1928. doi:10.1109/23.819255.

[15] R. Lecomte, Novel detector technology for clinical PET, European Journal of Nuclear Medicine and Molecular Imaging 36 (SUPPL. 1) (2009) 69–85. doi:10.1007/s00259-008-1054-0.

[16] S. Gundacker, E. Auffray, K. Pauwels, P. Lecoq, Measurement of intrinsic rise times for various L(Y)SO and LuAG scintillators with a general study of prompt photons to achieve 10 ps in TOF-PET, Physics in Medicine and Biology 61 (7) (2016) 2802–2837. doi:10.1088/0031-9155/61/7/2802.

[17] S. Gundacker, A. Heering, The silicon photomultiplier: fundamentals and applications of a modern solid-state photon detector, Physics in Medicine & Biology 65 (17) (2020) 17TR01. doi:10.1088/1361-6560/ab7b2d.
URL https://doi.org/10.1088{%}2F1361-6560{%}2Fab7b2d

[18] Y. Shao, A new timing model for calculating the intrinsic timing resolution of a scintillator detector, Physics in Medicine and Biology 52 (4) (2007) 1103–1117. doi:10.1088/0031-9155/52/4/016.

[19] R. M. Turtos, S. Gundacker, E. Auffray, P. Lecoq, Towards a metamaterial approach for fast timing in PET: Experimental proof-of-concept, Physics in Medicine and Biology 64 (18) (2019). doi:10.1088/1361-6560/ab18b3.

[20] S. Gundacker, A. Knapitsch, E. Auffray, P. Jarron, T. Meyer, P. Lecoq, Time resolution deterioration with increasing crystal length in a TOF-PET system, Nuclear Instruments and Methods in Physics Research, Section A: Accelerators, Spectrometers, Detectors and Associated Equipment 737 (2014) (2014) 92–100. doi:10.1016/j.nima.2013.11.025.
URL http://dx.doi.org/10.1016/j.nima.2013.11.025

[21] B. Singh, M. S. Marshall, S. Waterman, C. Pina-Hernandez, A. Koshelev, K. Munechika, A. Knapitsch, M. Salomoni, R. Pots, P. Lecoq, V. V. Nagarkar, Enhanced Scintillation Light Extraction Using Nanoimprinted Photonic Crystals, IEEE Transactions on Nuclear Science 65 (4) (2018) 1059–1065. doi:10.1109/TNS.2018.2811646.

[22] S. Korpar, R. Dolenec, P. Križan, R. Pestotnik, A. Stanovnik, Study of TOF PET using Cherenkov light, Physics Procedia 37 (2012) 1531–1536. doi:10.1016/j.phpro.2012.03.750.

[23] R. Ota, K. Nakajima, T. Hasegawa, I. Ogawa, Y. Tamagawa, Timing-performance evaluation of Cherenkov-based radiation detectors, Nuclear Instruments and Methods in Physics Research, Section A: Accelerators, Spectrometers, Detectors and Associated Equipment 923 (November 2018) (2019) 1–4. doi:10.1016/j.nima.2019.01.034.
URL https://doi.org/10.1016/j.nima.2019.01.034

[24] G. Gallina, P. Giampa, F. Retière, J. Kroeger, G. Zhang, M. Ward, P. Margetak, G. Li, T. Tsang, L. Doria, S. Al Kharusi, M. Alfaris, G. Anton, I. J. Arnquist, I. Badhrees, P. S. Barbeau, D. Beck, V. Belov, T. Bhatta, J. Blatchford, J. P. Brodsky, E. Brown, T. Brunner, G. F. Cao, L. Cao, W. R. Cen, C. Chambers, S. A. Charlebois, M. Chiu, B. Cleveland, M. Coon, A. Craycraft, J. Dalmasson, T. Daniels, L. Darroch, S. J. Daugherty, A. De, A. Der Mesrobian-Kabakian, R. DeVoe, J. Dilling, Y. Y. Ding, M. J. Dolinski, A. Dragone, J. Echevers, M. Elbeltagi, L. Fabris, D. Fairbank, W. Fairbank, J. Farine, S. Feyzbakhsh, R. Fontaine, P. Gautam, G. Giacomini, R. Gornea, G. Gratta, E. V. Hansen, M. Heffner, E. W. Hoppe, J. Hößl, A. House, M. Hughes, Y. Ito, A. Iverson, A. Jamil, M. J. Jewell, X. S. Jiang, A. Karelin, L. J. Kaufman, D. Kodroff, T. Koffas, R. Krücken, A. Kuchenkov, K. S. Kumar, Y. Lan, A. Larson, B. G. Lenardo, D. S. Leonard, S. Li, Z. Li, C. Licciardi, Y. H. Lin, P. Lv, R. MacLellan, T. McElroy, M. Medina-Peregrina, T. Michel, B. Mong, D. C. Moore, K. Murray, P. Nakarmi, R. J. Newby, Z. Ning, O. Njoya, F. Nolet, O. Nusair, K. Odgers, A. Odian, M. Oriunno, J. L. Orrell, G. S. Ortega, I. Ostrovskiy, C. T. Overman, S. Parent, A. Piepke, A. Pocar, J. F. Pratte, D. Qiu, V. Radeka, E. Raguzin, S. Rescia, M. Richman, A. Robinson, T. Rossignol, P. C. Rowson, N. Roy, R. Saldanha, S. Sangiorgio, K. Skarpaas, A. K. Soma, G. St-Hilaire, V. Stekhanov, T. Stiegler, X. L. Sun, M. Tarka, J. Todd, T. Tolba, T. I. Totev, R. Tsang, F. Vachon, V. Veeraraghavan, G. Visser, J. L. Vuilleumier, M. Wagenpfeil, M. Walent, Q. Wang, J. Watkins, M. Weber, W. Wei, L. J. Wen, U. Wichoski, S. X. Wu, W. H. Wu, X. Wu, Q. Xia, H. Yang, L. Yang, Y. R. Yen, O. Zeldovich, J. Zhao, Y. Zhou, T. Ziegler, Characterization of the Hamamatsu VUV4 MPPCs for nEXO, Nuclear Instruments and Methods in Physics Research, Section A: Accelerators, Spectrometers, Detectors and Associated Equipment 940 (2019) 371–379. arXiv:1903.03663, doi:10.1016/j.nima.2019.05.096.

[25] R. Abdeddaim, P. Lecoq, S. Enoch, Metamaterials: opportunities in medical imaging (2019) 15doi:10.1117/12.2523340.

[26] H.P.K.K., PMT devices.
URL https://www.hamamatsu.com/eu/en/product/optical-sensors/pmt/index.html

[27] C. S. Levin, S. H. Maramraju, M. M. Khalighi, T. W. Deller, G. Delso, F. Jansen, Design Features and Mutual Compatibility Studies of the Time-of-Flight PET Capable GE SIGNA PET/MR System, IEEE Transactions on Medical Imaging 35 (8) (2016) 1907–1914. doi:10.1109/TMI.2016.2537811.

[28] A. M. Grant, T. W. Deller, M. M. Khalighi, S. H. Maramraju, G. Delso, C. S. Levin, NEMA NU 2-2012 performance studies for the SiPM-based ToF-PET component of the GE SIGNA PET/MR system, Medical Physics 43 (5) (2016) 2334–2343. doi:10.1118/1.4945416.

[29] F. Acerbi, S. Gundacker, Understanding and simulating SiPMs, Nuclear Instruments and Methods in Physics Research, Section A: Accelerators, Spectrometers, Detectors and Associated Equipment 926 (April) (2019) 16–35. doi:10.1016/j.nima.2018.11.118.
URL https://doi.org/10.1016/j.nima.2018.11.118

[30] J. Barral, Study of Silicon Photomultipliers (July) (2001) 76.

[31] T. Pro, A. Ferri, A. Gola, N. Serra, A. Tarolli, N. Zorzi, C. Piemonte, New developments of near-UV SiPMs at FBK, IEEE Transactions on Nuclear Science 60 (3) (2013) 2247–2253. doi:10.1109/TNS.2013.2259505.

[32] V. Puill, C. Bazin, D. Breton, L. Burmistrov, V. Chaumat, N. Dinu, J. Maalmi, J. F. Vagnucci, A. Stocchi, Single photoelectron timing resolution of SiPM as a function of the bias voltage, the wavelength and the temperature, Nuclear Instruments and Methods in Physics Research, Section A: Accelerators, Spectrometers, Detectors and Associated Equipment 695 (2012) 354–358. doi:10.1016/j.nima.2011.12.039.
URL http://dx.doi.org/10.1016/j.nima.2011.12.039

[33] M. Anti, F. Acerbi, A. Tosi, F. Zappa, 2D simulation for the impact of edge effects on the performance of planar InGaAs/InP SPADs, in: L. Mazuray, R. Wartmann, A. P. Wood, M. C. de la Fuente, J.-L. M. Tissot, J. M. Raynor, D. G. Smith, F. Wyrowski, A. Erdmann, T. E. Kidger, S. David, P. Benítez (Eds.), Optical Systems Design 2012, Vol. 8550, International Society for Optics and Photonics, SPIE, 2012, pp. 605–614. doi:10.1117/12.2001704.
URL https://doi.org/10.1117/12.2001704

[34] NKT Photonics, PiLas Picosecond Diode Laser.
URL https://www.nktphotonics.com/lasers-fibers/product/pilas-picosecond-pulsed-diode-lasers/

[35] G. Collazuol, The SiPM Physics and Technology - a Review, PhotoDet 2012 (June) (2012) 74.
URL http://indico.cern.ch/event/164917/contribution/72/material/slides/0.pdf

[36] V. J. Kitsmiller, C. Campbell, T. D. O'Sullivan, Optimizing sensitivity and dynamic range of silicon photomultipliers for frequency-domain near infrared spectroscopy, Biomedical Optics Express 11 (9) (2020) 5373. doi:10.1364/boe.401439.

[37] Hamamatsu Photonics K.K., Physics and operation of the MPPC silicon photomultiplier.
URL https://hub.hamamatsu.com/jp/en/technical-note/sipm-physics-operation/index.html

[38] Ketek, SiPM Noise.
URL https://www.aptechnologies.co.uk/support/SiPMs/Noise

[39] A. N. Otte, D. Garcia, T. Nguyen, D. Purushotham, Characterization of three high efficiency and blue sensitive silicon photomultipliers, Nuclear Instruments and Methods in Physics Research, Section A: Accelerators, Spectrometers, Detectors and Associated Equipment 846 (June 2016) (2017) 106–125. arXiv:1606.05186, doi:10.1016/j.nima.

2016.09.053.
URL http://dx.doi.org/10.1016/j.nima.2016.09.053

[40] M. L. Knoetig, J. Hose, R. Mirzoyan, SiPM avalanche size and crosstalk measurements with light emission microscopy, IEEE Transactions on Nuclear Science 61 (3) (2014) 1488–1492. doi:10.1109/TNS.2014.2322957.

[41] Y. Nakamura, A. Okumura, H. Tajima, N. Yamane, A. Zenin, Characterization of SiPM optical crosstalk and its dependence on the protection-window thickness, arXiv 011003 (2019) 1–6. arXiv:1909.07529, doi:10.7566/jpscp.27.011003.

[42] M. Carminati, C. Fiorini, Challenges for Microelectronics in Non-Invasive Medical Diagnostics, Sensors 20 (13) (2020). doi:10.3390/s20133636.
URL https://www.mdpi.com/1424-8220/20/13/3636

[43] J. Mazorra, H. Chanal, A. Comerma, D. Gascón, S. Gómez, X. Han, N. Pillet, R. Vandaele, {PACIFIC}: the readout {ASIC} for the {SciFi} Tracker of the upgraded {LHCb} detector, Journal of Instrumentation 11 (02) (2016) C02021—-C02021. doi:10.1088/1748-0221/11/02/c02021.
URL https://doi.org/10.1088{%}2F1748-0221{%}2F11{%}2F02{%}2Fc02021

[44] J. Mauricio, D. Gascón, D. Ciaglia, S. Gómez, G. Fernández, A. Sanuy, MATRIX: A 15 ps resistive interpolation TDC ASIC based on a novel regular structure, Journal of Instrumentation 11 (12) (2016). doi:10.1088/1748-0221/11/12/C12047.

[45] D. Gascon, A. Comerma, L. Freixas, Readout circuits for multichannel photomultiplier arrays, European Patent: EP 12382516.8 (2012).

[46] F. Yuan, Low-voltage CMOS current-mode circuits: topology and characteristics, IEE Proceedings-Circuits, Devices and Systems 153 (2006) 219–230.
URL http://digital-library.theiet.org/content/journals/10.1049/ip-cds{_}20045058

[47] J. Ramirez-Angulo, R. G. Carvajal, A. Torralba, Low Supply Voltage High-Performance CMOS Current Mirror With Low Input and Output Voltage Requirements, IEEE Transactions on Circuits and Systems II: Express Briefs 51 (3) (2004) 124–129.
URL 10.1109/TCSII.2003.822429

[48] S. M. Park, C. Toumazou, Low noise current-mode CMOS transimpedance amplifier for giga-bit optical communication, Proceedings - IEEE International Symposium on Circuits and Systems 1 (1998) 293–296. doi:10.1109/iscas.1998.704419.

[49] R. del Rio-Fernandez, G. Linan-Cembrano, R. Dominguez-Castro, A. Rodriquez-Vazquez, Mismatch-insensitive high-accuracy high-speed continuous-time current comparator in low voltage CMOS, IEEE-CAS Region 8 Workshop on Analog and Mixed IC Design, Proceedings (1997) 111–116doi:10.1109/amicd.1997.637202.

[50] J. Trenado, J. M. Cela, A. Comerma, D. Gascon, R. Graciani, L. Freixas, J. Marin, G. Martínez, R. Masachs, J. M. Perez, P. Rato, D. Sanchez, A. Sanuy, I. Sarasola, Performance of FlexToT time based PET readout ASIC for depth of interaction measurements, Proceedings of Science (2014). doi:10.22323/1.213.0241.

[51] V. V. IvanovIgor, M. Filanovsky, Operational Amplifier Speed and Accuracy Improvement, 2004. doi:10.1007/b105872.

[52] G. De Geronimo, P. O'Connor, A. Kandasamy, Analog CMOS peak detect and hold circuits. Part 2. The two-phase offset-free and derandomizing configuration, Nuclear Instruments and Methods in Physics Research, Section A: Accelerators, Spectrometers, Detectors and Associated Equipment 484 (1-3) (2002) 544–556. doi:10.1016/S0168-9002(01)02060-5.

[53] G. De Geronimo, P. O'Connor, A. Kandasamy, Analog CMOS peak detect and hold circuits. Part 1. Analysis of the classical configuration, Nuclear Instruments and Methods in Physics Research, Section A: Accelerators, Spectrometers, Detectors and Associated Equipment 484 (1-3) (2002) 533–543. doi:10.1016/S0168-9002(01)02059-9.

[54] W. M. C. Sansen, Analog Design Essentials, 1st Edition, Springer US, 2006.
URL https://doi.org/10.1007/b135984

[55] P. E. Allen, D. R. Holberg, CMOS Analog Circuit Design, Oxford University Press, 2002.

[56] J. Van Sluis, J. De Jong, J. Schaar, W. Noordzij, P. Van Snick, R. Dierckx, R. Borra, A. Willemsen, R. Boellaard, Performance characteristics of the digital biograph vision PET/CT system, Journal of Nuclear Medicine 60 (7) (2019) 1031–1036. doi:10.2967/jnumed.118.215418.

[57] R. D. Badawi, H. Shi, P. Hu, S. Chen, T. Xu, P. M. Price, Y. Ding, B. A. Spencer, L. Nardo, W. Liu, J. Bao, T. Jones, H. Li, S. R. Cherry, First human imaging studies with the explorer total-body PET scanner, Journal of Nuclear Medicine 60 (3) (2019) 299–303. doi:10.2967/jnumed.119.226498.

[58] V. Nadig, B. Weissler, H. Radermacher, V. Schulz, D. Schug, Investigation of the Power Consumption of the PETsys TOFPET2 ASIC, IEEE Transactions on Radiation and Plasma Medical Sciences 4 (2020) 378–388.
URL https://doi.org/10.1109/TRPMS.2019.2955032

[59] F. Anghinolfi, P. Jarron, A. N. Martemiyanov, E. Usenko, H. Wenninger, M. C. S. Williams, A. Zichichid, NINO: an ultra-fast and low-power front-end amplifier/discriminator ASIC designed for the multigap resistive plate chamber, Nuclear Instruments and Methods in Physics Research Section A: Accelerators, Spectrometers, Detectors and Associated Equipment 533 (2004).
URL https://doi.org/10.1016/j.nima.2004.07.024

[60] S. Gundacker, E. Auffray, B. Frisch, P. Jarron, A. Knapitsch, T. Meyer, M. Pizzichemi, P. Lecoq, Time of flight positron emission tomography towards 100ps resolution with L(Y){SO}: an experimental and theoretical analysis, Journal of Instrumentation 8 (07) (2013) P07014—-P07014. doi:10.1088/1748-0221/8/07/p07014.
URL https://doi.org/10.1088{%}2F1748-0221{%}2F8{%}2F07{%}2Fp07014

[61] I. Sarasola, M. V. Nemallapudi, S. Gundacker, D. Sánchez, D. Gascón, P. Rato, J. Marín, E. Auffray, A comparative study of the time performance between NINO and FlexToT

ASICs, Journal of Instrumentation 12 (4) (2017). doi:10.1088/1748-0221/12/04/P04016.

[62] S. Ahmad, J. Fleury, J. Cizel, C. de la Taille, N. Seguin-Moreau, S. Gundacker, E. Auffray-Hillemanns, Petiroc2A: Characterization and Experimental Results, in: 2018 IEEE Nuclear Science Symposium and Medical Imaging Conference Proceedings (NSS/MIC), 2018, pp. 1–4.

[63] "Weeroc".
URL https://www.weeroc.com/products/{%}0Asee-catalogue

[64] R. Bugalho, A. Di Francesco, L. Ferramacho, C. Leong, T. Niknejad, L. Oliveira, M. Rolo, J. C. Silva, R. Silva, M. Silveira, S. Tavernier, J. Varela, Experimental characterization of the TOFPET2 ASIC, Journal of Instrumentation 14 (3) (2019). doi:10.1088/1748-0221/14/03/P03029.

[65] PETsys Electronics.
URL https://www.petsyselectronics.com/web/

[66] A. Comerma, D. Gascón, L. Freixas, L. Garrido, R. Graciani, J. Marín, G. Martínez, J. M. Pérez, P. Rato Mendes, J. Castilla, J. M. Cela, J. M. Fernández-Varea, I. Sarasola, FlexToT - Current mode ASIC for readout of common cathode SiPM arrays, in: 2013 IEEE Nuclear Science Symposium and Medical Imaging Conference (2013 NSS/MIC), 2013, pp. 1–2.

[67] J. M. Cela, L. Freixas, J. I. Lagares, J. Marin, G. Martinez, J. Navarrete, J. C. Oller, J. M. Perez, P. Rato-Mendes, I. Sarasola, O. Vela, J. M. Fernandez-Varea, D. Gascon, S. Gomez, R. Graciani, J. Mauricio, D. Sanchez, A. Sanuy, O. de la Torre, D. Badia, A Compact Detector Module Design Based on FlexToT ASICs for Time-of-Flight PET-MR, IEEE Transactions on Radiation and Plasma Medical Sciences 2 (6) (2018) 549–553. doi:10.1109/trpms.2018.2870927.

[68] S. Gundacker, R. M. Turtos, E. Auffray, M. Paganoni, P. Lecoq, High-frequency {SiPM} readout advances measured coincidence time resolution limits in {TOF}-{PET}, Physics in Medicine & Biology 64 (5) (2019) 55012. doi:10.1088/1361-6560/aafd52.
URL https://doi.org/10.1088{%}2F1361-6560{%}2Faafd52

[69] Infineon, BGA616 Silicon Germanium Broadband MMIC Amplifier RF and Protection Devices.
URL https://www.infineon.com/dgdl/Infineon-BGA616-DS-v02{_}01-en.pdf?fileId=db3a304314dca3890115419102bb163b

3

Pixelated detectors

Time-of-Flight Positron Emission Tomography (TOF-PET) scanners demand fast and efficient photo-sensors and scintillators coupled to fast readout electronics. Nowadays, there are two main configurations regarding the scintillator crystal geometry: the segmented or pixelated and the monolithic approach. Depending on the cost, spatial resolution and time requirements of the PET module, one can choose between one or another. The pixelated crystal is the most extensive configuration on TOF-PET scanners as the coincidence time resolution is better compared to the monolithic.

This chapter presents the HRFlexToT measurements with single pixelated crystals coupled to different SiPMs. These measurements show an energy linearity error of ≈3% and an energy resolution below 10% of the 511 keV photopeak. Single Photon Time Resolution (SPTR) measurements performed using an FBK SiPM NUV-HD (4 mm × 4 mm pixel, 40 μm cell) and a Hamamatsu SiPM S13360-3050CS are around 141 ps and 167 ps FWHM respectively. Coincidence Time Resolution (CTR) measurements with small cross-section pixelated crystals (LFS crystal, 3 m × 3 mm × 20 mm) coupled to a single Hamamatsu SiPM S13360-3050CS provides a CTR of 180 ps FWHM. Shorter crystals (LSO:Ce Ca 0.4%) coupled to a Hamamatsu S13360-3050CS SiPM or FBK-NUVHD 40 μm (4 mm × 4 mm) yields a CTR of ≈ 117 ps and ≈ 119 ps respectively.

Contents

3.1 Introduction

The scintillator is in charge of absorbing the ionizing radiation from the 511 keV gammas produced in the positron annihilation and convert the absorbed energy into photons according to its light yield [1]. The gamma-ray conversion generates a pulse of photons in a time scale in the order of nanoseconds to microseconds with a certain time uncertainty. Several factors contribute to the time resolution such as the fluctuation of the interaction depth of the gamma-ray, the scintillation mechanism itself and the light transport from the emission point to the sensor [2]. Common scintillator-based gamma-ray detectors employ lutetium oxyorthosilicate (LSO) crystals and lutetium-yttrium oxyorthosilicate (LYSO) doped with cerium due to their good timing resolution, high light yield and energy resolution [3]. There are two types of scintillators commonly used in gamma ray detectors referred as pixelated crystals [4] and monolithic blocks [5]. Pixelated crystals are formed by a matrix of individual crystals coupled to arrays of photo-sensors (matching its pixel active area or covering part of it), whereas monolithic blocks have a surface covering the active area of several photo-sensors, commonly, the area of an array of pixels.

The DOI information remains unknown for a simple one-to-one coupling with pixelated crystals since all the light from a pixel crystal is impinging in a single SiPM and no light sharing patter can be extracted. In this case, the spatial resolution is defined and limited by the crystal segment size. The following bullet-points summarize the limitation on using pixelated crystals with respect to a monolithic solution:

- Spatial resolution: as mentioned earlier, an improvement on spatial resolution comes with a reduction on the cross-section of the scintillation crystal. On the contrary, the manufacturing process increases the complexity, and this increments the cost of the crystal production and finally the detector module itself.
- Light output reduction as a consequence of the cross-section (A) reduction needs to be taken into account. Due to the fact that the crystal has a certain length (L) in order to stop as many gamma rays as possible, a large ratio L/A makes the scintillation photons undergo multiple reflections before reaching the photosensor. Since crystal surfaces are never perfectly reflective (not even with teflon or ESR materials), a fraction of the scintillation light will be lost. The light collection efficiency for segmented crystals is thus generally lower compared to monolithic crystals.
- Dead space: there is also a fixed dead space between adjacent segmented crystals because of the reflective material of each pixelated crystal, which has a certain width. Some techniques such as laser engraving are trying to limit this effect by reducing the dead space between pixelated crystals [6, 7].
- DOI information: as mentioned before, no DOI information can be recovered from a pixeleted crystal in a one-to-one configuration. Different techniques can be applied with a underlying difficult algorithm and implementation complexities using pixelated crystals, e.g. phoswich [8], double side readout [9], multiple layer stack [10], among others. However, they imply a cost increment with respect to a monolithic solution.

Nevertheless, the best timing performance is obtained using segmented crystals as the number of photons collected by a single SiPM channel is higher compared to monolithic blocks, where the light of a single gamma event is shared among the different SiPM array channels. Most commercial PET scanners do not offer DOI detection at expenses on having good TOF performance [11], and often have large detector rings while employing a small transaxial field-of-view (FOV) to reduce the parallax error (see section 1.2.3.2). This chapter will show a complete study on timing and energy performance of the HRFlexToT ASIC in combination with different segmented crystal materials and SiPM models.

3.2 Materials and instrumentation

3.2.1 Energy resolution setup

The linearity test was performed using an electrical pulse injected directly to the HRFlexToT ASIC, as depicted in Figure 3.1. A waveform generator that emulates the SiPM signal response sends the pulse to a programmable attenuator. This allows to sweep a wide range of attenuation factors in order to study the behavior of the ASIC with several signal amplitudes and hence, different input currents (from 30 μA to 35 mA).

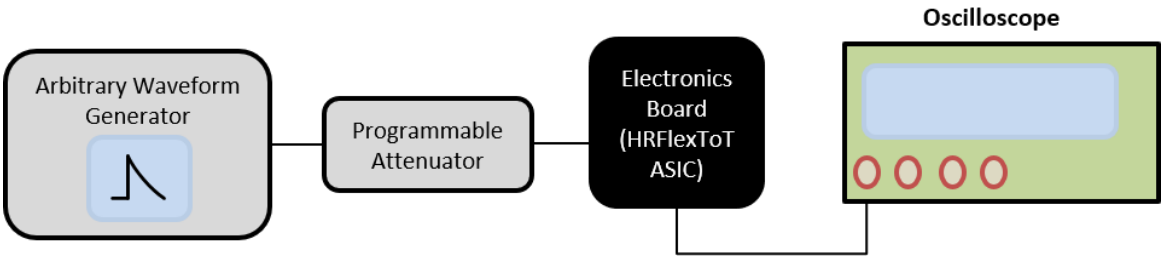

Figure 3.1.: Schematic representation of the experimental setup used to evaluate the linearity of the energy measurement.

3.2.2 Energy resolution setup

A simple setup embedded in a black box with stable temperature was used to perform energy resolution measurements. Figure 3.2 shows the set up used to obtain the desired energy spectrum from a radioactive source. The energy resolution was evaluated using an LFS crystal of size $3 \times 3 \times 20$ mm^3 wrapped in Teflon and a thin metal layer attached to a single channel S13360-3050CS MPPC.

The energy measurement provided by the HRFlexToT is encoded in a binary pulse that must be digitized using a TDC [12]. In this case, a TDC implemented in an FPGA with 94 ps FWHM time bin resolution was employed.

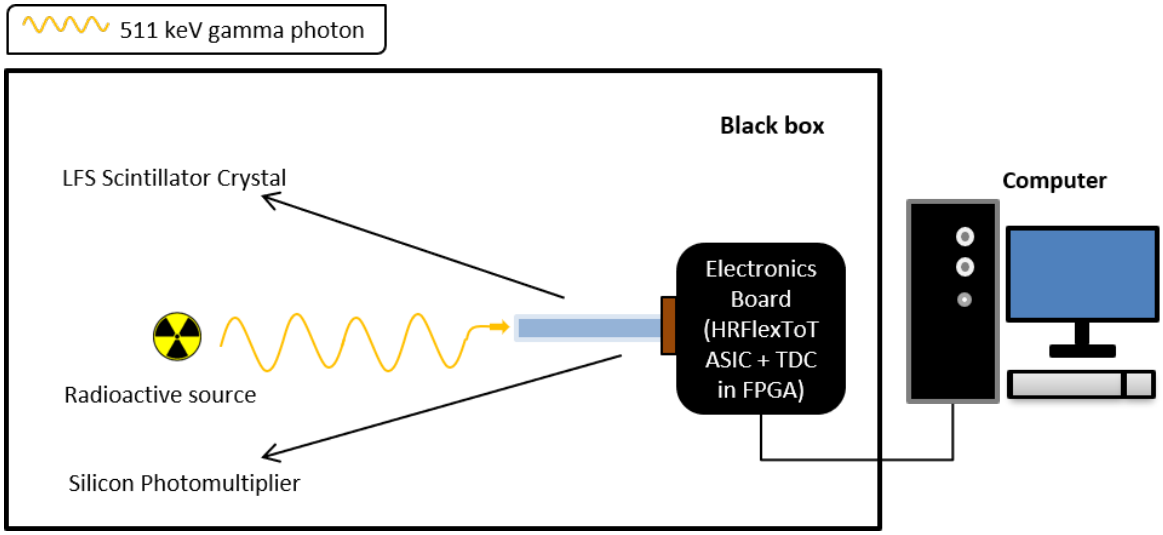

Figure 3.2.: Schematic representation of the experimental setup to perform spectroscopy.

3.2.3 SPTR setup

The setup used to perform SPTR measurements is shown in Figure 3.3. Firstly, an external trigger at 500kHz that sends a signal to both the laser driver and the oscilloscope. Secondly, the laser driver sends a pulse to the laser (Picosecond laser diode system 'PiL040X' at 405nm, jitter < 3 ps and < 45 ps pulse width from Advanced Laser Diode Systems A.L.S. GmbH). The laser generates a blue photon package that goes through a Single Mode Fiber (Throlabs 305A-FC SM) to a beam collimator. Coupled to this, there is a Liquid Crystal Optical Beam Attenuator from Thorlabs, which can change the attenuation factor depending on the voltage applied (from 0 V to 5 V, minimum to maximum attenuation correspondingly). Finally, the beam pulse arrives to a diffuser spreading the light homogeneously over the sensor. Additionally, temperature is stabilized around 15 °C to avoid gain variations and diminish dark count noise.

The time per event of each detector is acquired with an Agilent MSO 9404A 4 Ghz waveform analyzer (20 GS/s). More specifically, it captures the timestamp from the laser trigger, as well as the time signal generated from the photon detected by the SiPM and processed by the HRFlexToT leading edge comparator.

3.2.4 CTR setup

The process starts with the annihilation of the positron emitted by the ^{22}Na radioactive source. Thus, resulting in two gamma photons of 511 keV traveling in a back-to-back configuration. Then, when the gamma reaches the scintillator crystal there is a probability of interaction described by either photoelectric or Compton effect. If any of these two processes occurs, the energy is transferred to the crystal and it is converted into optical photons in the

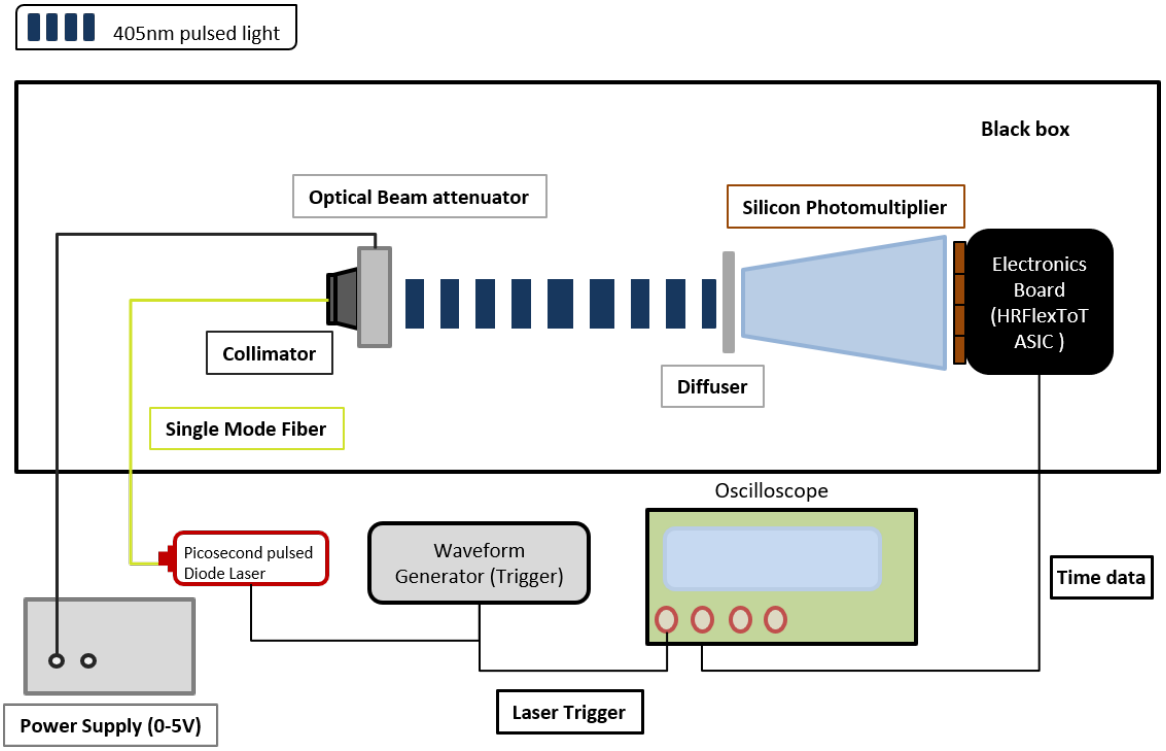

Figure 3.3.: Schematic representation of the experimental setup using the laser source for SPTR measurements.

optical range between 400-600 nm typically. A fraction of those photons will arrive to the photo-sensor, in this case a SiPM, and generate a current signal that will be collected by the FE electronics to extract both energy and time information. The setup configuration is shown in figure 3.4. Note that all measurements are taken in an isolated black box at a constant temperature of 20 °C if no other condition is specified.

The energy and time per event of each detector is acquired with an Agilent MSO 9404A 4 Ghz waveform analyzer (20 GS/s). The time delay is calculated by doing the time arrival difference between boards. Particularly, the events at 3 sigmas from the mean photopeak at 511 keV are the ones used to compute the CTR.

3.3 Experimental Results

The new redesigned HRFlexToT ASIC presents a power consumption reduced from 10 mW/ch to 3.5 mW/ch thanks to the employment of XFAB 0.18 μm CMOS technology instead of AMS 0.35 μm HBT BiCMOS technology as was utilized in the FlexToT. The aim of this section is to illustrate the potential capabilities of the HRFlexToT throughout different experimental tests. Firstly, the linearity and resolution of the energy acquisition system are provided. Then, SPTR measurements are performed with different SiPMs. Lastly, the ASIC is being tested with pixelated crystals to evaluate its CTR performance.

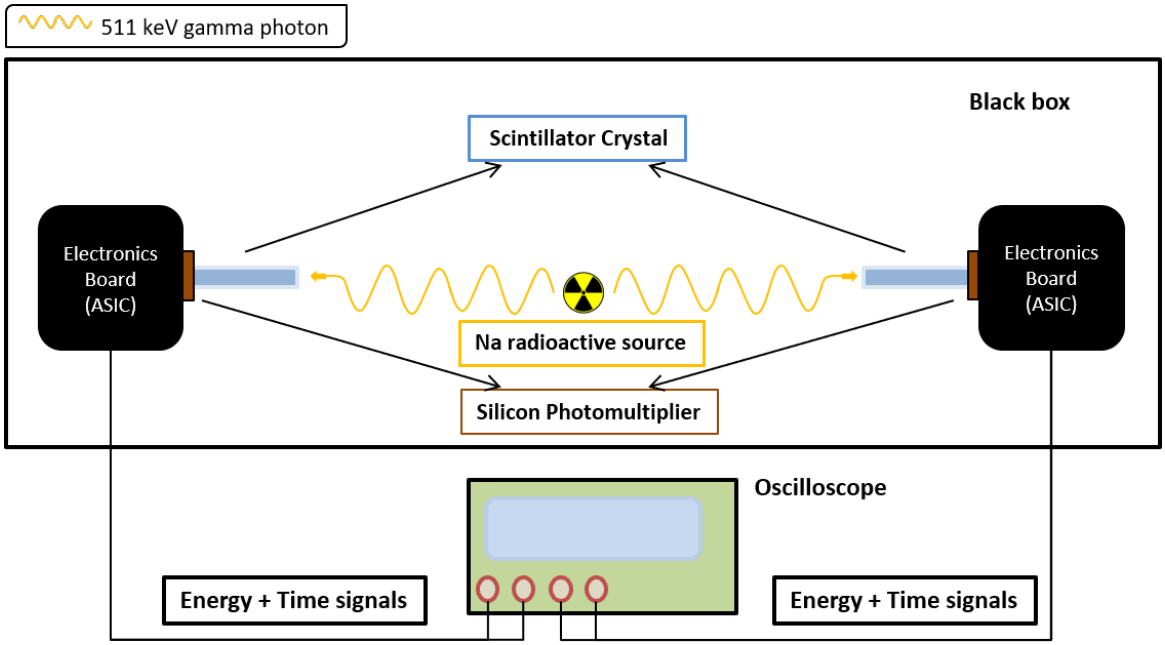

Figure 3.4.: Schematic representation of the experimental setup for gamma coincidence measurements.

3.3.1 Linearity of the energy measurement

In a real detector system, the number of photons collected by the sensor are directly related to the energy deposited by the original gamma ray into the scintillator crystal in a PET scanner. A good energy resolution over a wide range of energies is needed in several applications to achieve the best detector performance and consequently, increase the reconstructed image quality.

The linearity test was performed using the setup described in 3.2.1. The HRFlexToT can be configured with several gain modes that model the dynamic range response. As an example, Figure 3.5a and 3.5b show the highest and the lowest gain configurations, respectively. The maximum gain should be used for very low light level (single photon), whereas the minimum gain should be used for events where a high number of photons are collected (gamma ray detection using segmented scintillator crystals).

The energy response behaves linearly for different gain configurations with a linearity error of $\approx 3\%$. Lastly, this test was performed for all 16 channels and a gain uniformity error below 2% between the different channels for both gain configurations was found.

3.3.2 Energy spectroscopy

The setup involved is described in 3.2.2. A crystal with a relatively large height is used to maximize the probability of capturing the produced gammas, especially those of higher

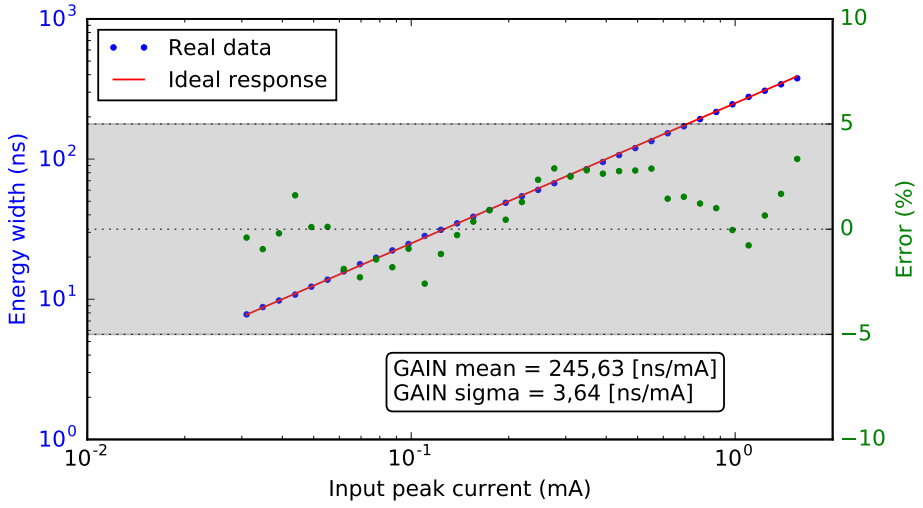

(a)

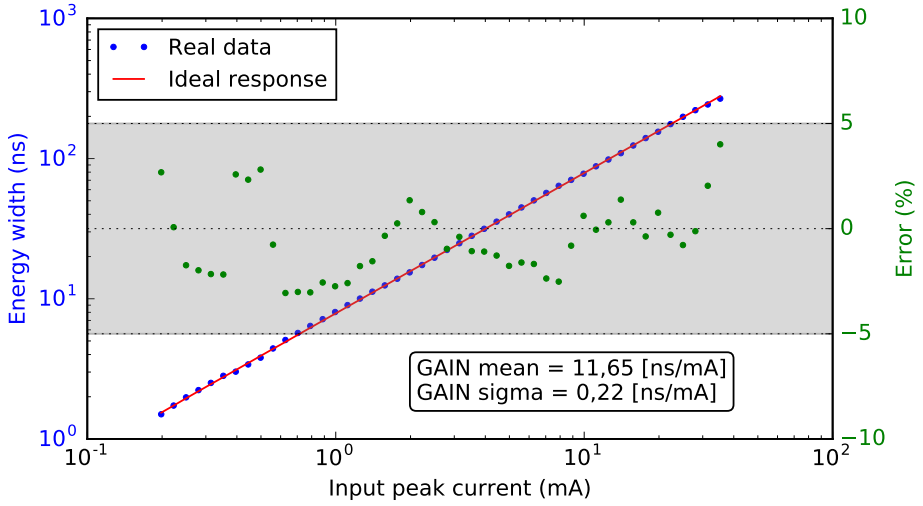

(b)

Figure 3.5.: Energy measurement for a given channel and the associated error. Gain mean and sigma between the 16 channels is also provided. (a) Highest gain. (b) Lowest gain.

energies. Figure 3.6 illustrates a gamma-ray spectroscopy acquisition of 2 radiation sources, ^{22}Na and ^{137}Cs.

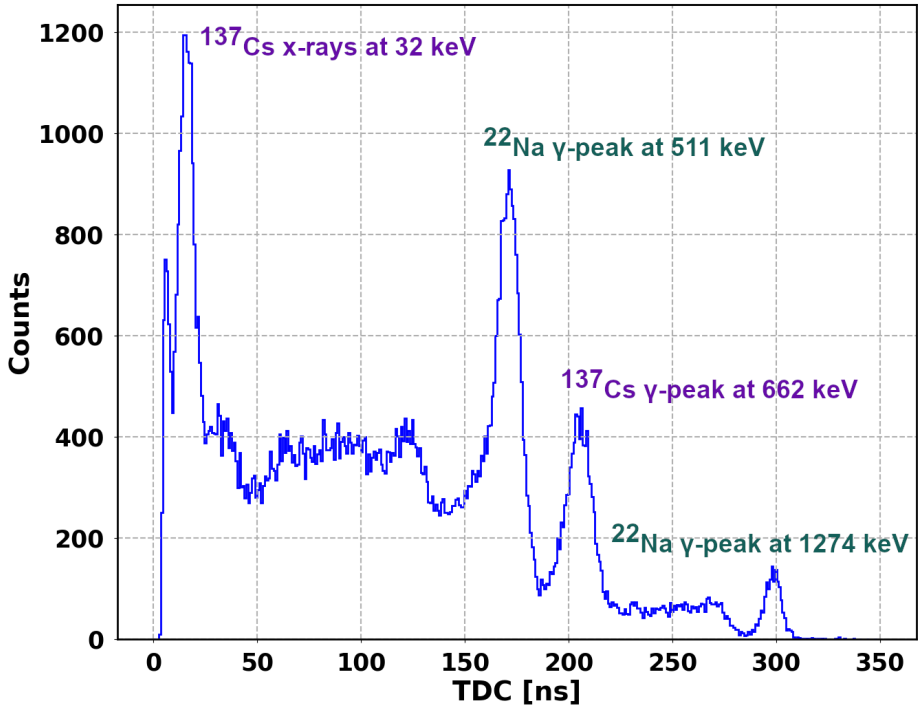

Figure 3.6.: ^{22}Na and ^{137}Cs spectrum in ns using the HRFlexToT ASIC and the TDC from the FPGA.

Figure 3.6 clearly shows a linearity problem since the distance from 0 to the first ^{22}Na γ-peak at 511 keV is larger than the distance between this peak and the second ^{22}Na γ-peak at 1274 keV. As previously seen, the ASIC configured in a low gain mode has a large dynamic range and thus the energy response should not be saturated. The SiPM S13360-3050CS reaches saturation above 2000 fired micro-cells [13], whereas the expected number of photons reaching the surface of the scintillator might be close to 7000. Hence, saturation effects might be observed, depending on the efficiency to collect those photons (a combination of fill factor and quantum efficiency). Note that, the scintillator might also present non-linear responses for large energy depositions, but in this experiment correcting the SiPM response ensures a linear spectrum. Lastly, besides of correcting the linearity of the system, the TDC response must be calibrated into keV for spectroscopy measurements.

The following equation takes into account this saturation effect to linearize the scale of the system:

$$N_{photon} \cdot PDE = -N_{total} \cdot ln\left[1 - \frac{N_{fired}}{N_{total}}\right] \tag{3.1}$$

where N_{photon} is the number of photons arriving to the sensor, PDE stands for the Photon Detection Efficiency, N_{total} is the total number of micro-cells, and N_{fired} is the number of fired micro-cells. Thus, the $N_{photon} \cdot PDE$ captures the detected photons following a linear behavior. In particular, N_{fired} is directly related to the collected energy following the expression:

$$N_{fired} = TDC[ns] \cdot f \tag{3.2}$$

where $TDC[ns]$ is the width of the energy signal in nanoseconds and f is the calibration factor corresponding to the number of fired micro-cells per nanosecond of the energy pulse width, i.e., the energy gain in photons/nanosecond units. The calibration factor f can be found using the energy ratio of the gamma peaks from the ^{22}Na source and the ratio of the detected photons at those energies as follows.

$$\frac{N_{photon} \cdot PDE[1274keV]}{N_{photon} \cdot PDE[511keV]} = \frac{1274}{511} = 2.49 \tag{3.3}$$

The linearized energy spectrum could be represented in terms of detected photons ($N_{photon} \cdot PDE$) using the calibration factor f and equation 3.2. Then, the energy in terms of electron-volts could be obtained using the detected photons as follows:

$$N_{photon} \cdot PDE = a + b * Energy[keV] \tag{3.4}$$

where a and b are coefficients that can be obtained as the linear regression equation of several calibration points. Figure 3.7 shows the linear regression to calibrate the system using the most significant peaks of several radiations sources: ^{22}Na (Compton backscatter peak, Compton Edge, 511 keV and 1274 keV gammas), ^{137}Cs (X-rays at 32 keV and 662 keV gamma peak), ^{241}Am (26 keV and 60 keV gamma peaks) and ^{60}Co (1173 keV and 1333 keV).

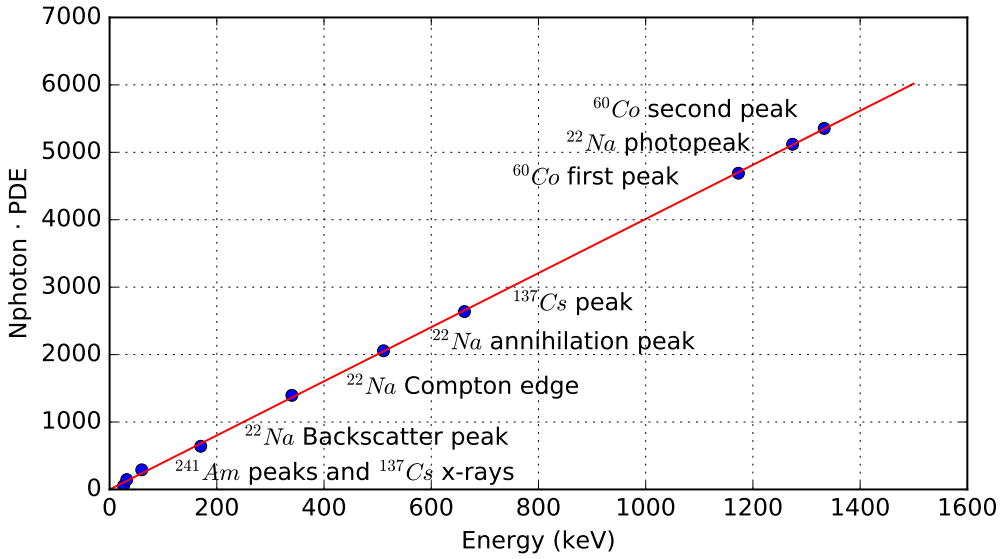

Figure 3.7.: Linear regression to calibrate the energy system with several radioactive sources.

Figure 3.8 illustrates the linearized energy spectrum in terms of keV for the two radiation sources, ^{22}Na and ^{137}Cs. Note that the gamma photopeaks of both radiation sources can be

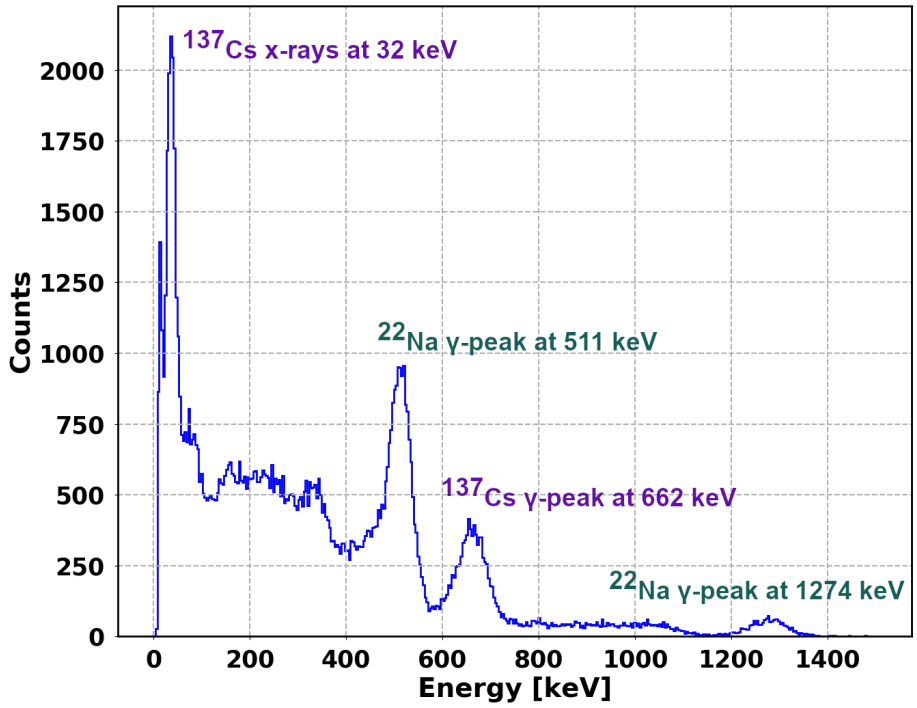

Figure 3.8.: ^{22}Na and ^{137}Cs spectrum in calibrated energy units (keV) using the HRFlexToT ASIC and the TDC from the FPGA after linearization of the SiPM response.

perfectly identified at their correspinding energy. Lastly, the energy resolution of a given radiation source, R, can be obtained using the following expression:

$$R = \frac{FWHM}{\mu} \tag{3.5}$$

where $FWHM$ is the full width at half maximum and μ is the mean of the Gaussian fit for a specific detected peak. The resolution at 511 keV from ^{22}Na is 9.77% and the resolution at 662 keV from ^{137}Cs is 10.27%.

3.3.3 SPTR measurements

The width of the time signal calculated using the non-linear ToT is required to identify the single photon events. The standard deviation of the delay between the trigger and the SiPM signal timestamps, i.e. the jitter corresponding to the single events, is known as the Single Photon Time Resolution (SPTR). Each peak is fitted following the traditional method of the Gaussian approximation, where the FWHM value of this Gaussian corresponds to the SPTR in FWHM. Moreover, each peak is fitted using a Gaussian convoluted with an exponential approximation where the FWHM also represents the SPTR and it captures more accurately the arrival time of the photons [14].

An example of the SPTR measurements can be seen in Figure 3.9 and Figure 3.10 for the Hamamatsu SiPM S13360-3050CS and the Fondazione Bruno Kessler (FBK) SiPM NUV-HD

(4 mm × 4 mm pixel, 40 μm cell) respectively. These figures illustrate the different photons captured (or firing cells) in the top plot, and the corresponding SPTR distribution on the bottom one. A time jitter of 142 ps FWHM is found using this configuration with the FBK SiPM NUV-HD and 167 ps FWHM with the Hamamatsu SiPM S13360-3050CS both with the HRFlexToT ASIC. Additionally, Table 3.1 details a comparison between the HRFlexToT and the NINO ASIC [15, 16, 31] in terms of SPTR showing that both ASICs achieve an excellent timing performance.

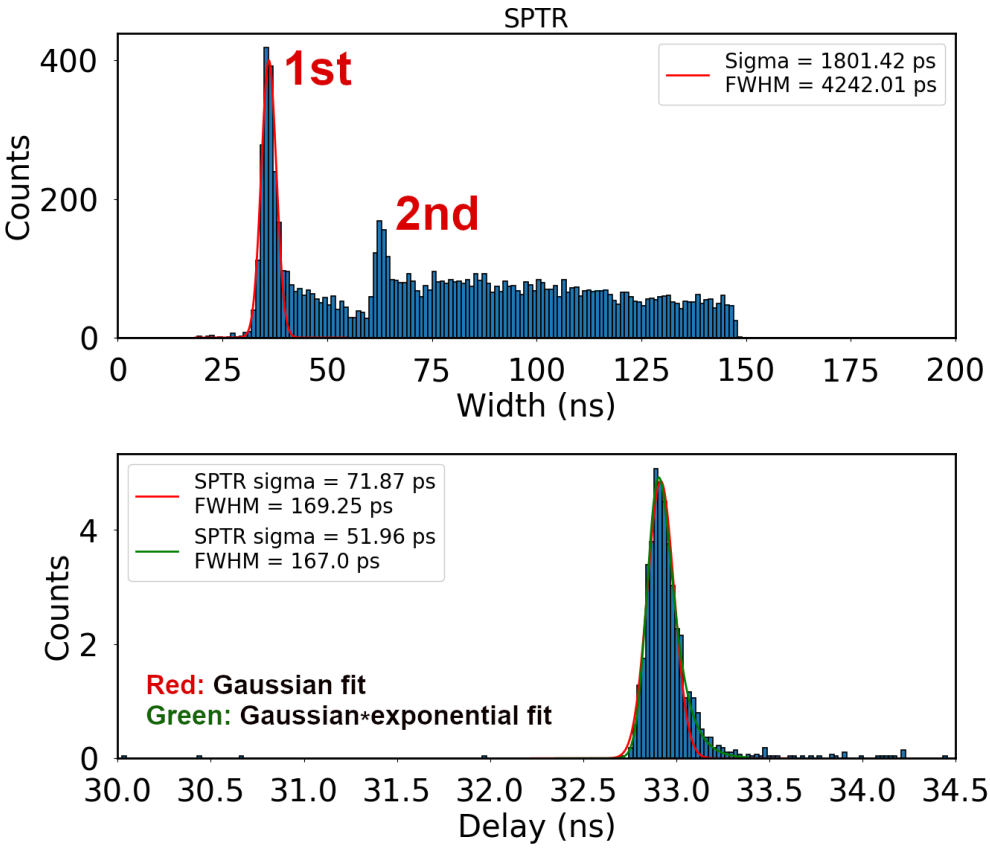

Figure 3.9.: (Above) non-linear ToT width distribution and (bottom) delay of arrival time of the first photon for Time output using HPKK SiPM S13360-3050CS (3 mm × 3 mm pixel, 50 μm cell).

Table 3.1.: SPTR comparison in FWHM between the HRFlexToT and NINO ASIC for the best over-voltage (VoV).

SiPM	NINO	HRFlexToT
HPKK S13360-3050CS (3 mm × 3 mm pixel, 50 μm cell)	160 ps FWHM (10V of Ov)	167 ps FWHM (10V of Ov)
FBK NUV-HD (4 mm × 4 mm pixel, 40 μm cell)	135 ps FWHM (12V of Ov)	142 ps FWHM (11.5V of Ov)

The SPTR performance of the HRFlexToT was also here compared to its predecessor FlexToT ASIC [17, 18]. Two consecutive acquisition runs with the same over-voltages, system

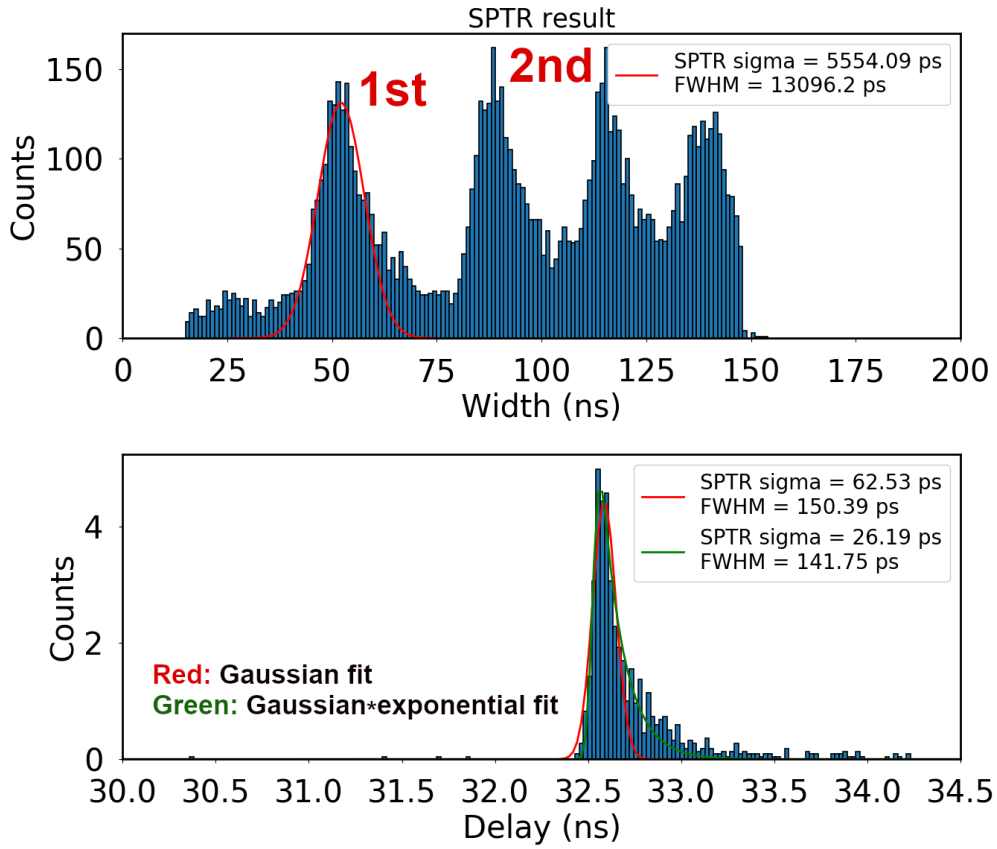

Figure 3.10.: (Above) non-linear ToT width distribution and (bottom) delay of arrival time of the first photon for Time output using FBK SiPM NUV-HD (4 mm× 4 mm pixel, 40 μm cell).

conditions (temperature stable at 18 °C) and optimal time threshold for each ASIC has been done. In this study, a laser firing red photons was employed (PicoQuant PDL 800-D laser at 635 nm, jitter $<$ 20 ps rms and 50 ps pulse width). Figure 3.11 shows the SPTR comparison between both ASICs. An improvement around 30-40% in the time resolution depending on the over-voltage with 3 times less power consumption can be observed. Note that the minimum SPTR (60 ps) achieved in this experiment is lower compared to the SPTR (71 ps) shown in Figure 3.9 for the same HPKK SiPM S13360-3050CS.

A possible explanation of this SPTR difference lies in the internal structure of the HPKK SiPM S13360-3050CS model which is built on p-on-n buried junction structure [19]. Red photons are mainly but not only absorbed beneath the junction where holes can trigger the avalanche, whereas photo-generation of blue photons occurs only close to the surface above the junction where only electrons trigger the avalanche. Note that red photons penetrate deeper further away from the surface due to the photon absorption length of silicon increases with wavelength [20]. This difference in the absorption point results in more penetration time spread towards the buried junction for blue photons and thus slightly larger jitter [21]. Note that this p-on-n structure is considered blue sensitive, despite of having better SPTR for red photons, since holes have a lower triggering probability than electrons and thus lower PDE for red wavelengths and larger PDE in the blue spectrum [22]. Hence, this sensor is

perfectly suitable for CTR measurements in a PET module where most of the events are captured in the blue region.

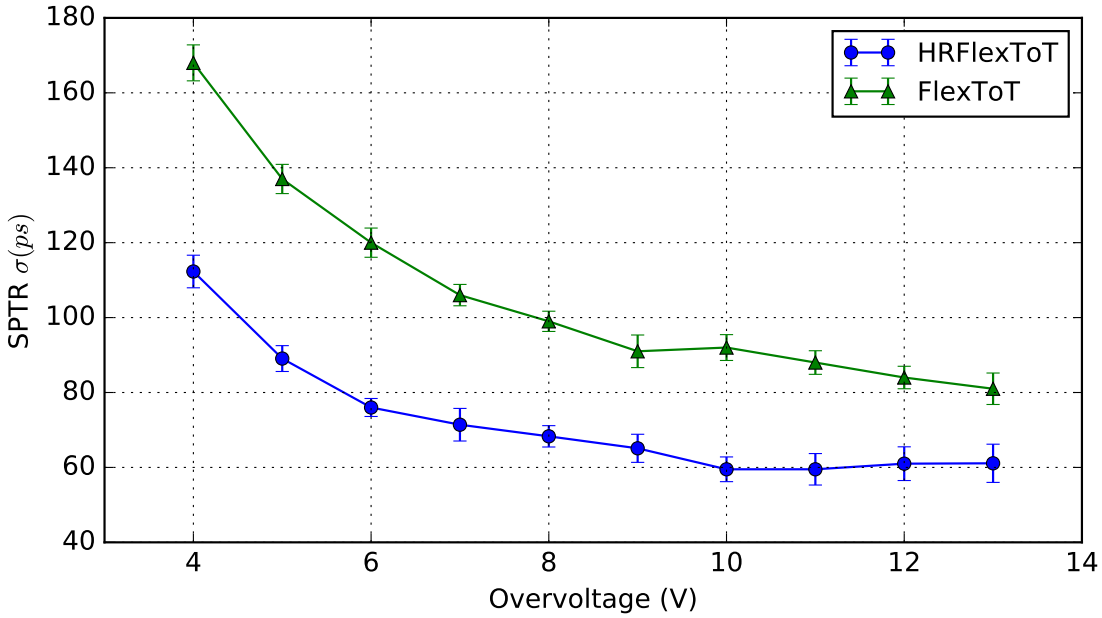

Figure 3.11.: SPTR comparison between the new HRFlexToT and the old FlexToT. Sensor used: HPKK SiPM S13360-3050CS (3 mm × 3 mm pixel, 50 μm cell)

3.3.4 Pixelated CTR measurements

The CTR of different scintillator crystals and SiPMs were evaluated and compared between the NINO ASIC, the old FlexToT version and the HRFlexToT at CERN Crystal Clear lab. The NINO ASIC readout with some discrete electronics used for CTR measurements is described in [23].

An example of the figure of merit for a typical CTR measurement can be seen in Figure 3.12. In this configuration, a small LSO:Ce Ca 0.4% co-doped scintillator crystal of 2 mm × 2 mm × 5 mm size is attached to the 3 mm × 3 mm Hamamatsu SiPM S13360-3050CS. On one hand, the plots on the top correspond to the energy deposited on each detector, where the 511 keV photopeak is clearly visibly. Note that the second peak from the typical ^{22}Na spectrum is not visible, due to the fact that the trigger is set in coincidence mode, and only events where both 511 keV gammas deposit energy on the crystal are recorded. On the other hand, the delay time between detectors for the events corresponding to the 511 keV peak is represented on the bottom plot. A CTR of 117 ps FWHM is achieved with the Hamamatsu SiPM S13360-3050CS.

The same crystal is used coupled to an FBK SiPM NUV-HD (4 mm × 4 mm pixel, 40 μm cell), as can be seen in Figure 3.13. The HRFlexToT readout shows an almost identical CTR measurement for the NUV-HD of 119 ps compared to the Hamamatsu SiPM. It is

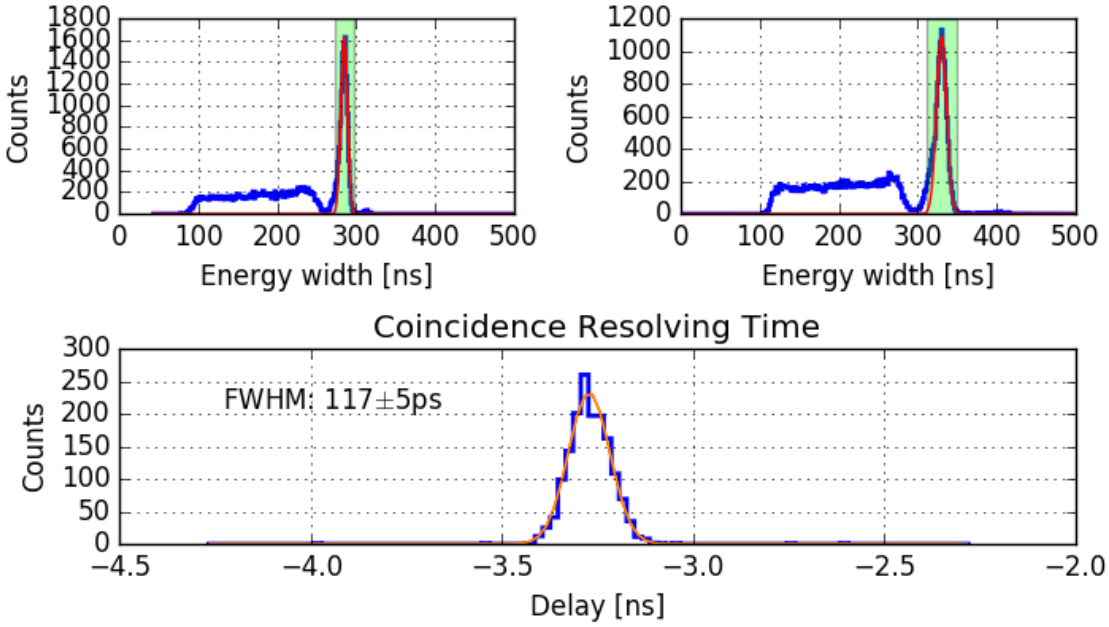

Figure 3.12.: CTR measurement with LSO:Ce Ca 0.4% of 2 mm × 2 mm × 5 mm size coupled to a S13360-3050CS SiPM at 8 V of over-voltage.

important to highlight that the NUV-HD despite of having a better SPTR compared to the Hamamatsu SiPM, the CTR behaves similarly. This discrepancy can be explained due to the increment in device capacitance for the FBK in contrast to the Hamamatsu sensor. This larger capacitance and thus larger recovery time might cause more pile-up effects which produce baseline fluctuations in the leading-edge comparator deteriorating the time response. Another reason could come from the intrinsic parameters of each sensor, PDE is similar in both sensors [24], but cross-talk is worse in the FBK SiPM and also deteriorating the CTR [25, 26].

This crystal and SiPM sensor were selected to compare with NINO ultimate performance. The CTR comparison between both electronics for a range of over-voltages between 3 V and 10 V can be seen in Figure 3.14. Observe that the NINO ASIC presents an $\approx 15\%$ better CTR compared to the HRFlexToT. This discrepancy could be explained due to the employment of a differential input for the readout of the SiPM instead of a single ended anode readout from the HRFlexToT.

The previous case study employing 5 mm long crystals is not commonly used in standard PET as the efficiency of the detector decreases with the thickness of the scintillator crystal. Nowadays, the 20 mm length is extensively used on PET devices [11] as the best trade-off between cost/efficiency/performance; small variations with 18 mm length can be also utilized as seen in [27]. Figure 3.15 shows that CTR values increases from 117 ps to 175 ps at FWHM for a crystal with 20 mm length. This effect is mainly caused by the increase of the light transit time spread and the gamma interaction point fluctuation related to the depth of interaction (DOI) of the crystal [28].

In this work, the CTR obtained with long crystals of 3 × 3 × 20 mm^3 made of LYSO material was compared with NINO, HRFlexToT and the old FlexToT ASICs. Figure 3.15

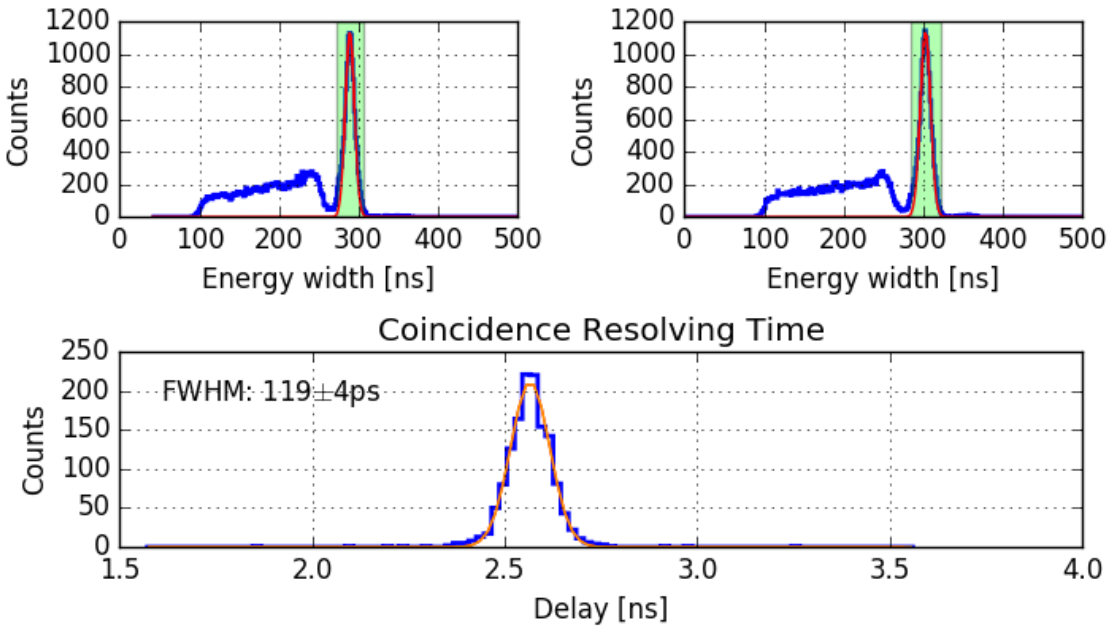

Figure 3.13.: CTR measurement with LSO:Ce Ca 0.4% coupled to a NUV-HD SiPM (4 mm × 4 mm pixel, 40 μm cell) at 9 V of over-voltage.

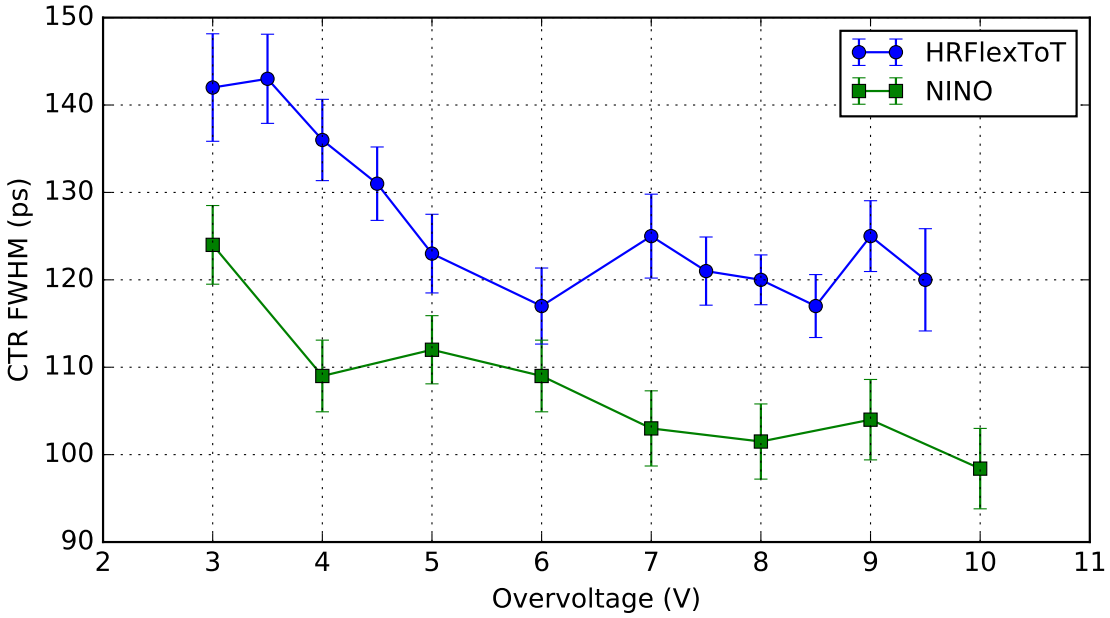

Figure 3.14.: CTR comparison between the new HRFlexToT and the NINO ASIC from CERN. Sensor used: Hamamatsu SiPM S13360-3050CS (3 mm × 3 mm pixel, 50 μm cell). Crystal used: 2 mm × 2 mm × 5 mm LSO:Ce 0.4% Ca

illustrates the improvement made on this last version of the chip and how they compare to NINO. The HRFlexToT shows an improvement of ≈ 15% in CTR with respect to the previous FlexToT ASIC, thus representing a big improvement in the electronic jitter contribution. Lastly, NINO also presents the same ≈ 15% better CTR compared to the HRFlexToT as seen with smaller crystals.

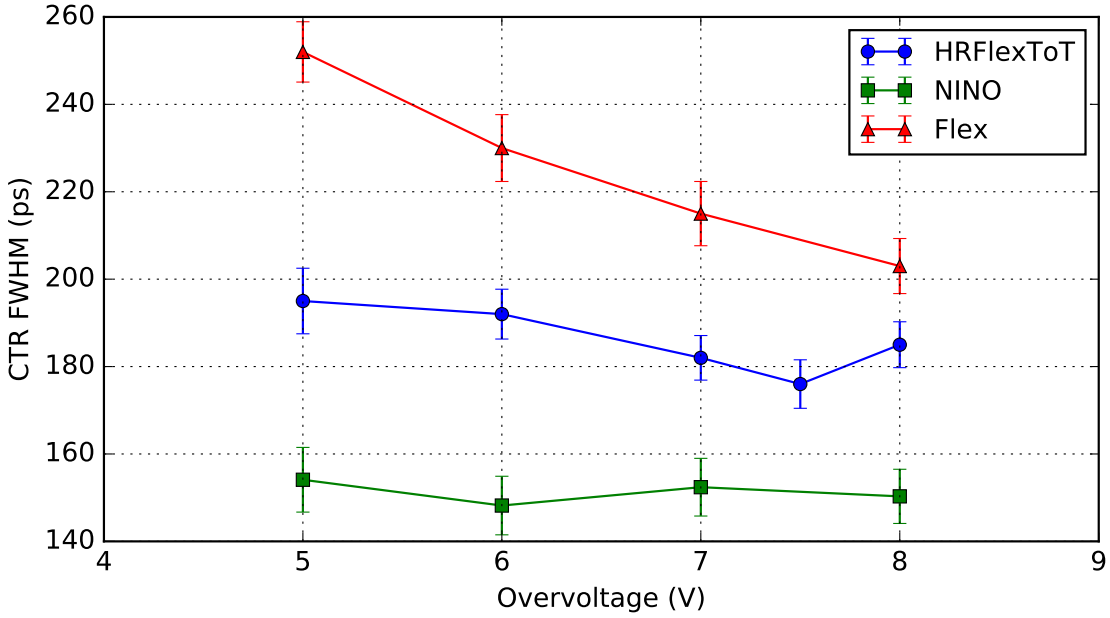

Figure 3.15.: CTR comparison between the new HRFlexToT, the old FlexToT and NINO ASIC from CERN. Sensor used: Hamamatsu SiPM S13360-3050CS (3 mm × 3 mm pixel, 75 μm cell). Crystal used: 3 mm × 3 mm × 20 mm LYSO

3.4 Conclusions

A complete evaluation of the HRFlexToT ASIC suitable for TOF-PET systems employing either pixelated or monolithic scintillators was here detailed. The new redesigned HRFlexToT presents a power consumption reduced from 11 mW/ch to 3.5 mW/ch and better time and energy performance compared to its predecessor. The ASIC provides promising performances at the same level or even better compared to other electronics. To the best of the authors knowledge, the HRFlexToT has the best time resolution in terms of SPTR (142 ps FWHM) for a FBK SiPM NUV-HD (4 mm × 4 mm pixel, 40 μm cell) compared to other ASICs available in the literature for TOF-PET systems.

Experimental results showed a CTR of 117 ps and 119 ps FWHM for crystals (LSO:Ce, Ca 0.4%) coupled to a Hamamatsu SiPM S13360-3050CS and FBK SiPM NUV-HD (4 mm × 4 mm pixel, 40 μm cell) respectively. The NINO ASIC still achieves a CTR of 97 ps for the same setup, but with nearly 8 times more power consumption and without a linear energy measurement to capture the 511 keV photopeak. The lower CTR achieved by NINO

might be obtained thanks to the employment of a differential input readout, whereas the HRFlexToT is connected to the SiPM via single ended anode connection. A module with two monolithic crystals with large cross-section (LFS crystal of 25 mm × 25 mm × 20 mm) and Teflon wrapped coupled to an SiPM array (S13361-6050NE-04, 6 mm × 6 mm, 50 μm pixel pitch) shows a CTR of 324 ps FWHM after time-walk and time-skew calibration.

A comparison between the HRFlexToT and other ASICs in the literature is shown Table 3.2. For instance, TOFPET2 or PETIROC2A achieve performances slightly worse than the HRFlexToT but include internal TDCs for digitization of timestamps. Note that NINO, despite obtaining the best time resolution for an ASIC, it does not provide a linear energy measurement. Moreover, the SPTR achieved by the HRFlexToT is rather close to the one obtained by the HF readout with a low power budget.

The HRFlexToT ASIC can be directly connected to the MATRIX ASIC [12], a 4-channel TDC chip with 10-ps time resolution and 11 mW/ch of power consumption, to digitize the Fast Timing OR output response provided by the HRFlexToT. Recently, the group developed a new version of the MATRIX ASIC, including 16 channels with the same time resolution (≈ 10 ps), lower power consumption (≈ 8.2 mW/ch) and capable of processing the time+energy output. The combination of the HRFlexTOT and the MATRIX ASICs will form a complete readout system providing digitized data for the TOF-PET image reconstruction.

Future work will include a complete analysis of the capabilities of the HRFlexToT with monolithic crystals. Experimental measurements with larger SiPM arrays including several HRFlexToT and MATRIX ASICs will be performed. Lastly, the HRFlexToT will be tested with other scintillator crystals capable of capturing prompt light, such as Cherenkov light [29, 30].

Table 3.2.: Performance comparison between different ASICs suitable for TOF-PET applications. The HF readout is also added to illustrate the time resolution that can be achieved with an almost "perfect" electronics with current sensors.

ASIC	Power in mW/ch	SPTR in ps FWHM	SiPM Model	Timestamp Time bin	Reference
HF readout	720	144 92	S13360-3050PE NUV-HD (4 × 4, 40 μm)	External	[29, 31]
NINO	27	160 135	S13360-3050CS NUV-HD (4 × 4, 40 μm)	External	[15, 31], This work
HRFlexToT	3.5	167 142	S13360-3050CS NUV-HD (4 × 4, 40 μm)	External	This work
FlexToT	11	214	S13360-3050CS	External	[16]
PETIROC2A	6	190	S13360-3050PE	30 ps	[32]
TOFPET2	8.2	212	S13361-3050AE-04	30 ps	[33]

3.5 Bibliography

[1] M. Dahlbom, Physics of PET and SPECT Imaging, CRC press, 2017.
URL https://doi.org/10.4324/9781315374383

[2] P. Lecoq, Pushing the Limits in Time-of-Flight PET Imaging, IEEE Transactions on Radiation and Plasma Medical Sciences 1 (6) (2017) 473–485. doi:10.1109/TRPMS.2017.2756674.
URL http://ieeexplore.ieee.org/document/8049484/

[3] S. Gundacker, F. Acerbi, E. Auffray, A. Ferri, A. Gola, M. V. Nemallapudi, G. Paternoster, C. Piemonte, P. Lecoq, State of the art timing in TOF-PET detectors with LuAG, GAGG and L(Y)SO scintillators of various sizes coupled to FBK-SiPMs, Journal of Instrumentation 11 (8) (2016). doi:10.1088/1748-0221/11/08/P08008.

[4] M. Pizzichemi, A. Polesel, G. Stringhini, S. Gundacker, P. Lecoq, S. Tavernier, M. Paganoni, E. Auffray, On light sharing {TOF}-{PET} modules with depth of interaction and 157 ps {FWHM} coincidence time resolution, Physics in Medicine & Biology 64 (15) (2019) 155008. doi:10.1088/1361-6560/ab2cb0.
URL https://doi.org/10.1088{%}2F1361-6560{%}2Fab2cb0

[5] E. Lamprou, A. Gonzalez, F. J. Sanchez, J. M. Benlloch, Exploring TOF capabilities of PET detector blocks based on large monolithic crystals and analog SiPMs, {ELSEVIER} Physica Medica 70 (2020) 10–18.
URL https://doi.org/10.1016/j.ejmp.2019.12.004

[6] T. Moriya, K. Fukumitsu, T. Sakai, S. Ohsuka, T. Okamoto, H. Takahashi, M. Watanabe, T. Yamashita, Development of PET detectors using monolithic scintillation crystals processed with sub-surface laser engraving technique, IEEE Transactions on Nuclear Science 57 (5 PART 1) (2010) 2455–2459. doi:10.1109/TNS.2010.2056387.

[7] M. Watanabe, A. Saito, T. Isobe, K. Ote, R. Yamada, T. Moriya, T. Omura, Performance evaluation of a high-resolution brain PET scanner using four-layer MPPC DOI detectors, Physics in Medicine and Biology 62 (17) (2017) 7148–7166. doi:10.1088/1361-6560/aa82e8.

[8] J. H. Jung, Y. Choi, Y. H. Chung, O. Devroede, M. Krieguer, P. Bruyndonckx, S. Tavernier, Optimization of LSO/LuYAP phoswich detector for small animal PET, Nuclear Instruments and Methods in Physics Research, Section A: Accelerators, Spectrometers, Detectors and Associated Equipment 571 (3) (2007) 669–675. doi:10.1016/j.nima.2006.10.293.

[9] S. Seifert, D. R. Schaart, Improving the time resolution of TOF-PET detectors by double-sided readout, IEEE Transactions on Nuclear Science 62 (1) (2015) 3–11. doi:10.1109/TNS.2014.2368932.

[10] K. Shibuya, F. Nishikido, T. Tsuda, T. Kobayashi, C. Lam, T. Yamaya, E. Yoshida, N. Inadama, H. Murayama, Timing resolution improvement using DOI information in a four-layer scintillation detector for TOF-PET, Nuclear Instruments and Methods in Physics Research, Section A: Accelerators, Spectrometers, Detectors and Associated Equipment 593 (3) (2008) 572–577. doi:10.1016/j.nima.2008.05.020.

[11] J. Van Sluis, J. De Jong, J. Schaar, W. Noordzij, P. Van Snick, R. Dierckx, R. Borra, A. Willemsen, R. Boellaard, Performance characteristics of the digital biograph vision PET/CT system, Journal of Nuclear Medicine 60 (7) (2019) 1031–1036. doi:10.2967/jnumed.118.215418.

[12] J. Mauricio, D. Gascón, D. Ciaglia, S. Gómez, G. Fernández, A. Sanuy, MATRIX: A 15 ps resistive interpolation TDC ASIC based on a novel regular structure, Journal of Instrumentation 11 (12) (2016). doi:10.1088/1748-0221/11/12/C12047.

[13] H. P. K.K., Physics and operation of the MPPC silicon photomultiplier.
URL https://hub.hamamatsu.com/jp/en/technical-note/sipm-physics-operation/index.html

[14] M. V. Nemallapudi, S. Gundacker, P. Lecoq, E. Auffray, Single photon time resolution of state of the art SiPMs, Journal of Instrumentation 11 (10) (2016). doi:10.1088/1748-0221/11/10/P10016.

[15] F. Anghinolfi, P. Jarron, A. N. Martemiyanov, E. Usenko, H. Wenninger, M. C. S. Williams, A. Zichichid, NINO: an ultra-fast and low-power front-end amplifier/discriminator ASIC designed for the multigap resistive plate chamber, Nuclear Instruments and Methods in Physics Research Section A: Accelerators, Spectrometers, Detectors and Associated Equipment 533 (2004).
URL https://doi.org/10.1016/j.nima.2004.07.024

[16] I. Sarasola, M. V. Nemallapudi, S. Gundacker, D. Sánchez, D. Gascón, P. Rato, J. Marín, E. Auffray, A comparative study of the time performance between NINO and FlexToT ASICs, Journal of Instrumentation 12 (4) (2017). doi:10.1088/1748-0221/12/04/P04016.

[17] A. Comerma, D. Gascón, L. Freixas, L. Garrido, R. Graciani, J. Marín, G. Martínez, J. M. Pérez, P. Rato Mendes, J. Castilla, J. M. Cela, J. M. Fernández-Varea, I. Sarasola, FlexToT - Current mode ASIC for readout of common cathode SiPM arrays, in: 2013 IEEE Nuclear Science Symposium and Medical Imaging Conference (2013 NSS/MIC), 2013, pp. 1–2.

[18] J. M. Cela, L. Freixas, J. I. Lagares, J. Marin, G. Martinez, J. Navarrete, J. C. Oller, J. M. Perez, P. Rato-Mendes, I. Sarasola, O. Vela, J. M. Fernandez-Varea, D. Gascon, S. Gomez, R. Graciani, J. Mauricio, D. Sanchez, A. Sanuy, O. de la Torre, D. Badia, A Compact Detector Module Design Based on FlexToT ASICs for Time-of-Flight PET-MR, IEEE Transactions on Radiation and Plasma Medical Sciences 2 (6) (2018) 549–553. doi:10.1109/trpms.2018.2870927.

[19] Hamamatsu Photonics K.K., Physics and operation of the MPPC silicon photomultiplier.
URL https://hub.hamamatsu.com/jp/en/technical-note/sipm-physics-operation/index.html

[20] D. Renker, E. Lorenz, Advances in solid state photon detectors, Journal of Instrumentation 4 (04) (2009) P04004—-P04004. doi:10.1088/1748-0221/4/04/p04004.
URL https://doi.org/10.1088{%}2F1748-0221{%}2F4{%}2F04{%}2Fp04004

[21] G. Collazuol, The SiPM Physics and Technology - a Review, PhotoDet 2012 (June) (2012) 74.
URL http://indico.cern.ch/event/164917/contribution/72/material/slides/0.pdf

[22] S. Gundacker, A. Heering, The silicon photomultiplier: fundamentals and applications of a modern solid-state photon detector, Physics in Medicine & Biology 65 (17) (2020) 17TR01. doi:10.1088/1361-6560/ab7b2d.
URL https://doi.org/10.1088{%}2F1361-6560{%}2Fab7b2d

[23] S. Gundacker, E. Auffray, B. Frisch, P. Jarron, A. Knapitsch, T. Meyer, M. Pizzichemi, P. Lecoq, Time of flight positron emission tomography towards 100ps resolution with L(Y){SO}: an experimental and theoretical analysis, Journal of Instrumentation 8 (07) (2013) P07014—-P07014. doi:10.1088/1748-0221/8/07/p07014.
URL https://doi.org/10.1088{%}2F1748-0221{%}2F8{%}2F07{%}2Fp07014

[24] F. Acerbi, S. Gundacker, Understanding and simulating SiPMs, Nuclear Instruments and Methods in Physics Research, Section A: Accelerators, Spectrometers, Detectors and Associated Equipment 926 (September 2018) (2019) 16–35. doi:10.1016/j.nima.2018.11.118.
URL https://doi.org/10.1016/j.nima.2018.11.118

[25] A. Gola, F. Acerbi, M. Capasso, M. Marcante, A. Mazzi, G. Paternoster, C. Piemonte, V. Regazzoni, N. Zorzi, NUV-sensitive silicon photomultiplier technologies developed at fondazione Bruno Kessler, Sensors (Switzerland) 19 (2) (2019). doi:10.3390/s19020308.

[26] Hamamatsu Photonics K.K., MPPCs for precision measurement: S13360 series.
URL https://www.hamamatsu.com/resources/pdf/ssd/s13360{_}series{_}kapd1052e.pdf

[27] R. D. Badawi, H. Shi, P. Hu, S. Chen, T. Xu, P. M. Price, Y. Ding, B. A. Spencer, L. Nardo, W. Liu, J. Bao, T. Jones, H. Li, S. R. Cherry, First human imaging studies with the explorer total-body PET scanner, Journal of Nuclear Medicine 60 (3) (2019) 299–303. doi:10.2967/jnumed.119.226498.

[28] S. Gundacker, A. Knapitsch, E. Auffray, P. Jarron, T. Meyer, P. Lecoq, Time resolution deterioration with increasing crystal length in a TOF-PET system, Nuclear Instruments and Methods in Physics Research, Section A: Accelerators, Spectrometers, Detectors and Associated Equipment 737 (2014) (2014) 92–100. doi:10.1016/j.nima.2013.11.025.
URL http://dx.doi.org/10.1016/j.nima.2013.11.025

[29] S. Gundacker, R. Martinez Turtos, N. Kratochwil, R. H. Pots, M. Paganoni, P. Lecoq, E. Auffray, Experimental time resolution limits of modern SiPMs and TOF-PET detectors exploring different scintillators and Cherenkov emission, Physics in Medicine and Biology 65 (2) (2020). doi:10.1088/1361-6560/ab63b4.

[30] G. Ariño-Estrada, G. S. Mitchell, H. Kim, J. Du, S. I. Kwon, L. J. Cirignano, K. S. Shah, S. R. Cherry, First Cerenkov charge-induction (CCI) TlBr detector for TOF-PET and proton range verification, Physics in Medicine and Biology 64 (17) (2019). doi:10.1088/1361-6560/ab35c4.

[31] S. Gundacker, R. M. Turtos, E. Auffray, M. Paganoni, P. Lecoq, High-frequency {SiPM} readout advances measured coincidence time resolution limits in {TOF}-{PET}, Physics in Medicine & Biology 64 (5) (2019) 55012. doi:10.1088/1361-6560/aafd52.
URL https://doi.org/10.1088{%}2F1361-6560{%}2Faafd52

[32] S. Ahmad, J. Fleury, J. Cizel, C. de la Taille, N. Seguin-Moreau, S. Gundacker, E. Auffray-Hillemanns, Petiroc2A: Characterization and Experimental Results, in: 2018 IEEE Nuclear Science Symposium and Medical Imaging Conference Proceedings (NSS/MIC), 2018, pp. 1–4.

[33] R. Bugalho, A. Di Francesco, L. Ferramacho, C. Leong, T. Niknejad, L. Oliveira, M. Rolo, J. C. Silva, R. Silva, M. Silveira, S. Tavernier, J. Varela, Experimental characterization of the TOFPET2 ASIC, Journal of Instrumentation 14 (3) (2019). doi:10.1088/1748-0221/14/03/P03029.

4

Monolithic detectors

Monolithic scintillator crystals for Time-of-Flight Positron Emission Tomography (ToF-PET) are increasing in popularity this last years due to their performance potential and price in front of the commonly used segmented crystals. On one hand, monolithic blocks allows to determine 3D information of the gamma-ray interaction inside the crystal, which enables the possibility to correct the parallax error (radial astigmatism) at off-center positions within a PET scanner, resulting in an improvement of the spatial resolution of the device. On the other hand, due to the simplicity during the crystal manufacturing process as well as for the detector design, the price is reduced compared to a regular pixelated detector.

In this chapter, results with different monolithic crystals and SiPM sensors using HRFlex-ToT ASIC will be presented. A Lutetium Fine Silicate (LFS) of 25 mm × 25 mm × 20 mm, a small LSO:Ce Ca 0.2% of 8 mm × 8 mm × 5 mm and a Lutetium-Yttrium Oxyorthosilicate (LYSO) of 25 mm × 25 mm × 10 mm has been experimentally tested. The SiPM active area employed goes from 2 mm × 2 mm to 6 mm × 6 mm, all detectors arranged in a 4 × 4 matrix configuration with an overall detector area matching the crystal XY dimensions. After subtracting the TDC contribution (82 ps FWHM), a coincidence time resolution (CTR) of 244 ps FWHM for the small LFS crystal and 333 ps FWHM for the largest LFS one is reported. Additionally, a novel time calibration correction method for CTR improvement that involves a pico-second pulsed laser will be detailed.

Contents

4.1 Introduction

The medical imaging devices for Positron Emission Tomography (PET) application have suffered a tremendous improvement during the last decade. PET is described as a molecular diagnosis technique that allows to track different biological processes, whose purpose is to show the cellular or molecular activity of a disease [1, 2]. The process implies the administration of a radiotracer, a biomolecule labeled to a radioactive atom emitting positrons (β^+). During the PET imaging, the positron emitted by the radiotracer undergoes annihilation with an electron and this process produces two 511 keV annihilation photons that travel approximately 180° from each other. Then, a near-simultaneous detection of these two gamma-rays takes place in a time window of a few nanoseconds. Nowadays, time information of the event is a must, and an accurate time measurement during the 511 keV photon detection will lead to a drastic improvement on the final image quality of the organ under study [3, 4, 5, 6].

Time resolution of a ToF-PET system is affected by each basic component involved in the gamma photon collection [7]. The basic PET module is composed by: first, a scintillator crystal that converts the gamma ray into visible light. Second, a photosensor which collects the optical photons and outputs an electrical signal. Lastly, a dedicated front-end (FE) electronics with amplitude or Analog/Time to Digital Converters (ADCs or TDCs [8]) that processes the sensor response, captures the arrival time of the photons and generates readable data that will be used to generate the final image of the activity distribution. In each part of this detection chain, the time is being degraded depending on the performance of each component. State-of-the-art photodetectors, along with the best scintillator crystals and fast readout electronics are needed in order to minimize the time resolution.

SiPMs are outperforming PMTs in all ToF-PET medical devices as the main photodetector [9], due to the astonishing improvements during the last 10 years. The silicon solid state detector is insensitive to magnetic fields, operates at low voltage compared to a PMT (20-60 V SiPM versus 1000 V for a PMT), and it has excellent timing performance [10]. Moreover, the scalability and cost effectiveness make them suitable for covering large detection areas.

There are several types of scintillator crystals with different compositions and optical properties to better adapt to the application requirements [11, 12]. Nowadays, LYSO and LSO scintillator crystals are extensively used in PET systems due to their high light yield (30 photons/keV), relatively fast emission decay time (tens of nanoseconds) and production cost [13]. In a PET module, the SiPM is coupled to the scintillator crystals using an optical coupler in order to increase the light extraction efficiency.

There are two traditional configurations of the detector based on how the crystal fits the photosensitive area. The first option is to employ pixelated or segmented crystals. Figure 4.1a shows the segmented approach, where all the light generated by the γ-ray interacting with the crystal is collected by a single SiPM channel, if one-to-one coupling configuration is used where one crystal segment is attached to only one SiPM channel, and thus improving the timing information. As a counterpart, the X-Y spatial resolution of such configuration is limited to the planar cross-section (pixel size), and no Z coordinate, i.e, Depth of Interaction

(DOI) information is recovered from the gamma event. Consequently, the main degradation on the time jitter comes from the light transfer time spread (LTTS) variations, which depends on the gamma absorption point along the crystal length [14]. Although this is the one-to-one coupling basic segmented configuration, light sharing technique, where crystal segments are not one-to-one coupled to the SiPM is the most widely used [15]. In this approach, the individual crystal section is smaller compared to the single channel sensor and the light shares among several channels, most of the times by using an optical waveguide interpose between the crystal and the sensor [16].

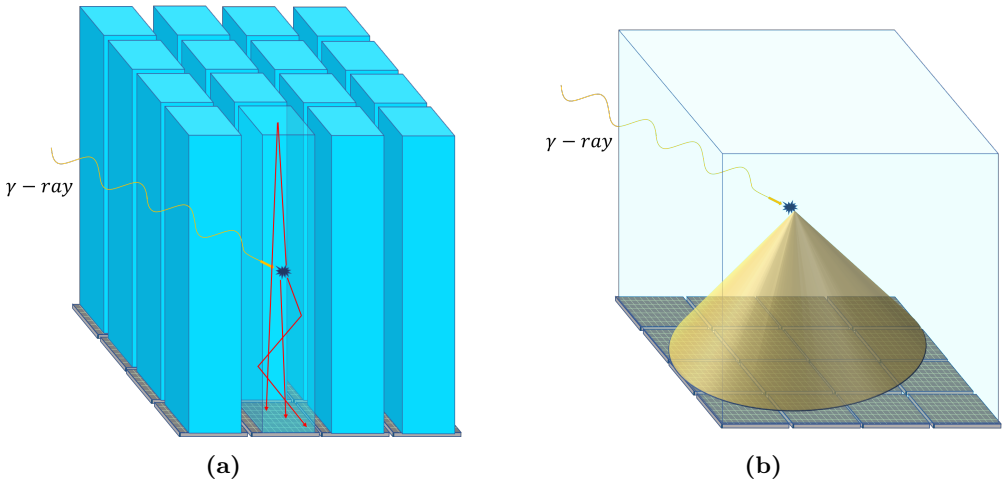

Figure 4.1.: Light distribution among the 16 SiPM channels depending on the crystal used. (a) Segmented crystal with crossection close to the SiPM channel area. (b) Monolithic block covering all 16 channels.

The second approach consists on using monolithic block crystals. Figure 4.1b illustrates this configuration, where the light generated in the γ-ray interaction is spread over many SiPMs [17]. In monolithic blocks, photons experience less bouncing to the walls as they have lower aspect ratio (thickness/cross-section). Thus, higher number photons could travel straight to the sensor area compared to pixelated crystals where most of the light reflects on the walls before reaching the sensor. The probability of capturing the first emitted optical photon following a straight direction is higher in monolithic blocks due to its larger cross-section. This could lead to a theoretically better Coincidence Time Resolution (CTR) compared to the segmented approach. However, the wide spread of the light across the detection area reduces the amount of collected photons at each sensor and thus each photodetector receives only a fraction of the total number of photons generated. This effect is translated into a degradation of the Signal to Noise Ratio (SNR), compared to the one-to-one coupling and thus degrading the timing response. Moreover, it can lead to false triggering by dark counts of the SiPM (if the minimum signal on a channel is at the same level as the dark counts) and time-walk errors.

The monolithic configuration enables the possibility of 3D reconstruction of the gamma event inside the crystal, and a sub-pixel X-Y spatial resolution can be easily achievable by using a basic center of gravity algorithm [18], or more sophisticated positioning schemes such as neural networks or nearest neighbors [19, 20]. Note that in this case, a special black painting surface treatment of the crystal is needed in order to suppress all the wall bouncing photons [21]. This advantage, makes monolithic crystals an attractive option for those

applications where the scanner has a limited coverage angle and high 3D spatial resolution is needed in the reconstruction process [22].

In this work, we combine monolithic crystals with various surface treatments, along with state-of-the-art SiPMs and a novel FE electronics. The HRFlexToT (High Resolution Flexible Time-over-Threshold) Application Specific Integrated Circuit (ASIC) [25] designed to work with both pixelated and monolithic crystals will be used to readout different SiPM matrices. Timing information involved in the gamma detection as well as the light spread among channels and the spatial resolution will be presented. Furthermore, a new approach to calibrate the time-walk and time-skew using a picosecond laser source is detailed in the following section.

4.2 Materials and Methods

This section describes the electronics employed for the readout of the SiPMs with monolithic crystals. Moreover, a detailed description of the experimental setups employed throughout the paper is here provided.

4.2.1 HRFlexToT ASIC readout

The HRFlexToT ASIC is a new version of the FlexToT chip [26] designed with an extended dynamic range suitable for the readout of pixelated and monolithic scintillator crystals. It features 16 channels, a low input impedance stage suitable for the readout of SiPMs with a common cathode connection and anode voltage control at the input for SiPM gain equalization due to voltage breakdown variations. Moreover, power consumption is reduced from 10 mW/ch to 3.5 mW/ch compared to its predecessor. Maximum channel hit rate is around 1M counts/s suitable for PET applications [25].

The HRFlextoT provides an individual time response and energy measurement per channel and thus renders the ASIC suitable for monolithic crystals where signal is spread among several channels. Time measurement is generated through a leading-edge comparator that provides a non-Linear Time over Threshold (ToT) response. More specifically, it encodes the arrival time of the detected events in the rising edge of a pulse with a low jitter (this time uncertainty depends on the detector capacitance), as depicted in figure 4.2. The energy measurement (proportional to the collected charge) has been totally redesigned compared to its predecessor to overcome the non-linearity problems at low energies [25]. This new energy processing generates a linear ToT output encoding the collected charge in a binary pulse width (figure 4.2) with an extended dynamic range and allowing a resolution of 10 bits. The energy measurement is achieved with a linearity error around 3%.

The signal processing is controlled with a trigger scheme that allows to generate data only when a desired event is captured, i.e. triggered event. Different trigger levels can be employed within the ASIC. Firstly, the timing signal can be used to start the acquisition in

those applications where the trigger must be set close to the first photoelectron. Secondly, a configurable low-level trigger is available to set the detection level above Dark Count events. Thirdly, a cluster high-level trigger is generated when the sum of the collected charge among several channels overpasses a configurable threshold. This trigger is designed for monolithic crystals where a single channel might not have enough signal to detect the event. Lastly, the possibility to introduce an external trigger is also available for pedestal calibration (minimum pulse width detected in the absence of signal).

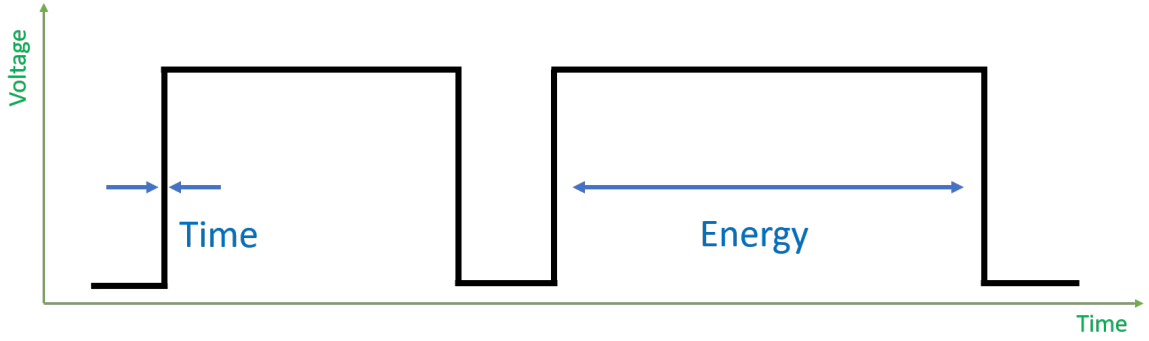

Figure 4.2.: Time and energy signal in the same output channel from the ASIC. Timestamp is read in the rising edge of the first pulse and energy is codified as the width of the second pulse.

An event captured by the ASIC includes two consecutive pulses codifying the time and energy of the corresponding detection. Arrival time and collected energy per channel are encoded in a binary pulse referred as *time + energy*, where the time pulse comes first followed by the energy pulse, as can be observed in figure 4.2. The time + energy information per channel must be digitized using a TDC before sending it to a computer.

All the experiments are carried out employing two identical boards containing mainly an HRFlexToT ASIC, a Field-Programmable Gate Array (FPGA) [27] for the data acquisition and chip control, and other components for power supply and USB connectivity. A TDC is built inside the FPGA introducing a time jitter of 40 ps (sigma) on the measurements. Moreover, the FPGA performs a coincidence verification process by comparing the delay time of the trigger signals from both boards in order to discard all the non-coincident events. A coincidence time window of 30 ns is used for this purpose. The filtering strategy is mandatory to reduce the amount of unnecessary data to be processed later, especially for monolithic crystals even with a few number of detectors. After this process, the FPGA sends the corresponding data block through the USB to a computer, where the software converts this raw data into a readable piece of information as can be seen in table A.1 from appendix A. Lastly, a cleaning software to identify the time and energy from the same event is needed, since some dark count events or corrupted data can be captured in the process.

4.2.2 Experimental setups for coincidence measurements

An overview of the setup for CTR measurements is shown in the schematic representation in figure 4.3. Two detectors and the ^{22}Na point source (coin shape with active core volume ⌀0.25 mm, 200 kBq) are mounted in an optical table using a common rail for a proper alignment, such that the relative position between both detectors can be controlled. All measurements are taken in an isolated black box at a constant temperature of 18 °C if no other condition is specified. This setup with different scintillator crystals and SiPMs is employed for all the measurements in the experimental results, detailed in section 4.4.

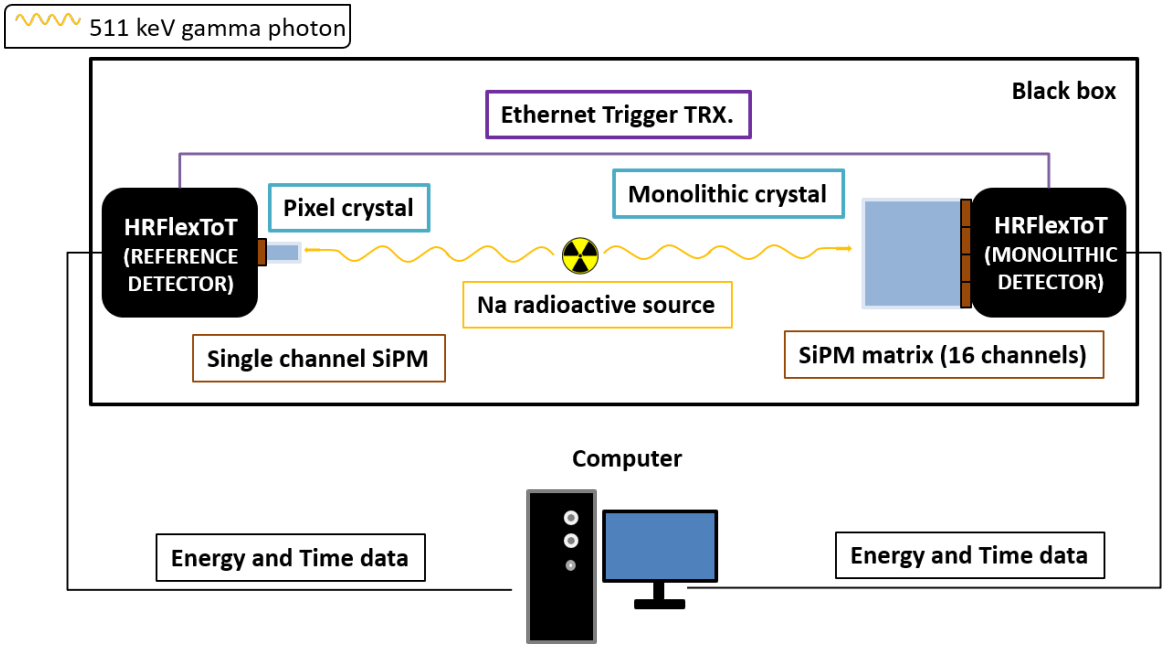

Figure 4.3.: Coincidence Time Resolution setup schematic representation.

The experimental test bench works as follows. An event can be captured when the pair of 511 keV back-to-back gamma photons arrive to each one of the detectors. The detection might occur following a probability function describing the interaction with the crystal by either photoelectric or Compton effect [28]. If any of these two interactions occur, the gamma photon deposits the energy in an specific region of the crystal, which is converted into optical photons (typically in the visible range between 380 to 600 nm), and a fraction of those will reach the photosensor, in this case a SiPM. Then, the electrical signal, or photoelectrons, generated in each SiPM is read out by the HRFlexToT ASIC, where time pick up and energy measurement takes place. This information is sent to the FPGA for digitization and coincidence filtering and then sent to the computer.

An additional element is added to the setup to collimate the gamma beam in order to generate a 2D flood map and compute the spatial resolution in the monolithic crystal, as can be seen in figure 4.4. A thick lead cylinder of 5 cm length and 7 cm diameter with a co-centered hole of ⌀3 mm was used for this purpose. Furthermore, the reference detector was placed at a distance of 100 mm to the ^{22}Na, resulting in a spot size of $\sim$ 1 mm on the

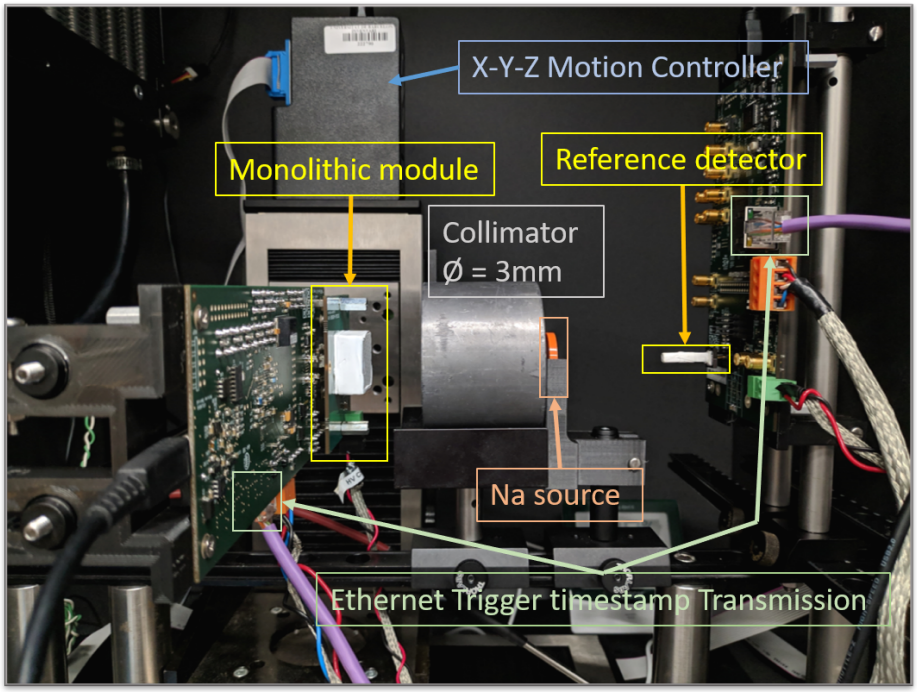

Figure 4.4.: Coincidence setup with a collimated gamma beam involving step motion controller and thick lead collimator.

monolithic entrance surface when both annihilation photons were detected. A three axis Newport EPS300 step motion controller was used to control the X-Y and Z impact position of the gamma beam. Note that only the 511 keV events were taken into account for the position analysis, using an energy window of $\pm 3\ \sigma$ around the photopeak. This method enables to avoid the majority of the Compton events and to suppress noisy triggers outside the primary interaction point.

The following list describes the three different configurations used:

1. A small scintillator crystal made of LSO:Ce Ca 0.2% of 8 mm × 8 mm × 5 mm size fully Teflon wrapped. For this configuration, a matrix of 4 × 4 SiPM channels S13361-2050NE-04 Hamamatsu model was used, each channel consists on a 2 mm × 2 mm with 50 μm pixel pitch and Through Silicon Via (TSV) technology.

2. A larger LFS scintillator crystal of 25 mm × 25 mm × 20 mm. The crystal was firstly wrapped in Teflon and secondly painted all in black in order to compare both performances. The Hamamatsu SiPM model S13361-6050-04NE with a SiPM channel size of 6 mm × 6 mm was used in this case.

3. A large LYSO scintillator crystal of 25 mm × 25 mm × 10 mm with plack painted lateral walls and a retro-reflective (RR) layer on top. The SiPM sensor is again the S13361-6050NE-04 with 6 mm × 6 mm channel size.

The reference detector is composed by a single channel SiPM S13360-3050CS from Hamamatsu coupled to a small crystal LSO:Ce 0.2% Ca codoped of 2 mm × 2 mm × 5 mm. A total jitter of 120 ps is measured for the reference detectors, including the TDC contribution

(82 ps FWHM) and the SiPM + crystal + FE (90 ps FWHM). This is obtained after doing a CTR measurement with 2 identical reference detectors.

4.2.3 Experimental setup using a laser source

The use of a laser permits to have a controlled light source to study the SiPM behavior in a wide range of light intensities, from single to thousands of photons. Figure 4.5 illustrates the setup involving a pulsed laser for time-walk studies as it will be shown later. First, the laser control unit sends an electrical trigger signal to the laser (PiLas Picosecond Diode Laser at 405 nm, 30 ps pulse width, and 15 ps trigger jitter) and to the detector board at a repetition rate of 500 kHz and a tuned intensity level of 50% as per the optimal operating conditions specified in the user manual. The TDC in the FPGA captures the timestamp of the trigger signal that the laser employs to generate the corresponding photon package. Then, those photons go through a Single Mode Fiber (Thorlabs 305A-FC SM) to a beam collimator coupled to a Liquid Crystal Optical Beam Attenuator from Thorlabs, which can change the attenuation factor depending on the voltage applied (from 0 V to 5 V, minimum to maximum attenuation correspondingly). The beam pulse arrives to a diffuser spreading the light homogeneously over the matrix array.

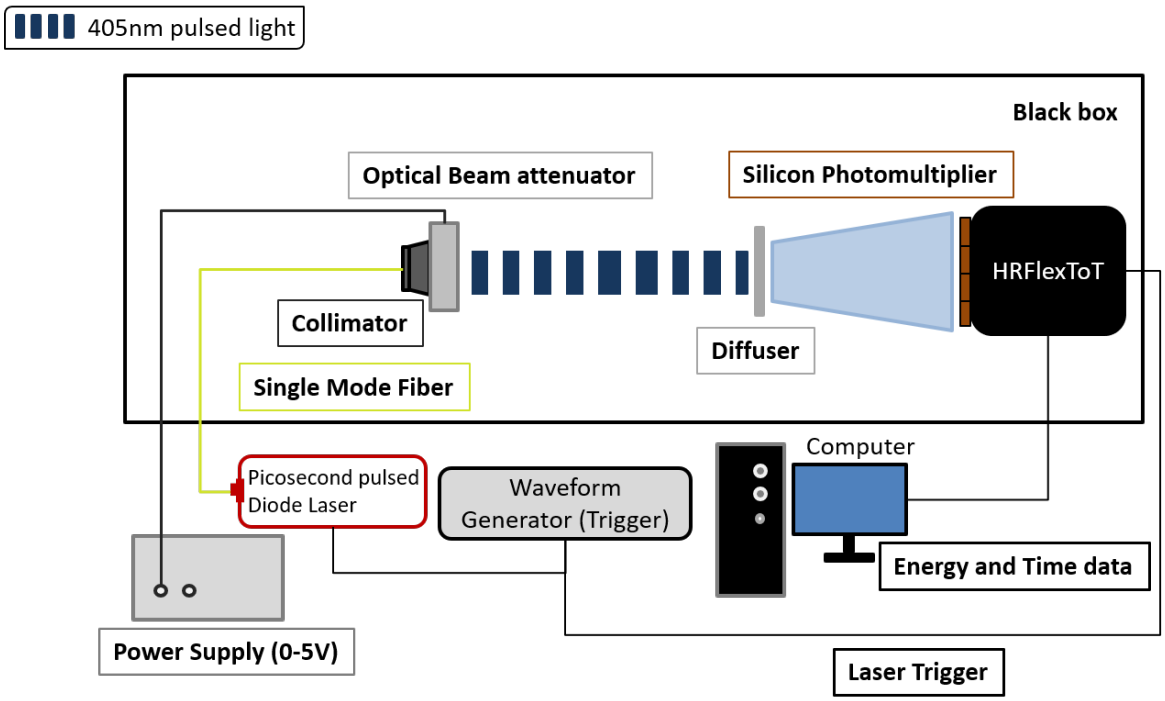

Figure 4.5.: Schematic view of the experimental setup using the laser source.

The SiPM generates a single photoelectron when a photon from the light beam hits the sensor. Note that the SiPM has a certain photon detection efficiency (PDE) and thus only a fraction of the emitted photons is captured. The photoelectron is read out by the HRFlexToT ASIC and digitized by the TDC. Lastly, the time + energy signals from each channel and the trigger timestamp are sent to the computer for a further offline analysis.

4.3 Time-walk and time-skew correction

A pre-calibration of the detector module is needed in order to avoid the intrinsic time differences originated at the sensor site or the PCB path lengths of the different channels. This section presents a new method to correct the time-walk and time-skew errors by employing a controlled laser source instead of the traditional method which employs the gamma energy deposited on a scintillator crystal. A detailed description on both methods is here described.

4.3.1 Compensation of time-walk and time-skew using a pulsed-laser

A leading-edge time pick-off circuit with a fixed ToT approach for the readout of analog SiPMs presents a major inconvenient known as time-walk [29, 30]. The light distribution at the sensor face can adopt different shapes depending on the 3D gamma interaction point inside the crystal. In other words, the SiPM channels could receive few photons or hundreds of those depending on the DOI [31]. Figure 4.6 illustrates this problem for a different number of photo-electron signals from the SiPM [32], showing that for a fixed threshold, the detection time varies depending on the amount of photons detected (energy from the gamma event). Hence, a calibration and compensation of this phenomena is needed to improve the time resolution of the system.

A new calibration method is presented in this work, which consists on using a pulsed laser working at different light intensities to generate a pre-calibrated Look-Up-Table (LUT). Note that the range of the light intensity applied has to be similar to the number of photons generated inside a scintillator crystal coupled to a SiPM in order to emulate the response of a gamma-ray detection.

The following acquisition procedure has being developed using the experimental setup detailed in figure 4.5. First, the repetition rate of the laser driver is set to 50 kHz. Then, the power supply that varies the attenuation factor of the liquid crystal is controlled by a python script through GPIB connection. The external control allows to perform a voltage sweep between the minimum and maximum attenuation. One hundred points across the full attenuation range are configured and the time+energy output is captured using the HRFlexToT ASIC during 1 second of acquisition time per point.

The energy signal width (proportional to the number of photons detected) versus the delay time is shown in figure 4.7. This delay time is calculated as the difference between the arrival time of the photons and the trigger signal generated from the driver of the laser. The delay time with respect to the energy will be later used for the time-walk compensation.

Figure 4.7 clearly shows the time-walk effect due to the fixed threshold scheme and thus showing a non-linear time difference with respect to the detected energy. Time-walk follows a logarithmic-like growth behavior with respect to the number of photons detected, i.e., it

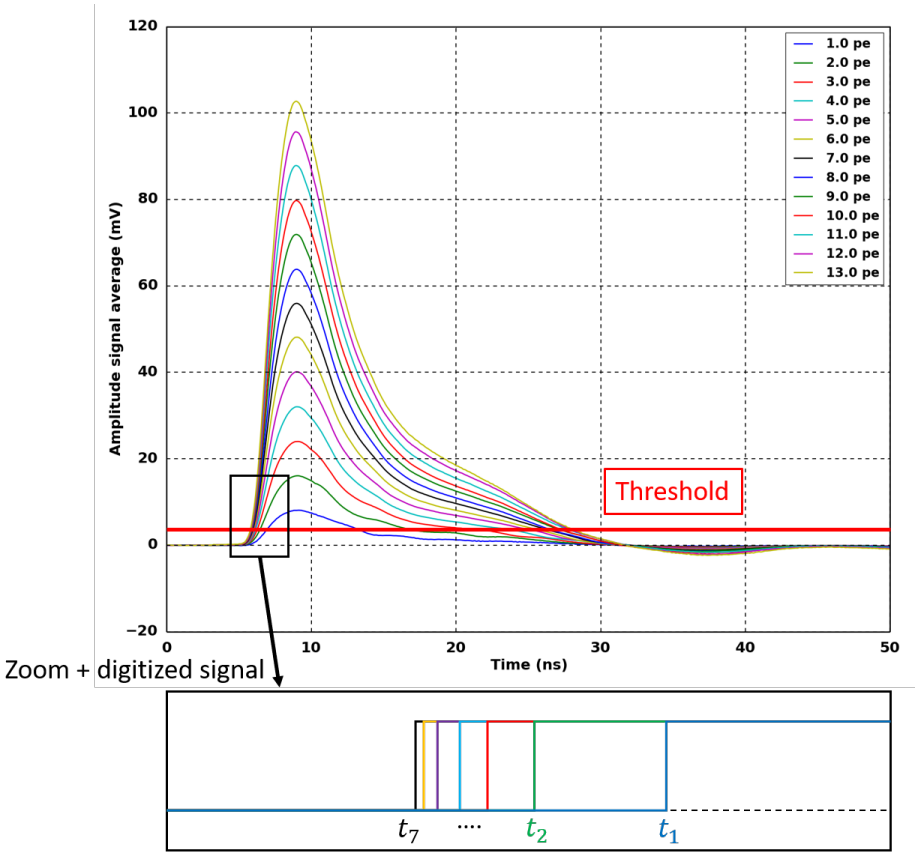

Figure 4.6.: Pure time-walk representation using ToT technique. Top: SiPM analog signal for different number of photons arriving. Figure acquired using MUSIC ASIC analog output [33]. Bottom: zoom at the rising edge of the ToT pulse after signal threshold applied for 1-7 photo-electron waveforms.

increases very fast for a few photons (low energies) and then follows a slower growth as the number of photons firing at the same time increases (larger energy). In this example, energies corresponding to less than 50 ns of pulse width suffer a higher time-walk effect with respect to larger energies. This effect is related to the slew rate of the analog SiPM response (signal seen at the input of the leading-edge comparator). As can be seen in Figure 4.6, the slew rate follows the same logarithmic-like growth as the time-walk.

Time-skew is a phenomenon in digital/binary signals in which the arrival time between channels is different due to systematic divergences, i.e., non-equalized signal paths along the ASIC, the FPGA and the Printed Circuit Board (PCB) traces containing both, and the SiPM sensor non uniformity. For more information about the PCB design for the HRFlexToT demonstrator please refer to appendix B. Time-skew compensation is performed as follows. First, the laser light intensity is set to a level high enough to avoid the intrinsic time-walk from the SiPM, which is more dominant at the low energy region. Following the example depicted in figure 4.6, energies corresponding to signal durations in a small region around 150 ns are here selected. Second, the HRFlexToT ASIC is employed to acquire the time + energy response at this light intensity. Third, an histogram of the arrival time in each of the channels (in this case, 16) of those events with an energy of 150 $\pm$ 2 ns is generated, as illustrated in figure 4.8. Without loss of generality, similar gain between all channels is presumed, limiting time-walk effects coming from gain variations. Otherwise, a SiPM gain

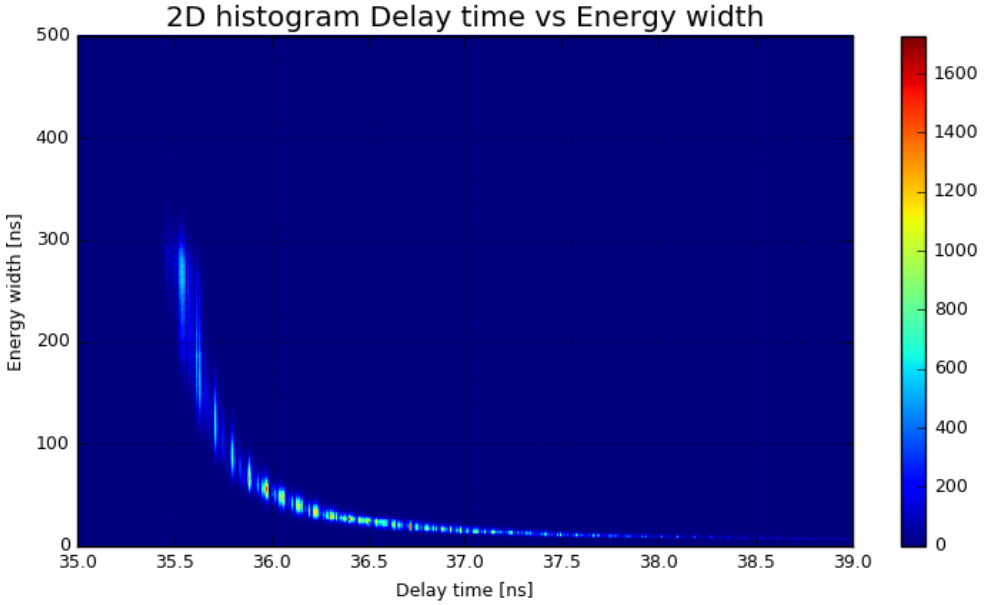

Figure 4.7.: Energy width (number of photons collected from the laser source) versus time of arrival for a given channel. Color bar shows the number of events captured per energy.

equalization must be performed in advance by modifying the anode voltage at the input of the circuit (option available in the HRFlexToT ASIC [26]). Henceforth, the time-skew between channels is the predominant factor.

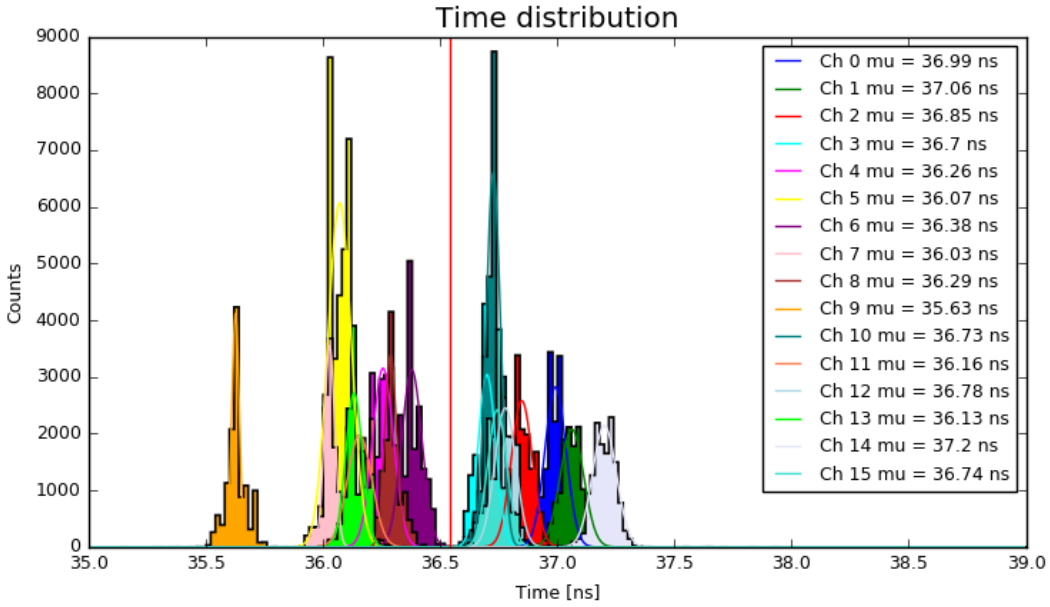

Figure 4.8.: Arrival time distribution per channel for energies between 148 - 152 ns range to calculate the time-skew and the time-reference for a later timestamp correction.

Fourthly, a common time-reference (T_{ref}) is selected by averaging all 16 Gaussian centroids from the different time distributions. This value is represented as a vertical red line in figure 4.8. Then, all timestamps ($T_{old,i}$) are corrected by adding the time difference between the time-reference and the centroid (mean value, μ_i)) for each one of the i-th channels. Hence, the new timestamp ($T_{new,i}$) is using the following expression:

$$T_{new,i} = T_{old,i} + (T_{ref} - \mu_i) \tag{4.1}$$

The resulting timestamp distribution and its corresponding time jitter at the selected energy (150 ± 2 ns) after correction is depicted in figure 4.9. A low time jitter of 44 ps (sigma), which comes from the convolution of different sources along the acquisition process (laser, SiPM and electronics), is obtained after the correction and thus proving the effectiveness of this method.

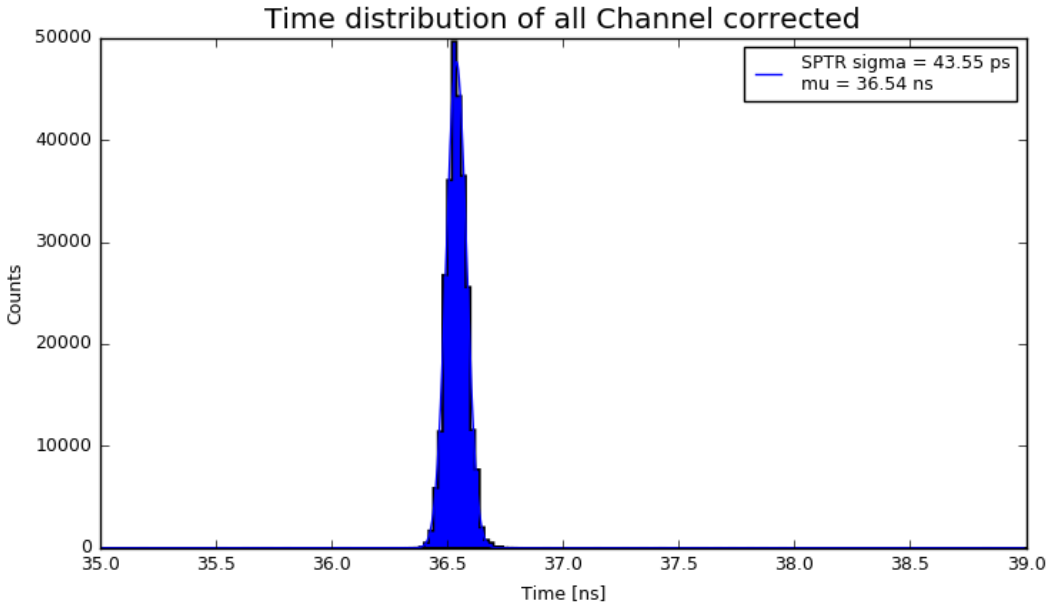

Figure 4.9.: Time jitter of all 16 channels after time-skew correction for energies between 148 - 152 ns range.

Finally, combining the information from the time-walk and time-skew, all timestamps can be corrected. The 2D histogram of the delay time with respect to the energy (figure 4.7) is projected in 1 ns energy slices. Then, the delay time distribution corresponding to this interval is fitted using a Gaussian approximation. A LUT for each of the channels is generated applying equation 4.1 for each energy step. As a result, an homogeneous time distribution among all channels is achieved (figure 4.10). This precalibration of the time misalignment from the detection module is expected to improve the CTR results as it will be shown in the section 4.4.

In summary, we developed a new pre-calibration method that will allow to correct both time-walk and time-skew on CTR measurements during the offline data analysis. An improvement with respect to traditional time error calibration methods is expected, where the light source comes from the gamma energy deposited on a scintillator crystal instead of a controlled laser source. A comparison between both methods will be provided next.

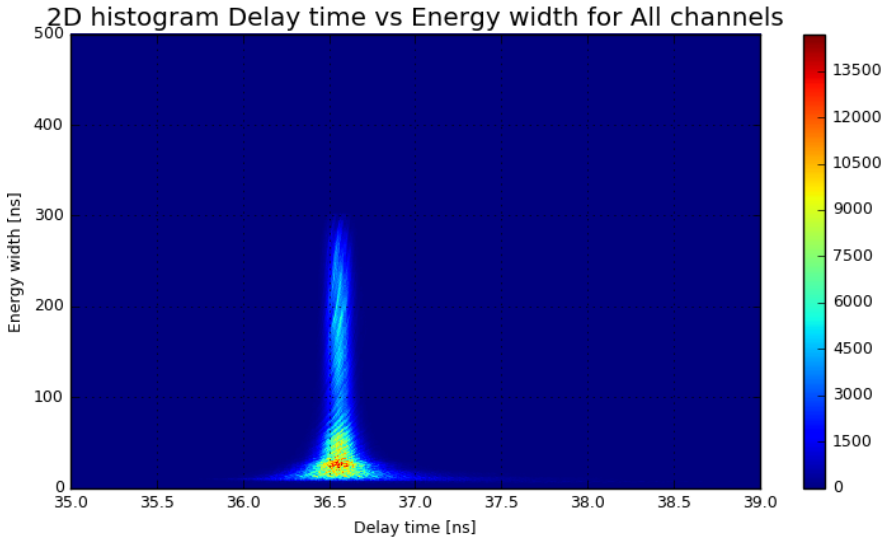

Figure 4.10.: 2D plot distribution of all 16 channels after time-walk and skew compensation.

4.3.2 Compensation of time-walk and time-skew using a scintillator crystal

A different approach regarding time error compensation will be explained in this section. In this case, instead of using a coherent laser source with a controlled amount of photons, the scintillator crystal light generated during the gamma interaction will be used [34]. For this purpose, the experimental test bench for CTR measurements is employed. In summary, this setup consists on a single reference detector (1 SiPM) confronted with the monolithic crystal coupled to a 16 channel SiPM array. On one side, the delay time is now the difference between the arrival time of the photons in each channel from the monolithic detector, and the timestamp recorded at the reference detector. On the other side, the deposited energy of the gamma interaction is proportional to the number of photons impinging in the SiPM channel. Figure 4.11a illustrates the delay time versus the deposited energy. Note that a similar behavior as shown in figure 4.7 can be appreciated, where for low energy signals the time-walk effect increases and thus causing a larger CTR degradation.

Time-skew is corrected using the same procedure explained in the previous section, but employing the energy released in the gamma interaction. A LUT with the corrected timestamp of each event is generated for each one of the channels, combining both measurements, time-walk and time-skew, and applying equation 4.1. After corrections, the delay time distribution of all channels is centered close to 0 as can be seen in figure 4.11b. This method allows to correct the time skew misalignment from the SiPM and the PCB produced from the nonlinear ToT in a faster way compared to crystal methods, where the whole operation takes several minutes or hours in comparison to few seconds using a pulsed laser. On the contrary, this method suffers from DOI uncertainty since the gamma ray interaction might happen in different points along the crystal [35]. Therefore, this correction mixes the time-walk and time-skew with the DOI impact. DOI resolution on a monolithic crystal will be addressed in section 4.4.3.

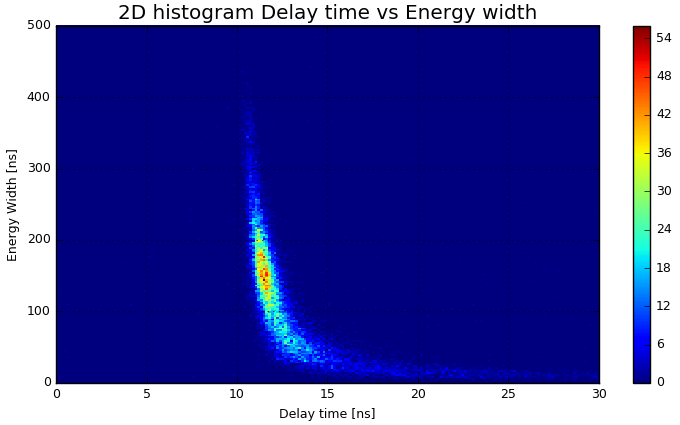

(a) Channel 9 time-walk plus skew effect.

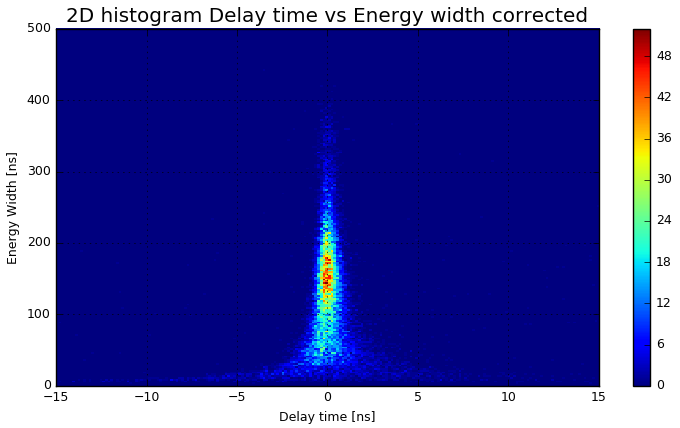

(b) Time distribution after correction.

Figure 4.11.: Energy width vs time of arrival distribution before (a) and after (b) correction.

4.4 Experimental results

4.4.1 Coincidence Time Resolution measurements

This section contains all CTR measurements regarding monolithic crystals using the HRFlexToT readout system as described in 4.2.2. Starting with a small LSO:Ce Ca 0.2% monolithic crystal of 8 × 8 × 5 mm^3 and followed by two different medium-size monolithic crystal, a LFS of 25 × 25 × 20 mm^3 and a LYSO of 25 × 25 × 10 mm^3 crystal size. Moreover, different surface covers will be employed, changing between full Teflon wrapped, black painting or combining black walls with retroreflector (RR) on top.

The first evaluation was carried out using the configuration number 1 as detailed in section 4.2.2, 8 × 8 × 5 mm^3 LSO:Ce Ca 0.2% crystal along with the 16 channel SiPM matrix.

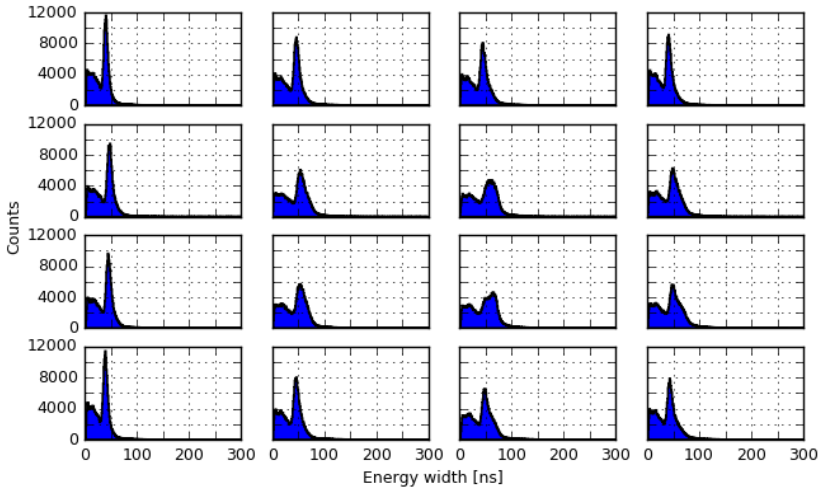

(a) Energy histogram per channel.

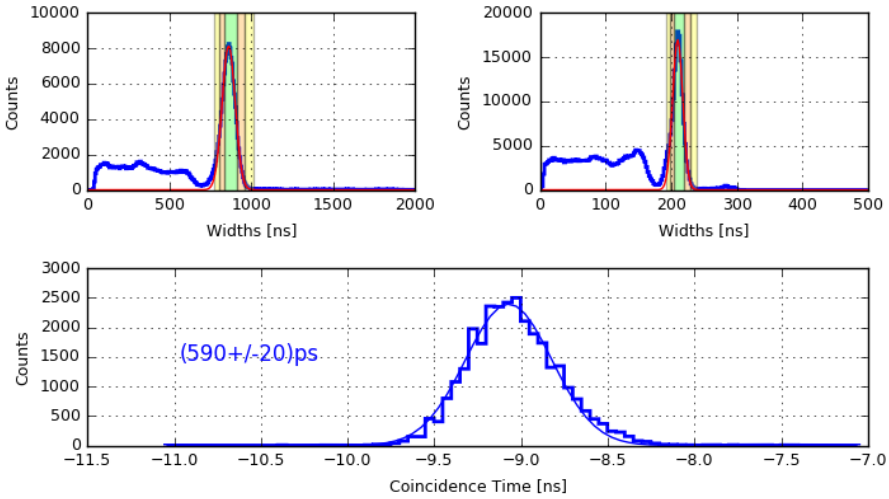

(b) Energy reconstruction and raw CTR result. Top-left: monolithic detector; Top-right: reference pixelated detector; Bottom: CTR measurement.

Figure 4.12.: SiPM: S13361-2050NE. Crystal: LSO:Ce Ca 0.2% of 8 mm × 8 mm × 5 mm teflon wrapped.

The time threshold of the leading-edge comparator is set above noise level, which corresponds to a value equivalent to the second photoelectron. The ^{22}Na energy spectrum distribution per channel of the monolithic crystal can be seen in figure 4.12a. Observe that the photopeak shape is less defined in the central channels, where the light spread has a bigger impact compared to the lateral sensors. The energy per channel is summed in the FPGA to obtain the reconstructed spectrum, as can be seen in figure 4.12b. Note that the overall energy spectrum considering all channels presents the photopeak well defined (energy resolution ∼12% in FWHM). Furthermore, a raw CTR of 590 ps in FWHM (without corrections) selecting only the events close to the photopeak at both detectors is obtained. From now on, the CTR values will be given in FWHM if nothing else is specified.

A first correction of the skew and time walk is performed using the energy deposited in the scintillator crystal as described in subsection 4.3.2. The CTR decreases to 530 ps applying this correction. A second strategy to improve the CTR measurements can be applied using the information of all the channels in the SIPM. Two different averaging methods are here employed that takes the n fastest channels, i.e., the smaller timestamps, to improve the CTR. The first one is a simple average (SA) of the timestamps and the second is an average weighted by the collected energy (EW) in each channel. These averaging methods are mathematically described as follows:

$$t_{SA} = \frac{\sum_{i=1}^{n} t_i}{n} \quad t_{EW} = \frac{\sum_{i=1}^{n} t_i \cdot C_i}{\sum_{i=1}^{n} C_i} \tag{4.2}$$

where C_i corresponds to the energy deposited in the i-th channel. Figure 4.13 illustrates the CTR with respect to the number of channels averaged. The best result obtained is close to 230 ps of CTR using the EW method, which is slightly better compared to the simple average approach. Taking this into account, an improvement of 60% compared to the raw measurement is obtained. The contribution to CTR from the monolithic detector can be obtained using the following expression:

$$\sigma^2_{mono} = \sigma^2_{module} - \sigma^2_{ref} - 2\sigma^2_{TDC} \tag{4.3}$$

After subtracting all the contributions (reference detector, 2 x TDC jitter from each board), a 173 ps time resolution of the monolithic module (crystal, SiPM and HRFlexToT ASIC) is obtained. The CTR of two identical modules is then calculated by multiplying this number by $\sqrt{2}$, i.e, a CTR of 244 ps. No further optimization was taken into account in this first case, the next setup will try to optimize the CTR as a function of the time threshold applied as well as for the bias voltage.

The second configuration following the description from 4.2.2, which implies a large 20 mm thick LFS crystal wrapped in Teflon was tested. First, a Dark Count Rate (DCR) analysis is performed in order to equalize the threshold of the time leading edge discriminator in each one of the channels, as can be seen in figure 4.14. The count rate indicates the number of dark pulses per second recorded, where the threshold LSB indicates the level of the leading-edge

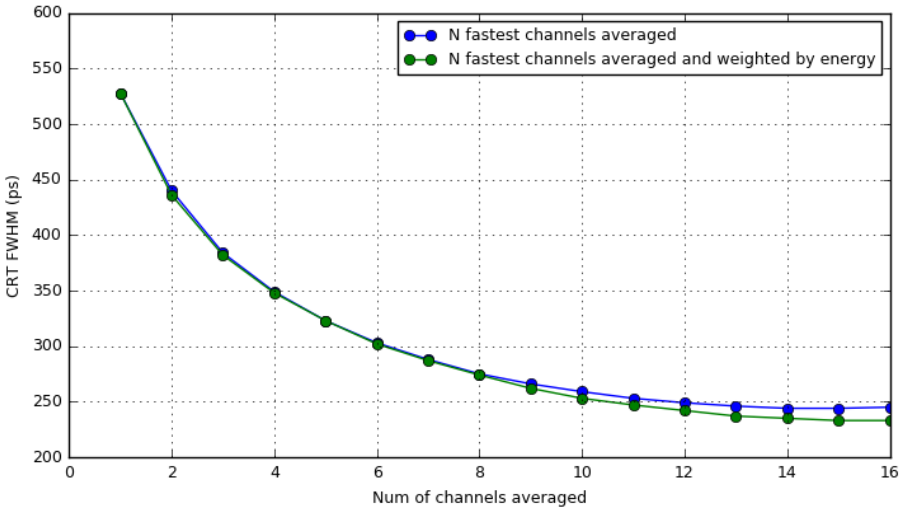

Figure 4.13.: CTR vs number of channels averaged at 6V of overvoltage. SiPM: S13361-2050NE. Crystal: LSO:Ce Ca 0.2% of 8 mm × 8 mm × 5 mm teflon wrapped.

comparator of the ToT inside the ASIC. The lower LSB value, the higher the threshold. Then, the threshold value of each channel is chosen as the closest one to the desired count rate value, e.g. 100 kHz as designated with the blue horizontal line in figure 4.14. A more exhaustive count rate sweep will be performed to determine the optimal value. Using this method, the threshold level on each channel is expected to be approximately equal, assuming a gain homogeneity over the SiPM array and without considering crosstalk. An additional overvoltage equalization should be performed as some degree of gain non homogeneity among all 16 channels may be present.

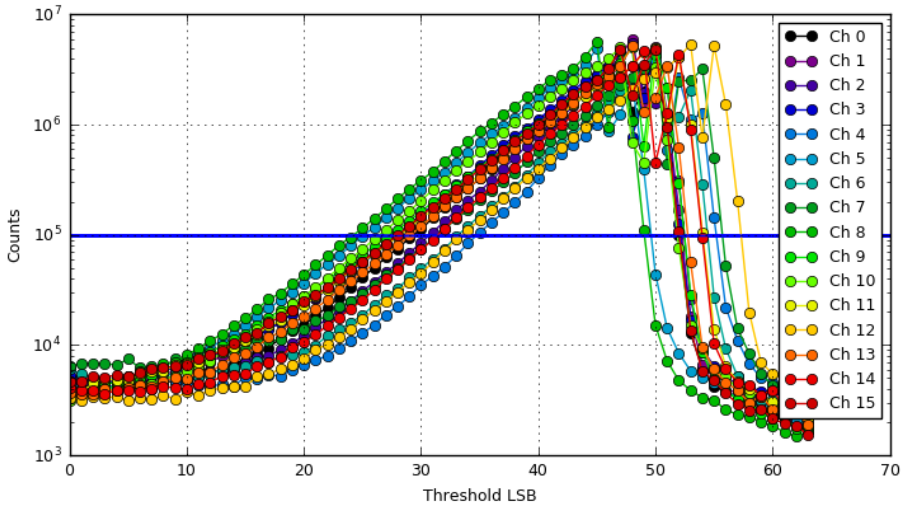

Figure 4.14.: DCR plot for the 16 channel SiPM array S13361-6050NE at 5V of overvoltage.

Figure 4.15 illustrates the EW averaging method when setting the time threshold at different levels. Observe from figure 4.15a that each threshold setting corresponds to a given Dark Count Rate in the absence of signal. Setting different Dark count rates is equivalent as configuring the threshold in terms of number of photons. This method is especially useful for

large area SiPMs, in this case 6 mm × 6 mm, where is difficult to distinguish the different photoelectron plateaus. Figure 4.15b depicts the CTR for different threshold levels averaging the optimum number of channels, which can be seen from figure 4.15a that is 14. Note that the optimum threshold is at 50 kHz of DCR which should correspond to approximately the 3rd photoelectron. On one hand, by increasing the threshold level (decreasing the kHz DCR), the CTR slowly degrades due to the worsening on photon statistics. On the other hand, the CTR increases very fast when the threshold level is as low as 1500 kHz which represents approximately the first photoelectron. The time degradation has two main factors. On one hand, the electronic noise and the Single Photon Time Resolution (SPTR) of the sensor. Lower threshold is translated into smaller slew rate of the signal, this allowing the electronic noise to be the dominating term. Furthermore, the long tails present on the SPTR distribution will cause a broadening on the photon statistic time of arrival, and therefore increasing the CTR and, on the other hand, the non-desired noise events coming from dark count and crosstalk pulses.

Figure 4.16 illustrates the CTR dependence on the overvoltage for the same number of channels (14) and the optimal threshold value. The improvement on the CTR while increasing the bias voltage can be explained by the improvement of the photon detection efficiency (PDE) of the sensor. Thus, allowing to capture more photons in each gamma interaction, which improves time resolution due to better photostatistics. Nonetheless, there is an optimum value, in this case at 7 V of overvoltage. At this point, increasing the bias voltage will increase the DCR and the crosstalk excessively and thereby dominate the CTR deterioration. Finally, a CTR of 280 ps at the most optimal point is obtained. For a single module using this crystal configuration, the jitter is calculated using equation 4.3 and thus resulting in a value of 236 ps after subtracting all the contributions (reference detector and TDC jitter). The CTR value is 333 ps after multiplying the module jitter by $\sqrt{2}$.

A third measurement was performed utilizing the same 20 mm LFS crystal with black painted walls instead of Teflon wrapped. In these conditions, a raw CTR of 2 ns is obtained at 6 V of overvoltage and the time threshold set closed to the 3rd photoelectron level. This value goes down to 750 ps after skew and time walk compensation, plus averaging the 7 fastest channels. This degradation on time resolution compared to the Teflon wrapping can be explained by the reduction in light collection, which leads to a poor photon statistics. As can be observed from figure 4.17, the difference in energy width captured at the photopeak selection depending on the crystal wrapping is directly translated into a variation in photon collection. After applying black painting in all surfaces, the number of photons arriving to the photosensor dropped by a factor 8 approximately, as the energy from the 511 keV peak reconstruction is 8 times smaller compared to the teflon configuration. The majority of them are absorbed at the black walls, thus causing an increment on the time resolution with respect to the Teflon wrapping by a factor of $\sqrt{8}$ as can be empirically derived from:

$$t_{black} = t_{white} \cdot \sqrt{8} = 280 \cdot \sqrt{8} = 791ps \tag{4.4}$$

The above formula expresses how the CTR can be degraded by the number of photons collected. In brief, the light output should be maximized in order to have good timing

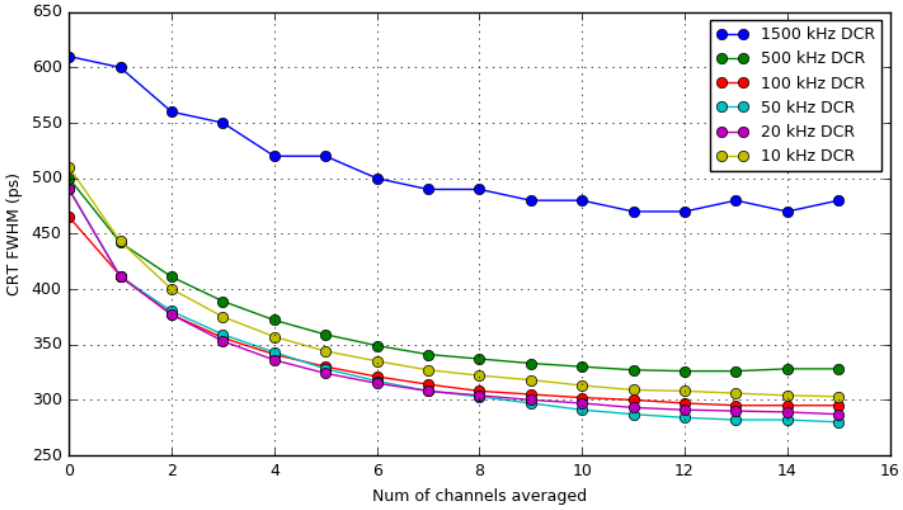

(a)

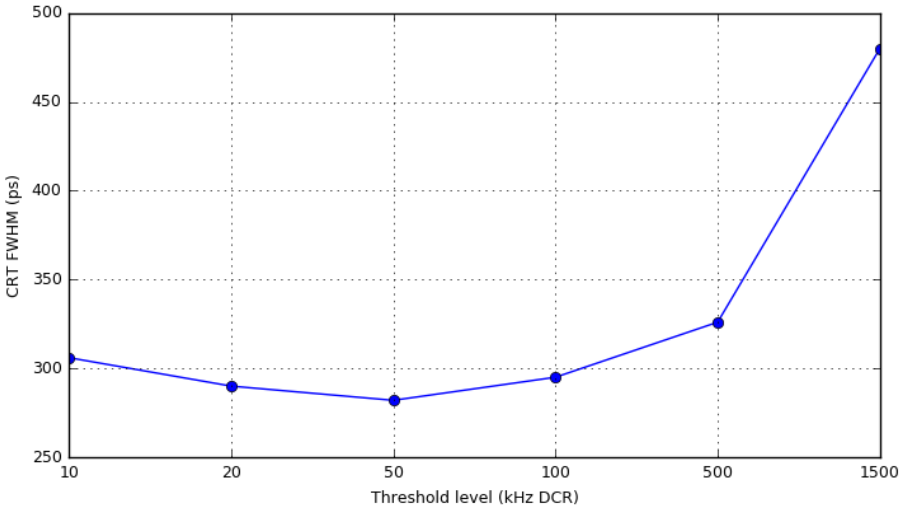

(b)

Figure 4.15.: CTR study varying the threshold level based on the DCR at 7V of overvoltage. SiPM: S13361-6050NE. Crystal: LFS of 25 mm × 25 mm × 20 mm. (a) CTR value at different thresholds. (b) Best CTR for each threshold.

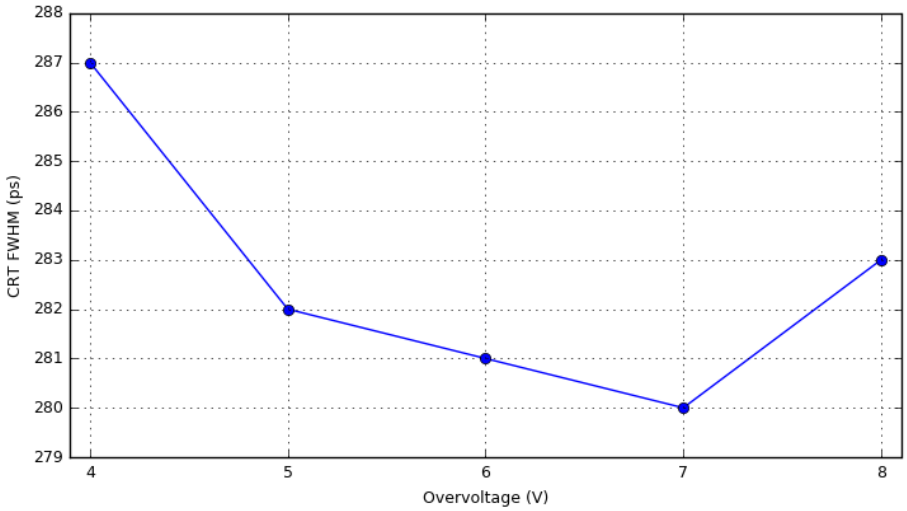

Figure 4.16.: CTR as a function of the overvoltage for the optimal threshold value. SiPM: S13361-6050NE. Crystal: LFS of 25 mm × 25 mm × 20 mm

capabilities. The next and last crystal measurement will show an intermediate CTR value by employing a retroreflective layer coupled to the gamma entrance face of the crystal as shown in section 4.2.2.

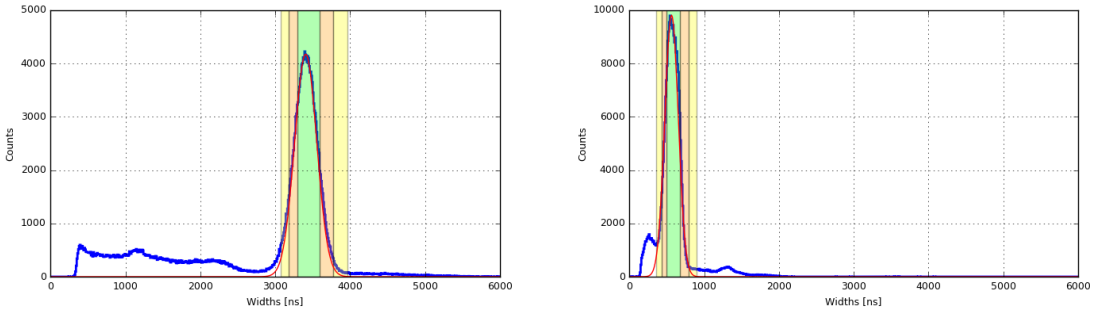

(a) **(b)**

Figure 4.17.: Energy spectrum for both crystal surface finish. SiPM: S13361-6050NE. Crystal: LFS of 25 mm × 25 mm × 20 mm. (a) Teflon wrapped. (b) Black painted surfaces.

The last experiment employs the 10 mm thick LYSO crystal with black walls and RR on top. In this configuration, both calibration methods, laser source and scintillator crystal are compared. For this purpose, the data taken in one CTR acquisition run is analyzed using those two approaches. A systematic lower CTR value is obtained using the laser LUT as can be seen in figure 4.18. Moreover, using a zero average, i.e., computing the CTR using the fastest timestamp of all channels, the corrected CTR is 35% better using the laser method instead of the classic crystal calibration.

This last configuration setup will be also used to characterize the spatial, energy resolution at different X-Y impact positions as well as the DOI capabilities in the following sections. For this reason, the CTR was calculated at 4 different positions, close-to-center one, lateral and two corners. Figure 4.19 illustrates these impact spots and the best CTR obtained.

A promising CTR of 419 ps is obtained in one of the corners of the crystal. A narrower

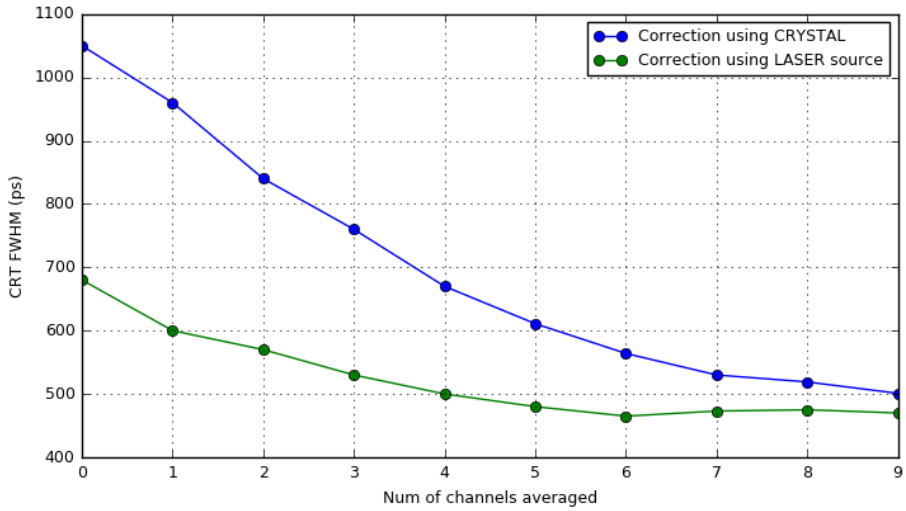

Figure 4.18.: CTR at different impact positions for 6V of overvoltage. SiPM: S13361-6050NE. Crystal: LYSO of 25x25x10 mm^3 RR on top, black lateral surfaces.

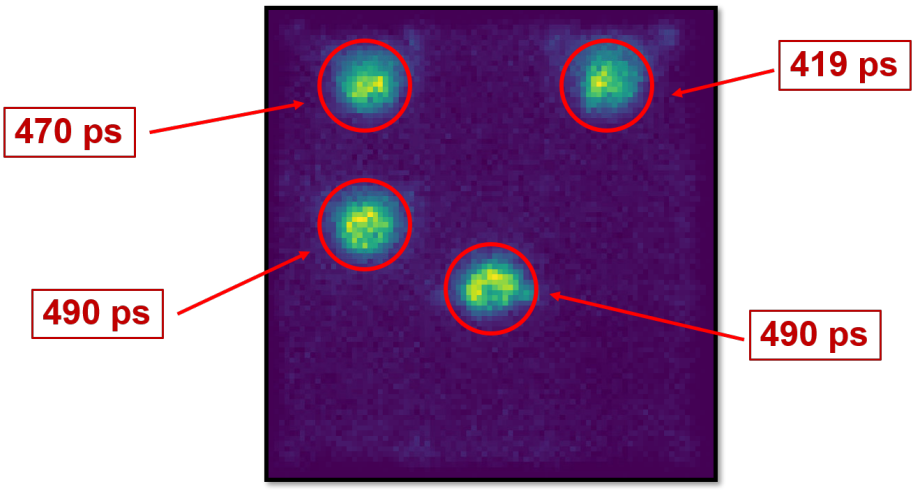

Figure 4.19.: CTR at different impact positions for 6V of overvoltage. SiPM: S13361-6050NE. Crystal: LYSO of 25x25x10 mm^3 RR on top, black lateral surfaces.

light spread (less time spread) over the corner, because of the black lateral surface absorption, can explain the improvement in this specific location. As previously mentioned, the CTR value obtained with this configuration is in between the Teflon and the black painting. In this case, the light output at the sensor site increases with respect to a totally black painted crystal due to the fact that the RR redirects the photons in the same path but in opposite direction and thus improving time resolution. In addition, this particular property of the RR preserves the scintillator light distribution, which is a key factor for the impact position reconstruction, as it will be shown next.

4.4.2 Spatial and Energy resolution

The following section presents the intrinsic spatial resolution X-Y of the already tested LYSO of 25 mm × 25 mm × 10 mm with RR on top, read out by the S13361-6050NE-04 SiPM with 6 mm × 6 mm channel size. A matrix of 5 × 4 different impact positions is scanned using the setup described in 4.2.2. Considering the collimator diameter as well as the distance between the collimator and the reference detector (10 cm), the spot at the crystal entrance face is ≈1.2 mm of diameter. A simple algorithm based on the Anger Center Of Gravity (COG) [36] is used for impact position reconstruction. The method employed here is a slightly modified version of this algorithm, named Rise To the Power (RTP), which improves the linearity compression effect (error on the centroid calculation along the edges of the crystal). The following equation shows how to compute the gamma interaction point with coordinates $X_{centroid}$ and $Y_{centroid}$.

$$X_{centroid} = \frac{\sum_{i=1}^{c} n_i^{\alpha} x_i}{\sum_{i=1}^{c} n_i^{\alpha}} \quad Y_{centroid} = \frac{\sum_{i=1}^{r} m_i^{\alpha} y_i}{\sum_{i=1}^{r} m_i^{\alpha}} \tag{4.5}$$

where x_i and y_i are the SiPM channel position in the array detector, r and c denotes the number of rows and columns of the sensor array (in this experiment, both are 4), n_i and m_i represents the energy projection in the x and y direction respectively and α is an empiric parameter that depends on the amount of light collected and the light distribution. In particular, $n_i = \sum_{j=1}^{c} n_{j,i}$ is computed as the sum of all components in row i and $m_i = \sum_{j=1}^{r} m_{j,i}$ is calculated as the sum of all components in column i.

As a counterpart of the RTP method, the positioning error increases with the alpha value. In this study, alpha is set to 1 (Anger COG) since a larger number would causes distortion on the centroid calculation. The resulting flood map can be seen in figure 4.20a. Compton events are not used and only events at $\pm 3\sigma$ from the photopeak are shown. All impact positions are separated 5 mm in X and Y direction.

After obtaining the centroids, data from the central column is taken to compute the Y-profile in the vertical direction as can be seen in figure 4.20a. Moreover, a multi-Gaussian fit of the data is performed and a position resolution of ≈ 2.2 mm is obtained as the median of the four FWHM's, as depicted in figure 4.20b. Additionally, this value reveals very promising results compared to a module with similar crystals but read out with higher granularity

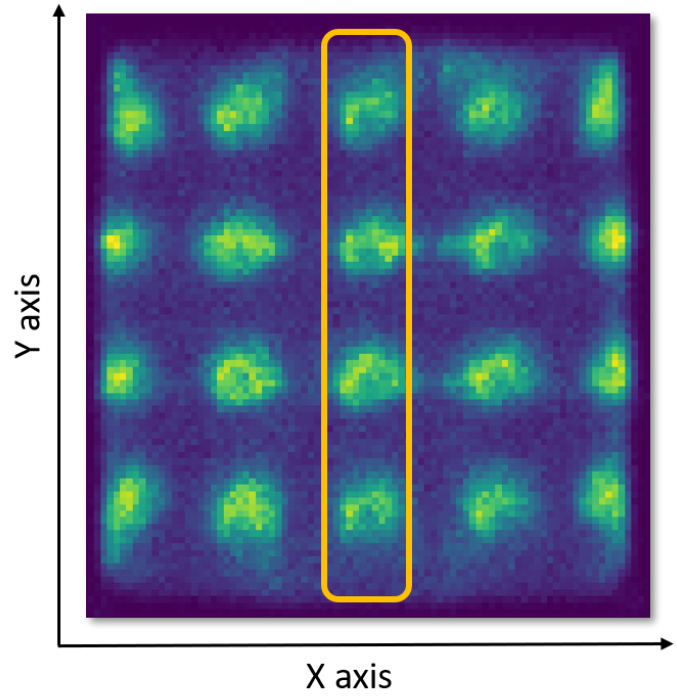

(a)

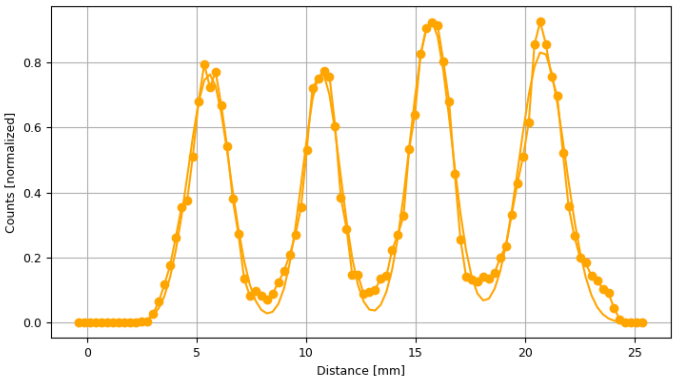

(b)

Figure 4.20.: SiPM: S13361-6050NE. Crystal: LYSO of 25x25x10 mm^3 RR on top, black lateral surfaces. (a) Floodmap of the ^{22}Na scan with distance 5 mm in X and Y. (b) Y profile for the orange delimited area in (a).

photosensors and different FE ASIC [17, 31]. For instance, a module read out with an array of 3 mm × 3 mm SiPMs instead of 6 mm × 6 mm, obtained a spatial resolution of around ≈ 1.6 mm [37].

Finally, the energy resolution of all 5 × 4 matrix impact locations is calculated. Figure 4.21 illustrates the energy resolution in terms of percentage of the FWHM at 511 keV. The best values are located close to the center of the crystal, whereas it degrades towards the edges due to the black walls reducing the photon collection. Even with this degradation, the monolithic crystal with black painted walls can lead to a really promising spatial resolution and maintain the energetic properties needed to select the desired photopeak with acceptable resolution. The next subsection will show the depth of interaction capabilities achievable with this specific detector.

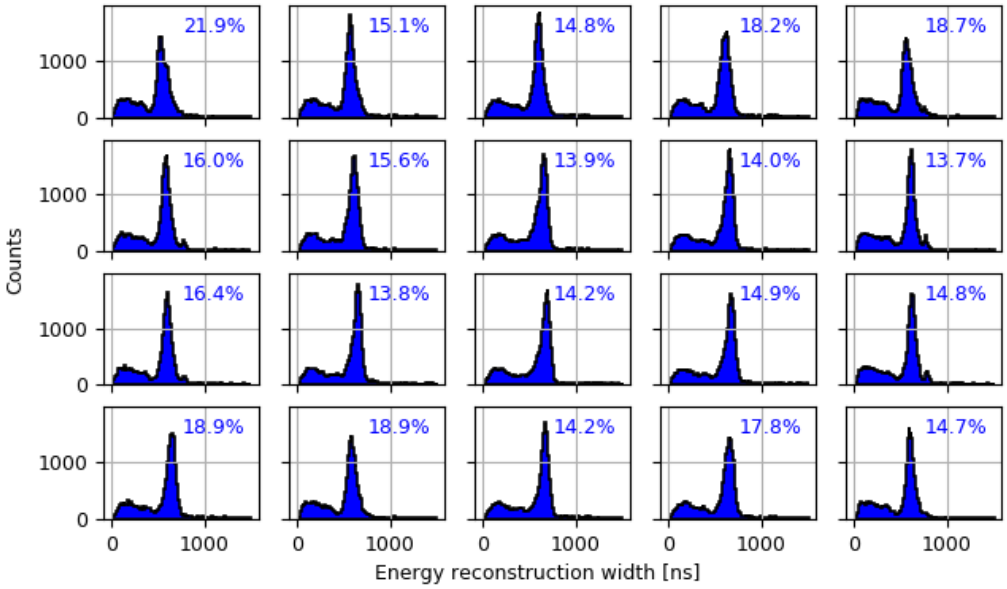

Figure 4.21.: Energy resolution depending on the gamma-ray position. SiPM: S13361-6050NE. Crystal: LYSO of 25 mm × 25 mm × 10 mm RR on top, black lateral surfaces.

4.4.3 Depth of Interaction capability

In this last section, we present a preliminary DOI measurement using the monolithic crystal LYSO of 25 mm × 25 mm × 10 mm with black painted lateral walls and a RR layer on top, read out by the S13361-6050NE-04 with 6 mm × 6 mm channel. The DOI is a key parameter to correct afterwards the timing information and improve the parallax error from the full ring of a scanner, thus allowing to calculate the true line of response. Otherwise, the information of the gamma absorption along the Z position is lost and the final reconstructed image will be degraded.

The setup is similar to the one shown in figure 4.4, although in this case the monolithic block is oriented horizontally in order to have a lateral gamma incidence. This configuration

enables to change the Z coordinate by using the motion controller. Given that the crystal is 10 mm long, two measurements at 2 mm and 6 mm with respect to the sensor face were taken. In both measurements, the light distribution in the sensor face is used to obtain the ratio $(N/I_{max})_{r,c}$, which is directly related to the DOI. N stands for the sum of all energies for rows or columns, while the I_{max} corresponds to the maximum energy in rows or columns respectively. Finally, a single value of the N/I_{max} is calculated as the average of N/I_{max} for rows and columns.

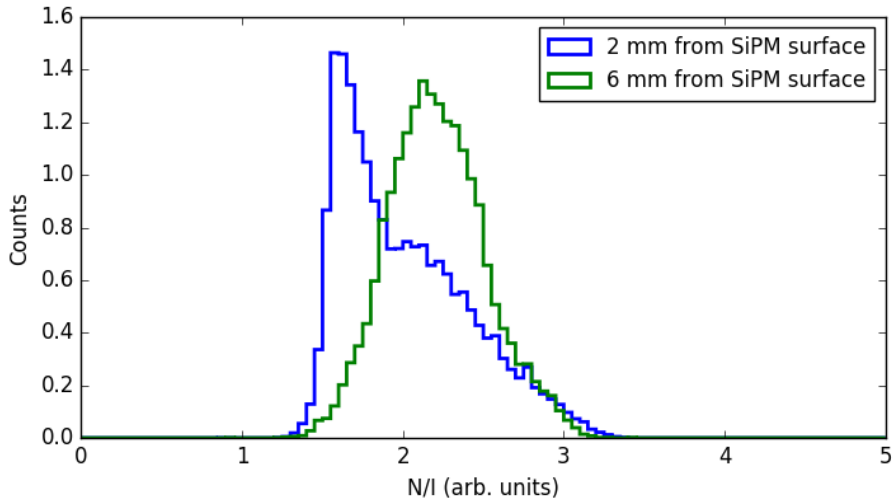

Figure 4.22.: DOI distribution for 2 mm and 6 mm depth on the lateral gamma ray impact position. SiPM: S13361-6050NE. Crystal: LYSO of 25 mm × 25 mm × 10 mm RR on top, black lateral surfaces.

The Z distance between both measurements is 4 mm which translates into approximately 0.6 N/I displacement in the distribution. Considering a linear trend we calculated a preliminary FWHM on both distributions (DOI resolution), which are 3.8 mm and 4.1 mm for the 2 mm and 6 mm DOI respectively, as illustrated in figure 4.22. An average of 3.95 mm DOI resolution is found as a first approximation. Further and more exhaustive DOI measurements involving a thicker crystal of 25 mm × 25 mm × mm 20 mm coupled with RR layer on top will be performed in the near future.

4.5 Conclusion

In this work we presented the latest results on a monolithic PET module using HRFlexToT technology as the readout for SiPM matrices and three different crystal shapes and covers. A promising result of 244 ps (FWMH) CTR was obtained for a single small LSO:Ce Ca 0.2% monolithic crystal module of 8 mm × 8 mm × 5 mm wrapped in teflon. The CTR value of 333 ps FWHM was recorded using a medium size LFS crystal of 25 mm × 25 mm × 20 mm. Moreover, a CTR of 750 ps FWHM measurement with the same crystal but with all the crystal surfaces painted black was reported, thus resulting in a time resolution degradation due to the poor photon light sharing over the SiPM matrix.

Finally a more exhaustive study utilizing a new developed time-walk and time-skew precalibration technique was carried out on a LYSO monolithic crystal of 25 mm × 25 mm × 10 mm. In this case, the crystal had a retroreflector on the top surface and black painted walls in order to achieve the best CTR possible while maintaining the spatial resolution. Hence a CTR of 419 ps and a spatial X-Y spatial resolution of 2.2 mm was reported. Additionally, the DOI capability was tested, and a preliminary measurement of ∼4 mm was found.

In brief, the HRFlexToT capabilities to readout a monolithic crystal was successfully studied. For the near future, a 64 channel PCB readout by 4 HRFlexToTs and a bigger monolithic crystal of 50 mm × 50 mm section size along with a deeper understanding on the light sharing will be studied. Additionally, a lower granularity configuration using 3 mm pixel pitch SiPM matrix will be tested, thus expecting better CTR and DOI resolution.

4.6 Bibliography

[1] T. Jones, D. Townsend, History and future technical innovation in positron emission tomography, Journal of Medical Imaging 4 (1) (2017) 011013. doi:10.1117/1.jmi.4.1.011013.

[2] S. Surti, Update on time-of-flight PET imaging, Journal of Nuclear Medicine 56 (1) (2015) 98–105. doi:10.2967/jnumed.114.145029.

[3] J. S. Karp, S. Surti, M. E. Daube-Witherspoon, G. Muehllehner, Benefit of time-of-flight in PET: Experimental and clinical results, Journal of Nuclear Medicine 49 (3) (2008) 462–470. doi:10.2967/jnumed.107.044834.

[4] M. Conti, Why is TOF PET reconstruction a more robust method in the presence of inconsistent data?, Physics in Medicine and Biology 56 (1) (2011) 155–168. doi:10.1088/0031-9155/56/1/010.

[5] J. Van Sluis, J. De Jong, J. Schaar, W. Noordzij, P. Van Snick, R. Dierckx, R. Borra, A. Willemsen, R. Boellaard, Performance characteristics of the digital biograph vision PET/CT system, Journal of Nuclear Medicine 60 (7) (2019) 1031–1036. doi:10.2967/jnumed.118.215418.

[6] R. D. Badawi, H. Shi, P. Hu, S. Chen, T. Xu, P. M. Price, Y. Ding, B. A. Spencer, L. Nardo, W. Liu, J. Bao, T. Jones, H. Li, S. R. Cherry, First human imaging studies with the explorer total-body PET scanner, Journal of Nuclear Medicine 60 (3) (2019) 299–303. doi:10.2967/jnumed.119.226498.

[7] P. Lecoq, Pushing the Limits in Time-of-Flight PET Imaging, IEEE Transactions on Radiation and Plasma Medical Sciences 1 (6) (2017) 473–485. doi:10.1109/TRPMS.2017.2756674.
URL http://ieeexplore.ieee.org/document/8049484/

[8] J. Mauricio, D. Gascon, D. Ciaglia, S. Gómez, G. Fernández, A. Sanuy, MATRIX: A novel two-dimensional resistive interpolation 15 ps Time-to-Digital Converter ASIC, 2016 IEEE Nuclear Science Symposium, Medical Imaging Conference and Room-Temperature Semiconductor Detector Workshop, NSS/MIC/RTSD 2016 2017-Janua (2017) 15–17. doi:10.1109/NSSMIC.2016.8069650.

[9] V. C. Spanoudaki, C. S. Levin, Photo-detectors for time of flight positron emission tomography (ToF-PET), Sensors (Switzerland) 10 (11) (2010) 10484–10505. doi:10.3390/s101110484.

[10] M. V. Nemallapudi, S. Gundacker, P. Lecoq, E. Auffray, Single photon time resolution of state of the art SiPMs, Journal of Instrumentation 11 (10) (2016). doi:10.1088/1748-0221/11/10/P10016.

[11] C. L. Melcher, Scintillation crystals for PET, Journal of Nuclear Medicine 41 (6) (2000) 1051–1055.

[12] P. Lecoq, Development of new scintillators for medical applications, Nuclear Instruments and Methods in Physics Research, Section A: Accelerators, Spectrometers, Detectors and Associated Equipment 809 (2016) 130–139. doi:10.1016/j.nima.2015.08.041.
URL http://dx.doi.org/10.1016/j.nima.2015.08.041

[13] D. N. Ter Weele, D. R. Schaart, P. Dorenbos, Comparative study of Co-doped and non Co-doped LSO:Ce and LYSO:Ce scintillators for TOF-PET, IEEE Transactions on Nuclear Science 62 (3) (2015) 727–731. doi:10.1109/TNS.2015.2431295.

[14] S. Gundacker, A. Knapitsch, E. Auffray, P. Jarron, T. Meyer, P. Lecoq, Time resolution deterioration with increasing crystal length in a TOF-PET system, Nuclear Instruments and Methods in Physics Research, Section A: Accelerators, Spectrometers, Detectors and Associated Equipment 737 (2014) (2014) 92–100. doi:10.1016/j.nima.2013.11.025.
URL http://dx.doi.org/10.1016/j.nima.2013.11.025

[15] M. Pizzichemi, A. Polesel, G. Stringhini, S. Gundacker, P. Lecoq, S. Tavernier, M. Paganoni, E. Auffray, On light sharing {TOF}-{PET} modules with depth of interaction and 157 ps {FWHM} coincidence time resolution, Physics in Medicine & Biology 64 (15) (2019) 155008. doi:10.1088/1361-6560/ab2cb0.
URL https://doi.org/10.1088{%}2F1361-6560{%}2Fab2cb0

[16] R. Marcinkowski, S. España, R. Van Holen, S. Vandenberghe, Optimized light sharing for high-resolution TOF PET detector based on digital silicon photomultipliers, Physics in Medicine and Biology 59 (23) (2014) 7125–7139. doi:10.1088/0031-9155/59/23/7125.

[17] E. Lamprou, A. Gonzalez, F. J. Sanchez, J. M. Benlloch, Exploring TOF capabilities of PET detector blocks based on large monolithic crystals and analog SiPMs, {ELSEVIER} Physica Medica 70 (2020) 10–18.
URL https://doi.org/10.1016/j.ejmp.2019.12.004

[18] R. S. Miyaoka, X. Li, C. Lockhart, T. K. Lewellen, Design of a high resolution, monolithic crystal, PET/MRI detector with DOI positioning capability, IEEE Nuclear Science Symposium Conference Record (2008) 4688–4692doi:10.1109/NSSMIC.2008.4774469.

[19] H. T. van Dam, S. Seifert, R. Vinke, P. Dendooven, H. Löhner, F. J. Beekman, D. R. Schaart, A practical method for depth of interaction determination in monolithic scintillator {PET} detectors, Physics in Medicine and Biology 56 (13) (2011) 4135–4145. doi:10.1088/0031-9155/56/13/025.
URL https://doi.org/10.1088{%}2F0031-9155{%}2F56{%}2F13{%}2F025

[20] H. T. van Dam, G. Borghi, S. Seifert, D. R. Schaart, Sub-200 ps {CRT} in monolithic scintillator {PET} detectors using digital {SiPM} arrays and maximum likelihood interaction time estimation, Physics in Medicine and Biology 58 (10) (2013) 3243–3257. doi:10.1088/0031-9155/58/10/3243.
URL https://doi.org/10.1088{%}2F0031-9155{%}2F58{%}2F10{%}2F3243

[21] A. Gonzalez-Montoro, J. M. Benlloch, A. J. Gonzalez, A. Aguilar, G. Canizares, P. Conde, L. Hernandez, L. F. Vidal, M. Galasso, A. Fabbri, F. Sanchez, Performance Study of a Large Monolithic LYSO PET Detector With Accurate Photon DOI Using Retroreflector

Layers, IEEE Transactions on Radiation and Plasma Medical Sciences 1 (3) (2017) 229–237. doi:10.1109/trpms.2017.2692819.

[22] M. Morrocchi, G. Ambrosi, M. G. Bisogni, F. Bosi, M. Boretto, P. Cerello, M. Ionica, B. Liu, F. Pennazio, M. A. Piliero, G. Pirrone, V. Postolache, R. Wheadon, A. Del Guerra, Depth of interaction determination in monolithic scintillator with double side SiPM readout, EJNMMI Physics 4 (1) (2017). doi:10.1186/s40658-017-0180-9.

[23] C. M. Pepin, P. Bérard, A. L. Perrot, C. Pépin, D. Houde, R. Lecomte, C. L. Melcher, H. Dautet, Properties of LYSO and recent LSO scintillators for phoswich PET detectors, IEEE Transactions on Nuclear Science 51 (3 II) (2004) 789–795. doi:10.1109/TNS.2004.829781.

[24] H. Poladyan, O. Bubon, A. Teymurazyan, S. Senchurov, A. Reznik, Gain invariant coordinate reconstruction for SiPM-Based pixelated gamma detectors with multiplexed readout, IEEE Transactions on Instrumentation and Measurement 69 (7) (2020) 4281–4291. doi:10.1109/TIM.2019.2942222.

[25] S. Gomez, D. Sanchez, D. Gascon, J. Cela, L. Freixas, R. Graciani, R. Manera, J. Marin, J. Mauricio, J. Navarrete, J. Oller, J. Perez, P. Rato Mendes, A. Sanmukh, O. Vela, A High Dynamic Range ASIC for Time of Flight PET with pixelated and monolithic crystals, in: 2019 IEEE Nuclear Science Symposium and Medical Imaging Conference, NSS/MIC 2019, 2019. doi:10.1109/NSS/MIC42101.2019.9059762.

[26] J. Trenado, J. M. Cela, A. Comerma, D. Gascon, R. Graciani, L. Freixas, J. Marin, G. Martínez, R. Masachs, J. M. Perez, P. Rato, D. Sanchez, A. Sanuy, I. Sarasola, Performance of FlexToT time based PET readout ASIC for depth of interaction measurements, Proceedings of Science (2014). doi:10.22323/1.213.0241.

[27] J. Wu, Several key issues on implementing delay line based TDCs using FPGAs, IEEE Transactions on Nuclear Science 57 (3 PART 3) (2010) 1543–1548. doi:10.1109/TNS.2010.2045901.

[28] D. NIKJOO, Hooshang; UEHARA, Shuzo; EMFIETZOGLOU, Interaction of radiation with matter, CRC press, 2012.

[29] F. Powolny, E. Auffray, S. E. Brunner, E. Garutti, M. Goettlich, H. Hillemanns, P. Jarron, P. Lecoq, T. Meyer, H. C. Schultz-Coulon, W. Shen, M. C. Williams, Time-based readout of a silicon photomultiplier (SiPM) for time of flight positron emission tomography (TOF-PET), IEEE Transactions on Nuclear Science 58 (3 PART 1) (2011) 597–604. doi:10.1109/TNS.2011.2119493.

[30] R. Vinke, H. Löhner, D. R. Schaart, H. T. Van Dam, S. Seifert, F. J. Beekman, P. Dendooven, Time walk correction for TOF-PET detectors based on a monolithic scintillation crystal coupled to a photosensor array, Nuclear Instruments and Methods in Physics Research, Section A: Accelerators, Spectrometers, Detectors and Associated Equipment 621 (1-3) (2010) 595–604. doi:10.1016/j.nima.2010.05.034.

[31] E. Lamprou, A. Aguilar, A. González-Montoro, J. M. Monzó, G. Cañizares, S. Iranzo, L. F. Vidal, L. Hernández, P. Conde, S. Sánchez, F. Sánchez, A. J. González, J. M. Benlloch, PET detector block with accurate 4D capabilities, Nuclear Instruments and

Methods in Physics Research, Section A: Accelerators, Spectrometers, Detectors and Associated Equipment 912 (September 2017) (2018) 132–136. doi:10.1016/j.nima.2017.11.002.
URL https://doi.org/10.1016/j.nima.2017.11.002

[32] F. Acerbi, S. Gundacker, Understanding and simulating SiPMs, Nuclear Instruments and Methods in Physics Research, Section A: Accelerators, Spectrometers, Detectors and Associated Equipment 926 (September 2018) (2019) 16–35. doi:10.1016/j.nima.2018.11.118.
URL https://doi.org/10.1016/j.nima.2018.11.118

[33] S. Gómez, D. Gascón, G. Fernández, A. Sanuy, J. Mauricio, R. Graciani, D. Sanchez, MUSIC: An 8 channel readout ASIC for SiPM arrays, Optical Sensing and Detection IV 9899 (April) (2016) 98990G. doi:10.1117/12.2231095.

[34] J. Du, J. P. Schmall, M. S. Judenhofer, K. Di, Y. Yang, S. R. Cherry, A Time-Walk Correction Method for PET Detectors Based on Leading Edge Discriminators, IEEE Transactions on Radiation and Plasma Medical Sciences 1 (5) (2017) 385–390. doi:10.1109/trpms.2017.2726534.

[35] S. E. Brunner, L. Gruber, J. Marton, K. Suzuki, A. Hirtl, New approaches for improvement of TOF-PET, Nuclear Instruments and Methods in Physics Research, Section A: Accelerators, Spectrometers, Detectors and Associated Equipment 732 (2013) 560–563. arXiv:1305.1560, doi:10.1016/j.nima.2013.05.028.
URL http://dx.doi.org/10.1016/j.nima.2013.05.028

[36] H. O. Anger, Scintillation camera, Review of scientific instruments 29 (1958) 27–33.

[37] R. Pani, A. J. Gonzalez, M. Bettiol, A. Fabbri, M. N. Cinti, E. Preziosi, C. Borrazzo, P. Conde, R. Pellegrini, E. D. Castro, S. Majewski, Preliminary evaluation of a monolithic detector module for integrated {PET}/{MRI} scanner with high spatial resolution, Journal of Instrumentation 10 (06) (2015) C06006—-C06006. doi:10.1088/1748-0221/10/06/c06006.
URL https://doi.org/10.1088{%}2F1748-0221{%}2F10{%}2F06{%}2Fc06006

5

Simulation enviornment

The Silicon Photomultiplier (SiPM) sensor is replacing the extensively use Photomultiplier Tube (PMT) in fast timing applications. Those applications go from medical imaging systems like Positron Emission Tomography (PET) to LIDAR technologies used in autonomous car driving. Medical applications, and more specific Time-of-Flight PET (ToF-PET), require further developments to achieve the 10 ps CTR in order to enable the real time reconstruction and in vivo molecular examination. The state-of-the-art ToF-PET systems can reach a Coincidence Time Resolution (CTR) of 200 ps. Lowering this value will require a cross-optimization of the scintillator crystal, the sensor and the electronics at the same time. Optimizing a PET system considering these three elements will be the key to boost the timing resolution of the complete system.

The aim of this chapter is to show a new developed simulation framework that will enable this cross-optimization of the PET system taking into consideration the photon physics interaction in the scintillator crystal, the sensor response (sensor size, pixel pitch, dead area, capacitance) and the readout electronics behavior (input impedance, noise, bandwidth, summation). This framework has allowed us to study a new promising approach that will help reducing the CTR parameter by segmenting a large area SiPM into "m" smaller SiPMs and then summing them to recover all the signal spread along these smaller sensors. A 15% improvement on time resolution is expected by segmenting a 4 mm $\times$ 4 mm single sensor into 9 sensors of 1.3 mm $\times$ 1.3 mm with respect to the case where no segmentation is applied.

Contents

5.1 Introduction

The Silicon Photomultiplier (SiPM) sensor is replacing the extensive use of the Photomultiplier Tube (PMT) in many applications. Nowadays, medical imaging systems such as Single Photon Emission Computed Tomography (SPECT) and Positron Emission Tomography (PET) are mainly running those new SiPMs. Moreover, most of the new upgrades in High Energy Physics (HEP) experiments are planning to use SiPMs [1], as well as for Cherenkov light detection [2, 3, 4, 5], cosmic ray and space exploration detectors such as HERD [6] and LIDAR applications in automotive [7, 8].

An application where the usage of SiPMs provides a noticeable performance improvement is medical imaging, in particular PET. PET is a molecular diagnosis technique that allows to track different biological processes, whose purpose is to show the cellular or molecular activity of the disease [9]. The process implies the administration of a radiotracer, a biomolecule labeled to a radioactive atom emitting positrons (β^+). During the PET imaging, the positron emitted by the radiotracer undergoes annihilation with an electron and this process produces two 511 keV gamma-rays that travel approximately 180 ° from each other. Then, a near-simultaneous detection of these two gamma-rays (coincidence time) in a ring of detectors takes place. The signal generated in this process allows to reconstruct the final image.

One approach to increase the sensitivity of the PET technique, thus reducing the dose to the patient or the scanning time, consist in pushing the limits of the ToF capabilities [10] by improving the CTR parameter of the system. This will have a direct impact on the image Signal-to-Noise (SNR), resulting in an improvement of the sensitivity by a theoretical factor of (equation 5.1):

$$SNR_{ToF}/SNR_{NONToF} = \sqrt{\frac{2D}{c \cdot CTR}} \tag{5.1}$$

where D is the diameter of the Field of View (FoV) and c corresponds to the speed of light.

The latest developments on ToF-PET imaging systems have achieved a CTR of 200 ps as shown in the Biograph Vision model from Siemens Healthineers [11]. In fact, this value corresponds to an improvement factor of 1.5 with respect to the previous version and to the rest of existing systems that have a time resolution between 300 ps to 400 ps for partial or total body PET systems [12].

Different research groups are trying to break the barrier on time resolution and reach the 10 ps of CTR [13]. A simple equation could be used to calculate the spatial resolution of a system with such an excellent time jitter:

$$\Delta x = \frac{1}{2}\, CTR \cdot c \tag{5.2}$$

where c stands for the speed of light and the factor 1/2 accounts for the half distance traveled by the two gamma photons. A 10 ps CTR system will lead to an uncertainty of around 1.5 mm along the line of response, which corresponds approximately to the mean free path of the positron before it annihilates with an electron. In brief, once we reach this point, the inherent physical processes involved in the gamma detection will be the limiting factor in the imaging system. Such accuracy would grant a direct 3D reconstruction of the positron interaction; therefore the back-projection or iterative algorithms will no longer be needed and the real time PET imaging could become a reality. As a result, it will bring obvious societal and economic benefits, such as screening and early diagnosis of cancer, cardiovascular and degenerative diseases [14].

The basic PET module is composed by: first, a scintillator crystal that converts the gamma ray into visible light. Second, a photo-sensor which collects the optical photons and outputs an electrical signal. Lastly, a dedicated electronics that processes this signal and generates readable data that will be used to generate the final image from the patient.

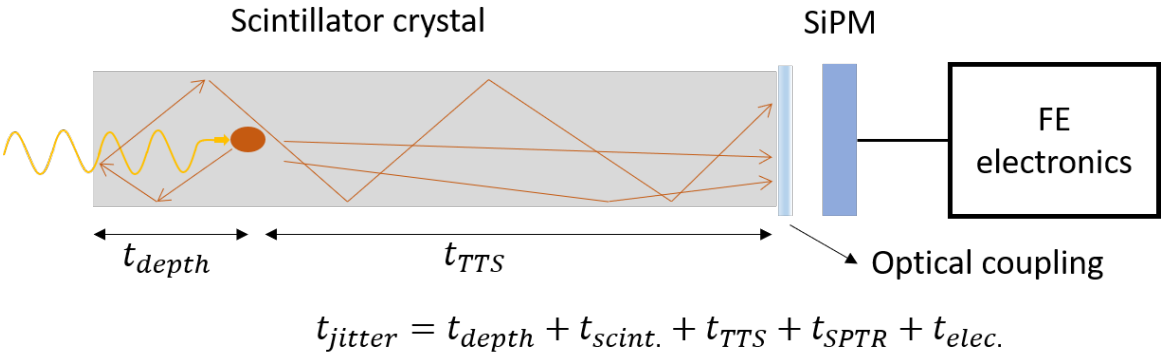

Figure 5.1.: Time jitter contributions in the gamma photon detection chain from crystal, SiPM and electronics.

Now a days, SiPMs are outperforming PMTs in all ToF-PET medical devices due to the astonishing improvements during the last 10 years. The silicon solid state detector is insensitive to magnetic fields, operates at low voltage compared to a PMT (20 V to 60 V) and it has excellent timing performance [15]. Moreover, the scalability and cost effectiveness make them suitable for covering large detection area. The accuracy of the SiPM in determining the time of arrival of a single photon is referred to Single Photon Time Resolution (SPTR) [15]. The SPTR of the SiPM is one of the key factors that affects the CTR, but there are several other sources that affect the time jitter during the detection chain as shown in figure 5.1 [16].

We can separate the contributions to the time jitter as:

- **Scintillator crystal**: it is the responsible of three contributions on the time jitter. First, the fluctuation on the interaction depth of the gamma photon (t_{depth}), which follows an exponential attenuation with the maximum at the entrance face. Then, the scintillator process determines the emission time of each one of the optical photons ($t_{scint.}$). Finally, the Transit Time Spread (TTS) which is the time needed for the optical photon to reach the photo-sensor (t_{TTS}) and it depends on the photon travel path. An optical coupler with a refractive index between the scintillator crystal and

the SiPM window is used to increase the photon extraction such as Meltmount 1.582 or BC 631 from Saint-Gobain.

- **SiPM**: The avalanche process inside the solid state detector along with the Photo-Detection Efficiency (PDE) is the main factor involved in the photon absorption [17]. Nowadays, the PDE has increased to almost 60 % [18], which means that the number of photons detected has to be multiplied by 0.6 with respect to the total extracted photons as a first approximation. Additionally, the avalanche process is a stochastic phenomena which implies that the trigger timestamps will vary among different avalanche events. This affects the time jitter at a single photon level (t_{SPTR}).

- **Electronics**: the analog signal generated from the SiPM is processed by a Front-End (FE) electronics and a Time to Digital Converter (TDC) that picks up the time of arrival (ToA) of the photons. Both circuits introduce time fluctuations to capture the ToA due to the electronic noise and therefore a time jitter that is represented as $t_{elec.}$ taking into account both contributions, the Front-End readout and the TDC time uncertainty.

The aim of this work is twofold. Firstly, to show a novel framework that will enable the optimization of a PET module, including the sensor, scintillator crystal and electronics. Secondly, using this framework, the time jitter of the current systems can be investigated by using the segmentation approach, where a single sensor is subdivided in smaller sensors and the individual signals summed as a single output.

Although this framework is here employed for ToF-PET time optimization, it is suitable for any application where the same detector module is required, as depicted in figure 5.1. High energy physics and any experiment involving optical photon collection and time resolution optimization are eligible to use it.

The following sections are organized as follows. Section 5.2 details how the complete framework works, starting by the physics simulator description and followed by the electrical simulator here used. Then, section 5.3 shows the theoretical approach on sensor segmentation and their impact on time performance. Afterwards, the simulation results for SPTR and CTR will be shown in section 5.4 and 5.5 respectively. Finally, the conclusions and future work regarding the use of the framework are described in section 5.6.

5.2 Simulation Framework

This section will present the simulation environment created to study and optimize the time jitter from the point of view of the photodetector and the electronics readout. First, we will explain how GATE, the physics simulator, tracks the detected photons and generates a readable output. Then, the next section will be focused on the electrical simulator used in this work, without loss of generality, Spectre simulator from Cadence Design Systems [19], and how this tool uses the information from GATE to compute the detector and electronics readout response.

5.2.1 Optical photon transport simulation: GATE

GATE is an advanced open-source software developed by the international collaboration OpenGATE [20] and dedicated to numerical simulations in medical imaging and radiotherapy based on GEANT4. Accurate modelling of photon interactions with crystal surfaces is essential in optical simulations, but the existing UNIFIED model in GATE is often inaccurate, especially for rough surfaces.

A new approach was developed for GATE, named Davis Model [21]. This method calculates the reflectance properties from the crystal topography previously measured with either an atomic force microscope (AFM) or a confocal laser scanning microscopy (CLSM). Figure 5.2 illustrates a small region from one of our scanned scintillator crystal surface using a CLSM. The data collected in this process are stored in a Look-Up-Table (LUT), and then used during the simulation to predict the photon direction after impinging into a crystal surface. This feature makes GATE a strong photon transport Monte Carlo generator that will be used to simulate the first steps in a gamma collection process, involving the gamma conversion into optical photons and their collection by the photosensor.

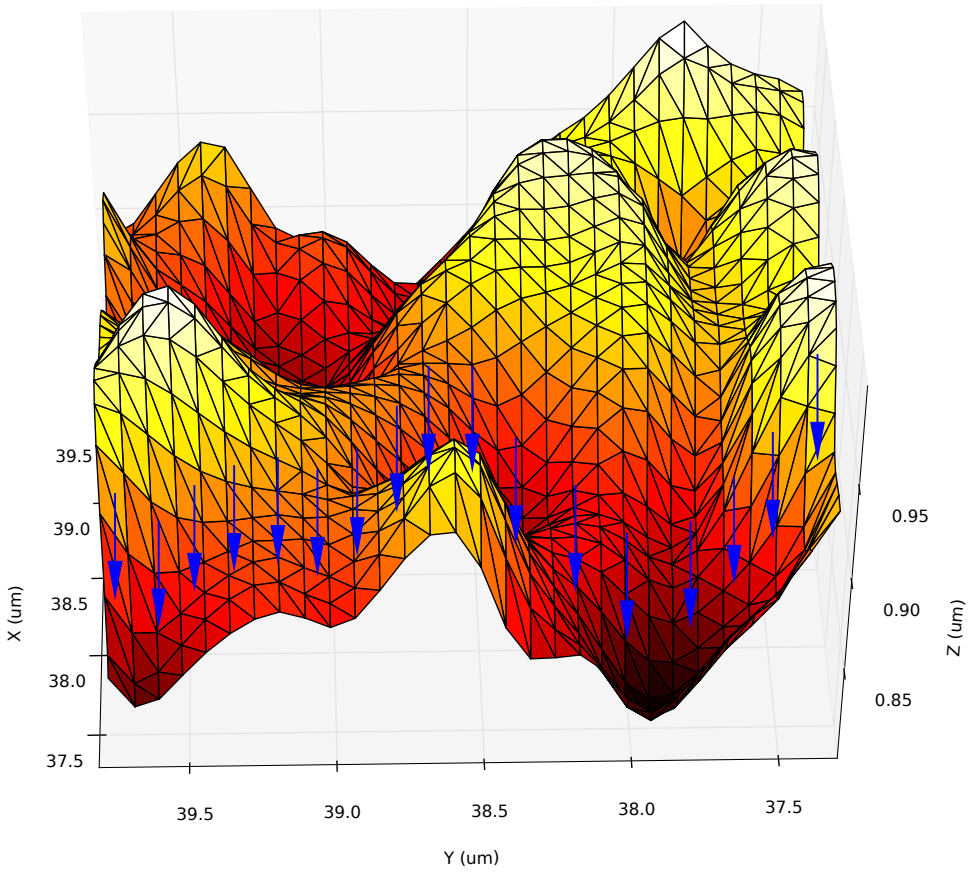

Figure 5.2.: 3D Surface representation and photon ray-tracing along different impact points (blue arrows). The resulting reflected and transmitted directions are stored in a LUT.

First, we define a CTR setup consisting of: a ^{22}Na point source in between two scintillator crystals of tunable length, both crystal surfaces wrapped in teflon if nothing different specified. Interface surfaces are defined accordingly to the DAVIS model parameters. As previously mentioned, we can generate our own DAVIS LUT from a prior scanned crystal surface using an AFM or CLSM. These crystals are coupled to a sensor with matching cross-sections by using an intermediate layer of optical grease, whose optical properties, such as the refraction index, can be adjusted in the simulation. The sensor PDE spectrum from the datasheet of the manufacturer can be introduced as a parameter in the simulator. Figure 5.3 illustrates the typical CTR setup described in a GATE simulation.

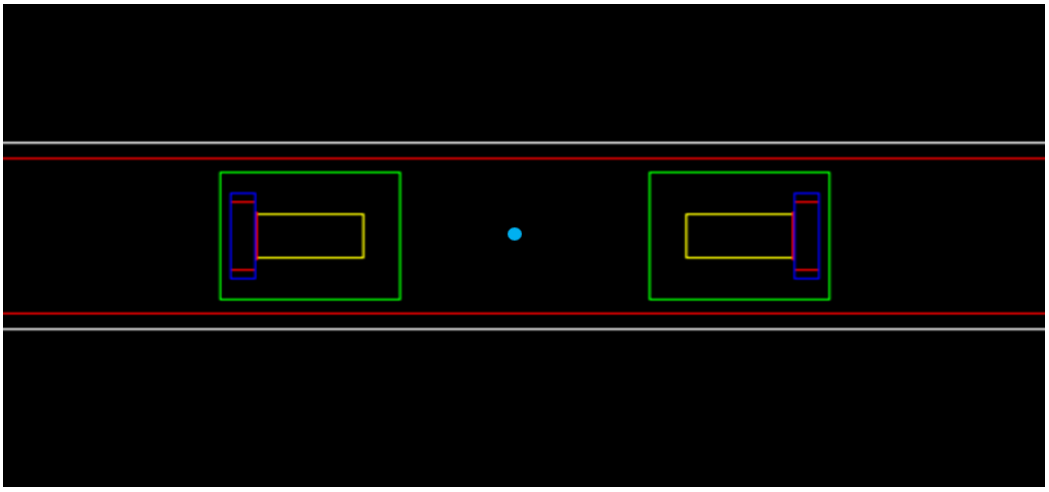

Figure 5.3.: CTR setup screenshot from GATE simulator. In Cyan, the ^{22}Na source between detectors and in green, the whole detector module. Inside the green box in yellow, the scintillator crystal and in red, the SiPM detector and the optical grease.

The full process starts by the emission of a positron from the ^{22}Na radioactive source which annihilates with an electron, resulting in two back-to-back 511 keV gamma photons. Each one of them interacts with the crystal depending on the physics interaction (Compton scattering or Photoelectric effect). Then, a certain number of photons are generated according to the light yield of the scintillating crystal. A fraction of those will reach the sensor at a given time depending on the travel path inside de crystal.

The root file output from GATE simulation includes the arrival times of each one of the scintillator photons, as well as the impact position on the sensor surface. Then, we prepare the data using a Python-root script that takes the raw file and generates a suitable output file to be used in a specific electrical simulator. Only photons with a specific arrival time below a certain threshold are selected. This threshold represents the maximum arrival time of the detected photons to be considered on the output file, any photon above this threshold will be discarded. Hence, reducing the simulation time consumption, whereas maintaining the performance since only a few tens of photons are needed to reconstruct the rising edge of the analog signal from the SiPM. This data simplification is only allowed for a leading-edge discriminator time pick-up approach that does not need the peak amplitude of the SiPM to extract the arrival time. For instance, a Constant Fraction Discriminator (CFD) or any other amplitude signal dependent method cannot apply this photon prune, since they need the amplitude to obtain the arrival time. In addition, the SiPM channel characteristics such as active area or micro-cell size can be taken into account within the input parameters in

the script. The cell size limits the number of photons collected, due to the fact that there is a dead time between two consecutive photons arriving on the same cell. Thus, losing photon detection at high light rates.

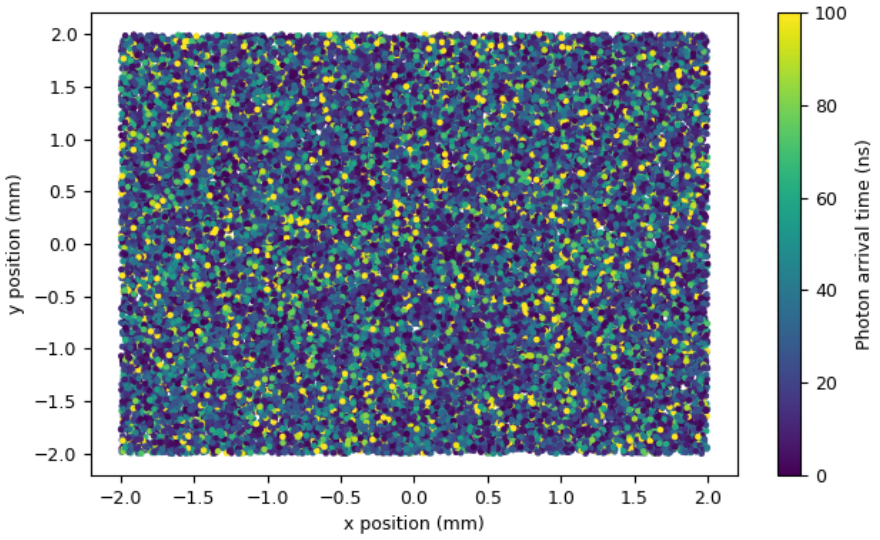

(a)

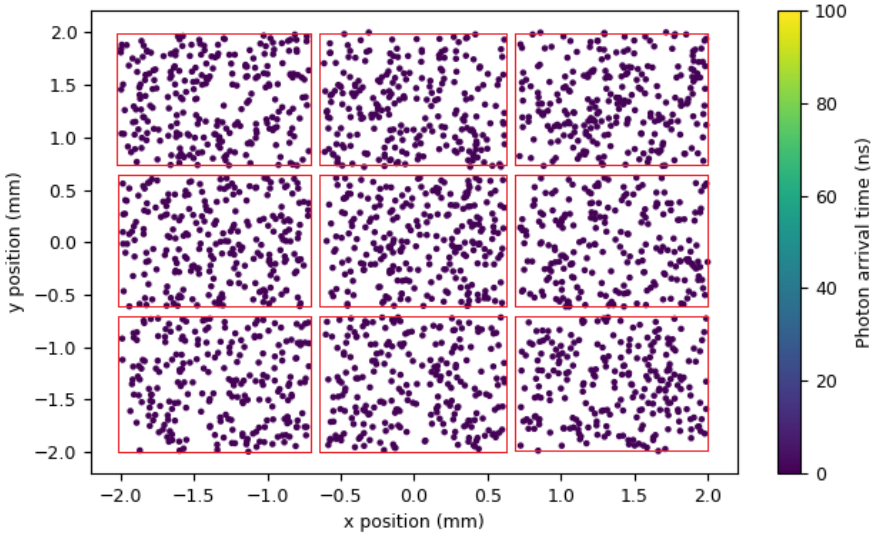

(b)

Figure 5.4.: Photon impact position and arrival time at the SiPM surface: (a) before cleaning the data. (b) after applying all constrains referring to SiPM channel, cell size and arrival time threshold.

Figure 5.4 shows the photon impact distribution as well as the associated arrival time ($t_{arrival}$). In this example, we set a total of 9 SiPM channels (red boxes) with 50 μm × 50 μm cell size, 0.1 mm of dead space between channels (blank space between one channel and the neighbor), as depicted in figure 5.4b, and 1 nanosecond threshold on the arrival time. The scintillator crystal is a LYSO of 4 mm × 4 mm × 10 mm and the SiPM employed is the S14160-4050HS from Hamamatsu at 5 V of over-voltage. The output file will contain the remaining photons after all the pruning process. Additionally, the intrinsic t_{SPTR} is

added right after the pruning. In this stage, a random timestamp generated by a Gaussian distribution is summed to the actual arrival time of the photon. The sigma of this Gaussian is directly the intrinsic SPTR of the modeled SiPM sensor. Thus, the contribution of the t_{SPTR} can be obtained using the following expression:

$$t_{SPTR} = \frac{1}{\sigma_{SPTR}\sqrt{2\pi}} exp\left[-\frac{t^2}{2\sigma_{SPTR}^2}\right] \tag{5.3}$$

For instance, the SiPM S14160-4050HS has a SPTR of 50 ps [18] in sigma. Combining the associated arrival time with the contribution of the SPTR, gives a final timestamp defined as:

$$timestamp_{final} = t_{arrival} + t_{SPTR} \tag{5.4}$$

The final timestamp of the selected photons is used as input in the electrical simulator to emulate the response of the SiPM [22]. Next section shows how the time information from the optical simulation is combined with the electrical response of the front-electronics.

5.2.2 SiPM signal generation

The SiPM is a semiconductor photodiode build of many Single Photon Avalanche Detectors (SPADs) or microcells joint together on silicon substrate with common load. Typically, in SiPMs, the microcells are of identical size and arranged in a rectangular pattern. Depending on the device, the size of a microcell varies from 10 μm to 100 μm and the number of microcells per device ranges from several hundreds to several tens of thousands, depending on the active area. The SiPM schematic circuit is modeled in the electronic simulator following the model detailed in [23]. A equivalent circuit of the SiPM electrical model can be seen in figure 5.5 [24].

Regarding the electrical simulation using this equivalent circuit, in this work we used Cadence Design environment with the Spectre simulator [19]. This toolkit enables the possibility to simulate the electrical response of the SiPM in combination with the arrival time of the photons and a dedicated Front-End electronics for its signal processing. Nonetheless, any other electrical simulators capable of introducing transient noise on the time domain could be adapted to work with the same input file.

The equivalent SiPM electrical circuit simulating the discharge of the cells works as follows. Before any photon detection, the switch S_A is opened and the detector capacitance (C_d) is charged to the SiPM bias voltage (V_{bias}) applied between the anode and cathode. When a photon arrives to the SiPM (using the timestamp of each photon from GATE's output file), this switch closes making the start of a breakdown event (N_f corresponds to the number of cells fired). We can control S_A closing time through a veriloga code that closes it as a function of the photon arrival time. At this moment, the avalanche begins, C_d capacitance discharges through R_d ($R_d << R_q$) with the rising time constant $R_d(C_d + C_q)$. The discharge is stopped

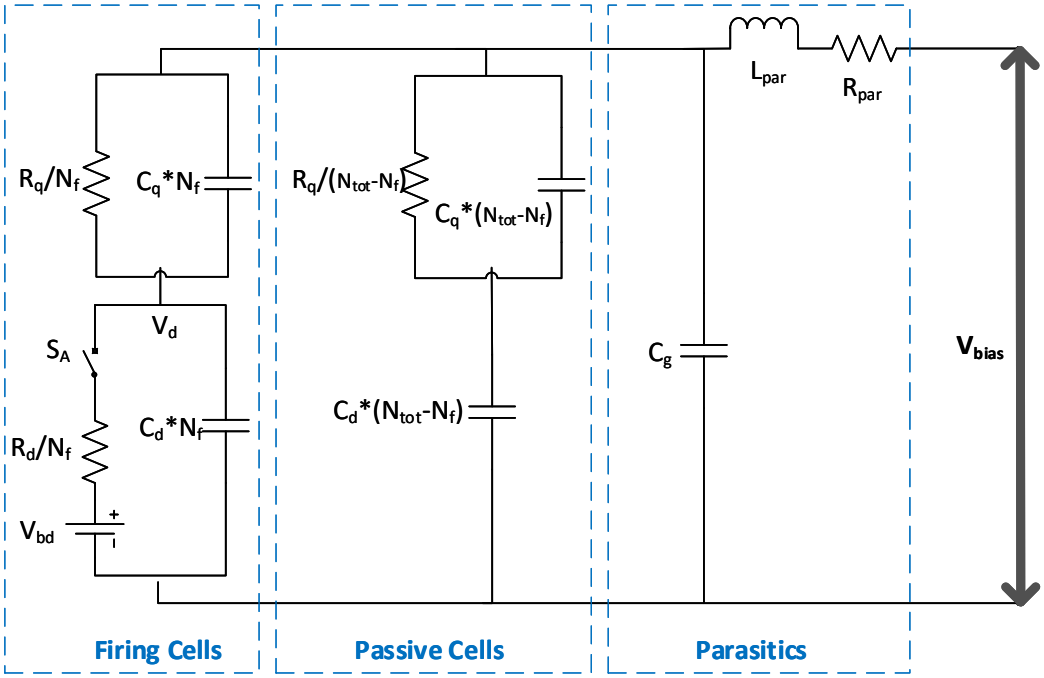

Figure 5.5.: Schematic representation of the SiPM model.

when the voltage across V_{bd} and R_d drops below a predefined threshold quenching current I_q[23] and thus quenching the avalanche. The external polysilicon resistor (R_q) decouples electrically each cell and limits the current drawn by the diode during breakdown.

Once the avalanche is quenched and switch S_A is opened, V_{bias} recharges C_d with an exponential process with two time constants [24, 25]. The first time constant is attributed to the fast supply path across C_d and the capacitive coupling through the parasitic quenching capacitance C_q with a fast time constant of $R_{load}C_{tot}$, where the overall capacitance C_{tot} is $C_g + N_{tot}(C_d + C_q)$ and the R_{load} is associated to the input impedance of the FE electronics. The second time constant, the slow component, is due to the exponentially decreasing recharge current flowing through the quenching resistor R_q. The slow component, known as the SiPM recovery time constant since dominates the tail of the response, is determined by $R_q(C_d + C_q)$ and it is in the order of tens to hundreds of nanoseconds. Recharge of the SiPM ends when V_D reaches V_{bias}.

The intrinsic parameters of the SiPM are extracted using the following procedure. Experimentally each sensor is tested using a large bandwidth and low noise pre-amplifier (PACTA pre-amplifier [26]) to better capture the response of the SiPM. In this scenario, a picosecond pulsed laser (PiLas Picosecond Diode Laser at 405 nm, 30 ps pulse width) sends a photon pulse to the SiPM through a single mode fiber and a Liquid Crystal Optical Beam Attenuator from Thorlabs. The optical photons are then converted into an small electrical current by the SiPM and the pulse is amplified by the PACTA chips, which is then recorded by an Agilent MSO9404A Mixed Signal oscilloscope 4 GHz (20 Gsa/s). An extended explanation on how to characterize a photodetector can be found in [27], while figure 5.6 illustrates the setup involved during the waveform acquisition.

$C_d + C_q$ was determined via the SiPM gain. Additionally, the signal shape of the first photon is acquired. Lastly, the R_q is obtained via the forward I-V characteristic curve. Then, using the SiPM (figure 5.5) and the PACTA electrical model with RC parasitics on the simulation environment (Cadence [19]), we can adjust the other parameters (R_d, C_d, C_q and C_g) by matching the simulated response with the pulse shape acquired in the measurements. In this process, the values for R_q and $C_d + C_q$ are taken from the previous characterization. Besides of adjusting the shape of the real data and the signal from the simulation, the SiPM gain in equation 5.5 must be as close as possible in order to guarantee an accurate simulation model to extract the parameters of the SiPM.

$$SiPM_{gain} = \frac{Q}{q} \tag{5.5}$$

where is Q the total charge from the single photon response and q is the electron charge.

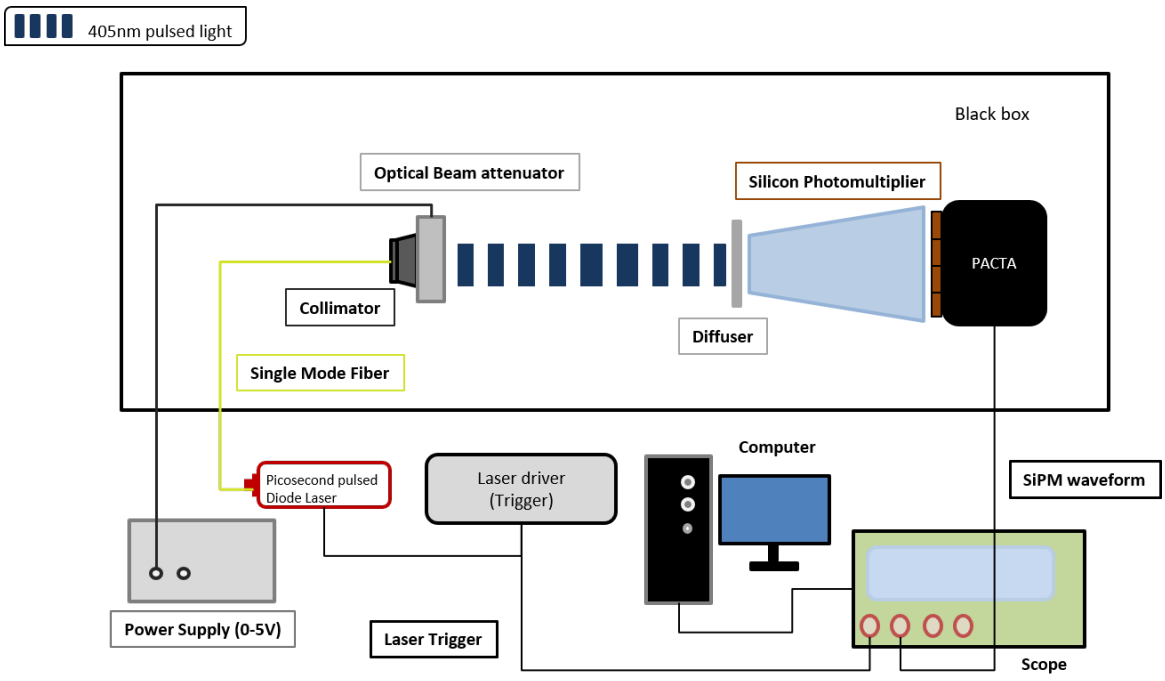

Figure 5.6.: Characterization setup using a picosecond pulsed laser.

An example of the resultant SiPM voltage waveform generated from 1 cell fired along with the simulated model can be seen in figure 5.7. Having a good and reliable model of all those parameters is critical for the time resolution optimization of the system. Note that the correlated and non-correlated noise, those including dark counts (DCR), crosstalk and afterpulsing, are not taken into account in this work. Future updates on the simulation framework will implement both of them.

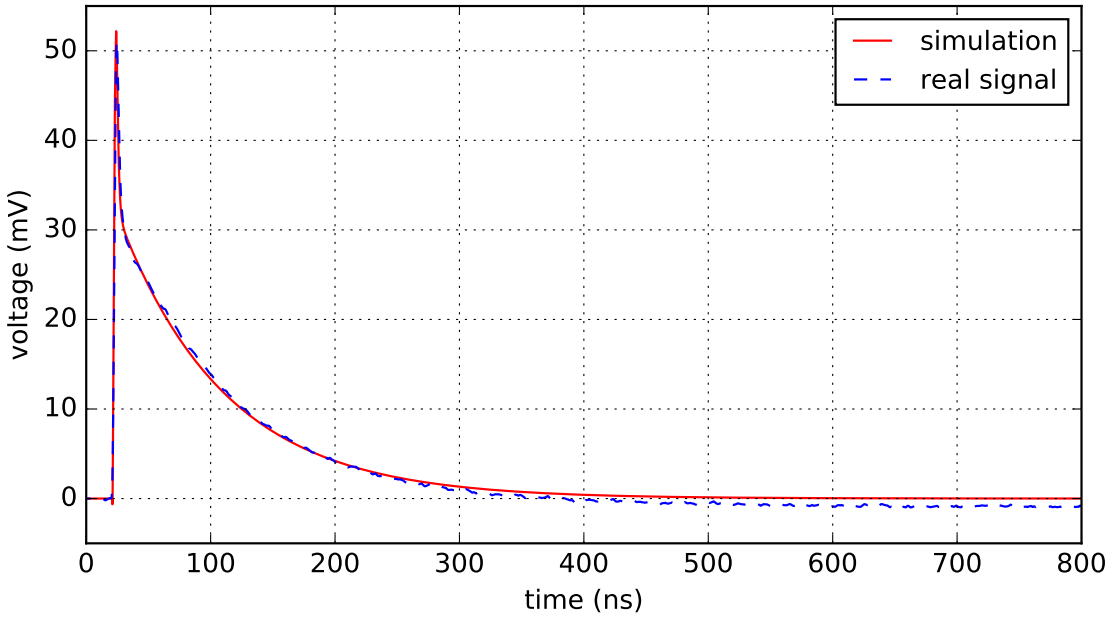

Figure 5.7.: SiPM signal waveform comparison between the simulated model and the real output for 1 fired cell acquired in the test bench using a FBK NUV-HD model of 4 mm × 4 mm readout by the PACTA preamplifier chip.

5.2.3 FE electronics

The output of the SiPM can be connected to a FE readout circuit to evaluate the time response of the overall system (scintillator, sensor and electronics). This framework can be employed with the complete FE electronics, part of it affecting to the time response or even with a simplified equivalent circuit of the readout electronics. Figure 5.8 shows a parameterized FE circuit which enables the possibility to study the impact on time resolution using a simplified model. In this case, a current sensing FE model has been employed, but a similar FE structure can be used for a voltage sensing. This FE has the following parameters: an input impedance represented as R_{in}, an equivalent input series noise voltage (e_n) and an equivalent input parallel noise voltage (i_n) as the two noise sources present on the FE. The parasitic inductance between the SiPM and the FE is represented by L_{par}. Additionally, the parameters R_{BW} and C_{BW} are related to the bandwidth limitation of the system by the following equation:

$$BW = \frac{1}{2\pi C_{BW} R_{BW}} \tag{5.6}$$

This simplified model that emulates the response of the readout circuit, enables to study different configurations of the FE electronics depending on the sensor employed. The simplified circuit makes the electrical simulation much faster than employing a full FE chips and thus different crystals, sensors and internal parameters can be optimized. Lastly, the time uncertainty introduced by the electronics is simulated with Cadence Design by

performing a transient noise simulation [28]. This analysis considers the noise sources of the electrical circuit and performs a simulation in the time domain to emulate the response of the complete system. Therefore, the time uncertainty or the jitter component of the electronics can be also taken into account in the overall response of the system.

Concluding, this framework permits to find an optimal configuration of the FE electronics for a given sensor (with its respective internal parameters). Moreover, it also permits to study the impact on changing some parameters of the sensor, such as C_q or R_q, on the timing response of the overall system.

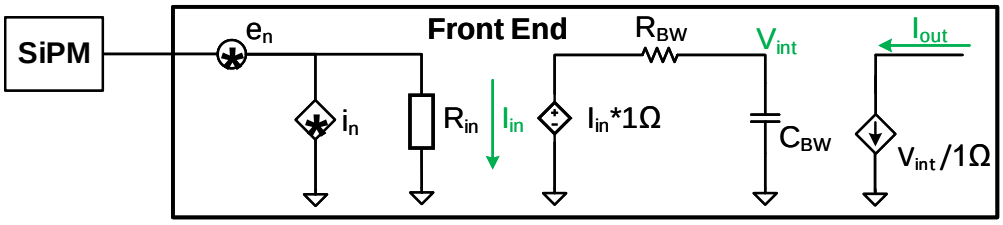

Figure 5.8.: Front end schematic representation used in the electrical simulator.

5.2.4 Framework validation

To have a broad overview of the framework, a general explanation on how it works can be read as follows: first, each SiPM channel generates an analog signal according to the number of photons and arrival time described in GATE's output file and the impulse response (single photon signal) obtained as described in subsections 5.2.1 and 5.2.2. Then, each signal is processed by a specific FE readout. This FE is basically composed by a pre-amplifier analog readout circuit to capture the response of the sensor and a discriminator, e.g., a leading-edge comparator, to provide the arrival time of the photons. Lastly, a transient noise simulation is performed to emulate the response of complete system. Note that the CTR is obtained as the standard deviation of the cumulative delay distribution from the time response of the two detectors. In brief, this electrical simulator allows to generate and process the signal from the SiPM in combination with the arrival time information from the photons simulated in GATE. Or in other words, this framework comprehends the whole physics involved in the fast timing optimization for PET application.

We compared real CTR data from a well-known setup and the simulation results obtained from the new GATE + Cadence environment. This setup was composed by: Lutetium Fine Silicate (LFS) scintillator crystals of 3 mm × 3 mm × 20 mm size, coupled to the SiPM of 3mm × 3mm and 50 μm × 50 μm micro-cell size, readout by a real FE electronics from an ASIC named HRFlexToT described in [29]. This ASIC provides the arrival time of the photons by using a low input impedance current conveyor and a leading-edge discriminator. Thus, we compared simulation results obtained using the framework with the HRFlexToT circuit with respect to direct measurements employing the same ASIC.

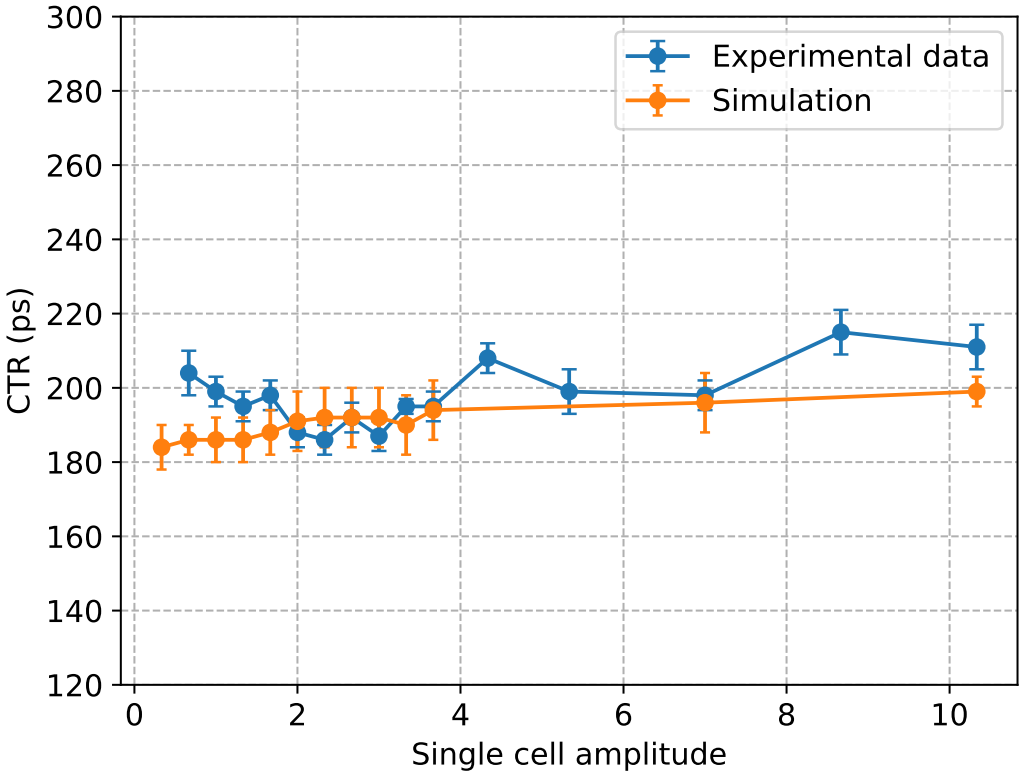

Figure 5.9.: Simulation results and laboratory measurements comparison. CTR in FWHM.

Figures 5.9 shows good agreement with the laboratory measurements. The trend of the CTR values as a function of the threshold are close between the simulated and experimental results, besides the first data points (0-2 firing cells), because of the intrinsic DCR noise which is not being simulated in the current scenario as previously mentioned. This result gives a trusting simulation tool to proceed with further and more complex scenarios, as shown in the next sections.

5.3 SiPM segmentation approach

SiPM suffers various inconveniences when increasing the area of the detector. The main effect comes from the intrinsic capacitance (equivalent capacitance at high frequency of a single cell [22, 24, 30]), which is a few orders of magnitude larger compared to the capacitance of a PMT, and additionally, it scales with the active area. This increase of the capacitance with the area changes the rising time of the SiPM electrical signal as the peak amplitude is proportional to C^{-1} [25]. Hence, a large SiPM also implies that the slew rate (SR) decreases with respect to a smaller SiPM (figure 5.10), thus worsening the timing properties on "fast" applications such as ToF-PET. Equation 5.7) details how the jitter or SPTR is being affected by the SR and the integrated output noise (σ_n).

$$\sigma_{telec.} = \frac{\sigma_n}{SR} = \frac{\sigma_n}{\partial I_{o1p}/\partial t} \tag{5.7}$$

∂I_{o1p} corresponds to the output current for the signal of 1 photon (1 cell fired).

Front End electronics coupled to large area SiPMs presents smaller slew rate and higher output noise, making $\sigma_{telec.}$ increase and therefore, degrading the time performance [31]. Nevertheless, the cumulative charge of the signal is constant with the capacitance but, as the capacitance increases, the integration time needed to recover the same charge is also larger and thus reducing the SNR.

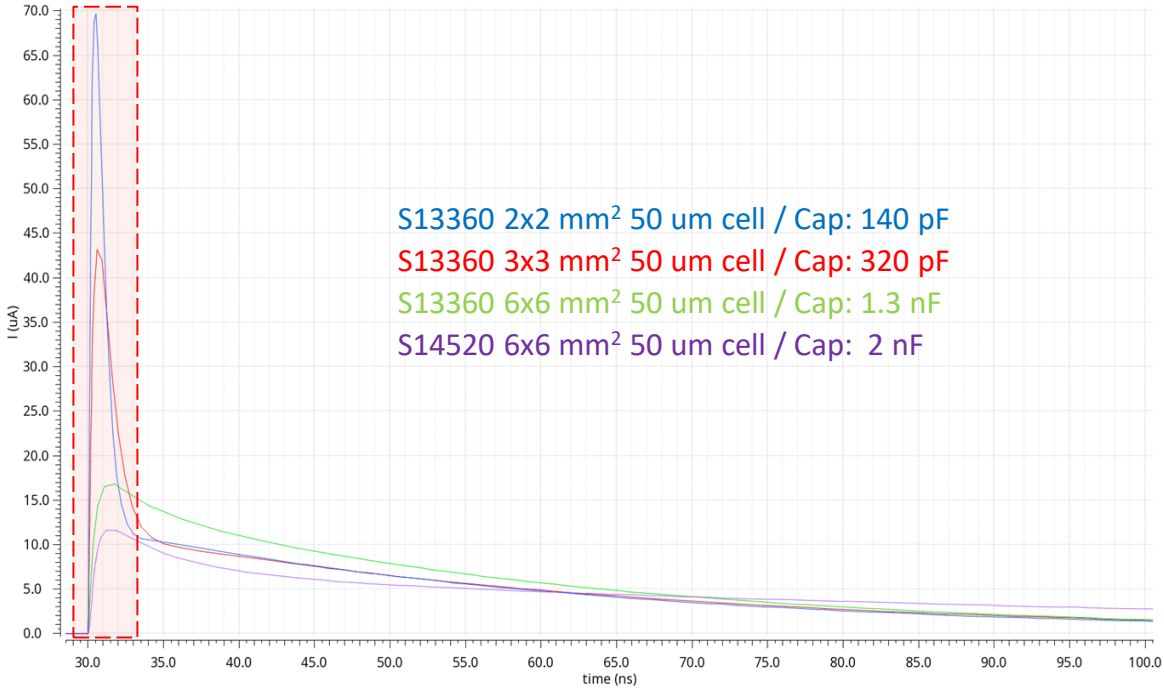

Figure 5.10.: Simulated single cell signal for different SiPM area. Observe the red region (beginning of the signal) where the peak amplitude and the SR of the signal increases when the capacitance decreases.

Segmenting a large area sensor into "m" smaller ones will help dealing with the problem of high intrinsic capacitance (at expense of increasing the power consumption). Hence, we would take advantage of the increase in slew rate of a small area SiPM and then, all analog signals will be summed up to recover the single signal output covering the same area. Figure 5.11 shows the schematic representation of the SiPM of area A divided in 4 smaller SiPMs with individual area of $A/4$, which implies 4 times smaller capacitance. The analog signal of each small sensor is read out by a dedicated FE circuit and then summed, i.e., using an ideal summation for this study. Finally, using a leading-edge comparator, in this case an ideal ToT, the time of arrival is obtained.

On one side, previous work from S. Deker, et. al. [32] studied the CTR performance of a 6 mm × 6 mm × 20 mm readout by 3 levels of SiPM segmentation: 1 SiPM of 6 mm × 6 mm, 4 SiPMs of 3 mm × 3 mm and 9 SiPMs of 2 mm × 2 mm. In each case, the individual sensor was readout by a NINO ASIC channel [33]. If more than one channel were used, the

timestamp of each channel was combined using weighted average methods and applying time walk and time skew corrections, similar to what is traditionally done in monolithic crystals. In this case, besides the improvement in noise achieved due to the smaller detector capacitance, the amount of photons detected in each channel is lower, which means a lower slew rate, and therefore the benefit of segmenting is lost and CTR is not improved.

On the other side, the segmentation approach can benefit for this reduction in detector capacitance if an active summation scheme inside the ASIC is performed in order to recover the signal spread over the different channels and improve the Slew Rate due to segmentation and therefore improve the CTR.

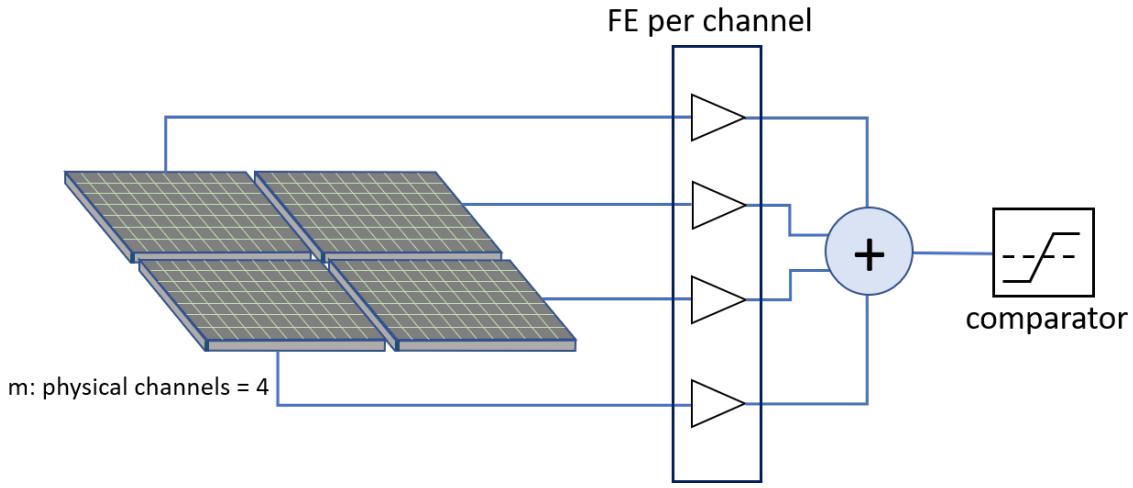

Figure 5.11.: Segmentation and analog summation scheme.

We assume that a large sensor can be divided into m smaller detectors, which implies that

$$C_{large} = m \cdot C_{small} \tag{5.8}$$

in this situation, if series noise dominates, the total noise becomes proportional to $\sqrt{C}$ [22], which is the typical scenario for SiPMs with capacitances in the order of at least tens of pF. Thus, the total noise of $\sigma_{n,large}$ becomes

$$\sigma_{n,large} \sim \sqrt{m} \cdot \sigma_{n,small} \tag{5.9}$$

then, if we sum m small detectors instead of the large one

$$\sigma_{n,m \cdot small} \sim \sqrt{m} \cdot \sigma_{n,small} \tag{5.10}$$

then, considering equations 5.9 and 5.10

$$\sigma_{n,large} \sim \sigma_{n,m \cdot small} \tag{5.11}$$

this means that the noise contribution of a large detector is approximately the same as the noise provided by the sum of m small detectors, assuming that series noise dominates and the impedance $Z_{DET} >> Z_{in}$.

The peak voltage (amplitude) generated by the SIPM is directly related to the capacitance of the detector and increases approximately with C^{-1}. The response of the SiPM can be approximated as the sum of two exponential signals with time constants $\tau_{fast} = R_{load}C_{tot}$ and $\tau_{slow} = R_q(C_d + C_q)$ following the expression [25]

$$V(t) \sim \frac{QR_{load}}{C_d + C_q}\left(\frac{C_q}{\tau_{fast}}e^{\frac{-t}{\tau_{fast}}} + \frac{C_d}{\tau_{slow}}e^{\frac{-t}{\tau_{slow}}}\right) \tag{5.12}$$

where the total charge released in the cell is $Q = V_{ov}(C_d + C_q)$. This expression is valid for low input impedance FE electronics if that R_{load} is much smaller than the R_q [25]. The peak voltage is produced when the avalanche is quenched at instant t=0 and thus

$$V_{peak} \sim R_{load}\left(\frac{Q_{fast}}{\tau_{fast}} + \frac{Q_{slow}}{\tau_{slow}}\right) \tag{5.13}$$

where the charge of the fast component is $Q_{fast} = Q\ C_q/(C_d + C_q)$ and the charge of the slow component is $Q_{slow} = Q\ C_d/(C_d + C_q)$. Equation 5.13 shows that the peak voltage is produced by the slow component which depends mainly on the intrinsic parameters of the SiPM (R_q, C_d and C_q), which are independent on the total area or number of micro-cells of the SiPM and the fast component which is inversely proportional to C_{tot}^{-1}. Considering that the fast time constant is normally much more smaller than the slow time constant and thus the charge produced by the fast component of the SiPM dominates, we can approximate the (V_{peak}) as:

$$V_{peak} \sim R_{load}\left(\frac{Q_{fast}}{\tau_{fast}}\right) \sim V_{ov}\left(\frac{C_q}{C_{tot}}\right) \tag{5.14}$$

Thus, we can conclude that the peak voltage is approximately inversely proportional to the overall capacitance of the cell and it is determined by the different number of micro-cells that forms the detector, i.e., the total capacitance. Then, considering the SiPM divided into m smaller detectors (same C_q but m times smaller C_{tot}), as detailed in equation 5.8, the peak voltage of an small detector would be

$$V_{peak,m\ \cdot\ small} \sim m\ \cdot\ V_{peak,large} \tag{5.15}$$

Therefore, a potential reduction of $t_{elec.}$ by a factor up to m ($m = 4$ for the case depicted in figure 5.11) can be achieved using the segmentation method approach. In practice, even if the series noise is dominating over the parallel noise, the reduction factor will be $m < 4$ as parallel noise is not negligible. It is important to highlight that this SPTR improvement requires a large bandwidth and low noise FE electronics to handle the fast response of the smaller sensor and not lose the benefit of segmentation.

5.4 Results on electronics jitter using segmentation

Using this new framework, we performed a transient noise simulation with Cadence Design using the test bench described in figure 5.11. The sigma from the electronics jitter (σ_{telec}) is obtained as the standard deviation of the arrival time of the first photon (photons are fired ideally at a given t0, but transient noise generates variations on the waveform, thus giving different arrival times as a result). The following simulations employ parts of the circuits of the HRFlexToT ASIC involved in the time response (pre-amplifier and discriminator) and a summation circuit based on a current mirror.

The FE parameters used in the following simulations are taken from the HRFlexToT ASIC.

Figure 5.12 shows the σ_{telec} of the analog summation for different current thresholds at the comparator to determine the arrival time of the photon. In this particular simulation, the SiPM has a 50 μm $\times$ 50 μm cell size with intrinsic capacitance of 90 fF per cell and quenching resistance of 300 kΩ. Depending on the number of cells, the total capacitance of the devices varies between 36 pF and 324 pF for the 1 mm $\times$ 1 mm and 3 mm $\times$ 3 mm SiPM channel respectively, covering a total area of 3 mm $\times$ 3 mm. Note that the response of each SiPM has a different slew rate, noise figure and peak amplitude, hence changing the optimal threshold.

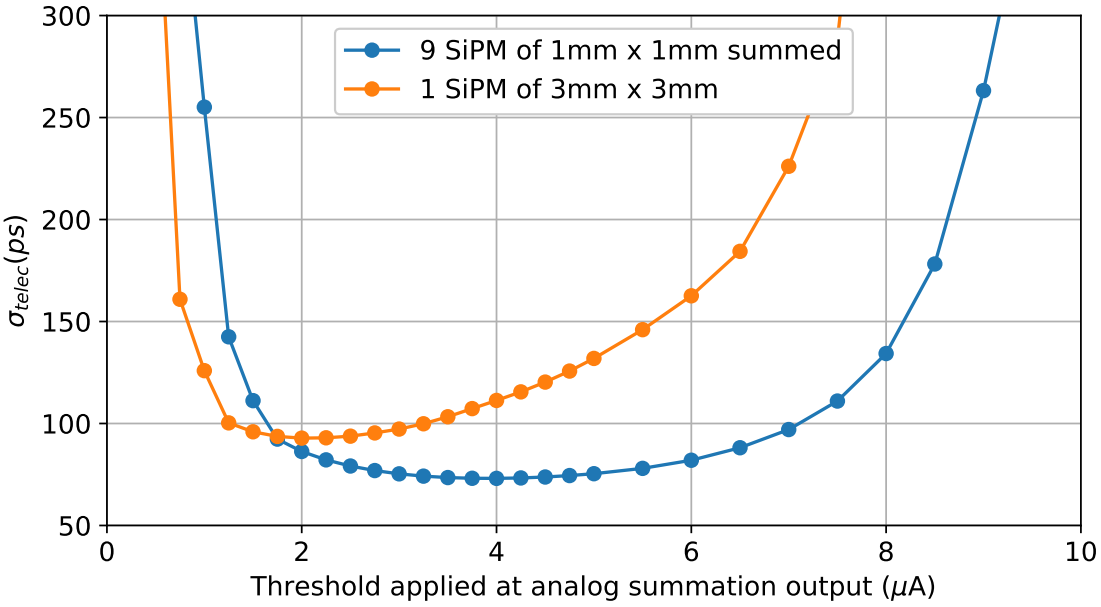

Figure 5.12.: Standard deviation comparison between single channel and segmentation. Total detection area equal to 9 mm^2.

The framework is used to simulate larger detection areas involving a higher number of channels and adding the 6 mm $\times$ 6 mm SiPM sensor, with total capacitance of almost 1.3 nF. Table 5.1 illustrates the benefits of adding small SiPMs to cover a large detection area

instead of using a large sensor with a larger capacitance. Small SiPMs present a larger peak amplitude and lower capacitance and therefore a better SNR. Moreover, they can benefit for its larger slew rate that provides a better time response. On the contrary, small SiPMs require a smart readout electronics to sum the signals from different SiPMs and thereby cover the same detection area of a large SiPM. This can lead to an increment on power consumption and complexity on the FE development.

Table 5.1.: σ_{telec} comparison between different combinations of SiPMs with different detection areas. Micro-cell area of each sensor is the same.

SiPM ch. $[mm^2]$	1×1	3×3	1×1	3×3	3×3	6×6
num. of channels	9	1	18	2	4	1
det. area $[mm^2]$	9	9	18	18	36	36
σ_{telec} [ps]	79.1	92.9	100.1	139.2	224.3	378.7

From the above table we can see an improvement between 15% to 60%, depending on the detection area and segmentation, for the first photon time jitter. These results shows a solid prove of concept that the time resolution can be improved by using segmentation on large area SiPMs. Next section provides a detailed study on the impact of segmentation in the CTR.

5.5 Results on CTR using segmentation

A detailed study on CTR performance using the framework was done by simulating different SiPM sizes covering a given area. In the subsequent test cases, the electronics will be modeled using the equivalent FE circuit detailed in 5.8. The FE values regarding parallel and series noise are chosen based on the HRFlexToT performance, 10 $pA/\sqrt{Hz}$ and 1.5 $nV/\sqrt{Hz}$ respectively. Input resistance is set to 15 Ω and the bandwidth of the FE is set to 1 Ghz. The crystal is coupled to the SiPM using the thermoplastic Meltmount 1582 as optical coupler with a refraction index of 1.582. Lastly, we introduce a 0.1 mm dead spaces in all matrix distributions.

The first setup is composed by a LYSO crystal of 25 mm $\times$ 25 mm $\times$ 20 mm with all faces black painted except the one coupled to the photo-sensor. We evaluated four array configurations and their impact on timing performance. Different number of channels and same micro-cell size of 50 μm $\times$ 50 μm in all cases. In this case, only the FE electronics and an ideal leading-edge comparator has been used, i.e., analog summation is not applied, in order to be able to compare the simulation with experimental results using the 16 channels HRFlexToT ASIC (it does not have a summation circuit). In this case, the CTR is computed taking the pickup time from the fastest channel.

For the 6 mm $\times$ 6 mm SiPM size we have experimentally measured the CTR of the system using the 16 channels HRFlexToT readout. A CTR of 700 ps was obtained, indicating a small discrepancy with the simulation mainly due to the employment of the equivalent FE

Table 5.2.: CTR comparison between different combinations of SiPMs sizes with a 25 mm × 25 mm × 20 mm LYSO scintillator monolithic crystal.

SiPM ch. [mm^2]	1.5 × 1.5	2 × 2	3 × 3	6 × 6
num. of channels	256	144	64	16
det. area [mm^2]	625	625	625	625
CTR [ps]	430	419	465	642

circuit. We can observe that the smaller the SiPM channel, the better the CTR value, except for the smallest one where the CTR shows a degradation. One possible reason for that could be an increment on the parallel noise, which implies that our previous hypothesis of series noise domination (detailed in 5.3) might not be longer valid. Another reason could be that the number of collected photons by an smaller detection area is lower and thus losing slew rate. This second reason implies that a summation scheme is needed to recover the signal (the collected photons) across several channels to avoid losing slew rate.

The next setup targets a better CTR using smaller crystals (less TTS) and teflon wrapping in order to collect as much light as possible during the photon-conversion. In ToF-PET scanners, one of the biggest contributions to the CTR worsening came from the scintillator crystal, as the travel time spread and the uncertainty on the depth of interaction for the gamma ray increases as a function of the crystal length. For this reason, this study case consists on a 4 mm × 4 mm × Z mm LYSO crystal teflon wrapped using Davis surface model coupled to a SiPM array of the same section and differently segmented. This Z variable corresponds to the length of the crystal and we simulated four different cases, 5 mm, 10 mm, 15 mm, and 20 mm.

A CTR study for all four crystal lengths and a S14160-4050CS SiPM without segmentation and dividing it in a 2 × 2 array, where all four outputs are summed and the single resulting output is calculated as depicted in figure 5.11. The final CTR plot versus the crystal length can be seen in figure 5.13. It shows the degradation of the CTR with respect to the crystal length and the improvement in terms of CTR by segmenting the sensor. Hence, a CTR below 100 ps would be only possible using LYSO crystals for lengths lower than 10 mm.

Table 5.3 shows more clearly how segmenting a large single SiPM can improve the CTR performance of the detector. We simulated three levels of segmentation: no-segmentation with a single SiPM of 4 mm × 4 mm. An array of 2 × 2 SiPMs of approximately 2 mm × 2 mm each. And a smaller channel of 1.3 mm × 1.3 mm in a 3 × 3 array distribution. The LYSO crystal size is set to 4 mm × 4 mm × 10 mm.

In this case, the CTR can be improved up to a 15% by implementing the segmentation technique. Observe that the intrinsic limit of the system is around 85 ps of CTR assuming perfect photon collection efficiency (PDE 100%) and no electronic noise, i.e., considering only the jitter from the optics (scintillator and SiPM). At a high segmentation value, the summation scheme allows for a further reduction in terms of CTR. Although, this improvement is becoming smaller due to fact that the parallel noise is starting to be more significant for lower capacitances of the sensor [22]. At this point, further studies of the FE parameters considering also bandwidth, power consumption, larger segmentation and the

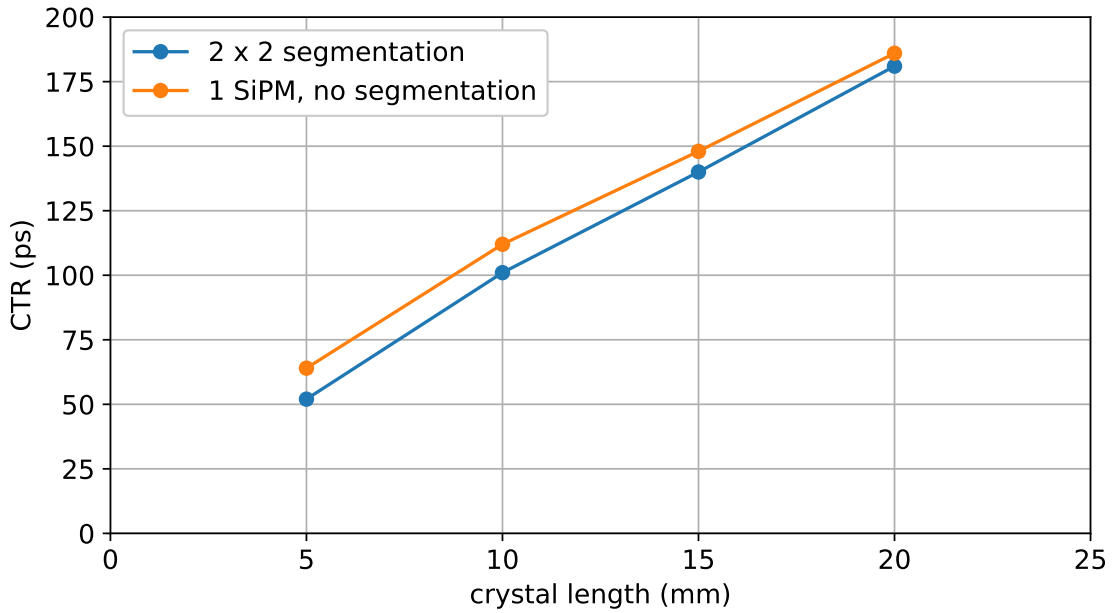

Figure 5.13.: Crystal length impact on the CTR performance plus comparison between 1 large SiPM (S14160-4050CS) and segmenting it into a 2×2 array.

Table 5.3.: Segmentation impact on CTR performance with a 10 mm long LYSO crystal and different segmentation factor of a S14160-4050CS SiPM. Ideal sensor corresponds to 100% on PDE, considering only the jitter from the optics (scintillator and SiPM SPTR).

SiPM ch. $[mm^2]$	4×4	2×2	1.3×1.3	Ideal
num. of channels	1	4	9	1
det. area $[mm^2]$	4	4	4	4
CTR [ps]	112	101	97	85

implementation of the FE electronics at transistor level with different topologies are planned for the near future.

5.6 Conclusions and future research

We provide a new design framework that will enable a global optimization of the PET system that considers the scintillator, the sensor (sensor size, pixel pitch, dead area, capacitance) and the readout electronics (input impedance, noise, bandwidth, summation). This framework gives the possibility to choose the best sensor considering both the light generation and transport employing GATE and the readout response using an electrical simulator. Furthermore, the framework enables a comprehensive optimization of sensor and front end, considering a segmentation of the sensor which allows potential optimization of the overall CTR.

Simulation results showed that the segmentation technique might allow a potential reduction of the CTR achieving resolutions at the order of 100 ps with small crystals. Although, it is clear that to go below 50 ps new scintillators coupled to fast efficient electronics will be mandatory. Future work will include the implementation of uncorrelated (DCR) and correlated (afterpulsing and crosstalk) noise at the sensor level. Implementation of efficient FE electronics at transistor level applying the segmentation technique. Moreover, exploration of new geometries and scintillator materials are planned. All these new features, will studied using the here presented simulation framework.

5.7 Bibliography

[1] E. Garutti, Silicon photomultipliers for high energy physics detectors, Journal of Instrumentation 6 (10) (2011). arXiv:1108.3166, doi:10.1088/1748-0221/6/10/C10003.

[2] N. Otte, B. Dolgoshein, J. Hose, S. Klemin, E. Lorenz, R. Mirzoyan, E. Popova, M. Teshima, The potential of SiPM as photon detector in astroparticle physics experiments like MAGIC and EUSO, Nuclear Physics B - Proceedings Supplements 150 (1-3) (2006) 144–149. doi:10.1016/j.nuclphysbps.2004.10.084.

[3] H. Miyamoto, M. Teshima, SiPM development for the imaging Cherenkov and fluorescence telescopes, Nuclear Instruments and Methods in Physics Research, Section A: Accelerators, Spectrometers, Detectors and Associated Equipment 623 (1) (2010) 198–200. doi:10.1016/j.nima.2010.02.194.
URL http://dx.doi.org/10.1016/j.nima.2010.02.194

[4] S. Korpar, R. Dolenec, P. Križan, R. Pestotnik, A. Stanovnik, Study of TOF PET using Cherenkov light, Nuclear Instruments and Methods in Physics Research, Section A: Accelerators, Spectrometers, Detectors and Associated Equipment 654 (1) (2011) 532–538. doi:10.1016/j.nima.2011.06.035.

[5] A. T. Fienberg, L. P. Alonzi, A. Anastasi, R. Bjorkquist, D. Cauz, R. Fatemi, C. Ferrari, A. Fioretti, A. Fankenthal, C. Gabbanini, L. K. Gibbons, K. Giovanetti, S. D. Goadhouse, W. P. Gohn, T. P. Gorringe, D. W. Hertzog, M. Iacovacci, P. Kammel, J. Kaspar, B. Kiburg, L. Li, S. Mastroianni, G. Pauletta, D. A. Peterson, D. Počanić, M. W. Smith, D. A. Sweigart, V. Tishchenko, G. Venanzoni, T. D. Van Wechel, K. B. Wall, P. Winter, K. Yai, Studies of an array of PbF2 Cherenkov crystals with large-area SiPM readout, Nuclear Instruments and Methods in Physics Research, Section A: Accelerators, Spectrometers, Detectors and Associated Equipment 783 (2015) 12–21. doi:10.1016/j.nima.2015.02.028.

[6] C. Perrina, The future of the high energy cosmic ray detection: HERD, EPJ Web of Conferences 209 (201 9) (2019) 1040. doi:10.1051/epjconf/201920901040.

[7] R. Agishev, A. Comerón, J. Bach, A. Rodriguez, M. Sicard, J. Riu, S. Royo, Lidar with SiPM: Some capabilities and limitations in real environment, Optics and Laser Technology 49 (2013) 86–90. doi:10.1016/j.optlastec.2012.12.024.

[8] G. Adamo, A. Busacca, Time of Flight measurements via two LiDAR systems with SiPM and APD, AEIT 2016 - International Annual Conference: Sustainable Development in the Mediterranean Area, Energy and ICT Networks of the Future (2016). doi:10.23919/AEIT.2016.7892802.

[9] T. Jones, D. Townsend, History and future technical innovation in positron emission tomography, Journal of Medical Imaging 4 (1) (2017) 011013. doi:10.1117/1.jmi.4.1.011013.

[10] S. Surti, Update on time-of-flight PET imaging, Journal of Nuclear Medicine 56 (1) (2015) 98–105. doi:10.2967/jnumed.114.145029.

[11] J. Van Sluis, J. De Jong, J. Schaar, W. Noordzij, P. Van Snick, R. Dierckx, R. Borra, A. Willemsen, R. Boellaard, Performance characteristics of the digital biograph vision PET/CT system, Journal of Nuclear Medicine 60 (7) (2019) 1031–1036. doi:10.2967/jnumed.118.215418.

[12] R. D. Badawi, H. Shi, P. Hu, S. Chen, T. Xu, P. M. Price, Y. Ding, B. A. Spencer, L. Nardo, W. Liu, J. Bao, T. Jones, H. Li, S. R. Cherry, First human imaging studies with the explorer total-body PET scanner, Journal of Nuclear Medicine 60 (3) (2019) 299–303. doi:10.2967/jnumed.119.226498.

[13] S. Gundacker, E. Auffray, K. Pauwels, P. Lecoq, Measurement of intrinsic rise times for various L(Y)SO and LuAG scintillators with a general study of prompt photons to achieve 10 ps in TOF-PET, Physics in Medicine and Biology 61 (7) (2016) 2802–2837. doi:10.1088/0031-9155/61/7/2802.

[14] J. J. Vaquero, P. Kinahan, Positron Emission Tomography: Current Challenges and Opportunities for Technological Advances in Clinical and Preclinical Imaging Systems., Annu Rev Biomed Eng. (2015) 385–414.
URL doi:10.1146/annurev-bioeng-071114-040723

[15] M. V. Nemallapudi, S. Gundacker, P. Lecoq, E. Auffray, Single photon time resolution of state of the art SiPMs, Journal of Instrumentation 11 (10) (2016). doi:10.1088/1748-0221/11/10/P10016.

[16] P. Lecoq, Pushing the Limits in Time-of-Flight PET Imaging, IEEE Transactions on Radiation and Plasma Medical Sciences 1 (6) (2017) 473–485. doi:10.1109/TRPMS.2017.2756674.
URL http://ieeexplore.ieee.org/document/8049484/

[17] N. Dinu, Z. Amara, C. Bazin, V. Chaumat, C. Cheikali, G. Guilhem, V. Puill, C. Sylvia, J. F. Vagnucci, Electro-optical characterization of SiPM: A comparative study, Nuclear Instruments and Methods in Physics Research, Section A: Accelerators, Spectrometers, Detectors and Associated Equipment 610 (1) (2009) 423–426. doi:10.1016/j.nima.2009.05.101.
URL http://dx.doi.org/10.1016/j.nima.2009.05.101

[18] S. Gundacker, R. Martinez Turtos, N. Kratochwil, R. H. Pots, M. Paganoni, P. Lecoq, E. Auffray, Experimental time resolution limits of modern SiPMs and TOF-PET detectors exploring different scintillators and Cherenkov emission, Physics in Medicine and Biology 65 (2) (2020). doi:10.1088/1361-6560/ab63b4.

[19] Cadence Design Systems, Inc.
URL https://www.cadence.com

[20] S. Jan, G. Santin, D. Strul, S. Staelens, K. Assié, D. Autret, S. Avner, R. Barbier, M. Bardiès, P. M. Bloomfield, D. Brasse, V. Breton, P. Bruyndonckx, I. Buvat, A. F. Chatziioannou, Y. Choi, Y. H. Chung, C. Comtat, D. Donnarieix, L. Ferrer, S. J. Glick, C. J. Groiselle, D. Guez, P. F. Honore, S. Kerhoas-Cavata, A. S. Kirov, V. Kohli,

M. Koole, M. Krieguer, D. J. van der Laan, F. Lamare, G. Largeron, C. Lartizien, D. Lazaro, M. C. Maas, L. Maigne, F. Mayet, F. Melot, C. Merheb, E. Pennacchio, J. Perez, U. Pietrzyk, F. R. Rannou, M. Rey, D. R. Schaart, C. R. Schmidtlein, L. Simon, T. Y. Song, J. M. Vieira, D. Visvikis, R. Van de Walle, E. Wieërs, C. Morel, GATE: A simulation toolkit for PET and SPECT, Physics in Medicine and Biology 49 (19) (2004) 4543–4561. arXiv:0408109, doi:10.1088/0031-9155/49/19/007.

[21] M. Stockhoff, S. Jan, A. Dubois, S. R. Cherry, E. Roncali, Advanced optical simulation of scintillation detectors in GATE V8.0: First implementation of a reflectance model based on measured data, Physics in Medicine and Biology 62 (12) (2017) L1–L8. doi:10.1088/1361-6560/aa7007.
URL https://doi.org/10.1088/1361-6560/aa7007

[22] J. M. Fernandez-Tenllado, R. Ballabriga, M. Campbell, D. Gascon, S. Gomez, J. Mauricio, Optimal design of single-photon sensor front-end electronics for fast-timing applications, 2019 IEEE Nuclear Science Symposium and Medical Imaging Conference, NSS/MIC 2019 (2019). doi:10.1109/NSS/MIC42101.2019.9059805.

[23] S. Seifert, H. T. Van Dam, J. Huizenga, R. Vinke, P. Dendooven, H. Löhner, D. R. Schaart, Simulation of silicon photomultiplier signals, IEEE Transactions on Nuclear Science 56 (6) (2009) 3726–3733. doi:10.1109/TNS.2009.2030728.

[24] F. Acerbi, S. Gundacker, Understanding and simulating SiPMs, Nuclear Instruments and Methods in Physics Research, Section A: Accelerators, Spectrometers, Detectors and Associated Equipment 926 (September 2018) (2019) 16–35. doi:10.1016/j.nima.2018.11.118.
URL https://doi.org/10.1016/j.nima.2018.11.118

[25] G. Collazuol, The SiPM Physics and Technology - a Review, PhotoDet 2012 (June) (2012) 74.
URL http://indico.cern.ch/event/164917/contribution/72/material/slides/0.pdf

[26] A. Sanuy, D. Gascon, M. Paredes, L. Garrido, M. Ribó, J. Sieiro, Wideband (500 MHz) 16 bit dynamic range current mode PreAmplifier for the CTA cameras (PACTA), Journal of Instrumentation 7 (1) (2012). doi:10.1088/1748-0221/7/01/C01100.

[27] N. Dinu, Instrumentation on silicon detectors : from properties characterization to applications DIRIGER DES RECHERCHES Instrumentation on Silicon Detectors : from properties characterization to applications Nicoleta DINU, Ph.D. thesis (2013).

[28] T. Noulis, CMOS process transient noise simulation analysis and benchmarking, Proceedings - 2016 26th International Workshop on Power and Timing Modeling, Optimization and Simulation, PATMOS 2016 (2017) 70–75doi:10.1109/PATMOS.2016.7833428.

[29] S. Gomez, D. Sanchez, D. Gascon, J. Cela, L. Freixas, R. Graciani, R. Manera, J. Marin, J. Mauricio, J. Navarrete, J. Oller, J. Perez, P. Rato Mendes, A. Sanmukh, O. Vela, A High Dynamic Range ASIC for Time of Flight PET with pixelated and monolithic crystals, in: 2019 IEEE Nuclear Science Symposium and Medical Imaging Conference, NSS/MIC 2019, 2019. doi:10.1109/NSS/MIC42101.2019.9059762.

[30] F. Corsi, C. Marzocca, A. Perrotta, A. Dragone, M. Foresta, A. Del Guerra, S. Marcatili, G. Llosa, G. Collazzuol, G. F. Dalla Betta, N. Dinu, C. Piemonte, G. U. Pignatel, G. Levi, Electrical characterization of silicon photo-multiplier detectors for optimal front-end design, IEEE Nuclear Science Symposium Conference Record 2 (2006) 1276–1280. doi:10.1109/NSSMIC.2006.356076.

[31] P. Buzhan, B. Dolgoshein, L. Filatov, A. Ilyin, V. Kaplin, A. Karakash, S. Klemin, R. Mirzoyan, A. N. Otte, E. Popova, V. Sosnovtsev, M. Teshima, Large area silicon photomultipliers: Performance and applications, Nuclear Instruments and Methods in Physics Research, Section A: Accelerators, Spectrometers, Detectors and Associated Equipment 567 (1 SPEC. ISS.) (2006) 78–82. doi:10.1016/j.nima.2006.05.072.

[32] S. M. Decker, M. Pizzichemi, A. Polesel, M. Paganoni, E. Auffray, S. Gundacker, The Digital-Analog SiPM Approach: A Story of Electronic and Excess Noise, 2019 IEEE Nuclear Science Symposium and Medical Imaging Conference, NSS/MIC 2019 (2019). doi:10.1109/NSS/MIC42101.2019.9059792.

[33] F. Anghinolfi, P. Jarron, A. N. Martemiyanov, E. Usenko, H. Wenninger, M. C. S. Williams, A. Zichichid, NINO: an ultra-fast and low-power front-end amplifier/discriminator ASIC designed for the multigap resistive plate chamber, Nuclear Instruments and Methods in Physics Research Section A: Accelerators, Spectrometers, Detectors and Associated Equipment 533 (2004).
URL https://doi.org/10.1016/j.nima.2004.07.024

6

Industrial PhD conclusions and Future Work

This thesis was focused on the evaluation of the new front-end electronics for SiPM readout developed by our group. It has been proved to be at the state-of-the art technology regarding the usage of both segmented and monolithic scintillator crystals in a ToF-PET module. Furthermore, a novel simulation framework that enables the possibility to study the whole detection chain, from gamma emission to electronic signal generation was created. This section summarizes the main contributions, outlines the publications and conference participation derived from this thesis and provides some interesting future research that will open the way to excellent timing performance.

Contents

6.1 Conclusions

The main goal of this dissertation was to provide a new gamma detector module devoted to TOF-PET scanners composed by a monolithic crystal readout by a SiPM sensor and the FE electronics developed in our group, although it can be used also with a segmented configuration. In the process a simulation framework was also developed to optimize the time resolution of this kind of systems. The main contributions along this thesis were: (1) the best time resolution in terms of SPTR (141 ps FWHM) for a FBK SiPM NUV-HD (4 $\times$ 4 mm^2 pixel, 40 μm cell) compared to other ASICs available in the literature. (2) CTR measurements using segmented and monolithic crystals achieving state-of-the-art results comparing with other ASICs. Thus, including a new time walk calibration method using a pulsed laser system. (3) New framework combining physics and electric simulators in a whole-module optimization environment.

Firstly, a complete evaluation of the HRFlexToT ASIC including electrical and optical characterization was performed in order to assert the capabilities of the ASIC in terms of energy and time resolution. The new redesigned HRFlexToT presents a power consumption reduced from 10 mW/ch to 3.5 mW/ch and better time and energy performance compared to its predecessor. The extended dynamic range on the energy linearity regime allows to work with both segmented and monolithic crystals. The ASIC provides promising performances at the same level or even better compared to other electronics. Segmented crystals were tested at first with CTR results as low as $\approx$117 ps and $\approx$119 ps for crystals (LSO:Ce Ca 0.4%) coupled to a Hamamatsu SiPM S13360-3050CS and FBK SiPM NUV-HD (4 $\times$ 4 mm^2 pixel, 40 μm cell) respectively. These can be translated into $<$2 cm spatial resolution in a real detector system. Although this comes with a relatively low detector efficiency as it decreases with the crystal thickness.

Secondly, the capabilities from the HRFlexToT ASIC reading monolithic crystals were evaluated. Traditionally, this configuration was not used in TOF-PET detectors as the time resolution is not as good as for the segmented approach. However, the spatial resolution and DOI information recovered from the gamma interaction in the monolithic crystal could increase the interest of the PET community on this approach, along with the price reduction in the scintillator crystal manufacturing. Although the timing performance is not optimal, a promising result of 173 ps for a single small LSO:Ce Ca 0.2% monolithic crystal module of 8 mm $\times$ 8 mm $\times$ 5 mm. A module timing of 236 ps was recorded using a medium size LFS crystal of 25 mm $\times$ 25 mm $\times$ 20 mm. All this results were obtained at single module level, a multiplication by $\sqrt{2}$ is needed to obtain the CTR value. Furthermore, a more exhaustive study utilizing a new developed time-walk and time-skew pre-calibration technique was carried out. This includes a pulsed laser with a tunable intensity in order to scan a big range of energies, thus generating a LUT for timestamp correction. Finally, a spatial X-Y spatial resolution of 1.6 mm was reported using a 6 mm $\times$ 6 mm SiPM matrix, and a DOI preliminary measurement of $\sim$4 mm was found.

Thirdly, new design framework which enables a global optimization of the PET system was proposed. It considers the scintillator, the sensor (sensor size, pixel pitch, dead area,

capacitance) and the readout electronics (input impedance, noise, bandwidth, summation). The framework gives the possibility to choose the best sensor considering both the light generation and transport employing GATE and the readout response using an electrical simulator. Furthermore, the framework enables a comprehensive optimization of sensor and front end, considering a segmentation of the sensor which allows potential optimization of the overall CTR. Thereupon, the sensor segmentation approach was studied. The idea of segmenting the sensor in smaller peaces and then applying active summation would allow to improve the time resolution of the system.

6.2 Publications and conference records

The list of contributions are outlined in this section:

1. *Article in Refereed Conference:* J. Trenado, J.M. Cela Ruiz, A. Comerma, D. Gascon, R. Graciani Diaz, L. Freixas, J. Marín, G. Martínez, R. Masachs, J.M. Perez, P. Rato, D. Sanchez, A. Sanuy, I. Sarasola, "Performance of FlexToT Time Based PET Readout ASIC for Depth of Interaction Measurements", In Technology and Instrumentation in Particle Physics, Vol. 213, p. 241, 2014.

2. *Article in Refereed Conference:* J. M. Cela, J. M. Fernández-Varea, L. Freixas, L. Garrido, D. Gascón, R. Graciani, J. Marín, G. Martínez, J. Mauricio, J. C. Oller, J. M. Pérez, P. Rato-Mendes, D. Sánchez, A. Sanuy, I. Sarasola, O. de la Torre, O. Vela, "Performance of the FlexToT v2 ASIC on the readout of different detector designs for PET", In IEEE Nuclear Science Symposium and Medical Imaging Conference (NSS/MIC), pp. 1-2, 2015.

3. *Article in Refereed Conference:* S. Gómez, D. Gascón, G. Fernández, A. Sanuy, J. Mauricio, R. Graciani, D. Sánchez, "MUSIC: An 8 channel readout ASIC for SiPM arrays", In Optical Sensing and Detection IV, Vol. 9899, p. 98990G, International Society for Optics and Photonics, 2016.

4. *Article in Refereed Journal:* I. Sarasola, M.V. Nemallapudi, S. Gundacker, D. Sánchez, D. Gascón, P. Rato, J. Marín, E. Auffray, "A comparative study of the time performance between NINO and FlexToT ASICs", Journal of Instrumentation (JINST), vol. 12, no 04, p. P04016, 2017.

5. *Article in Refereed Workshop:* D. Sánchez, X. Llovet, R. Graciani and F. Salvat, "A tracking algorithm for Monte Carlo simulation of surface roughness in EPMA measurements", In IOP Conf Ser Mater Sci Eng, Vol. 304, p. 012015, January 2018.

6. *Article in Refereed Journal:* J. M. Cela, L. Freixas, J. I. Lagares, J. Marín, G. Martínez, J. Navarrete, J. C. Oller, J. M. Pérez, P. Rato-Mendes , I. Sarasola, O. Vela, J. M. Fernández-Varea, D. Gascón, S. Gómez, R. Graciani, J. Mauricio, D. Sánchez, A. Sanuy, O. de la Torre, and D. Badia, "A Compact Detector Module Design based on FlexToT ASICs for Time-of-Flight PET-MR", IEEE Transactions on Radiation and Plasma Medical Sciences, vol. 2, no 6, p. 549-553, 2018.

7. *Article in Refereed Journal:* P. Carra, M. Bertazzoni, M. G. Bisogni, J. M. Cela Ruiz, A. Del Guerra , D. Gascon, S. Gomez, M. Morrocchi, G. Pazzi, D. Sanchez, I. Sarasola, G. Sportelli , and N. Belcari, "Auto-calibrating TDC for a SoC-FPGA data acquisition system", IEEE Transactions on Radiation and Plasma Medical Sciences, vol. 3, no 5, p. 549-556, 2018.

8. *Article in Refereed Conference:* D. Gascón, D. Sánchez, J. Mauricio, R. Graciani, R. Manera, L. Garrido, J. M. Fernández-Varea, "A High Dynamic Range ASIC for Time of Flight PET with monolithic crystals", In Topical Workshop on Electronics for Particle Physics (TWEPP), Vol. 17, p. 21, 2018.

9. *Article in Refereed Conference:* D. Sánchez, S. Gómez, D. Gascón, L. Garrido, R. Graciani, R. Manera, J. Mauricio, A. Sanmukh, and P. Garcia, "Multimodal Simulation of Large Area Silicon Photomultipliers for Time Resolution Optimization", In IEEE Nuclear Science Symposium and Medical Imaging Conference (NSS/MIC), pp. 1-3, 2019.

10. *Article in Refereed Conference:* S. Gómez, D. Sánchez, D. Gascón, J. M. Cela, L. Freixas, R. Graciani, R. Manera, J. Marín, J. Mauricio, J. J. Navarrete, J. C. Oller, J. M. Pérez, P. Rato Mendes, A. Sanmukh, and O. Vela, "A High Dynamic Range ASIC for Time of Flight PET with pixelated and monolithic crystals", In IEEE Nuclear Science Symposium and Medical Imaging Conference (NSS/MIC), pp. 1-3, 2019.

6.3 Future research

The limits on time resolution has been studied in this thesis, where the crystal, the SiPM and the readout electronics are found as the three elements involved on time degradation. The future research will be focused on each one of these elements limitations as described below:

- The scintillator crystal is the gamma energy converter and therefore, the element that controls the amount of light generated in every detection event. A high stopping power, high LY and fast rise and decay time is needed to achieve the ultimate time resolution performance, i.e. the 10 ps CTR on a TOF-PET system. However, even if this perfect scintillator crystal is somehow developed, there are more physical intrinsic limitations, i.e. the DOI uncertainty, which the geometrical length of the crystal is responsible for. To solve this problem, the monolithic approach is preferred in front of the segmented crystal. In this case, the light sharing pattern among the SiPM matrix allows to identify the 3D impact position of the gamma. Thus, allowing to have excellent spatial resolution and DOI information, which will allow time correction on the detector side. Hence, a future where a TOF-PET scanner is composed by monolithic crystals made of a certain perfect material could be feasible.

- The next step on the gamma detection corresponds to the photodetector. The SiPM is consolidated as the standard photosensor for TOF-PET imaging. Properties such

as electromagnetic insensitivity, high PDE and impressive SPTR makes it the perfect candidate. Although this are the desired properties of a SiPM, the future technology should achieve an intrinsic SPTR below 10 ps, which nowadays is reaching its limit somewhere about 50 ps. In this road map, the future photodetector has to overcome the actual PDE of >60%, decreases the correlated and uncorrelated noise, and also increase the time resolution. Some implementations such as the Through Silicon Vias (TSV) which increases the PDE, or the trenches between microcells which decreases the crosstalk noise are insufficient to achieve this goal and extra research and technology developments are needed.

- Finally the front-end electronics is the responsible for the readout of the signal generated from the SiPM and extract the energy and time information. Nowadays the ASICs are replacing desecrate components for SiPM readouts as they are much more compact and power saving, which is a key factor in a full ring of a PET scanner. HRFlexToT, the ASIC used in this thesis, will have subsequent versions trying to reduce the electronic noise as much as possible. At the same time, different approaches such as 3D integration, where the SiPM and the ASIC are mounted on the same chip, are being studied in order to shorten the routing paths and therefore reduce the parasitic inductance generated by using long connection paths. Another solution consist on the analog summation of several microcells so the timing properties of the single microcells are preserved while the capacitance is reduces as seen in section 5.3. This last approach is implemented in the FASTIC chip. This ASIC was developed in our group and it will allow to test the summation approach for timing improvement.

6.4 Industrial PhD valorization

This thesis has been done under the framework of an Industrial PhD collaboration between the University of Barcelona as the academic partner, and the company Hamamatsu Photonics France sucursal in Spain as the industrial part. Thanks to that, I can speak freely to say that I had the opportunity to experience many different topics that otherwise are really restricted in a purely academic research environment, i.e. technology transfer, industrial knowledge and client needs, patent and project management... All these parts give a general idea on how the R&D are being developed and shared between academic and industry. Regarding the duration of the program, I think it is too short as a 3 year PhD involving novel technology and fabrication processes are really difficult to fit in this time lapse. In my humble opinion, an extra year is needed in order to close project with excellent results.

With that being said, the industrial PhD project as allowed me to acquire and improve many work capabilities, and it gave me the confidence to lead projects and help my co-workers in many aspects and fields, even those who was not supposed to have a strong background before I started working on it (engineering and industrial knowledge mainly).

As a result of this process, a state-of-the art electronics has been proved to have an excellent performance on TOF-PET applications in monolithic and segmented configuration. Additionally, this technology could be used in many other fields such as LIDAR and

autonomous vehicle, high energy physics, and any other with heavy requirements on timing resolution.

A

Data output example from HRFlexToT 16 channels

Table A.1 shows a data block from a captured event firing all 16 SiPM channels. #WID column indicates the channel where a pulse has being captured. The timestamp and width of every pulse is recorded. TIMESTAMP_PS column corresponds to the rising edge timestamp of a certain pulse in picoseconds. WIDTH_PS column records the pulse width duration in picoseconds. The red row shows a spurious pulse in channel 2 that must be clean out before any data analysis.

Table A.1.

#EVT	#WID	TIMESTAMP_PS	WIDTH_PS
0	0	439315942375	405071
1	0	439317439994	130323
2	1	439315938203	480429
3	1	439315938203	184759
4	2	439315939655	495799
5	2	439317439566	175376
6	2	439317892204	22474
7	3	439315936642	533505
8	3	439317439643	290792
9	4	439315939829	469100
10	4	439317439448	165128
11	5	439315937161	550903
12	5	439317440212	326096
13	6	439315947084	308327
14	6	439317439990	108784
15	7	439315941057	441237
16	7	439317440369	163705
17	8	439315939833	523682
18	8	439317440293	172520
19	9	439315946069	385058
20	9	439317439893	125731
21	10	439315936267	534110
22	10	439317439456	310883
23	11	439315938238	497047
24	11	439317439193	171407
25	12	439315936176	554656
26	12	439317438731	369130
27	13	439315942899	811329
28	13	439317439260	117349
29	14	439315939630	464054
30	14	439317439280	159110
31	15	439315941115	324682
32	15	439317439713	121136

B

Printed Circuit Board of HRFlexToT

Here the 3D images of the PCB demonstrator used in this thesis is shown. Figure B.1 and B.2 are 3D images of an HRFlexToT board capable of testing both single SiPM channels throw a simple pin connector (yellow) and 16 channel arrays by mounting a SAMTEC female (orange) connector on top.

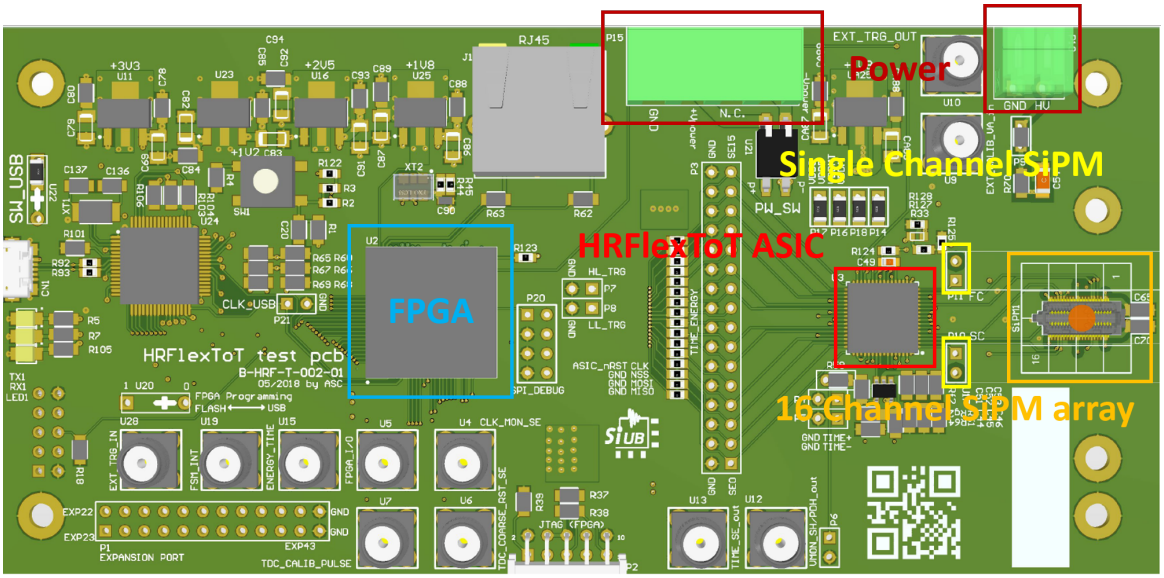

Figure B.1.: Top view for a 16 channel HRFlexToT PCB board. FPGA, ASIC and the most interesting connectors can be identified

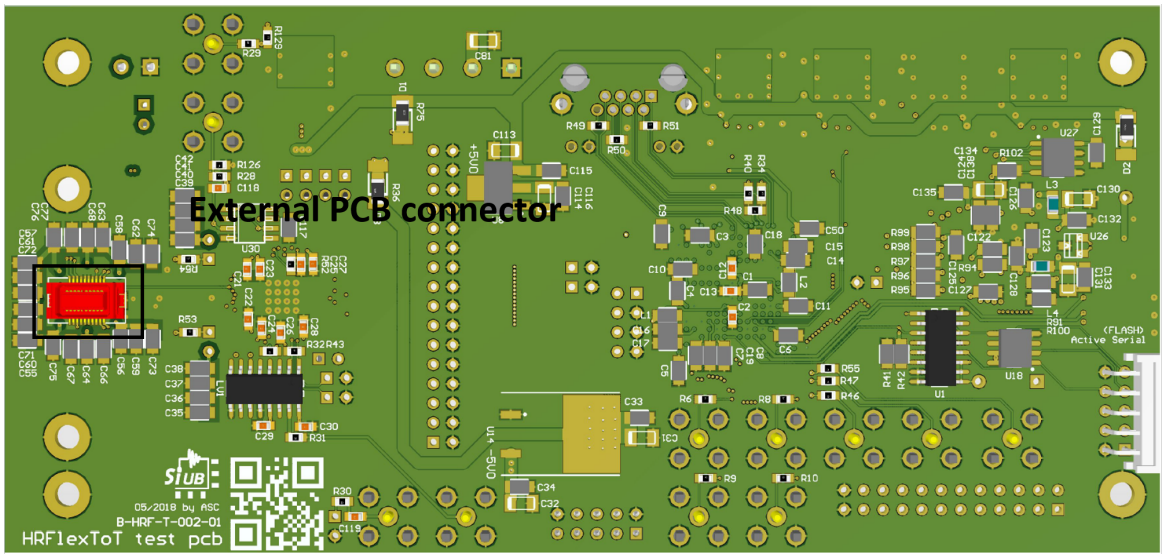

Figure B.2.: Bottom view for a 16 channel HRFlexToT PCB board. The external PCB connector for a custom SiPM PCB into the main demonstration board can be distinguished.